

# **Nanomedicines for the Treatment of** **Tuberculosis**

**Samantha Mary Kate Donnellan**  
*BSc MSc*

Submitted for the degree of Doctor of Philosophy

**Heriot-Watt University/Moredun Research Institute**

School of Life Sciences/Mycobacteria Research Group

**March 2016**

The copyright in this thesis is owned by the author. Any quotation from the thesis or use of any of the information contained in it must acknowledge this thesis as the source of the quotation or information.

---

## ABSTRACT

*Mycobacterium tuberculosis* (*Mtb*) is the bacterium responsible for the human disease tuberculosis (TB). This study aimed to develop a rapid, low cost assay for screening the anti-mycobacterial properties of new therapies. This assay employed a Green Fluorescent Protein reporter strain of *Mycobacterium avium* subspecies *paratuberculosis* (*Map*), a pathogenic species causing paratuberculosis in ruminants that can be considered a model for *Mtb*. Mycobacterial growth over time was monitored by fluorescence, testing new potential therapies including metal and drug nanoparticles (NPs), over a range of concentrations for up to 7 days. The new *Map*-based assay was sufficiently sensitive to distinguish between the toxicity of different metal/metal oxide NPs, ranked: Ag>Cu(II)O>ZnO. Solid drug NPs (SDNs) of TB antibiotics (rifampicin, isoniazid and pyrazinamide) were compared to conventional antibiotics. SDNs of rifampicin were found to be 100 times more toxic to *Map* than the conventional antibiotics. Fluorescence microscopy revealed the uptake of SDNs by infected macrophages with possible co-localisation with *Map*. Pilot data supports the ability of the SDN to kill the intracellular *Map*. These results support the benefits of nanomedicine and suggest that drug doses could be reduced, if delivered as a nano-formulation.

*First and foremost, I would like to dedicate this PhD thesis to my parents, Jessie and Nicholas.*

*You are both simply the best.*

## ACKNOWLEDGMENTS

I have thoroughly enjoyed this PhD project, which was supported by a James Watt Scholarship (Heriot Watt University and the Moredun Research Institute) and the Scottish Government Rural and Environment Science and Analytical Services Division. I would like to sincerely thank both of my supervisors, Karen Stevenson and Vicki Stone. It was inspiring to work with two leading female experts. Both of you were very approachable and supportive. I thank you both for all your help and advice these past 3 years and for your support during the mad rush at the end. Also, thank you for allowing me to attend all those conferences, I think I was particularly lucky! Additionally, warmest thanks go to Helinor Johnston, who also was involved in the supervision of this project. Your astute comments and superfast feedback was much appreciated and it was great to have someone who was a friend as well as a colleague.

I would also like to thank a number of colleagues, at Moredun and Heriot Watt for their support and input to this work. I am especially grateful to Joyce McLuckie, Craig Watkins and David Brown. All of you were an immense support during the lab work. Joyce who knew everything there was to know about culturing mycobacteria, Craig who seemed to have the solution to any problem and David who knew the answer to any question. I am grateful also to Nilesh Kanase for keeping me right with lab supplies, Daniele Pantano for guidance on using PROAST software, Hannah Ensor for comments on my data analysis, Helen Todd for microscopy training, Keith Ballingall for the lunchtime seminars and Ruth Fowler and Elisabeth Dyrynda for constructive feedback during my PhD reviews. A big thank you to Lee Innes and Julie Fitzpatrick who agreed to fund me for a 3-month extension, it was a huge help during the write-up!

Thank you to the project collaborators Andrew Owen and Marco Giardiello at the University of Liverpool, particularly Marco who answered all my millions of questions with great patience, and to Ben Swift at the University of Nottingham for last minute training on the phage assay. I also need to thank the team at Kings Building's (University of Edinburgh) for help with TEM and ICP OES (particularly Stephen Mitchell), and I really appreciate the time my new manager Giancarlo Biagini has allowed me to finish my thesis whilst at the Liverpool School of Tropical Medicine. A big thank you to Lang Tran (Institute of Occupational Medicine) for the upbeat support and encouragement, your enthusiasm for this work was infectious!

On a more personal note, I am forever indebted to my immediate family. I would like to thank my mum and sisters, Jessie, Tanya, Natasha and Freya for all their support (dog walking, cat sitting and flat moving *etc*), particularly my dad Nick for the many hours spent editing the thesis and his helpful comments throughout. Hugely appreciated! I would also like to acknowledge my two best friends Rona and Kerrie for always being at the end of a phone call, even though you both had a very tough couple of years. I am lucky to have you both. My boyfriend Stefan, a massive thank you for your genius IT skills, patience, supportive words and love these past 5 years, during both the MSc and then the PhD. It would have been much, much harder without you! Lastly, my furballs, Alvin, Lucy and Loki (and Jackson), for making me laugh every single day.

**Thank you.**

# DECLARATION



## Research Thesis Submission

---

### Declaration

In accordance with the appropriate regulations I hereby submit my thesis and I declare that:

- 1) the thesis embodies the results of my own work and has been composed by myself
- 2) where appropriate, I have made acknowledgement of the work of others and have made reference to work carried out in collaboration with other persons
- 3) the thesis is the correct version of the thesis for submission and is the same version as any electronic versions submitted\*.
- 4) my thesis for the award referred to, deposited in the Heriot-Watt University Library, should be made available for loan or photocopying and be available via the Institutional Repository, subject to such conditions as the Librarian may require
- 5) I understand that as a student of the University I am required to abide by the Regulations of the University and to conform to its discipline.

Signature of Candidate:		Date:	
-------------------------	--	-------	--

---

### Submission

Submitted By ( <i>name in capitals</i> ):	
Signature of Individual Submitting:	
Date Submitted:	

### For Completion in the Student Service Centre (SSC)

Received in the SSC by ( <i>name in capitals</i> ):			
Method of Submission ( <i>Handed in to SSC; posted through internal/external mail</i> ):			
<b>E-thesis Submitted</b> (mandatory for final theses)			
Signature:		Date:	

## **Table of Contents**

<b>ABSTRACT</b>	<b>ii</b>
<b>ACKNOWLEDGMENTS</b>	<b>iv</b>
<b>DECLARATION</b>	<b>v</b>
<b>LIST OF FIGURES</b>	<b>xi</b>
<b>LIST OF TABLES</b>	<b>xiii</b>
<b>ABBREVIATIONS</b>	<b>xiv</b>
<b>CHAPTER I</b>	<b>1</b>
<b>INTRODUCTION</b>	<b>1</b>
<b>1.1 Mycobacteria</b>	<b>2</b>
1.1.1 <i>Mycobacterium tuberculosis</i> Complex (MTBC) Evolution	3
1.1.2 MTCB Lineages	6
<b>1.2 The Mycobacterial Cell Envelope</b>	<b>7</b>
<b>1.3 <i>Mycobacterium tuberculosis</i> (Mtb) and tuberculosis (TB)</b>	<b>8</b>
1.3.1 World TB	10
1.3.2 Main points from recent WHO reports	10
1.3.3 TB in the United Kingdom	14
1.3.4 TB Funding	16
<b>1.4 Aetiology of TB</b>	<b>17</b>
<b>1.5 Pathogenesis</b>	<b>17</b>
1.5.1 Intracellular Survival of <i>Mtb</i>	21
1.5.2 Adaptive immunity	22
1.5.3 Primary and Secondary TB	23
1.5.4 Clinical Symptoms	24
<b>1.6 Diagnosis of TB</b>	<b>25</b>
<b>1.7 TB vaccine</b>	<b>28</b>
1.7.1 <i>M. bovis bacillus</i> Calmette-Guerin (BCG) vaccine	28
1.7.2 Vaccine development	29
1.7.2.1 MVA85A	29
1.7.2.2 M72 +AS01E	30
1.7.2.3 <i>M. vaccae</i>	30
<b>1.8 Current Treatments</b>	<b>31</b>
<b>1.9 The Antibiotic Apocalypse</b>	<b>36</b>
1.9.1 Problems with current treatments	37
1.9.2 The Yin-Yang model	39
1.9.3 Mechanisms of <i>Mtb</i> Drug Resistance	40
<b>1.10 <i>Mycobacterium avium</i> subsp. <i>paratuberculosis</i></b>	<b>43</b>
1.10.1 Aetiology of Johne's disease	44
1.10.2 Diagnosis of Johne's disease	44
1.10.4 Crohn's disease	45
1.10.5 <i>Map</i> K10 strain	46
<b>1.11 Nanotechnology</b>	<b>47</b>
1.11.1 Nanomedicine	48

1.11.2 Health Implications of NPs	52
<b>1.12 NPs and TB: current literature review</b>	<b>57</b>
<b>1.13 Summary</b>	<b>63</b>
<b>1.14 PhD Proposal</b>	<b>64</b>
<b>CHAPTER II</b>	<b>65</b>
<b>GENERAL METHODS AND MATERIALS</b>	<b>65</b>
<b>2.1 Culture of mycobacteria (using aseptic techniques in a microbiological safety cabinet [class 2])</b>	<b>66</b>
2.1.1 Growth conditions	66
2.1.2 Sub-culturing: broth cultures	66
2.1.3 Sub-culturing: slopes	67
2.1.4 Preparation of glycerol stocks	67
2.1.5 Retrospective colony counts	67
<b>2.2 Nanoparticles (NPs)</b>	<b>68</b>
2.2.1 Preparation	68
2.2.2 Dynamic light scattering (DLS)	68
<b>2.3 Macrophage (J774A.1) cells</b>	<b>69</b>
2.3.1 Macrophage cell culture conditions	69
2.3.2 Macrophage stocks (storage)	69
2.3.3 Macrophage stocks (revival)	70
<b>2.4 Alamar blue assay</b>	<b>70</b>
<b>2.5 Cell counts</b>	<b>71</b>
2.5.1 Macrophage counts	71
2.5.2 Mycobacteria counts	72
<b>2.6 Medium preparation</b>	<b>73</b>
2.6.1 Middlebrooks 7H9 (+ Tween 80) broth (7H9K <sup>+</sup> )	73
2.6.2 Middlebrooks 7H9 (- Tween 80) broth (7H9K)	73
2.6.3 Middlebrooks 7H11 agar	73
2.6.4 RPMI	74
<b>2.7 Fixatives</b>	<b>74</b>
2.7.1 4% Paraformaldehyde	74
2.7.2 3% Glutaraldehyde in 0.1M sodium cacodylate	75
<b>CHAPTER III</b>	<b>76</b>
<b>FLUORESCENCE MICROTITER ASSAY FOR SCREENING THE ANTI-MYCOBACTERIAL PROPERTIES OF NPS</b>	<b>76</b>
<b>3.1 Introduction</b>	<b>77</b>
3.1.1 Virtual screening	78
3.1.2 High throughput screening	79
3.1.3 Aims	84
<b>3.2 Materials and Methods</b>	<b>85</b>
3.2.1 Mycobacterium avium subsp. paratuberculosis (Map) K10/GFP: the surrogate organism	85
3.2.2 A new protocol for screening the anti-mycobacterial properties of NPs	86
3.2.3 Mycobacterial growth on solid agar	87
<b>3.3 Results</b>	<b>88</b>

3.3.1 Bacterial Growth: monitored by McF and fluorescence	88
3.3.2 Fluorescent microtiter assay optimisation	91
3.3.3 Fluorescence microtiter assay	95
3.3.4 Processing raw fluorescence data: novel approach	96
<b>3.4 Discussion</b>	<b>97</b>
3.4.1 Assay optimisation	97
3.4.2 Assay advantages	99
3.4.3 Assay disadvantages	100
3.4.4 Assay improvements	101
3.4.5 Next steps	102
<b>3.5 Conclusions</b>	<b>103</b>
<b>CHAPTER IV</b>	<b>104</b>
<b>ANTI-MYCOBACTERIAL PROPERTIES OF METAL/METAL OXIDE NPS</b>	<b>104</b>
<b>4.1 Introduction</b>	<b>105</b>
<b>4.1.1 NP selection</b>	<b>106</b>
4.1.1.1 Ag NPs	106
4.1.1.2 Cu(II)O NPs	108
4.1.1.3 ZnO NPs	109
4.1.2 Aims	110
<b>4.2 Methods and Materials</b>	<b>111</b>
4.2.1 NP preparation and characterisation	111
4.2.1.1 Transmission electron microscopy (TEM)	111
4.2.1.2 DLS	112
4.2.2 Metal salt controls	112
4.2.3 Inductively coupled plasma optical emission spectrometry (ICP-OES)	112
4.2.3.1 Ionic fraction analysis	113
4.2.3.2 Total concentrations analysis	113
4.2.4 Metal/Metal Oxide NP 96 well Plate setup for toxicity assessment	114
4.2.5 Data Analysis for fluorescence assay	115
4.2.6 Colony counts	115
4.2.7 Cytotoxicity of NPs to macrophages	116
4.2.8 Imaging	116
4.2.8.1 Infected macrophages treated with metal/metal oxide NPs for TEM imaging	116
4.2.8.2 Macrophages treated with metal/metal oxide NPs for fluorescence imaging	117
<b>4.3 Results</b>	<b>118</b>
4.3.1 NP Characterisation	118
4.3.1.1 DLS	119
4.3.1.2 TEM	122
4.3.2 Assessment of NP Dissolution (ICP-OES)	127
4.3.3 Anti-mycobacterial properties of NP	129
4.3.4 Anti-mycobacterial properties of NPs compared with salt controls	134
4.3.5 Colony Counts	138
4.3.6 Cytotoxicity of NPs to macrophages	140
4.3.7 Imaging macrophages following treatment with metal/metal oxide NPs	142
<b>4.4 Discussion</b>	<b>149</b>
4.4.1 Ag and AgNO <sub>3</sub>	155
4.4.2 Cu(II)O and CuSO <sub>4</sub>	157
4.4.3 Zn and ZnCl <sub>2</sub>	158
<b>4.5 Conclusions</b>	<b>160</b>



**SOLID DRUG NANOPARTICLES: SCREENING THEIR EFFICACY AND UPTAKE INTO MACROPHAGES** \_\_\_\_\_ **161**

<b>5.1 Introduction</b>	<b>162</b>
5.1.1 Current treatments: the costs and complications	162
5.1.2 The intracellular pathogen	165
5.1.3 Solid drug nanoparticles (SDNs)	168
5.1.4 Aims	169
<b>5.2 Methods and Materials</b>	<b>170</b>
5.2.1 SDN development	170
5.2.2 SDN Preparation and characterisation	170
5.2.3 Aqueous drug preparation	171
5.2.4 Dynamic light scattering	171
5.2.5 SDN 96 well plate setup	171
5.2.6 Colony counts	172
5.2.7 Cytotoxicity of substances to macrophages	172
5.2.8 Macrophage infections and drug treatments	173
5.2.8.1 Infection	173
5.2.8.2 Macrophage uptake of SDNs	174
5.2.9 Staining and fixed cell imaging	175
5.2.10 Phage amplification assay to quantify viable mycobacteria following drug contact	175
5.2.11 Data analysis	177
<b>5.3 Results</b>	<b>178</b>
5.3.1 SDN characterisation	178
5.3.1.1 Particle drug loading	178
5.3.1.2 DLS	178
5.3.2 Screening the anti-mycobacterial properties of SDNs and aqueous drugs against Map K10/GFP	180
5.3.2.1 Statistical Analysis 1	182
5.3.2.2 Statistical Analysis 2	188
5.3.2.3 Statistical Analysis 3	191
5.3.2.4 Statistical Analysis 4	193
5.3.3 Colony Counts	196
5.3.4 Cytotoxicity of substances to macrophages	198
5.3.5 Map K10/GFP macrophage infection	199
5.3.6 Uptake of SDNs by macrophages	204
5.3.6.1 Macrophages and 20 nm carboxylated polyester NP beads	204
5.3.6.2 Macrophages and uptake of SDNs	207
5.3.6.3 Macrophages and SDNs: 3D images	211
5.3.7 Map K10/GFP infected macrophages and SDNs	214
5.3.7.1 RIF SDNs and infected macrophages	214
5.3.7.2 TRIPLE SDNs and infected macrophages	218
5.3.8 Excitation/emission crosstalk	220
5.3.9 Intracellular fluorescence intensity	221
5.3.10 Phage amplification assay to quantify viable mycobacteria following drug contact	222
<b>5.4 Discussion</b>	<b>225</b>
5.4.1 SDNs: an overall summary	226
5.4.1.1 DLS	227
5.4.1.2 TRIPLE SDNs	227
5.4.1.3 DUAL SDN	228
5.4.1.4 RIF SDNs and aqueous drug	229

5.4.1.5 SDN drug loading	230
5.4.2 Cytotoxicity to macrophages	230
5.4.3 Macrophage infection models	231
5.4.4 Intracellular killing of <i>Map</i> K10/GFP	233
5.4.5 Other studies	234
5.4.6 Future work with SDNs	237
5.4.7 Conclusions	238
<b>CHAPTER VI</b>	<b>240</b>
<b>GENERAL DISCUSSION</b>	<b>240</b>
6.1 Final Discussion	241
6.2 Future work	246
6.3 Concluding remarks	247
<b>APPENDICES</b>	<b>249</b>
<i>Appendix A</i>	249
<i>Appendix B</i>	252
<i>Appendix C</i>	262
<b>PUBLISHED ARTICLE AND PRESENTATIONS</b>	<b>263</b>
<b>LIST OF REFERENCES</b>	<b>274</b>

## LIST OF FIGURES

<b>CHAPTER 1</b>	<b>PAGE</b>
<b>Figure 1.1</b> Global phylogeography of MTBC	<b>6</b>
<b>Figure 1.2</b> Basic Structure of <i>Mtb</i> Cell Wall	<b>7</b>
<b>Figure 1.3</b> Estimated TB Incident Rates, 2014	<b>12</b>
<b>Figure 1.4</b> Number of MDR TB cases estimated to occur among the 2014 pulmonary cases	<b>13</b>
<b>Figure 1.5</b> Number of Patients with confirmed XDR-TB on treatment	<b>13</b>
<b>Figure 1.6</b> Three-year average TB rates by local authority health boards in the UK, 2011-13	<b>15</b>
<b>Figure 1.7</b> TB funding 2011-13 (\$, million) showing donors on the left and recipients on the right	<b>16</b>
<b>Figure 1.8</b> Schematic diagram of a TB Granuloma Complex	<b>20</b>
<b>Figure 1.9</b> The Yin-Yang models of (a) persisters and replicating bacteria and (b) latent infection (LITB) and overt disease	<b>39</b>
<b>Figure 1.10</b> Schematic diagram of a 'native' drug compared to a nanomedicine passing through a barrier	<b>52</b>
<b>Figure 1.11</b> Preparation of Glu-CS-PLGA+RIF NPs	<b>60</b>
<b>CHAPTER 3</b>	
<b>Figure 3.1</b> The recombinant plasmid pWES4	<b>86</b>
<b>Figure 3.2 (a-b)</b> Biphasic growth of <i>Map</i> K10/GFP over 35 days in 10 mL cultures in 7H9K <sup>+</sup> and Biphasic growth of wildtype <i>Map</i> K10 over 35 days in 10 mL cultures in 7H9K <sup>+</sup>	<b>89</b>
<b>Figure 3.3</b> Growth of <i>Map</i> K10/GFP over 11 days in 10 mL cultures in 7H9K <sup>+</sup> (using McF standards) at different passage numbers	<b>90</b>
<b>Figure 3.4</b> Growth of <i>Map</i> K10/GFP over 7 days monitored by fluorescence in 7H9K <sup>+</sup>	<b>90</b>
<b>Figure 3.5 (a-b)</b> Assay Optimisation: determining plate type and determining colony forming units (CFU) per well	<b>93</b>
<b>Figure 3.6</b> The 96 well plate set up for NP/drug efficacy screening	<b>94</b>
<b>Figure 3.7</b> <i>Map</i> K10/GFP growth with hygromycin in 200 $\mu$ L of 7H9 in a microtiter format	<b>95</b>
<b>CHAPTER 4</b>	
<b>Figure 4.1</b> Schematic drawing of a bacterial structure	<b>108</b>
<b>Figure 4.2</b> Size intensity graphs (DLS)	<b>121</b>
<b>Figure 4.3</b> TEM-images of NP suspensions in 7H9 medium and distilled water	<b>124-126</b>
<b>Figure 4.4</b> Ionic analysis using ICP-OES: Assessment of dissolution of the NPs and salts in 7H9	<b>128</b>
<b>Figure 4.5</b> A measure of the total amount of metal in each solution using ICP-OES	<b>128</b>
<b>Figure 4.6</b> Viability Testing: data transformation	<b>131-132</b>
<b>Figure 4.7</b> Growth of <i>Map</i> K10/GFP with 3 NPs normalised to the control	<b>133</b>
<b>Figure 4.8</b> NP v Metal Salt Efficacy against <i>Map</i> K10/GFP	<b>134</b>
<b>Figure 4.9</b> NP v Salt efficacy: comparison between NP and salt controls on the growth of <i>Map</i> K10/GFP NP normalised to the control	<b>136</b>
<b>Figure 4.10</b> The half maximal effective concentration (EC <sub>50</sub> ) for each compound with the upper and lower 90% confidence intervals	<b>137</b>
<b>Figure 4.11</b> Colony counts after 12 weeks culture on 7H11 agar	<b>139</b>
<b>Figure 4.12</b> NP cytotoxicity 96 well plate following 24-hour incubation with ZnO NPs	<b>141</b>
<b>Figure 4.13</b> NP cytotoxicity to macrophages after 24-hour incubation.	<b>141</b>
<b>Figure 4.14</b> Macrophages by TEM	<b>142</b>

<b>Figure 4.15</b>	Macrophages following treatment with NPs	<b>144-146</b>
<b>Figure 4.16</b>	NP treated (12.5 µg/mL) macrophage by fluorescence microscopy	<b>147</b>
<b>Figure 4.17</b>	<i>Map</i> K10/GFP by TEM	<b>148</b>
<b>Figure 4.18</b>	J774.1 cells incubated with 10 µg/mL Ag NPs	<b>156</b>
<hr/> <b>CHAPTER 5</b> <hr/>		
<b>Figure 5.1</b>	Schematic diagram of an SDN (e.g. RIF) with stabilising excipients.	<b>169</b>
<b>Figure 5.2</b>	Growth of <i>Map</i> K10/GFP with different substances normalised to the control	<b>181</b>
<b>Figure 5.3</b>	Comparison between the substances on the growth of <i>Map</i> K10/GFP normalised to the control and re-plotted in PROAST 38.9	<b>184</b>
<b>Figure 5.4</b>	The half maximal effective concentration (EC <sub>50</sub> ) for each treatment with the upper and lower 95% confidence intervals	<b>185</b>
<b>Figure 5.5</b>	Calculating the EC <sub>50</sub> (a and b)	<b>187</b>
<b>Figure 5.6</b>	Impact of RIF SDN on mycobacterial growth.	<b>190</b>
<b>Figure 5.7</b>	Impact of RIF aqueous on mycobacterial growth	<b>190</b>
<b>Figure 5.8</b>	Treatment data summary	<b>192</b>
<b>Figure 5.9</b>	Colony counts after 12 weeks culture on 7H11 agar.	<b>197</b>
<b>Figure 5.10</b>	SDN/drug cytotoxicity to macrophages after 24-hour incubation.	<b>198</b>
<b>Figure 5.11</b>	Controls for optimisation: macrophages with nuclei stain	<b>201</b>
<b>Figure 5.12</b>	Controls for optimisation: macrophages with nuclei and F-actin stain	<b>201</b>
<b>Figure 5.13</b>	Infected macrophages	<b>202</b>
<b>Figure 5.14</b>	<i>Map</i> K10/GFP infected macrophage	<b>203</b>
<b>Figure 5.15</b>	Control for optimisation: macrophages exposed to NP beads.	<b>205</b>
<b>Figure 5.16</b>	Control for optimisation: infected macrophages exposed to NP beads.	<b>206</b>
<b>Figure 5.17</b>	RIF SDN treatment to macrophages	<b>209</b>
<b>Figure 5.18</b>	TRIPLE SDN treatment to macrophages	<b>210</b>
<b>Figure 5.19</b>	Separated Z-stacks of macrophages following 4 hour incubation with 10 µg/mL RIF SND	<b>212</b>
<b>Figure 5.20</b>	3D images	<b>213</b>
<b>Figure 5.21</b>	Infected macrophages treated with RIF SDNs	<b>215</b>
<b>Figure 5.22</b>	3D image of infected macrophages	<b>215</b>
<b>Figure 5.23</b>	Infected macrophages with TRIPLE SDN	<b>216</b>
<b>Figure 5.24</b>	Infected macrophages with RIF SDN	<b>218</b>
<b>Figure 5.25</b>	Infected macrophages with TRIPLE SDN	<b>219</b>
<b>Figure 5.26</b>	Crosstalk test	<b>220</b>
<b>Figure 5.27</b>	Control test: GFP intensity	<b>221</b>
<b>Figure 5.28</b>	Positive control ( <i>Map</i> K10/GFP with no treatment following lysing of macrophage cells).	<b>222</b>
<b>Figure 5.29</b>	Plaque forming units (pfu/mL) counted for each treatment	<b>224</b>

## **LIST OF TABLES**

<b>CHAPTER 1</b>		<b>PAGE</b>
<b>Table 1.1</b>	TB Patterns from the WHO Global TB Reports	<b>12</b>
<b>Table 1.2</b>	Recent UK TB cases	<b>15</b>
<b>Table 1.3</b>	First Line TB Drugs	<b>33</b>
<b>Table 1.4</b>	Second Line TB Drugs	<b>34</b>
<b>Table 1.5</b>	MDR TB Drugs	<b>35</b>
<b>Table 1.6</b>	Some main factors influencing the development of MDR/XDR and treatment problems	<b>42</b>
<hr/>		
<b>CHAPTER 4</b>		
<b>Table 4.1</b>	Mechanisms and the attributes of metal/metal oxide NPs toxicity to bacterial	<b>110</b>
<b>Table 4.2</b>	NP Information. The nominal sizes and properties as provided by the supplier	<b>118</b>
<b>Table 4.3</b>	Kermanizadeh <i>et al.</i> , (2013) Characterisation Data	<b>118</b>
<b>Table 4.4</b>	DLS Results	<b>120</b>
<b>Table 4.5</b>	$\beta$ Values	<b>132</b>
<b>Table 4.6</b>	EC <sub>50</sub> value for each substance with the lower (CEDL) and upper (CEDU) 90% confidence intervals	<b>137</b>
<hr/>		
<b>CHAPTER 5</b>		
<b>Table 5.1</b>	Drug types and drug loading (%)	<b>179</b>
<b>Table 5.2</b>	DLS Results	<b>179</b>
<b>Table 5.3</b>	EC <sub>50</sub> value for each substance with the lower (CEDL) and upper (CEDU) 95% confidence intervals	<b>196</b>
<b>Table 5.4</b>	Difference in bacteria growth between days when treated with RIF SDN	<b>195</b>
<b>Table 5.5</b>	Difference in bacteria growth between days when treated with RIF aqueous	<b>195</b>

## ABBREVIATIONS

AFU	Arbitrary fluorescent units
AIDS	Acquired immune deficiency syndrome
API	Active Pharmaceutical Ingredient
BCG	Bacillus Calmette–Guérin
BDQ	Bedaquiline
CEDL	Lower 90% confidence intervals
CEDU	Upper 90% confidence intervals
CFU	Colony forming units
DIC	Differential interference contrast
DiD	4-Chlorobenzenesulfonate salt
DLS	Dynamic light scattering
DNA	Deoxyribonucleic acid
DOTS	Directly overserved treatment short course
DUAL SDN	Dual drug combination nanoparticle (RIF and INH)
DW	Distilled water
EMB	Ethambutol
GFP	Green fluorescent protein
HIV	Human immunodeficiency virus infection
HTS	High throughput screening
EC <sub>50</sub>	Half maximal inhibitory concentration
ELISA	Enzyme-linked immunosorbent assay
ICP OES	Inductively coupled plasma optical emission spectrometry
INH	Isoniazid
J774A.1	Macrophage
LTBI	Latent TB infection
<i>M.</i>	<i>Mycobacterium</i>
<i>Map</i> K10/GFP	<i>Mycobacterium avium</i> . subsp <i>paratuberculosis</i> GFP
McF	McFarland standards
MDR	Multiple drug resistant tuberculosis
MOI	Multiplicity of infection
MDGs	Millennium Development Goals
mL	Milliliter
mM	Millimolar
<i>Mtb</i>	<i>Mycobacterium tuberculosis</i>
MTBC	<i>Mycobacterium tuberculosis</i> complex
NA	Not applicable
NPs	Nanoparticles
NMs	Nanomaterials
nm	Nanometer
OD	Optical density
PBS	Phosphate buffer saline
PCR	Polymerase chain reaction
PLGA	Poly (lactide-co-glycolide) acid
PZA	Pyrazinamide
RIF	Rifampicin
RIF SDN	Rifampicin solid drug nanoparticle
RNS	Reactive nitrogen species
ROS	Reactive oxygen species
SDN	Solid drug nanoparticle

STR	Streptomycin
TB	Tuberculosis
TEM	Transmission Electron Microscopy
TRIPLE SDN	Triple drug combination nanoparticle (RIF, INH and PZA)
µg	Microgram
UK	United Kingdom
µL	Microliter
µM	Micromolar
WHO	World health organisation
XDR TB	Extensively drug resistant tuberculosis

*"It is the over-crowded dwellings of the poor that we have to regard as the real breeding places of consumption; it is out of them that the disease always crops up; and it is to the abolition of these conditions that we must first and foremost direct our attention if we wish to attack the evil at its root and wage war against it with effective weapons."*

**Dr. Robert Koch, 1901, the 'father of the scientific study of tuberculosis'**

The Journal of Laryngology, Rhinology, and Otology / Volume 16 / Issue 08 / August 1901, pp 387-402



# **CHAPTER I**

## **INTRODUCTION**

## 1.1 Mycobacteria

*Mycobacterium* is the sole genus in the *Mycobacteriaceae* family, some members of which cause many serious infectious diseases in humans and animals. Mycobacteria belong to the order Actinomycetales, which comprises the genera, *Corynebacterium*, *Mycobacterium*, *Nocardia* (the CMN group) and *Rhodococcus* (Cocito et al. 1994; Barry & Beaman 2006). CMN members are aerobic, non-motile, non-spore forming bacilli which possess a complex, thick cell wall rich in lipids and glycolipids with a unique outer cell membrane. Cell walls of CNM group members contain mycolic acids, long chain fatty acids, highly impermeable to many solutes, which makes the cell waterproof. The mycobacteria grouped within the *Mycobacterium tuberculosis* complex (MTBC) match by 99.9% at the nucleotide level, but vary in their host selection, phenotypes and pathogenicity (Brosch et al. 2002). Rare synonymous single-nucleotide polymorphisms (sSNP) in the genomes have allowed for identification of individual mycobacterial species, which has provided vital information on the evolution and origin of the family (Smith 2003). Within MTBC, the closely related species are zoonotic and generally infect different hosts. They include *Mycobacterium tuberculosis* (*Mtb*), *Mycobacterium* (*M.*) *bovis* (and the *Bacillus Calmette–Guérin* [BCG] strain), *M. africanum*, *M. microti*, *M. caprae*, *M. canetti* and *M. pinnipedii* (Hussain et al. 2013). The *Mycobacterium avium* complex (MAC) is a large group of related mycobacteria, which includes *M. avium* subsp. *avium*, *M. avium* subsp. *paratuberculosis*, *M. avium* subsp. *silvaticum* and *M. avium* subsp. *hominissuis*.

### **1.1.1 *Mycobacterium tuberculosis* Complex (MTBC) Evolution**

The closely related bacterial species and sub-species of the MTBC have caused human and animal diseases for many thousands of years, with *Mtb* being a predominant killer by humans in causing tuberculosis (TB) (Smith 2003). Humans are the only known host where infection by *Mtb* and *M. africanum* causes TB with rapid and efficient transmission. It was originally believed that *Mtb* originated from *M. bovis*, appearing when cattle were very first domesticated and farmed (Collins 1997; Smith 2003). Domestication of cattle is thought to have occurred some 10,000-25,000 years ago, and early findings suggest that bacteria in the genus *Mycobacterium* originated in the soil, where they readily passed to mammalian hosts, such as cattle (Smith 2003). As such, it was believed that *M. bovis* was the evolutionary precursor of *Mtb*. However, this hypothesis is now widely contradicted in the literature. It is hypothesised, due to sSNP data analysis, *Mtb* and *M. bovis* either evolved simultaneously but independently, they share the same common ancestor (e.g. *M. canetti*) or that early ancestral lineages of *Mtb* were the original cause of TB (Sreevatsan, Stockbauer, et al. 1997; Brosch et al. 2002; Smith 2003; Brites & Gagneux 2015). As aforementioned, bacterial species and sub-species of the MTBC share up to 99.9% DNA sequence but differ in their host range. As they display great levels of genetic homogeneity it is assumed that members of the group are the clonal progeny of the same single species that underwent an evolutionary bottleneck somewhere between 15,000 and 35,000 years ago (Sreevatsan, Pan, et al. 1997; Brosch et al. 2002; Gutierrez et al. 2005). Evolution of the MTBC is a complex story, yet it is generally accepted that essential, core genes were inherited (and more conserved than nonessential genes) and horizontal gene transfer occurred between species, thus allowing the acquisition of foreign DNA, aiding in the pathogenicity of species like *Mtb*. Whether this can be described as an evolutionary arms race or not, it is clear that gene transfer occurred and members of the MTBC have evolved, most likely

from an African origin (Gutierrez et al. 2005; Gagneux et al. 2006; Comas et al. 2013; Brites & Gagneux 2015).

Debate is widespread in the literature concerning the absolute origins of the MTBC with many contradictory reports existing (Brosch et al. 2002; Smith 2003; Fabre et al. 2004; Smith 2006; Comas et al. 2010; Comas et al. 2013; Brites & Gagneux 2015). By analysing the genomes of 100 strains of mycobacteria, Brosch *et al* state that MTBC descended from a human (not animal) pathogen, which is now a widely accepted hypothesis (Brosch et al. 2002). Through comparing insertions and deletions in the genomes of various strains, they suggest that *M. canetti* and/or *Mtb* are likely to be the direct descendants from a tubercle bacilli, a human pathogen, from which other strains eventually emerged. *M. canetti* is often referred to as the progenitor species from which *Mtb* evolved; yet it differs from the others in the MTBC (Gagneux 2012). Unlike other members, very smooth and shiny colonies propagate on growth medium. There is a distinct lack of reports that individuals infected with this mycobacteria are able to transmit it to others to cause disease (Gagneux 2012). Transmission of *M. canetti* among humans has not been demonstrated, therefore it is thought that they are likely attained from the environment, although it is unknown where from (Brites & Gagneux 2015).

Following the bottleneck hypothesis and knowledge of mutation rates, by characterising strains from patients from East Africa and using the DNA sequence of six housekeeping genes, Gutierrez *et al.*, propose that the MTBC emerged from an ancient species they termed '*Mycobacterium prototuberculosis*' which engulfed *M. canetti* and other smaller species (Gutierrez et al. 2005). They state that tubercle bacilli existed with early hominids in East Africa, thus making the origin date to the dawn of man at the Horn of Africa some 3 million years ago, making TB older than the plague or any other human affliction (Gutierrez et al. 2005), yet some debate about this dating theory exists (Smith 2006).

Through use of genetic markers, statistical analysis and a mathematical algorithm approach, another study reported that the MTBC is composed of two major lineages; one composed of *Mtb* lineages from humans only and the other of both animal and human isolates, thus further suggesting an original human host (not animal) (Wirth et al. 2008). They report that this coincides with the beginning of modern human populations migrating from the Horn of Africa into settlements approximately 40,000 years ago (Wirth et al. 2008). Wirth *et al.*, also termed the first tubercle bacilli '*Mycobacterium prototuberculosis*' from which the MTBC clone emerged from the progenitor pool, that co-migrated with humans out of Africa (Wirth et al. 2008; Gutierrez et al. 2005). This report affirms that humans most likely infected their livestock; cattle and goats, which were the first to be domesticated and not the other way around (Wirth et al. 2008).

Comas *et al.*, created a global genome-wide phylogeny using next generation DNA sequencing for 220 strains in the MTBC to demonstrate the evolutionary relationship between members of the MTBC (Fig 1.1) (Comas et al. 2010). Using sequencing techniques and statistical modelling this work supports the theories that TB originated in Africa, *Mtb* evolved with its human host at least 70,000 years ago, an increase in population size (not zoonotic transfer) was responsible for MTBC's success and that member species have adapted with the changing human populations to ensure survival (Comas et al. 2013). It is possible that members of the MTBC did not follow the typical evolutionary arms race of evolution, but have instead evolved to suit their host, by immune subversion (Comas et al. 2010).

A recent review by Gutierrez *et al* (2015) conclude that recent studies on the evolution of the MTBC concur on their main hypotheses; co-evolution of humans and some MTBC lineages occurred yet there is debate among reports on a 'molecular' clock for MTBC.

### 1.1.2 MTCB Lineages

There are 6 phylogenetically distinguished human lineages identified from around the globe: Lineage 1 (Indo-Oceanic), Lineage 2 (East Asian) Lineage 3 (Central and South Asia/East Africa), Lineage 4 (Euro-American), Lineage 5 ([*M. africanum*] West African 1) and Lineage 6 ([*M. africanum*] West African 2) (Fig 1.1) (Comas et al. 2010). From the six main lineages identified *M. africanum* is the most basal and each Lineage is associated with different human populations (Comas et al. 2010). By following genetic differences and similarities between species, many individual strains have been identified. For example, following recent TB epidemics, ‘modern’ strains ‘Beijing’ (Lineage 2) and ‘Haarlem’ (Lineage 4) have been recognised through the loss of a genetic deletion (TbD1), hence all strains missing this gene are considered modern. Modern strains seem to cause a diseased state in infected patients more readily over the ancient strains, thus suggesting that modern strains have evolved to avoid latent forms of disease so they are more virulent (Gagneux 2012).

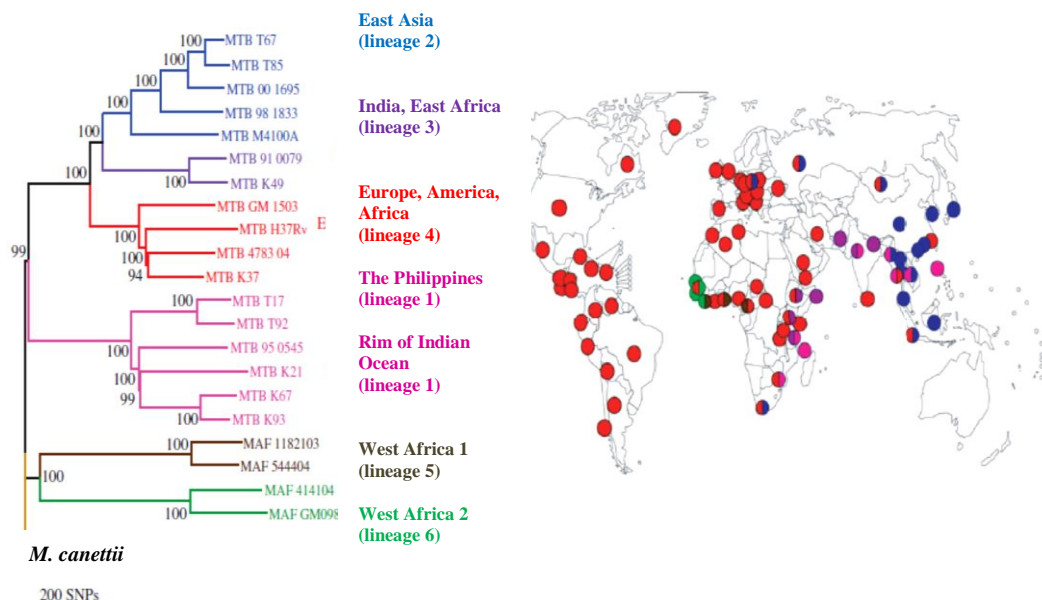


**Figure 1.1 Global phylogeography of MTBC**  
(adapted from Gagneux 2012)

## 1.2 The Mycobacterial Cell Envelope

The unique make-up of the mycobacterial envelope gives the bacteria a survival advantage over other bacterial species, making them impermeable to many drugs and insensitive to most antibiotics. It is a complex, physically resilient, layered structure made predominantly from sugars and lipids (Smith 2011), hence why mycobacteria are renowned for resistance to many compounds and chemicals (Verschoor et al. 2012). The outmost layer is called the capsule, mainly composed of glycans. Below the capsule, the cell membrane is highly concentrated in lipids with long chain,  $\beta$ -hydroxy fatty acids; mycolic acids. Mycolic acids are arranged tightly packed, perpendicular to the cell surface making the structure highly impermeable to many solutes and waterproof (Favrot & Ronning 2012). *Mtb* contain the largest of the mycolic acids ( $C_{60}$ – $C_{90}$ ), accounting for its great resilience, acid/alcohol fastness. The lipid layer is attached to a layer of arabinogalactan polysaccharides, which in turn is attached to a peptidoglycan layer that surrounds the cell phospholipid bilayer (Fig 1.2). It is this complex, layered structure that many anti-mycobacterial drugs target, such as isoniazid (INH), which affects mycolic acid synthesis.

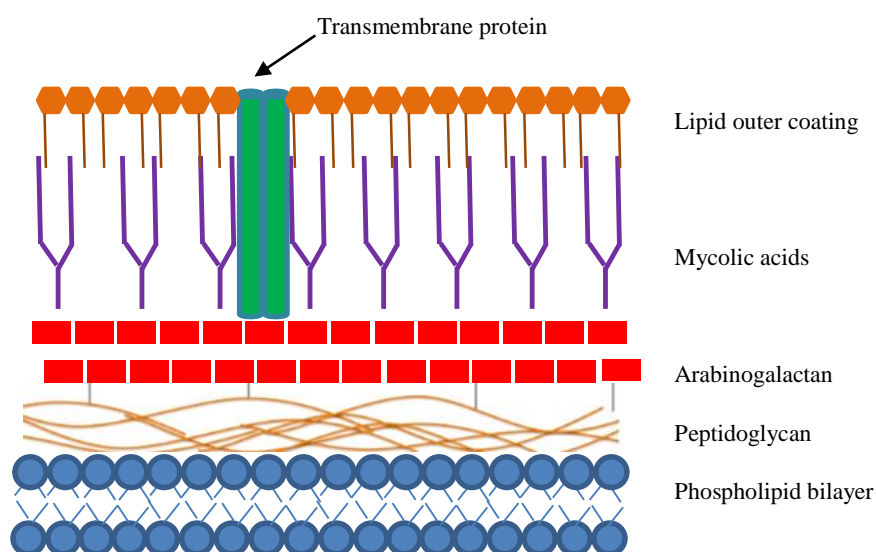


**Figure 1.2 Basic Structure of *Mtb* Cell Wall**

### 1.3 *Mycobacterium tuberculosis* (*Mtb*) and tuberculosis (TB)

*Mtb* has been of particular interest to medical science for many decades. *Mtb* developed as a facultative intracellular parasite, which usually infects and takes up residence within two of the host's immune cells; macrophages and dendritic cells. Hence, the disease is essentially a disease of the immune system. *Mtb* is an unusual bacterial species, falling somewhere between Gram-positive and Gram-negative bacteria. It has a very slow generation time dividing approximately every 16-20 hours, and a complex, waxy cell surface. TB continues to kill up to 2 million people each year (WHO 2013; WHO 2014b; WHO 2015b). A third of the world's population is estimated to be infected with latent TB (LTBI [latency is defined as the presence of an *Mtb* infection, without the diseased state of active TB]) (WHO 2015b). LTBI presents a vast reservoir of possible disease reactivation and transmission.

Skeletal remains from Neolithic Europe (8000 BC), ancient Egypt (1000 BC) and the United Kingdom (UK) during the Iron Age (800 BC) displaying evidence of TB in the form of osteotuberculosis lesions assert that this disease is not a new affliction infecting only modern populations (Collins 1997; Ohara 2012; Brites & Gagneux 2015). Although such evidence suggests that the disease has long been infecting humans (although Comas *et al* (2013) predate all archaeological evidence), it was during the Industrial Revolution of the 18<sup>th</sup> and 19<sup>th</sup> centuries that the TB rapidly spread. During this period, great influxes of individuals migrating from their rural homes to the developing cities for employment were cramped in appalling conditions, suffering from malnutrition, poor health and great physical hardship. These unsanitary working and impoverished living conditions subsequently led to a TB epidemic, as the infection positively thrives in such environments (Collins 1997). By the 20<sup>th</sup> century, the mortality rates of TB had significantly decreased through improved living conditions, the administration of



antibiotics and the use of the *M. bovis*-BCG vaccine (Cooper 2009). However, in poverty-stricken countries, infection rates and deaths from the disease are still alarmingly high, due to poor living conditions, inadequate medical supplies and antibiotic resistance. As a result, the disease is still classified as a health epidemic by the World Health Organisation (WHO) (WHO 2011; WHO 2012; WHO 2013; WHO 2014b; WHO 2015b).

After centuries of infecting humankind, TB has evolved to become the greatest killer of humans along with the Human Immunodeficiency Virus (HIV)/Acquired Immunodeficiency Syndrome (AIDS), where 95% of TB deaths occur in the developing world (Pandey & Khuller 2006; Sosnik et al. 2010; Seth et al. 2011; WHO 2014b; WHO 2015b). The ever-increasing number of drug resistant strains and the susceptibility of HIV patients to TB infection add to this burden and equates to the global crisis. Reports of ‘totally-drug resistant TB’ emerging from India only increases concerns for health practitioners (Rowland 2012). Current literature suggests that after nearly 50 years only 10 new drug candidates and 15 vaccine candidates are in the pipeline, with only the diarylquinoline Bedaquiline (BDQ) and Delamanid (in special circumstances) recently being approved by the Food and Drug Administration (FDA). The only approved vaccine is the BCG vaccine, developed almost 100 years ago, and its efficacy among adults and some ethnic populations is debatable (genetic differences, exposure to different pathogens are some possible reasons) (Ohara 2012). The disease is highly transmittable; passing from infected individuals to others when expelled through coughing and sneezing. Hence the disease prevails in countries such as Africa, India and Bangladesh where many individuals live in crowded, restricted and destitute conditions, often slums, with little access to medical aid (WHO 2012; WHO 2013; WHO 2014b; WHO 2015b).

### ***1.3.1 World TB***

The WHO has published a report on global TB annually since 1997. Last year, 2015, marked the deadline set in the Millennium Development Goals (MDGs) and ‘Stop TB Partnership’ aims whose main vision was to reduce TB deaths by 50% by 2015 (compared to 1990), and to create a TB-free world by 2050 (WHO 2014b; WHO 2015b). Established by the United Nations, MDGs offers a framework for the International community relating to improving health of the poor and reducing global poverty with a strong emphasis on TB. The Stop TB Partnership is a collective organisation including governments, funding agencies and researchers who work towards accelerating progress on TB research into diagnostics and treatments. TB deaths have been reduced by 47% since 1990 at an average rate of 1.5% per year and disease incidents in all countries surveyed has been reduced with approximately 43 million lives saved, thus being a hugely significant achievement (WHO 2015b). An annual report is produced by Public Health England, Wales, Northern Ireland and the Scottish Mycobacteria Reference Laboratory (who report to Health Protection Scotland), which covers TB incidents and rates in detail for the UK.

### ***1.3.2 Main points from recent WHO reports***

TB remains the deadliest infectious disease to humans and is present in all parts of the world surveyed with 1.5 million deaths occurring in 2014 (Table 1.1, Fig 1.3). As shown in Figure 1.3, TB remains most prevalent in developing parts of the world. Overall incidents are slowly declining, however approximately 3.5% of global cases are multi drug resistant (MDR) and 9% of these cases are considered to be extensively drug resistant (XDR) (see section 1.7) (Figs 1.4, 1.5). MDR TB cases largely occur in India and China (Fig 1.4) whereas XDR is mostly found in South Africa, Ukraine and India

(Fig 1.5). Last year, India reported the highest reports of XDR in 5 years and incidents in India are higher than elsewhere (The Times of India 2016) (Fig 1.4, 1.4). Over half of reported TB cases occurred among men (60%), but TB remains in the top three killers of women globally (WHO 2015b). Approximately 13% of global cases were HIV infected (Choudhary & Kusum Devi 2015). WHO has reported that \$8 billion (USD) is required per year for TB detection and treatment, and a new target to reduce TB deaths by 95% by 2035 has been set (WHO 2014b; WHO 2015b).

**Table 1.1 TB Patterns from the WHO Global TB Reports**  
(created using WHO 2011, 2012, 2013, 2014, 2015b)

YEAR	APPROXIMATE GLOBAL CASES OF TB*	GLOBAL INCIDENT CASES OF HIV-TB	GLOBAL TB RELATED DEATHS	GLOBAL NUMBER OF INFECTED CHILDREN (<15 years)**	MDR TB CASES	XDR TB CASES***	UK TB Cases****
2010	8.8 Million	1.1 Million	1.45 Million	-	650,000	-	8,587
2011	12 Million	1.1 Million	1.4 Million	490,000	630,000	56,700	8,963
2012	12 Million	1.1 Million	1.3 Million	530,000	450,000	43,200	8,751
2013	9 Million	1.1 Million	1.5 Million	550,000	480,000	43,200	7,863
2014	9.6 Million	1.1 Million	1.5 Million	350,000	480,000	46,560	7,077

\* Of this number, the majority of cases occurred in Asia and Africa

\*\* 2012 was the first WHO report to include the estimates of the burden of TB on children

\*\*\* 9.7% of MDR TB cases are estimated to be XDR-TB (2014)

\*\*\*\* Approx. 60% of UK cases are pulmonary

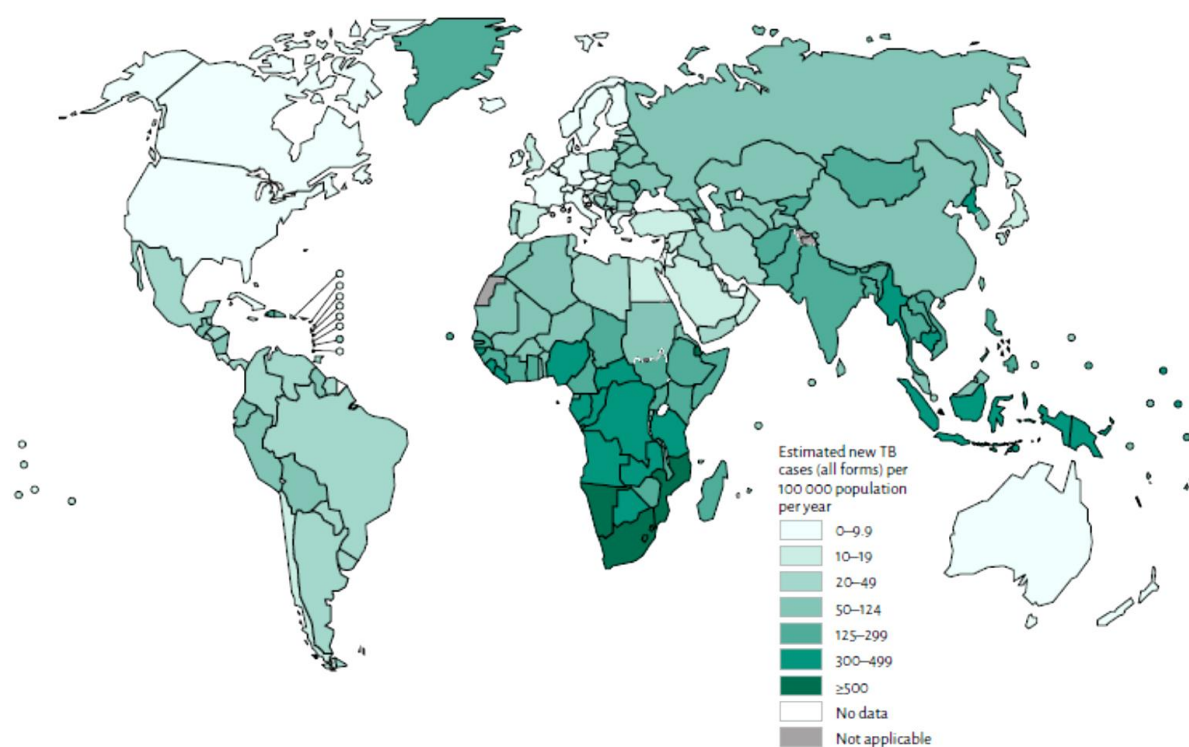


**Figure 1.3 Estimated TB Incident Rates, 2014**  
(Taken from WHO 2015b)

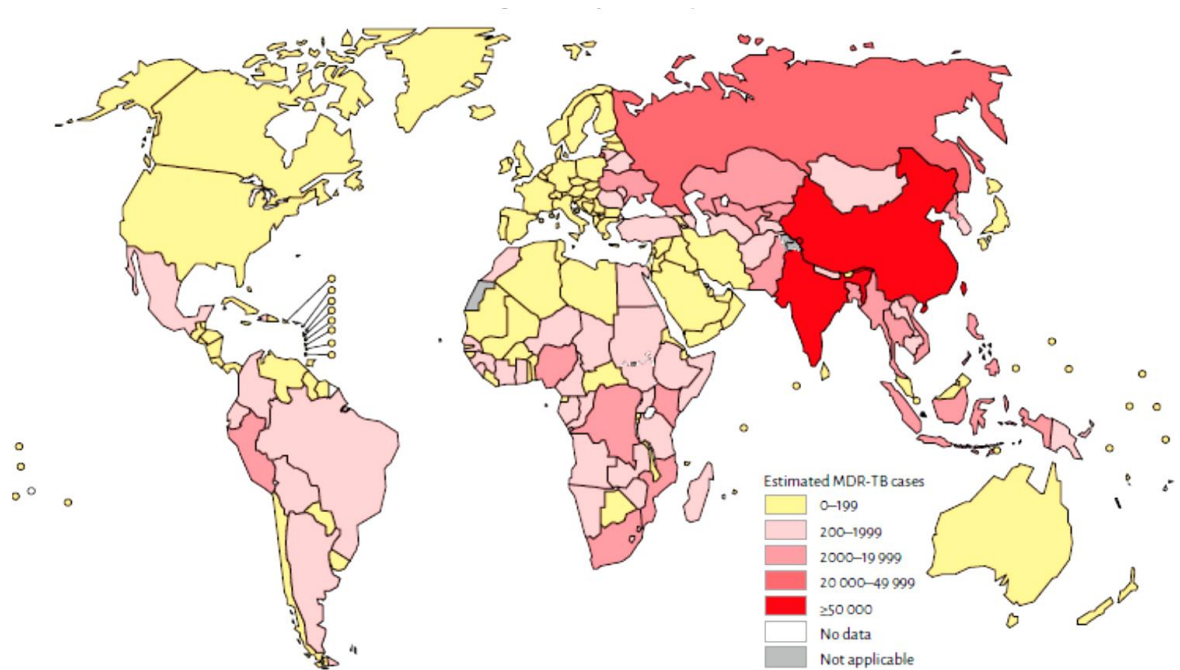


**Figure 1.4 Number of MDR TB cases estimated to occur among the 2014 pulmonary cases**  
(Taken from WHO 2015b)

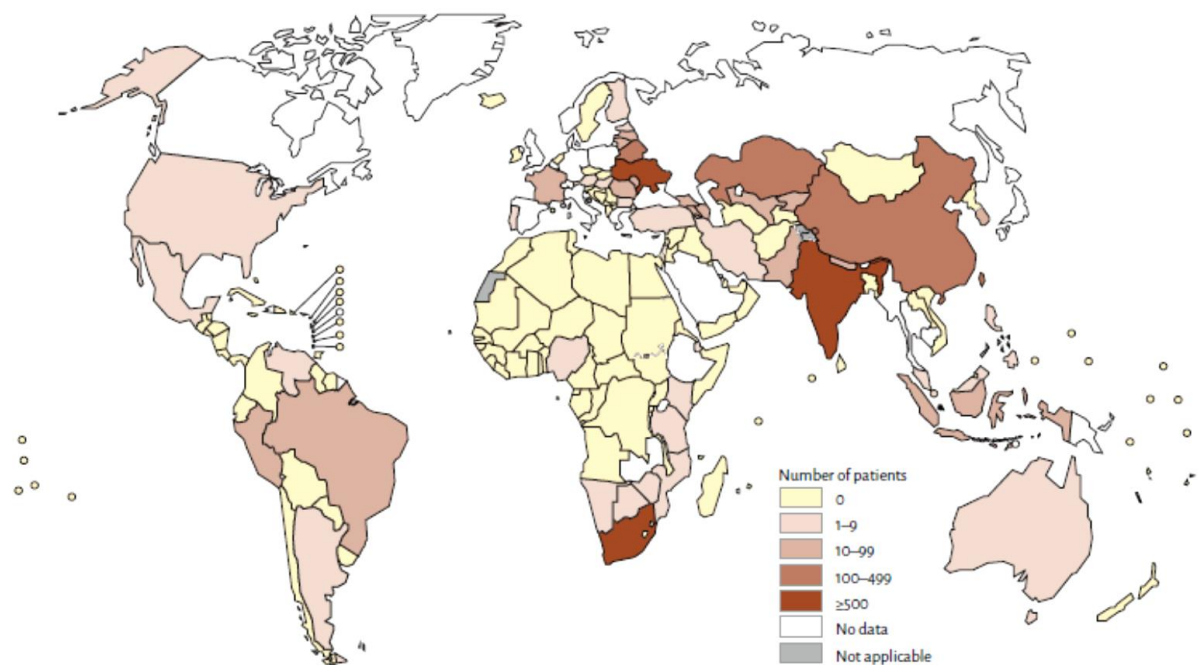


**Figure 1.5 Number of Patients with confirmed XDR-TB on treatment**  
(Taken from WHO 2015b)

### ***1.3.3 TB in the United Kingdom***

The occurrence of TB in the UK generally increased between 2000 and 2011, but there has been a gradual annual decline over the past 4 years (Public Health England 2015). TB is predominantly found in the larger cities (Fig 1.6), with current levels sitting at approximately 7,000 cases per year with 350 of these from Scotland in 2014 (Table 1.2) (Public Health England 2014b; Public Health England 2015; Health Protection Scotland 2015; Laurenson & Smith 2015). In Scotland 2014 there was an increase in the number of drug resistant cases reported (22 cases), thus being the highest number since 2000 (Health Protection Scotland 2015). The UK has the second highest rate of TB in western Europe, with many cases occurring in London and as such the NHS in England is investing £11.5 million to try to eradicate the disease here (NHS 2015). Disease incidents in the UK remain very high (73%) among those born out-with the country (e.g. India, Pakistan and Somalia) with most cases reported in deprived areas of the UK and patients having at least one social risk factor (e.g. imprisonment and/or drug, alcohol dependency) (Public Health England 2014a; Public Health England 2015). A recent news report highlighted that London now has higher rates of TB than parts of Iraq and Rwanda (BBC Health News 2015). The BCG inoculation introduced as a routine vaccine for all UK schoolchildren in 1953 was discontinued in 2005 and is now only available to children living in certain regions or those deemed to be at high risk of exposure. This is arguably not the best strategy and is linked to funding. The BCG is recommended for babies born in London, yet out of the 32 London boroughs, 24 do not offer this as a routine vaccination (BBC Health News 2015). The UK government is one of the main donors to TB funding (along with the US and Canada [Fig 1.7]) but there is a reported gap in the funding required to tackle the increase in MDR and XDR TB (WHO 2015b).

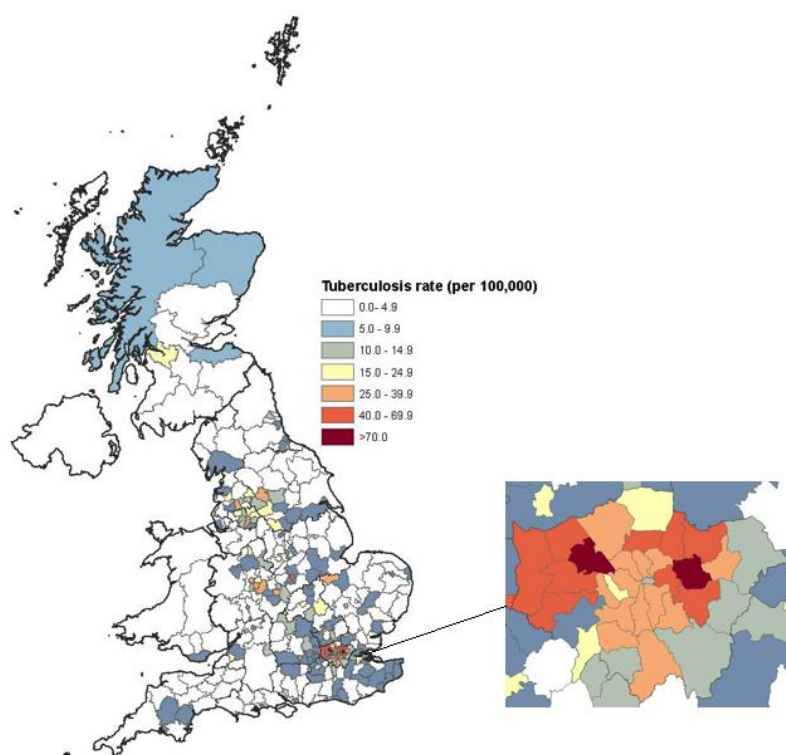


**Figure 1.6 Three-year average TB rates by local authority health boards in the UK, 2011-13 (London area enlarged).**

(taken from

[https://www.gov.uk/government/uploads/system/uploads/attachment\\_data/file/360335/TB\\_Annual\\_report\\_\\_4\\_0\\_300914.pdf](https://www.gov.uk/government/uploads/system/uploads/attachment_data/file/360335/TB_Annual_report__4_0_300914.pdf))

**Table 1.2 Recent UK TB cases**

(created using Tuberculosis in England 2015 Public Health Report, Health Protection Scotland website and the Scottish Mycobacteria Reference Laboratory Annual Report 2015)

Country	2014 TB cases	Rate per 100,000 (95% CI*)	MDR cases	Comments
<b>England (London)</b>	6520 (2,572)	12.0 (11.7 -12.3) (30.1 [29.0 -31.3])	52	Incidents of TB are unacceptably high
<b>Scotland</b>	350	6.5 (5.8 -7.2)	2	Incidents of TB are generally stable and low
<b>Wales</b>	115	3.7 (3.1 -4.5)		As above
<b>Northern Ireland</b>	95	5.2 (4.2 -6.3)		As above

\*Confidence Interval (CI)

### 1.3.4 TB Funding

Treating and diagnosing TB is very expensive. The cost of treating a drug susceptible patient is \$100-1000, whereas treating a MDR TB strain ranges from \$6000-21000 (WHO 2015b), with hospitalisation requirement being a main factor influencing costs. Approximately \$8 billion was required to respond to the global TB epidemic in 2015 (excluding funding for drug, vaccine and diagnostics development). The WHO (2015) reported that only \$6.6 billion was available in 2015, thus highlighting a significant shortfall. As shown in Figure 1.7 the USA, UK, Germany, France and the Bill and Melinda Gates foundation are main donors to TB research with Asian countries (predominantly China and India) being major recipients.

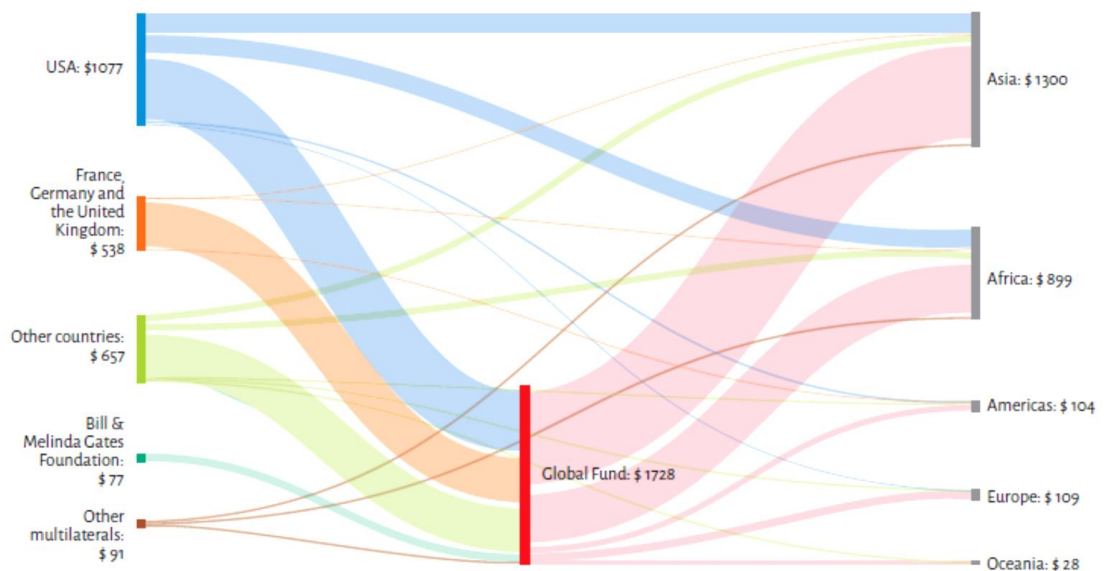


**Figure 1.7 TB funding 2011-13 (\$, million USD) showing donors on the left and recipients on the right.**  
(Taken from WHO 2015b)



## 1.4 Aetiology of TB

Historically, TB was described as “the white plague”, “the consumption” or the “wasting disease” (Ducati et al. 2006) and the aetiology was much debated throughout the 19<sup>th</sup> and 20<sup>th</sup> centuries until the persuasive work of Robert Koch in 1882. In 1865, the French surgeon Jean Antoine Villemin undertook research into the disease and through inoculation of rabbits using serum from human TB patients, he concluded that the disease was highly contagious and did not affect only certain ‘classes’ of people as proposed by Herman Pidoux who believed it to be hereditary (as did Hippocrates [460 BC]). However Villemin’s findings were initially ignored, until Koch’s research almost two decades later (Smith 2003). Koch’s work confirmed Villemin’s theory, which was later reasserted by Edward Trudeau. Koch, described as the founder of modern bacteriology, was awarded the Nobel Prize for his fundamental discovery and scientific evidence that TB was caused by an infectious bacterium. Trudeau suggested that a healthy diet, rest and fresh air aided in the survival and development of immunity from *Mtb*, thus being the rationale behind the ‘Adirondack Cottage Sanatorium,’ the first of its kind in 1884, set up for wealthy city dwellers suffering from the disease (Collins 1997). Trudeau concluded that those living in poverty were more at risk from contracting the disease and dying from it, as they were unable to receive appropriate aid, which unfortunately remains the case today.

## 1.5 Pathogenesis

*Mtb* is an acid fast, non-spore-forming, non-motile, obligate aerobe, which is long, thin, slightly curved/rod-like in shape and 2-4 µm in length. The bacilli have a thick waxy coat and tend to reside in the upper lobes of the lungs where oxygen levels are highest (Health

Protection Agency 2012). The most common route of infection is the respiratory route whereby bacteria enter through aerosol droplet nuclei (1-5  $\mu\text{M}$ ), passed from an individual infected with pulmonary or laryngeal TB to a susceptible individual through coughing and sneezing. Once infected, the time lapse to when TB develops into the active diseased state, can vary (Smith 2003). Initiating from the inhalation of tubercle bacilli into the lungs, the bacilli are ingested by alveolar macrophages and dendritic cells; the host's first line of defence (Crevel et al. 2002).

Macrophages are 'eaters' which clear cellular debris as well as foreign bacteria and are capable of engulfing particles up to 10  $\mu\text{M}$  in diameter (Byrne et al. 2011). Upon maturing from monocytes, they provide immune surveillance. Following bacterial contact with alveolar macrophages, *Mtb* is recognised as a pathogen through pattern recognition receptors that sense various components of the mycobacterial structure. This leads to a specific intracellular signalling cascade, triggering the assembly of the globular protein actin and associated proteins, initiating the secretion of pro-inflammatory cytokines (e.g. tumor-necrosis factor alpha [TNF- $\alpha$ ], interferon gamma [IFN- $\gamma$ ]) thus allowing macrophage uptake of *Mtb* into cytosolic vesicles in the phagosome, where bacteria are usually destroyed through the process of phagocytosis. The entry of *Mtb* into immune cells can occur via one of many receptor molecules due to its complex cell surface, and the entry route taken relates to the type of immune response by the host (Pieters 2008). For example, if the pathogen enters via Fc receptors, this leads to an inflammatory response within the macrophages, however if it enters the host cell via a CR3 receptor (requiring host plasma membrane cholesterol), macrophages are not activated (Byrne et al. 2011; Pieters 2008). Toll-like receptors (TLRs) interact with *Mtb*-specific ligands, leading to the uptake of *Mtb*, and initiate an intracellular signalling cascade in which induces production of cytokines thus being essential to inducing the adaptive immune response (Hossain & Norazmi 2013).

Upon bacterial uptake, phagosome-lysosome fusion occurs and undergoes a series of fusion and fission events within the endocytic pathway creating a hostile internal environment within the phagosome. Acidification, release of enzymes/toxic peptides, activation of the NADPH oxidase (which generates superoxide) and other reactive nitrogen intermediates occur, which ultimately kills most microorganisms (Smith 2003). However, studies reveal that living *Mtb* remains in vacuoles where usually dead bacteria reside following phagocytosis along the endosomal-lysosomal pathway (Crevel et al. 2002; Russell et al. 2010). In the lungs a primary lesion of inflammation; the ‘Ghon Focus’ rapidly appears, thus being the initial site of parenchymal concentration. Within the host cell, the surviving *Mtb* multiply, inhibit phagosome maturation and disrupt the macrophages. The disrupted macrophages attract other immune cells such as monocytes and dendritic cells to the infection site through the production of chemokines, leading to the second stage of infection (Crevel et al. 2002; Ehlers & Schaible 2012). Monocytes differentiate into macrophages, and again attempt to engulf and kill all the mycobacteria, but prove unsuccessful (Smith 2003). Dendritic cells (as well as others) present antigens to T-cells, thus prompting adaptive T-cell immunity, which develops to create antigen specific T lymphocytes (particularly CD4<sup>+</sup> and CD8<sup>+</sup> T-cells) that activate macrophages to destroy the *Mycobacterium* (Crevel et al. 2002; Tameris et al. 2013). This build up forms granulomas; clusters of *Mtb* infected macrophages surrounded by many immune cells (Pieters 2008), securing *Mtb*, preventing both its growth and replication due to the acidic conditions with low oxygen availability, but not destroying the pathogen or preventing it from generating energy (Smith 2003; Ehlers & Schaible 2012).

Granuloma formation is a hallmark trait of *Mtb* infection (particularly pulmonary LTBI) and plays a pivotal role in immune-pathogenesis. Their main function is to localise and contain the infection. These complex aggregates of immune cells protect the host from the infectious mycobacteria in 90% of cases, and it has been found that HIV infected

patients exhibit a lack of granulomas, further asserting their role in host protection (Ehlers & Schaible 2012). The granuloma is composed of many immune cells, blood derived infected and uninfected macrophages, epithelioid cells surrounded by lymphocytes (T-cells and B-cells) and foamy macrophages (caused by the accumulation of intracellular lipids) (Fig 1.8). The high lipid content foamy macrophages are a nutrient rich reservoir for long-term persistence. Infected macrophages will eventually die, releasing *Mtb* into the centre of the granuloma, forming a necrotic zone (Fig 1.8), which over time, can rupture (if a host's immune system is breached [e.g. HIV infection, diabetes, cancer]) thus releasing the dormant mycobacteria into circulation. Disease may progress weeks or even years later (Crevel et al. 2002; Russell et al. 2010).

Therefore, upon initial exposure and the uptake of *Mtb* by alveolar macrophages, the immune system calls for an inflammatory response, which slows the spread/growth of *Mtb*, but a time where the pathogen can lay dormant, housed within the immune cells. The severity of the infection that follows depends on the efficiency of the host's immune system and/or the time lapsed in receiving antibiotics.

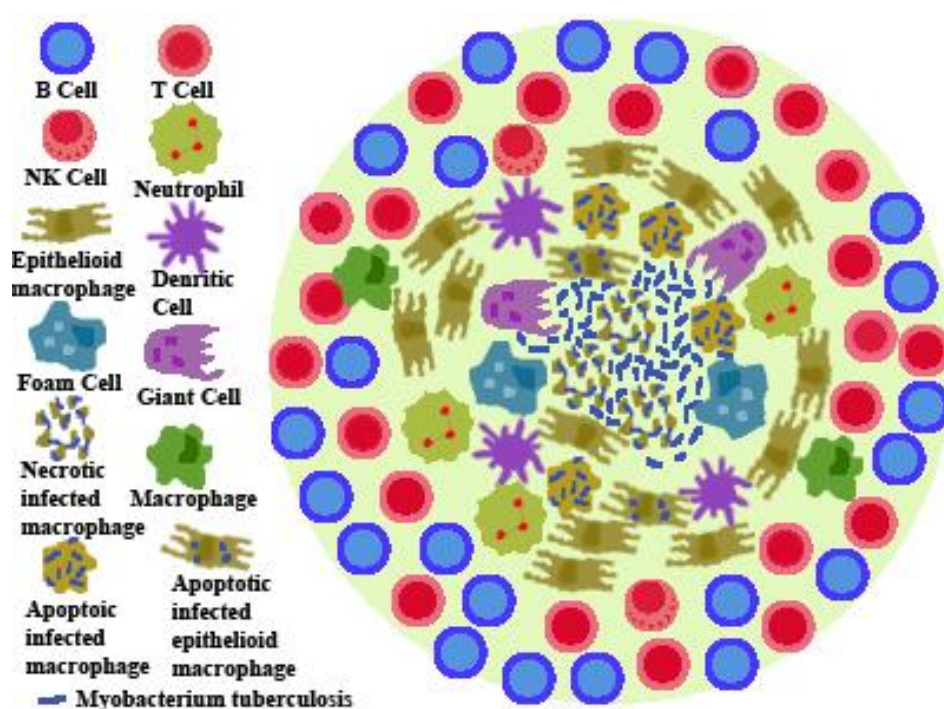


Figure 1.8 Schematic diagram of the TB Granuloma Complex

### 1.5.1 Intracellular Survival of *Mtb*

*Mtb* virulence is often defined by its transmission and intracellular survival ability, which is complex and is yet to be fully understood (Hussain et al. 2013; Simeone et al. 2015). It is established that the pathogen can adapt, allowing it to avoid the hostile environment of the phagosome, but the means by which *Mtb* achieves intracellular survival is not fully elucidated, as the lysosome is a complex organelle, which holds many different enzymes with the capability of degrading many microorganisms. For these enzymes to function efficiently, they must be maintained in optimum conditions within the lysosome. The enzymes must be kept at a pH of approximately 5 which is maintained by a proton-pumping ATPase (Dubnau & Smith 2003). Upon phagosome-lysosome fusion, the enzymes are transferred into the subcellular compartment holding the microorganism to be phagocytosed. *Mtb* is known to disrupt the phagosome fusion, thus preventing its exposure to a highly acidic environment and allowing it to reside within a partly fused phagosome, in a pH of approximately 6.2 (Song et al. 2012).

*Mtb* glycolipids block trafficking regulated by phosphatidylinositol 3-phosphate (PI3P), a membrane protein, required for phagosome-lysosome fusion (Pieters 2008). By inhibiting the activity of a phosphatidylinositol 3-kinase (PI3 kinase) vHP34 using a cell wall component lipoarabinomannan (LAM), *Mtb* prevents PI3P being generated on the phagosomal membrane. *Mtb* also prevents the build-up of PI3P on phagosomes, through secretion of a phosphatase (SapM), preventing fusion of the phagosome complex (Pieters 2008).

It has also been suggested that *Mtb* targets  $\text{Ca}^{2+}$  dependent signalling mechanisms (Malik et al. 2000).  $\text{Ca}^{2+}$  is an important regulator of pathogen responses such as the regulation of the reactive nitrogen intermediates and the release of microbicidal proteins/peptides

and TNF- $\alpha$ . Malik *et al.*, demonstrated that *Mtb* residing in the phagosome inhibited Ca<sup>2+</sup> mediated signal transduction (Malik et al. 2000). The generation of reactive oxidative species (ROS) by macrophages is also affected by *Mtb* infection. Certain proteins secreted by *Mtb* were found to directly down regulate ROS production in the immune cells, thus preventing antibacterial responses used by macrophages during infection (Ganguly et al. 2008).

Tan *et al.*, has shown that Cl<sup>-</sup> concentration increases during phagosomal maturation (Tan et al. 2013). Cl<sup>-</sup> channels are found on the endosomal membrane, involved in the regulation of [H<sup>+</sup>]. The role of Cl<sup>-</sup> channels on a phagosome is not well understood, but it was observed that an increase in Cl<sup>-</sup> resulted in a lowering of pH within the phagosome complex, and intriguingly, *Mtb* displayed a transcriptional response to Cl<sup>-</sup> levels. This research has suggested that Cl<sup>-</sup> and pH have an inverse correlation, but most importantly, it suggested that *Mtb* utilises host signals to its own advantage, using Cl<sup>-</sup> as an environmental indicator of pH levels (Tan et al. 2013).

Dubnau & Smith outline some other possibilities, such as retention of certain proteins which interfere with the processes of the phagosome complex (Dubnau & Smith 2003) whereas Simeone *et al.*, discuss *Mtb* instigating phagosomal rupturing (Simeone et al. 2015). Overall, it seems the mechanism of *Mtb* intracellular survival is by no means a straightforward feat. It is through highly complex cell signalling pathways and genetic mutation, most of which are not well documented and/or understood.

### ***1.5.2 Adaptive immunity***

The adaptive immune system in a highly complex organisation but reacts in two main ways to *Mtb* invasion; antibody and cell-mediated response executed by B-cell or T-cell lymphocytes. *Mtb* infection control is generally determined by the efficacy of the host's

adaptive immune system. T-cells, which include antigen specific CD4<sup>+</sup> and CD8<sup>+</sup> cells, are the most important in the immune response against *Mtb*. CD4<sup>+</sup> T-cells (type 1 helper cells [Th1 cells]) produce the cytokines IFN- $\gamma$  and TNF- $\alpha$  which are known to be protective through the activation of functions in macrophage cells, that can control intracellular *Mtb* (Kaufmann 2013). Th17 cells are known to produce interleukin (IL)-17 (a pro-inflammatory cytokine), which attracts and activates neutrophils, often to the site of a granuloma formation, thus asserting their protective role (Prezzemolo et al. 2014). Although over production of IL-17 can cause tissue damage, (Prezzemolo et al. 2014), it has been discovered that from this recruitment, over half of the bacilli present in infected patients are found within neutrophil cells (Wong & Jacobs 2016). Upon encountering *Mtb* that have burst from necrotic macrophages (Repasy et al. 2013), neutrophils undergo 'NETosis' whereby they produce an extracellular trap which prevents the spreading of *Mtb* (Wong & Jacobs 2016). These traps are chromatin structures with antimicrobial molecules and the process of NETosis is described as a form of pathogen-induced cell death (Remijnsen et al. 2011). CD8<sup>+</sup> T-cells are known to differentiate into effector cells which produce cytolytic molecules and cytokines which can kill *Mtb* (Kaufmann 2013). They recognise antigenic peptides in cytosolic compartments following *Mtb* uptake into immune cells. The process of adaptive immunity in an *Mtb* infection is highly complex, with activation of many immune cells, pathways and modulators.

### ***1.5.3 Primary and Secondary TB***

Primary TB infection is the initial exposure to the infectious bacilli, which enter the respiratory tract and are ingested by alveolar macrophages. Depending on whether the bacilli are destroyed or not, will depend on whether active primary TB results. If active

TB results, the onset of clinical symptoms soon occurs. If bacteria are ingested and inhibited by the hosts immune system, characterised by a Ghon focus/granuloma, containing a parenchymal subpleural lesion, and enlarged lymph nodes, the bacilli will be contained (Health Protection Agency 2012).

Secondary TB is the reactivation of a past, usually a subclinical infection. The bacilli are released following rupture of the granuloma centre housing them, as aforementioned. The released bacilli spread throughout the lungs, and onto other sites. Consequently, the individual becomes contagious, and the bacilli are transmittable to other individuals. Secondary TB is usually symptomatic (Health Protection Agency 2012).

#### ***1.5.4 Clinical Symptoms***

Symptoms can vary between individuals and can be very nonspecific. Clinical manifestations vary by the severity and type of infection. The common pulmonary strain of the disease causes a persistent cough (often containing blood in the spittle), fatigue, elevated temperature, loss of appetite, chest pain and weight loss (NHS 2011; NHS 2014). Miliary TB, being the most serious form, is found throughout the body and can cause leukaemia-like symptoms. If the bacilli reach the bone marrow, the infected patient can become severely anaemic (NHS 2011). TB pleuritis, identified by lymphocytosis in the pleural fluid, can be self-limiting whereas extrapulmonary forms of the disease can manifest in the brain, spine/joints (Pott's disease) and skeleton, the latter giving an insight into the ubiquitous nature of TB (Crevel et al. 2002). Depending on the location of infection, some patients suffer with haematuria and if the brain becomes infected in severe cases, seizures and psychosis.



## 1.6 Diagnosis of TB

Rapid diagnosis of TB is vital; it prevents morbidity and decreases mortality rates (Boehme et al. 2011; WHO 2015b). The tuberculin skin test (TST) or Mantoux test, is an easy and effective way of diagnosing TB (Yang et al. 2012). The individual is injected with tuberculin purified protein derivative (PPD) into their forearm and are monitored for 48-72 hours. The level of induration is measured at the injection site, which directly relates to the diagnosis of TB. The TST can be problematic in giving false-positives, as it can detect readings from other mycobacteria or even the BCG vaccination because PPD is prepared from the culture filtrate of *Mtb* containing many antigens which are homologous to vaccine strains of the BCG and non-tuberculosis mycobacteria (Higuchi et al. 2007; Yang et al. 2012). It also requires skilled staff, which increases the costs of its use.

Where the global burden of TB is greatest in the developing countries, diagnosis is mainly carried out by microscopic analysis of stained sputum smears for the identification of the acid-fast bacilli, with each diagnosis requiring three specimens per patient (Patino et al. 2008). Sputum smear microscopy is an inexpensive means with few technical requirements, yet it often misdiagnoses many infected patients (in extra pulmonary cases), allowing for disease progression and there are always problems associated with detection of MDR/XDR strains (Boehme et al. 2011; Patino et al. 2008).

Conventional light microscopy uses carbol fuchsin Ziehl-Neelsen acid-fast stained smears. The diagnostic tests' sensitivity can depend on the quality/quantity of the specimen, and the quality of laboratory staff training (the process is labour intensive). However, this test is generally deemed highly specific and therefore particularly useful in global areas of high TB prevalence (Patino et al. 2008). Fluorescence microscopy

using fluorochrome dyes has reported sensitivity 10% higher than direct sputum smear microscopy and hence it is regarded as more conclusive (Patino et al. 2008). This means of testing however, has a greater financial burden related to the high costs of fluorescent staining dyes/microscopes. Based on sensitivity, cultivation of the tubercle bacilli is the most sensitive means, detecting 100 bacilli per mL of sputum. This is a slow and expensive process and unfortunately not commonly used in developing countries. A more modern technique is the use of the light-emitting diode fluorescent microscopy (LED-FM). It is deemed to be cheaper as a mercury lamp is not required, it has less power requirements and it does not require a dark room (Bhadade et al. 2015).

A real-time PCR assay; Xpert MTB/RIF<sup>®</sup>, has been developed to detect rifampicin (RIF [a first line TB antibiotic]) resistant strains of *Mtb* (Boehme et al. 2011). This molecular diagnostic test developed by the GenXpert platform is highly recommended by WHO in cases where MDR TB strains are suspected or in HIV infected individuals. WHO suggest that Xpert MTB/RIF<sup>®</sup> will offer a 3 fold increase in diagnosis in patients with MDR TB and a 2 fold increase in HIV infected patients (WHO Factsheet 2012). WHO is currently endorsing the Xpert MTB/RIF<sup>®</sup> assay as a means of accurate diagnosis, with results being available as soon as 2 hours. WHO reports that 69% of countries use it as the initial diagnosis test when patients are at risk of being MDR TB infected (WHO 2015b).

Other methods of diagnosis have been investigated, such as the QuantiFERON<sup>®</sup>-TB Gold test (QFT-2G) which measures cellular immune response to *Mtb* specific proteins; early secreted antigenic target-6kDa (ESAT-6) and culture filtrate protein-10 kDa (CPF-10) which are encoded by the RD-1 region of *Mtb* genome (Ganguly et al. 2008). Both ESAT-6 and CPF-10 are absent from all BCG strains, and most other non-tuberculosis mycobacteria (Higuchi et al. 2007). It has been reported to show low levels of false-positives, high specificity for *Mtb* and the diagnosis is unaffected by previous BCG vaccinations, thereby allowing its use in diagnosing LTBI (Higuchi et al. 2007). QFT-

2G uses whole blood samples for *in vitro* laboratory testing for IFN- $\gamma$  presence through ELISA, which is secreted upon *Mtb* infection, however, the requirement of blood samples to be transported to laboratories allows room for contamination and as this test involves cell culture, the time taken in getting samples to a laboratory can be a problem. Additionally, more testing of the diagnosis is required on individuals infected with HIV. As aforementioned QFT-2G is able to detect LTBI, but it cannot differentiate between LTBI and active TB.

Recommendations from the National MDR TB Task Force following an increase in drug resistant strains, state that drug susceptibility testing must be performed on all *Mtb* isolates collected from patients (Ardito et al. 2001). This is mainly carried out in the liquid culture system BACTEC MGIT 960 (and the original BACTEC 460) (Becton, Dickinson and Company, USA) (Robbe-Austerman et al. 2013). These systems detect acid-fast bacilli growth, differentiation and allows for susceptibility testing (this system is not *Mtb* specific and PCR is required to identify strains).

The widely adopted MGIT (mycobacteria growth indicator tube) system is used for the detection and recovery of mycobacteria. As growing *Mtb* utilise oxygen, the BACTEC MGIT 960 system records the level of oxygen depletion from the tube via fluorescence readings, thus indicating both mycobacterial presence and growth. The BACTEC 460 radiometric system works by supplying *Mtb* with radioactive labelled substrate that is utilised by the mycobacteria to produce  $^{14}\text{CO}_2$ , detected in the system. The level of  $^{14}\text{CO}_2$  produced is directly proportional to rate of bacterial growth. The MGIT 960 is often referred as the world's first automated drug testing system, by testing the antimicrobial susceptibility to SIRE (streptomycin [STR], INH, RIF, ethambutol [EMB] [and pyrazinamide [PZA]]) through use of a modified Middlebrook 7H9 broth in a tube, impregnated with a fluorescence quenching oxygen sensor on the test tube base (Ardito et al. 2001). Results are available within 4-7 days, which cut previous waiting times by

weeks. The BACTEC 460 system has been replaced the BACTEC MGIT 960 since becoming commercially available in 2002, although throughout the literature there are reports of higher contamination rates using this system (Robbe-Austerman et al. 2013).

A recent report states that both systems (the MGIT 960 and Xpert MTB/RIF<sup>®</sup>) are imperfect at detecting MDR TB and that further investigation (e.g. gene sequencing) is required to confirm RIF resistance (Mokaddas et al. 2015).

## **1.7 TB vaccine**

### ***1.7.1 M. bovis bacillus Calmette-Guerin (BCG) vaccine***

Currently there is only one vaccine available against TB, the *M. bovis*-BCG vaccine, created in 1921 by Albert Calmette and Camille Guérin (Ohara 2012). To create the vaccine, Calmette and Guérin subcultured a virulent strain of *M. bovis* collected from an infected cow. Over 13 years and 230 passages later, the strain was no longer virulent and could be used as a vaccine in animal models (Ohara 2012). The efficacy of the vaccine against adult pulmonary TB is debated throughout the literature, however, common agreement is made on its effectiveness at preventing childhood forms of TB, such as miliary and TB meningitis (Ohara 2012; Trunz et al. 2006).

In the UK, the BCG was introduced in 1953, during a period where the incidents of TB were already on the decline due to the improved health services and standards of living, but it was decided to vaccinate all children. However, this vaccination of school children was withdrawn from the NHS in 2005 (NHS 2012). Vaccination is now based on risk assessment, depending on where the baby/child will be living and whether they are likely to visit high risk TB areas (NHS 2012).

Upon infection of *Mtb*, effective phagocyte activation can reduce the growth of the mycobacteria, but this requires an acquired specific cellular response which is the basis of vaccine development (Cooper 2009). Unfortunately, the vaccination for tuberculosis has not improved since the introduction of the BCG, which is often not available in many high TB burden countries. The BCG vaccine is not recommended in infants known to be infected with HIV due to; the risk of BCG disease, it is not always effective at preventing pulmonary TB in adults and its overall efficacy is questionable, ranging from 0 to >80% depending on the global region (WHO 2014b). There are 2 main strategies in vaccine development; to develop a new vaccine to replace the BCG, or create a booster vaccine to accompany the BCG for use in adolescents and adults (WHO 2014b). Vaccine development is expensive and slow especially when beginning human trials, but for the first time there has been a great surge in vaccine development with many (up to 15) reaching clinical trials (phase I-III), although nothing suitable has yet been developed this is a positive step (Montoya et al. 2013; Tameris et al. 2013; WHO 2014b).

### ***1.7.2 Vaccine development***

#### ***1.7.2.1 MVA85A***

A potential novel vaccine has recently been developed by Oxford University; modified Vaccinia Ankara virus. It is an attenuated vaccinia virus-vectored vaccine expressing immunodominant *Mtb* antigen 85A (MVA85A) (Tameris et al. 2013). Developed as a booster vaccine to accompany the BCG, Phase IIb clinical trials have been completed and results are published (WHO 2014b; Tameris et al. 2013). Although it was well tolerated by infants, with few adverse side effects reported, it had no significant efficacy against *Mtb* and results overall were very disappointing (Tameris et al. 2013). The results differed greatly from *in vitro* and animal trials, where the vaccine induced a great increase

in CD4 T-cells, which enhanced protection against *Mtb*. It was found to enhance IFN- $\gamma$  secreting T-cells significantly, particularly in infants who had been previously vaccinated with the BCG, and it has been suggested that this vaccine may be able to enhance the current BCG vaccine and be more suitable for adolescents rather than infants but clearly further work is required (Tameris et al. 2013).

#### **1.7.2.2 M72 +AS01E**

GlaxoSmithKline (GSK) and Aeras combined their efforts to create a protein subunit vaccine to enhance immunogenicity (Montoya et al. 2013). ‘M72’ is an antigen, a recombinant fusion of 2 proteins expressed in *Mtb*, which induce IFN- $\gamma$  production and ‘AS01<sub>E</sub>’ is a liposome based Adjuvant System, which can activate the innate immune system to enhance the adaptive system, specifically inducing a strong T-cell mediated response. Trials have been undertaken to determine dosages and tolerance (Phase IIb), no adverse side-effects were found and further trials are continuing (Montoya et al. 2013).

#### **1.7.2.3 *M. vaccae***

Anhui Zhifei Longcom’s vaccine is currently in Phase III of clinical trials in China (WHO 2014b) and is being investigated for preventing a diseased state in LTBI (WHO 2015b). *M. vaccae* is an environmental mycobacterium with a low pathogenicity to humans and it expresses antigens common to *Mtb*, thus a lysate of *M. vaccae* has been developed as a vaccine to modify host immune responses following infection. It is the largest trial of its kind in over a decade with 10,000 people enrolled (WHO 2015b). Further information is not yet available.

## 1.8 Current Treatments

Before the discovery of STR in 1944, there was no effective treatment against *Mtb* infection. STR, being the first antibiotic in the fight against TB, provided hope for a TB-specific treatment. It was administered intramuscularly and initially it was an effective treatment. As resistant mutant strains of the disease persisted, treatments had to be increased and disease management now includes long-term administration of multiple antibiotics (four); a regime of drugs over a long time period, usually between 6 months and 2 years. The WHO currently recommends the DOTs (directly observed treatment short-course) strategy for treating TB (Davies 2003; WHO 2015b). This strategy has five distinct components, government commitment (political), detection by microscopy (sputum smear), adequate drug supplies, a standardised, monitored treatment and efficacious drug regimens supported by health professionals (Davies 2003). The first phase of intensive treatment is 2 months (every day) of RIF, INH, EMB and PZA then a further 4 months (every day) of RIF and INH (Table 1.3) (NHS 2014) reducing the treatment period by 12 months. This regime was designed 40 years ago and currently has a cure rate of approximately 90% in HIV-negative patients (WHO 2014b; WHO 2015b). There have been recent clinical trials to further reduce this period from 6 to 4 months, through the addition of a fluoroquinolone, yet this proved unsuccessful (Gillespie et al. 2014; Gninafon et al. 2014).

As resistant mutant strains of the disease persist, treatments have had to be adapted and increased. Therefore, disease management includes a regimen of second line drugs over a longer period, usually up to 2 years (Table 1.4). Second-line TB treatments include the oral and/or injectable aminoglycosides and fluoroquinolones. Such treatment plans are not possible to maintain in certain parts of the world, particularly sub-Saharan Africa, an area heavily burdened with TB infection (Russell 2011). MDR TB strains which are

resistant to first line drugs RIF and INH, take over 20 months to treat and XDR TB strains which are resistant to first and second line drugs and at least one of the injectable drugs (amikacin, kanamycin, or capreomycin) are very complex to treat and often have high mortality rates (Green & Garneau-Tsodikova 2013). Except for BDQ, Delamanid and Pretomanid (formally PA-824) (Table 1.5), drug development for TB is inadequate and due to the propensity of *Mtb* to develop resistance, treatment is difficult.

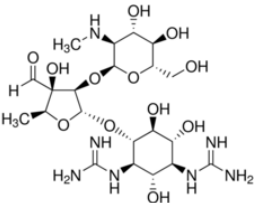
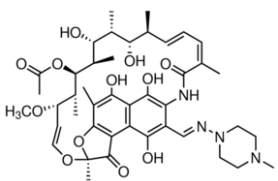
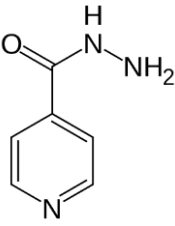
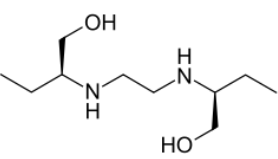
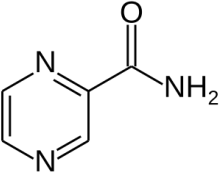
There are a number of ‘prodrugs’ currently in use; these are substances that must be metabolically activated before they can effectively attack the TB causing pathogen. The fundamental objectives in the development of novel TB drugs is to curtail the long treatment period, tackle the problem of drug resistance, provide safer treatments and eradicate the drug-drug interactions seen in patients with HIV/TB infections (Franzblau et al. 2012).

A list of the first line drugs and their minimum inhibitory concentrations (MICs) are displayed in Table 1.3\*. Generally, MICs are defined as being the lowest concentration of drug that inhibits the measurable ( $\geq 99\%$ ) growth of an organism after incubation. Minimum bactericidal concentrations (MBCs) are the lowest concentration of drug required to kill an organism.

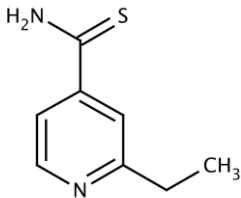
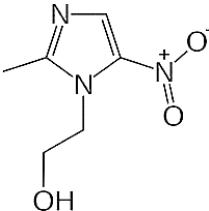
*\*please note drug structures were obtained from manufacturer’s websites.*



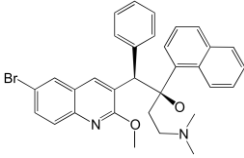
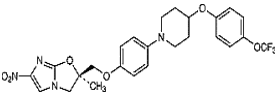
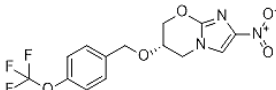
**Table 1.3 First Line TB Drugs**

Drug Name/ Structure	Minimum Inhibitory Concentrations	Mechanism of Action(s)	Further information
<b>Streptomycin (STR)</b> 	0.5-2 µg/mL	STR inhibits <i>Mtb</i> protein synthesis through binding the 30S ribosomal subunit thus causing the misreading of the mRNA during translation.	STR is an aminoglycoside antibiotic, the first used to treat TB. It affects only replicating bacilli (Yajko et al. 1995a).
<b>Rifampicin (RIF)</b> 	0.05-1 µg/mL	RIF inhibits RNA synthesis of <i>Mtb</i> by binding the β subunit of the RNA polymerase thus preventing elongation of the RNA chain. RIF is active against bacilli in both growth and stationary log phases.	RIF is a bactericidal antibiotic, which is often termed the primary 'backbone' of TB treatment (Zhang & Yew 2009).
<b>Isoniazid (INH)</b> 	0.02-0.2 µg/mL	INH targets the InhA enzyme (enoyl-acyl carrier protein reductase) involved in mycolic acid synthesis, thus it affects the cell wall structure of <i>Mtb</i> . It is active against bacilli in the growth log phase and is used in conjunction with other drugs.	INH is a hydrophilic, bactericidal prodrug, hence it is administered in an inactive state requiring activation from a catalase-peroxidase KatG, encoded by the <i>katG</i> gene in <i>Mtb</i> (Zhang & Yew 2009).
<b>Ethambutol (EMB)</b> 	0.5-2 µg/mL	EBM increases the <i>Mtb</i> cell wall permeability through inhibition of the arabinosyl transferase, thus inhibiting arabinogalactan (a structural component of the mycobacterial cell wall) synthesis.	EMB is bacteriostatic affecting growing bacilli (Laurenzo & Mousa 2011).
<b>Pyrazinamide (PZA)</b> 	16-50 µg/mL	PZA works in an unusual manner against <i>Mtb</i> . It is only effective in acidic pHs in anaerobic conditions during active inflammation and is not active against <i>Mtb</i> in 'normal' culture conditions at neutral pHs levels. PZA kills non-replicating bacilli which is the opposite to many antibiotics and it seems to disrupt the membrane potential of <i>Mtb</i> .	PZA is a bactericidal prodrug, activated to pyrazinoic acid (POA) by the pyrazinamidase enzyme encoded by the <i>pncA</i> gene of <i>Mtb</i> and it is used in conjunction with INH and RIF (Zhang et al. 2003; Zhang & Yew 2009).

**Table 1.4 Second Line TB Drugs**

Drug name/type Structure	Mechanism of Action(s)	Further information
<b>Ethionamide (ETH)</b> 	<p>ETH is both a bacteriostatic and bactericidal thioamide antibiotic prodrug activated by S-oxidation, which inhibits InhA thus preventing mycolic acid synthesis. Its activity is therefore similar to that of INH and it is a derivative of isonicotinic acid (Zhang &amp; Yew 2009; Lorenzo &amp; Mousa 2011).</p>	<p>As ETH shares the same target as INH, if drug resistance is found in one of these drugs, it is also found in the other (Lorenzo &amp; Mousa 2011).</p>
<b>Metronidazole (MTZ)</b> 	<p>MTZ (specific for anaerobes) is a nitroimidazole and an antitubercular, which can kill dormant bacilli in hypoxic/anaerobic conditions. MTZ inhibits DNA synthesis and causes DNA damage by oxidation, which leads to DNA degradation and cell death (Löfmark et al. 2010).</p>	<p>MTZ has been investigated as a treatment to prevent the reactivation of LTBI (Lin et al. 2012). It is hoped it will be useful against MDR TB strains.</p>
<b>Fluoroquinolones</b>	<p>Fluoroquinolones are a group of anti-bacterial drugs, which work by inhibiting the essential mycobacterial enzyme DNA gyrase encoded by <i>gyrAB</i>. DNA gyrase is a type II topoisomerase that catalyzes the ATP-dependent negative super-coiling of double-stranded DNA and its inhibition results in microbial death.</p>	<p>Includes ciprofloxacin, ofloxacin, levofloxacin, gatifloxacin and moxifloxacin. Gatifloxacin and moxifloxacin in particular have become important in the treatment of MDR TB and appear to have minor/no side effects (Lorenzo &amp; Mousa 2011).</p>
<b>Aminoglycosides</b>	<p>Aminoglycosides are a group of antibiotics including STR, kanamycin, amikacin and capreomycin. Kanamycin (and its derivative amikacin) prevent <i>Mtb</i> protein synthesis by modifying the 16S ribosome and capreomycin, a polypeptide bacteriostatic antibiotic commonly used to treat MDR TB, works in a similar means.</p>	<p>Discovered in the 1940's these drugs have had unprecedented use since. Although resistance is seen in some of these drugs, when used in combination they can be effective (Zhang &amp; Yew 2009).</p>

**Table 1.5 MDR TB Drugs**

Drug name/ Structure	Mechanism of Action(s)	Further information
<b>Bedaquiline (BDQ)</b> 	<p>BDQ works by inhibiting the proton pump of <i>Mtb</i> adenonsine triphosphate (ATP) synthase, by binding to the oligomeric and proteolipic subunit C, which is essential for energy production. It is effective against bacilli in both the growth and stationary log phase.</p>	<p>BDQ was approved by the FDA in late December 2012. It was the first new anti-TB drug to be licensed for human use in over 40 years. It must be used with caution as its safety is still under investigation (Goel 2014). Five time higher death rates (compared with placebo) in clinical trials have recently been observed (Gumbo, Angulo-Barturen, et al. 2015).</p>
<b>Delamanid (OPC-67683)</b> 	<p>Delamanid affects cell wall components of <i>Mtb</i> by effecting mycolic acid synthesis. It is a prodrug, activated by cellular enzyme Rv3547.</p>	<p>Currently undergoing Phase III clinical trials, it was granted conditional approval by the European Medicine Agency in 2013 in certain medical cases (WHO 2015b). Its use in treating MDR TB in children is also ongoing (WHO 2014b). There is hope it may be used in XDR TB strain treatment (Lee et al. 2015).</p>
<b>Pretomanid</b> 	<p>Mechanism of action is not well understood, but it requires activation and appears to inhibit protein and lipid synthesis (not nucleic acids) and generates ROS (Ginsberg et al. 2009).</p>	<p>Developed by the Global TB Alliance, it is being tested for drug susceptible and MDR TB strains (WHO 2015b). MICs range from 0.015-0.53 µg/mL.</p>

## 1.9 The Antibiotic Apocalypse

Through lack of availability and/or poor drug management, drug resistant strains of TB have emerged and are constantly developing new resistance to drug therapies (Minh et al. 2012). Drug resistance and MDR TB is an ever increasing problem in all areas of medicine and with the media reporting that an ‘Antibiotic Apocalypse’ is imminent, it is becoming of increasing public concern (BBC Health News 2013; WHO 2015b). However, this is often attributed to over-prescription of antibiotic drugs or through improper use, hence drug resistant TB can be described as a manmade phenomenon. MDR TB is present in nearly all countries surveyed, with approximately 480,000 cases worldwide in 2014 (WHO 2015b). Such strains only respond to some specific drug lines, while XDR TB strains are often deemed untreatable (Smith 2011).

MDR TB can be separated into 3 categories; *primary resistance* is a newly infected patient with a drug resistant strain of TB, *acquired resistance* is when a previously infected patient with a susceptible strain of *Mtb* eventually develops a MDR TB strain and *mixed resistance* terms cases where the patients treatment history is not known, thus making it impossible to determine whether the MDR TB strain was due to infection by a drug resistant strain or due to acquired resistance following drug therapy (Laurenzo & Mousa 2011).

XDR TB strains have prevented successful eradication attempts by WHO and currently 9% of MDR cases are reported to be XDR TB, a figure which is expected only to increase (WHO 2012; WHO 2013; WHO 2014b; WHO 2015b). In 2014 there were 46,560 cases of XDR TB (Table 1.1) (WHO 2015b). First-line TB treatments INH and RIF are ineffective on XDR TB strains and therefore patients require longer treatment time with more toxic drugs. First line drug treatments in combination with other drugs and expensive fluoroquinolones along with one of the second line antibiotics; amikacin

(AMK), kanamycin (KAN) or capreomycin (CAP) are ineffective on XDR TB strains, for which there is no consensus on how to treat (Georghiou et al. 2012; Maartens & Wilkinson 2007). Cases without treatment unfortunately have high mortality rates, and HIV positive patients are more susceptible to early development of the disease when infected (WHO 2015b). In southern parts of Africa, the spread of HIV has caused a great increase in the number of TB cases; approximately 1.2 million of the TB cases (12% globally) were HIV positive and 390,000 people who died from TB in 2014 were HIV positive (WHO 2015b).

### **1.9.1 Problems with current treatments**

Adverse effects from drug regimens are often problematic in treating any disease, but this is augmented when multiple drugs are administered over prolonged periods as in the treatment of TB. As aforementioned, poor therapy, management and patient noncompliance can lead to complications and the adverse reactions to anti-TB drugs can cause significant problems. There have been reports that the drug-drug interactions between RIF and INH can lead to severe liver damage (Makhlouf et al. 2008; Onoshita et al. 2010). Infact hepatotoxicity has been linked to RIF, INH and PZA use, which is enhanced when these drugs are in combination. Studies outline that up to 31% of patients following a first line anti-TB drug regime experienced drug related hepatotoxicity (Tostmann et al. 2008; Hassen Ali et al. 2013), so being a serious concern. Other reported side effects from the use of RIF include gastro-intestinal problems, headache, acute retinal failure, menstrual disturbances, discolouration of body fluids and influenza-like symptoms.

There are an estimated 36.9 million people infected with HIV (WHO 2015a) and due to immunosuppression in these patients they are highly susceptible to contracting active TB and reactivation of LTBI, therefore, treatment regimes become complicated. RIF induces the activity of the CYP3A enzyme system in the liver, this cytochrome metabolises most antiretroviral drugs, therefore decreasing the concentration of these drugs in the blood (Swaminathan & Narendran 2008). As such, they cannot be used in conjunction.

A recent review by Longo *et al.*, discusses a major problem following initial treatment. After the first 2-month intensive phase, there are subpopulations of bacilli that respond differently to the drugs, as one is rapidly killed whereas the other is not (Longo et al. 2015). These surviving bacilli are known as persistent bacteria, or ‘persister’ cells (Longo et al. 2015). Persister cells are subpopulations of tubercle bacilli that survive following antibiotic treatment (Zhang et al. 2012; Zhang 2014). They are heterogeneous bacterial populations that can inhabit intra- and extracellular locations. Persister cells are genetically identical to drug susceptible strains, but are capable of surviving, either in a non-replicating or slow replication state, but under the appropriate conditions, can regrow (Zhang et al. 2012). These subpopulations are thought to be in a distinctly different metabolic state, or genetically or phenotypically different under host immune pressure which renders them less susceptible to antibiotics (Longo et al. 2015). The authors then go onto explain that another reason for the poor killing of the persistent subpopulations is the poor absorption of some drugs, for example when drugs are taken alongside food, (RIF, INH and PZA) antibiotics levels are reduced (Longo et al. 2015). Such phenomena are well defined by the ‘Yin-Yang’ TB model (section 1.9.2).

### 1.9.2 The Yin-Yang model

Two Yin-Yang models have been proposed to explain the problems with bacillary response to drug treatment. The first model is the persister/heterogeneous model and the second is on LTBI over active disease. Model one is the Yin and Yang of persisters and replicating bacteria, illustrating a subpopulation of persisters (Yin) and a subpopulation of growing bacteria (Yang) (Fig 1.9). This model is used to demonstrate why after initial treatment (2 months) of RIF, INH, PZA and EMB, *Mtb* can begin to grow again, but can be killed by further treatment in the continuing treatment regime (Zhang et al. 2012). This model highlights the possible transition of latent persister cells to actively growing cells. Model two is the Yin and Yang of latent infection (Yin) and active, overt disease (Yang) (Fig 1.9). Active disease states can vary, and following treatment/immune response, persister cells can remain and become latent (Zhang et al. 2012). The latent persister cells can then go onto reactive disease. The endurance of persister cells makes TB treatment immensely difficult. Even with the appropriate treatment, an active diseased state can be reintroduced.

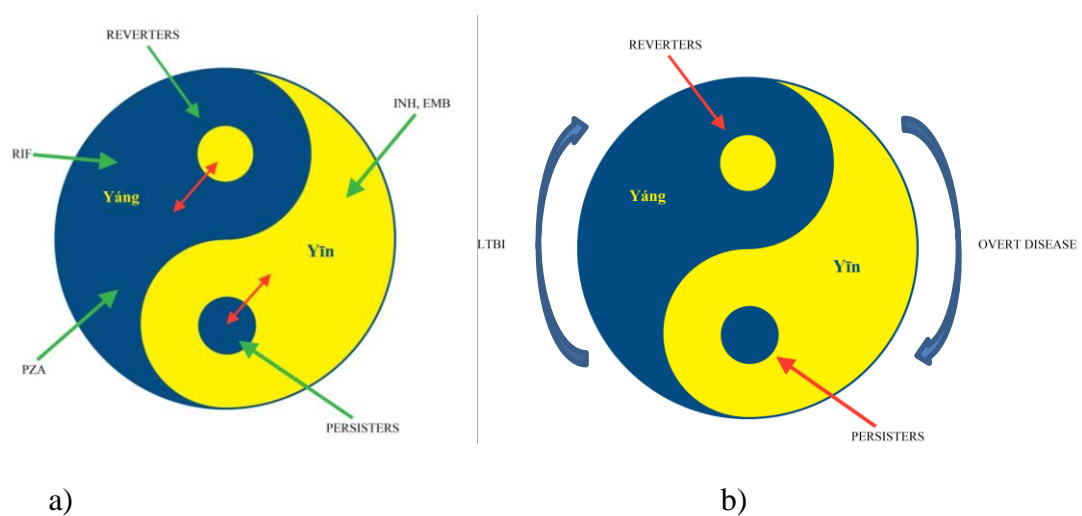


**Figure 1.9 (a-b) The Yin-Yang models of (a) persisters and replicating bacteria and (b) latent infection (LTBI) and overt disease.**  
(adapted from Zhang et al., 2012)

### 1.9.3 Mechanisms of *Mtb* Drug Resistance

The sporadic appearance of drug resistant strains of *Mtb* was an inevitable consequence of multi-drug therapy. MDR and XDR TB phenotypes are acquired by a sequence of cumulative mutations in specific genes.

RIF resistance is often deemed as an indicator of a MDR TB strain, as resistance to this drug is generally uncommon, but usually indicates resistance to both RIF and INH (Laurenzo & Mousa 2011). RIF resistance is caused by the mutation(s) in the well-defined 81 bp (21 codons) region of the *rpoβ* gene. The *rpoβ* gene encodes the β subunit of the RNA polymerase; RIF's main target. The mutations in amino acids 507-533, the main cluster region (with mutations in 516, 526 and 531 being the most common) of the *rpoβ* gene are responsible for 95-97% of RIF resistant strains (Laurenzo & Mousa 2011; Zhang & Yew 2009; Somoskovi et al. 2001). Strains with a mutation in codon S531L are particularly resistant and such strains are classed as having high level of drug resistance with resistance also to other drugs of the rifamycin family (Zhang & Yew 2009).

Mutations in different codons confer different levels of RIF resistance; 526 and 531 mutations result in very high levels of resistance (MIC > 64 µg/mL) which total up to 86% of resistant strains, whereas mutations in codons 511, 516, 519 and 522 confer low levels of resistance (MIC < 64 µg/mL) (Somoskovi et al. 2001). It is reported that this 81 bp region of the genome is the main region searched for mutations, but that other areas may also have alterations, that may lead to MDR TB. Heep *et al.*, 2000 reported that mutations in the 59 region of the *rpoβ* gene could possibly lead to rifamycin resistance in *Mtb*, as it had in similar species. Also three out of six *Mtb* species carried the V176F mutation conferring a high level of RIF resistance (Heep et al. 2000).



INH resistance is relatively common. Strains resistant have lost the catalase-peroxidase KatG encoded by the *katG* gene in *Mtb*. Mutations within *katG* are the main cause of resistance to INH, as the pro-drug is not activated, which are associated with high levels of resistance. The KatG S315T mutation is the most common. However, other mutations resulting in the over-expression of InhA or mutations effecting the InhA active site, have lowered the affinity to INH, are also responsible for resistance (Zhang & Yew 2009). Strains with mutations in the *inhA* gene are generally deemed to have low levels of resistance, but commonly also have resistance to EMB.

EMB like INH is a pro-drug requiring activation, thus mutations leading to resistance are found mainly in the *ethA*, *inhA*, *embB* genes (particularly codon 306 of the *embB* gene) which effect the drug's activation, or through the increased production of arabinosyl transferase which overwhelms the drug (Bakuła et al. 2013). As much as 4% of all *Mtb* clinical isolates tested displayed resistance to EMB, thus it is relatively common. The concurrent persistence of resistance between INH and EMB has been reported to be as high as 96.6% (Madison et al. 2002), yet overall there is scarce literature on EMB resistance and mechanisms.

PZA resistance occurs though mutations in the *pncA* gene that encodes the pyrazinamidase enzyme, which allows activation of this pro-drug (da Silva & Palomino 2011). Mutations include deletions throughout the 561bp of the *pncA* gene, similar to the mutations in the *rpoβ* gene in RIF resistance (Degano et al. 2014).

**Table 1.6 Some main factors influencing the development of MDR/XDR TB and treatment problems**  
(created using Kato-Maeda *et al.* 2001, WHO 2014 & 2015b, Russell *et al.* 2010)

<b>Factors</b>	<b>Reasons</b>
<b>1. Patient non-compliance</b>	<ul style="list-style-type: none"> <li>• Not completing full prescriptions</li> <li>• Drug side-effects</li> <li>• Selling of prescription drugs to others</li> <li>• Myths/perceptions of TB/TB treatments</li> <li>• Financial</li> <li>• Time required off work/school</li> </ul>
<b>2. Medical profession errors</b>	<ul style="list-style-type: none"> <li>• Wrong dosing</li> <li>• Wrong drug prescription</li> <li>• Failure to detect MDR/XDR</li> </ul>
<b>3. Genetic</b>	<ul style="list-style-type: none"> <li>• Mutations</li> <li>• Gene transfer</li> </ul>
<b>4. Persister cells</b>	<ul style="list-style-type: none"> <li>• Re-growth of cells following treatment</li> <li>• Re-activation of disease</li> </ul>
<b>5. Other</b>	<ul style="list-style-type: none"> <li>• Lack of funding</li> <li>• Inadequate storage facilities for drugs</li> <li>• Drug addiction/alcoholism</li> <li>• Drug supply shortage</li> <li>• Financial</li> </ul>

### ***1.10 Mycobacterium avium subsp. paratuberculosis***

*Mycobacterium avium. subsp paratuberculosis (Map)* is an infectious mycobacterium principally of ruminants, which causes paratuberculosis or Johne's disease, a chronic granulomatous enteritis resulting in diarrhoea, anorexia and eventually death (Hermon-Taylor 2009; Zhang et al. 2015) yet only 3-10% of animals are asymptomatic (Hughes et al. 2007). *Map* is a slow growing (over 20 hours doubling time), acid-fast pathogen of 0.5-1.5  $\mu$ M and infects its host primarily through the faecal-oral route, through the ingestion of contaminated faeces, feed, water and/or milk (Cocito et al. 1994). Like *Mtb*, experiment studies show that *Map* is found in intestinal macrophages soon after infection via the orofecal route. *Map* is shed from infected animals in faeces and milk where it can survive in the environment for prolonged periods of time (Zhang et al. 2015).

*Map* has been studied extensively due to its prevalence among many animal species, particularly dairy and beef cows, goats and sheep. There is currently no effective treatment for the disease. Antibiotics used for treating TB can be utilised but this is not advisable for animals destined for the food chain therefore treatment is used for valuable animals such as zoo specimens or rare breeds. Control measures are practised such as vaccination, the testing and culling of infected animals and management procedures to reduce exposure to infected animals or a contaminated environment (Beard et al. 2001).

Younger animals are more susceptible to infection than older, however the disease displays no clinical signs until over 2 years of incubation within the infected host (Beard et al. 2001). As ruminants shed live *Map* in their faeces and milk, the spreading of infection among farm animals has become a great problem, particularly when these animals are in the dairy and food production chain (Beard et al. 2001). Johne's disease creates a major financial burden on livestock producers in terms of reduced milk

production and high infection rates. Infected animals, at the clinical stage, produce 19.5% less milk than those uninfected (Benedictus et al. 1987).

#### ***1.10.1 Aetiology of Johne's disease***

Johne's disease was first identified over 100 years ago by Johne and Frothingham, 1895, who recognised a connection between cattle enteritis and accumulation of acid-fast microorganisms in the intestine (Cocito et al. 1994). Johne's disease was originally believed to be caused by an intestinal mycobacterial infection (which caused TB in birds [later called *M. avium*]), but Twort and Ingram, 1912 isolated and recognised *Map* as the causative agent thus providing the aetiology.

#### ***1.10.2 Diagnosis of Johne's disease***

Infection can be detected by measuring an animal's immune response and these tests are relatively quick (Burrells et al. 1998; Waters et al. 2003). Screening processes for the detection of the bacteria are slow however, with *Map* taking 6-8 weeks to culture in liquid broth and up to 16 weeks on agar (Behr & Collins 2010). Faecal culture offers high levels of sensitivity, and is considered the gold-standard for diagnosis, but it is a slow and highly expensive process requiring medium additives such as mycobactin J, and hence not ideal for high throughput (Stevenson & Sharp 1997). Faecal smears are used to detect *Map* infection through staining, however this is highly dependent upon the number of organisms present and thus the disease stage the infected animal is at, so overall this means is not deemed reliable for early diagnosis. The widely used ELISA assay is regarded as a rapid technique in detecting antibodies in sera or milk yet displays low

sensitivity and specificity in early stages of the disease (Behr & Collins 2010). As ELISA offers a quick diagnosis, this is the preferred method for herd screening.

#### ***1.10.4 Crohn's disease***

Whether *Map* is a zoonotic agent or not, is still under investigation, but as Crohn's disease has no known aetiology, *Map* has been suggested as a possible aetiological agent. There are many pathological similarities between Johne's disease and Crohn's disease (Beard et al. 2001; Li et al. 2005; Sartor 2005). Crohn's disease is a chronic inflammatory intestinal disease which displays lesions from the mouth to the anus of humans (along the gastrointestinal tract), and is described as being episodic (Chacon et al. 2004). Evidence whether *Map* is the causative agent or not is contradictory, but the hypothesis dates back to almost one century ago (Dalziel 1913; Sartor 2005). Symptoms in both Johne's and Crohn's disease are clinically analogous, with the infected suffering from chronic diarrhoea, excessive weight loss and eventually death if left untreated. Crohn's disease currently has no known cure; courses of antibiotic drugs are available yet relapses of the diseased state do frequently occur (Behr & Collins 2010). Experimental evidence confirms that *Map* infects many different hosts and causes a diseased state in ruminants, camelids, rabbits and hares, hence another possible link of *Map* to humans. However, *Map* is rarely visualised using Ziehl-Neelsen staining in the tissues of Crohn's disease patients and the number of human *Map* isolates grown in pure culture in epidemiological studies have been low, suggesting that disease caused by *Map* in humans is uncommon (Behr & Collins 2010). Yet many studies report that *Map* DNA has been detected in many Crohn's patients (Kirkwood et al. 2009; Sechi et al. 2005; Zhang et al. 2015) and it has been cultured from the breast milk of Crohn's sufferers (Naser et al. 2000).

Additionally, a recent study reported that *M. avium* subsp. *hominissuis* was successfully cultured from a Crohn's patient, this being a very close member to *Map* in the MAC (Zhang et al. 2015). As viable *Map* has been detected in commercially sold pasteurised milk, it seems reasonable that the human population is exposed to *Map* (Ellingson et al. 2005; Kirkwood et al. 2009; Botsaris et al. 2016). It is a very controversial topic in the literature, yet overall data seems to be more in favour of *Map* being pathogenic to some humans than not (Kuenstner et al. 2015; Hermon-Taylor 2009; Kuenstner 2006; Cohen 2005; Zanetti et al. 2006; Botsaris et al. 2016).

#### **1.10.5 *Map* K10 strain**

*Map* is particularly homologous to *M. avium* subsp. *avium* (*Maa*), *M. avium* subsp. *hominissuis* and *M. avium* subsp. *silvaticum* (*Mas*) at the genetic level (Li et al. 2005), however, *Map* is structurally comparable to *Mtb*, with a very similar cell envelope. The *Map* strain K10 was isolated from a clinically affected American dairy cow and the genome was sequenced by Li *et al* 2005 (Li et al. 2005). The strain has been successfully subjected to genetic manipulation and a reporter strain transformed with the Green Fluorescent Protein (GFP) marker is available (*Map* K10/GFP) (Harris et al. 2002b). *Map* K10 has a circular sequence of 4,829,781 bp with a very high G and C content of approximately 69.3% and 4300 genes (Li et al. 2005). *Mtb* (laboratory strain H37Rv) has a circular sequence of 4,411,529 bp with approximately 67% G and C content and 4000 genes (Smith 2003). *Map* (K10) and *Mtb* (H37Rv) both have 1 rRNA operon, 45 tRNAs and > 3000 homologous genes (Li et al. 2005). Additionally, *Map* is known to be particularly heat resistant compared to other mycobacteria, as well as resistant to many chemicals, akin to *Mtb*.

*Map* K10/GFP was used as a surrogate organism in this project as it is representative of the slow growing pathogenic mycobacteria for which survival within macrophages is a hallmark trait, akin to *Mtb*, and is very similar at the structural and genetic level (Hostetter et al. 2002; Tan et al. 2013; Plain et al. 2011; Li et al. 2005). It is also resistant to a broad spectrum of antibiotic drugs similar to *Mtb*.

### **1.11 Nanotechnology**

Nanotechnology holds great promise to improve human health and is predicted to significantly benefit all of human society (Etheridge et al. 2013). The ability to create nano-scaled materials has allowed advancements in medicines, targeted drug delivery, diagnostic tools as well as offering a novel set of anti-microbial agents (Byrne et al. 2011). Nanomaterials (NMs) are natural or manufactured particles with one or more external dimensions between 1-100 nm while nanoparticles (NPs) have three dimensions in the nano-scale (European Commission 2015 retrieved from [http://ec.europa.eu/health/scientific\\_committees/opinions\\_layman/nanomaterials2012/en/glossary/mno/nanoparticle.htm](http://ec.europa.eu/health/scientific_committees/opinions_layman/nanomaterials2012/en/glossary/mno/nanoparticle.htm) on 11/11/15). NMs often exhibit novel properties that differ from the larger forms of the bulk material, and these novel properties are exploited in diverse applications (Albrecht et al. 2006). NPs can be made from many materials such as metals, organic molecules *etc.*, and with varying physical characteristics such as size, morphology, charge or surface chemistry. A categorisation scheme for NPs based on their chemical composition e.g. metals (e.g. gold), metal oxides (e.g. silicon dioxide), carbon based materials (e.g. carbon nanotubes) and organics (e.g. polymers) has recently been discussed by the Organisation for Economic Co-operation and Development (OECD) working party on manufactured nanomaterials (OECD 2015, retrieved from

<http://www.epa.gov/reviewing-new-chemicals-under-toxic-substances-control-act-tsca/meeting-materials-oecd-expert> on 10/10/15).

Nanotechnology is applied to many disciplines including engineering, medicine, electronics and alternative energy research (Oberdörster et al. 2007) and NPs are found within an array of products, from toothpastes, wound dressings and paints, to applications in the treatment of diseases (section 1.10.1). Their exploitation in many areas allows for pioneering developments within each field. NPs can be created to interact with cells/tissues at the molecular level, thus allowing their breakthrough into the medical industry (Navalakhe & Nandedkar 2007). Exploitation of nanomedicine in a clinical setting is expected to be diverse and this area of research is very exciting. For example, the anti-microbial properties of some NPs are well established so they can be exploited in many areas of medicine (e.g. use in wound dressings, plasters, coatings on surgical equipment) (Zinjarde 2012). NPs can also be used as delivery systems for therapeutics and/or diagnostics (Pandey & Khuller 2006; Liu et al. 2007).

### **1.11.1 Nanomedicine**

The European Technology Platform on Nanomedicine (ETPN) gives the following definition for nanomedicine “...*Nanomedicine is the application of nanotechnology to achieve innovation in healthcare... It exploits the improved and often novel physical, chemical, and biological properties of materials at the nanometric scale... nanomedicine has the potential to enable early detection and prevention and to drastically improve diagnosis, treatment and follow-up of many diseases...*” (ETPN 2015 retrieved from <http://www.etp-nanomedicine.eu/public/about-nanomedicine/what-is-nanomedicine> on 26/01/16).



Studies investigating the uses of NPs in medicine are becoming hugely popular, evidenced by the dedication of journals to nanomedicine and nanotoxicology, and the increased prevalence of international conferences focusing on this topic. Some of the benefits (and risks) offered by nanomedicine will be discussed.

Research into the use of NPs in medicine is predominantly focused around cancer and their use as drug carriers to treat and diagnose diseases. Nano-devices (e.g. nanowires and cantilevers), nanocrystals, dendrimers and nanoshells are nanomedicine structures that are becoming more customary in medical research (Navalakhe & Nandedkar 2007). As of 2013 there were 32 FDA approved nanomedicines available on the market and many different nano-devices available (Etheridge et al. 2013) this number is thought to now be over 50 (McDonald et al. 2015) with 70 currently undergoing clinical trials (ETP 2015).

There are currently 4 main types of nanomedicine; nanocarriers (e.g. liposomes), polymer therapeutics (e.g. polymer-drug conjugates), solid drug nanoparticles (SDNs [e.g. nanocrystals]) (Fig 1.10) and NPs themselves (e.g. metal NPs for magnetic resonance imaging [MRI]) (Busquets et al. 2015; Niemirowicz et al. 2012; McDonald et al. 2015). By encapsulating drugs either in NPs or by adhering them to NP surfaces, nanocarriers are utilised to transport drugs. Through the conjugation of water-soluble polymers and drugs, polymer therapeutics are achieved. Upon degradation of the joining bond between the polymer and drug, the drug is released, ideally in a target site, which offers controlled release. SDNs are a novel development in nanomedicine (McDonald et al. 2014). These are simply NPs of solid drug (Fig 1.10), often stabilised by polymers and will be further discussed in Chapter 5.

There are many advantages to using nanomedicine for therapeutic uses. A main advantage is the possibility of lowering the drug dose administered to patients, thus

causing fewer side effects and possibly reducing the treatment time. This is achieved through improved targeting of the NP (e.g. nanocarrier/SDNs) to the required target site, therefore enhancing the drug concentration at specific sites while decreasing delivery to non-target sites (Byrne et al. 2011). Targeting (which can be active or passive) can be achieved by modifying NP surfaces with polymers and/or through bio-conjugation of antibodies and specific ligands. This can prevent NPs binding with non-specific blood components and targets them to specific receptors (McCarron et al. 2008; Kamaly et al. 2012a). This can also increase the blood circulation time of nanomedicines which may be achieved by reducing the phagocytic clearance of a drug (Kamaly et al. 2012b). Polyethylene glycol (PEG) is a polymer and when added to the surface of NPs, renders the NP hydrophilic. This addition reduces reticuloendothelial system uptake of NPs (e.g. liver, spleen), thus allowing it to stay in circulation longer (Jokerst et al. 2011). PEG is also reported to reduce the formation of aggregates (Jokerst et al. 2011). Additionally if drugs are encapsulated by NPs (e.g. liposomes), they can be protected from enzymatic degradation (e.g. in the blood) and this could also improve drug stability. Nanocarriers can be designed to control drug release (e.g. some carriers will only release drugs at a certain pH) possibly further enhancing drug absorption at specific sites (McDonald et al. 2015).

NPs can aid in early diagnosis, which can be paramount in many diseases to lower mortality rates (Niemirowicz et al. 2012; Choudhary & Kusum Devi 2015; Cheon et al. 2016). For example, quantum dots (QDs [semiconductor devices]) are NPs which can be designed with specific antibodies on their surface that have been utilised to detect cancer biomarkers (e.g. in blood or tissue samples) via fluorescence (Farias et al. 2009). This breakthrough has been very advantageous for cancer diagnostics, where due to metastasis early diagnosis is paramount. QDs have been shown to be highly specific, accurate and sensitive at detecting cancer cells during early tumour formation where conventional

methods are not (Pericleous et al. 2012). This also offers a direct financial benefit, as early disease diagnosis often means less treatment time, less medication requirement and therefore a better overall prognosis.

Drugs can be administered (pulmonary, intestinal, subcutaneous and intravenous) and transported into the blood from the exposure site. Some nanomedicines can pass through the blood brain barrier (BBB), fine capillary blood vessels and offer improved drug uptake across other barriers (e.g. lung and intestinal) (Onoue et al. 2014; De Jong & Borm 2008). This advantage provides alternative routes of drug delivery and allows the drug to avoid pathways where it may be lost or reduced (e.g. acid digestion in the stomach). There are effective barriers (e.g. epithelial) designed to prevent the entry of foreign particles/substances into the human body, cells and organs. Such barriers can prevent optimal drug delivery and concentration reaching target sites.

NPs have a large surface area relative to their volume, and their size is comparable to intracellular macromolecules and organelles such as proteins and DNA. Their small size allows nanomedicines to interact with targets on cell surfaces and internally (Navalakhe & Nandedkar 2007). Macrophages uptake and phagocytose smaller entities more readily than larger forms of the same material (Clift et al. 2008). Therefore, if drugs are in the nano-form this could be advantageous in treating some diseases where bacteria reside in immune cells (e.g. TB) or in cancer treatments where its reported that liposomes <130 nm have a higher level of selectivity and tumour accumulation over larger liposomes (Meerovich et al. 2008). This is a phenomenon of the ‘enhanced permeability and retention’ (EPR) effect, another means of targeting NPs to specific sites (size dependent). Additionally, in the nano-form, drug bioavailability can be increased due to the relatively high surface area available allowing for higher local concentration as illustrated in Figure 1.10.

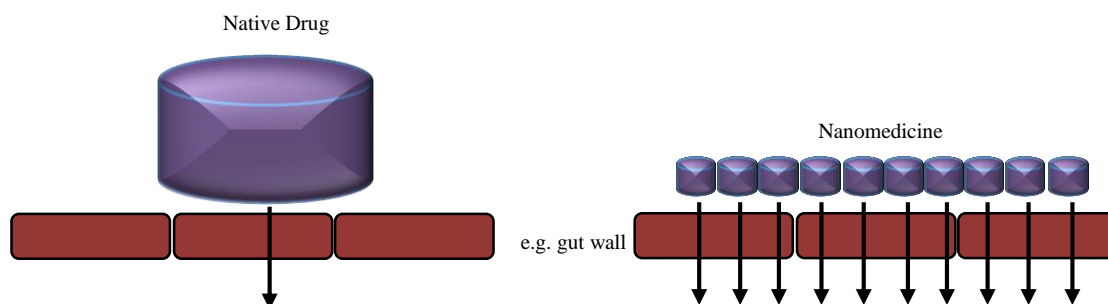


**Figure 1.10 Schematic diagram of a ‘native’ drug compared to a nanomedicine passing through a barrier.** As illustrated, in the nano-form there is increased bioavailability. The passing (diffusion or transcytosis or endocytosis *etc*) through a barrier (e.g. the gut wall, BBB, capillaries) is likely enhanced when in the nano-form.

In the design stages of nanomedicines, particle size, shape and surface chemistry is highly important to allow for effective delivery and targeting (Byrne et al. 2011; Perry et al. 2011). There are various methods to construct nanomedicines (e.g. PRINT, nanomilling, emulsion templated freeze drying) (Perry et al. 2011; McDonald et al. 2014). Nanomilling works by adding powdered drug in water (containing stabilisers) to a milling chamber where shear forces reduce the powdered drug (with adhered stabilisers) to SDNs. Although well established, this technique has reportedly low drug loading ability for single SDNs (rarely > 25%) (McDonald et al. 2014). Emulsion templated freeze-drying is a similar technique which can also be employed to create SDNs and it was this method that the SDNs utilised in this project were created (Chapter 5).

### **1.11.2 Health Implications of NPs**

The toxicology literature provides evidence that there are potential health risks associated with exposure to some types of NPs (Kermanizadeh et al. 2014; Fernández-Cruz et al. 2012; Song et al. 2009; Christensen et al. 2010; Johnston et al. 2015; Johnston et al. 2012; Chen et al. 2011; Onoue et al. 2014). Therefore, prior to use in products (e.g. foods and

medicines) the hazards must be evaluated (Johnston et al. 2012; Semete et al. 2010; Song et al. 2009; Onoue et al. 2014). Much of the evidence available, is indicative that the unique properties of NPs (which make them useful in some fields) also renders them more harmful to humans (Bondarenko et al. 2013a). NP physico-chemical properties are different to their bulk counterparts and as such investigations into the toxicology of NPs is an important area of research. The USA and EU are therefore urgently seeking the health and safety status of NPs to be established. Although NPs may be more suitable at targeting desired cells, organs (e.g. liver) or organisms (e.g. bacteria) their effects on non-target cells, organs or organisms may be detrimental.

The risk (i.e. probability of causing an adverse health effect) of a NP is founded on the level of exposure, the toxicity of the NP and exposure route (Kermanizadeh et al. 2014). Following exposure to NPs (e.g. oral [intestine], inhalation [lung], dermatological [skin]), it is possible for the NP to induce toxicity at the exposure site (local toxicity) and secondary target sites (systemic toxicity) (Johnston et al. 2012). (Johnston et al. 2012). Only a small proportion of NPs can cross lung, skin and intestinal barriers (Vandebriel & De Jong 2012; Jachak et al. 2012). However, bio-distribution studies have identified that the liver is a primary site of NP accumulation, regardless of exposure route (Kermanizadeh et al. 2014). Hazard studies therefore need to assess NP toxicity at a range of target sites. The mode of action of NP toxicity has not been extensively investigated. However, the main toxic effects observed from NP exposure include oxidative stress, inflammation, ROS production, carcinogenicity and genotoxicity (Johnston et al. 2015; Li et al. 2008; Kermanizadeh et al. 2012; Kermanizadeh et al. 2014; Gaiser et al. 2013). The relationship between NP physico-chemical properties and their toxicity has been investigated. Size (and surface area), shape, charge, crystallinity, surface modifications, and aggregation/agglomeration status, are all characteristics that play significant roles in influencing toxicity (Warheit et al. 2009). The large surface area

of small NPs is assumed to mediate the formation of free radicals that consequently leads to a signally cascade involving many factors which drives oxidative stress, thus ultimately triggering an inflammatory response (Byrne & Baugh 2008; Johnston et al. 2015). The large surface area provides a large surface over which ROS can be produced as at small sizes the curvature of the NP surface is high therefore there is limited space available for electrons to form stable bonds between atoms within the particle structure, making the bonds more reactive, hence the surface reactivity.

The exposure route is important to consider for NP toxicology studies. As with the disastrous effects following asbestos (micron scale fibres) exposure to the lungs, inhalation is one of the main routes for the entry of NPs and once inhaled they are deposited in the lungs. Like most foreign bodies, NPs are likely to be engulfed by alveolar macrophages (Geiser 2010). Studies have revealed that exposure to some NPs (e.g. Cu(II)O or ZnO NPs), over certain time points (e.g. 1 day), doses (e.g. 5 mg/kg) and size (e.g. < 50 nm), caused chronic lesions and inflammation in the lungs (inflammation is generally characterised by increased cytokine/chemokine production) and prolonged exposure to the NPs increased the risk of pulmonary infection (Sandhya et al. 2013; Gantedia et al. 2012). The transport of NPs across the lung epithelium is still under investigation, but the literature provides evidence for trafficking via endocytosis and by other means (Elsaesser & Howard 2012). Choi *et al.*, found that organic NPs < 34 nm were rapidly translocated from the lung to the kidneys via the bloodstream *in vivo* (Choi et al. 2010) and Geiser *et al.*, reported the uptake and clearance of titanium dioxide (TiO<sub>2</sub>) NPs by lung phagocytes which was said to be ‘sporadic’ and unspecific (Geiser et al. 2008). Yacobi *et al.*, reported translocation of NPs, but not via the usual endocytic pathways, but by possible diffusion through plasma membranes (Yacobi et al. 2010). As it is assumed that NPs can be trafficked from origin sites, this increases the requirement to recognise the potential toxicity these NPs may have following inhalation/ingestion, on

sites such as the liver or brain. Investigations into the effects of NPs on hepatocytes (the major cellular component of the liver) has demonstrated that both silver and zinc oxide NPs increased pro-inflammatory cytokine production using a human cell line (C3A) (Kermanizadeh et al. 2012). The route of administration and the size of the NPs were important factors in toxicity, with intravenous administration and smaller NPs producing adverse effects (Kermanizadeh et al. 2014).

Song *et al.*, reported a human case study where healthy females contracted progressive lung fibrosis following exposure to a spray paint. Upon analysis of the paint as well as the chest fluid of the patients, 30 nm diameter NPs were detected (Song et al. 2009). By use of specialised microscopy techniques, aggregates of NPs were revealed in the cytoplasm of epithelial and mesothelial cells and the authors believe this lead to malignant tumour formation and various other disorders. The authors concluded that as these results were similar to controlled *in vivo* animal experiments, it was very likely that the NPs in the paint caused this advanced diseased state in the females over a very short period of time (5-13 months), where 2 out of 7 patients died within 21 months from symptoms onset (Song et al. 2009). Although these were industrial NPs, it warrants great concern and this appears to be the first documented case on human fatalities following NP exposure. However, there are serious problems with this report and although there is compromising evidence suggesting the NPs were the causative agents, the authors were unable to offer specific information on the NPs, or on exposures the women may have had to other toxic chemicals (either in the work place or at home). No characterisation or chemical analysis on the NPs was performed, thus highlighting many flaws in the study design.

It is widely accepted that smaller NPs exert greater toxicity (Donaldson et al. 1998; Ferin et al. 2009; Kermanizadeh et al. 2014). Which concurs with reports that exposure to smaller NPs (<50 nm) exerts a greater inflammatory response than exposure to larger

particles (200 nm) (Byrne & Baugh 2008; Donaldson et al. 1998; Ferin et al. 1992). Actually, most of the literature on the toxicity of NPs has data that strongly advocates NP exposure can cause an inflammatory response in both *in vivo* and *in vitro* settings. Going back nearly 25 years, Ferin *et al.*, reported that when rats were exposed (via inhalation) to ‘ultrafine’ (<21 nm) or ‘fine’ (250 nm) TiO<sub>2</sub> NPs, the smaller NPs were found to translocate across the pulmonary interstitium more readily and were retained in the lungs for longer periods of time compared with the larger NPs. The NPs caused an acute inflammatory response indicated by an increase in polymorphonuclear leukocytes (Ferin et al. 1992). Johnston *et al.*, reported that silver NPs (< 50 nm) induced production of pro-inflammatory cytokines following exposure (4-24 hours at 7-15 µg/mL) to neutrophil-like cells, eventually leading to apoptosis (Johnston et al. 2015). Cha *et al.*, demonstrated that when silver NPs were fed to mice over 3 days, there was a strong inflammatory response in the livers (lymphocyte infiltration). Using microarray analysis, the authors detected changes in gene expression of genes directly related to apoptosis and inflammation, supporting their initial conclusions (Cha et al. 2008). As well as occupational exposure to NPs (as with the case study outlined), combustion derived NPs exist in the atmosphere (e.g. diesel NPs) and *in vivo* studies have shown them to cause inflammatory and fibrotic events in the lungs (Tran et al. 2000).

The use of poly (lactide-*co*-glycolide) acid (PLGA) polymer NPs as drug delivery systems is very popular in nanomedicine (McCarron et al. 2008; Semete et al. 2010; Panyam et al. 2002; Dube et al. 2013; Onoshita et al. 2010). PLGA are biodegradable polymers, particularly attractive as they are FDA approved for clinical use in humans, they convey very low toxicity and due to the ability to modify surface properties they offer enhanced interaction with biological materials (Onoshita et al. 2010). Using PLGA, drugs can be delivered to specific sites, where the polymer can degrade intracellularly thereby releasing the drug(s) (Kalluru et al. 2013). Although PLGA polymers are FDA



approved, their use as nanocarriers required investigation. A study investigated the toxicity exerted by PLGA NPs compared to industrial NPs *in vitro* and *in vivo*. The authors reported that PLGA NPs had no cytotoxic effect on both human colorectal carcinoma and epithelial carcinoma cells lines (Semete et al. 2010). However, following 7 days of ingestion of NPs *in vivo* (mice) tissue distribution tests were carried out and 40% of PLGA NPs were detected in liver, 25% in the kidney, 11% in the heart and 3% in the brain (Semete et al. 2010). Although the authors report no cytotoxicity from *in vitro* tests on two cell lines, caution must be exercised from these results. For example, there was no investigation into whether there was an inflammatory response and it demonstrated that PLGA NPs can cross the BBB efficiently, which is advantageous when considering drug transportation to sites in the brain (e.g. for some chemotherapies), yet this may also have harmful consequences, especially if aggregates were to form. If aggregates formed, the drug may not be able to be cleared or metabolised thus preventing efficiently drug delivery. Additionally, the formation of aggregates of drug-loaded carriers in organs could have serious consequences, possibly leading to an inflammatory response.

Overall, there are many desirable characteristics associated with the use of NPs in consumer products and medicines, but in spite of these traits, due to the possibility of inducing oxidative stress and genetic damage, their use for clinical applications should be thoroughly investigated.

### **1.12 NPs and TB: current literature review**

The antimicrobial properties of NPs are well documented (Ansari et al. 2011; Sharma et al. 2009; Ren et al. 2009; Neyrolles et al. 2013; Azam, Ahmed, M. Oves, et al. 2012;

Islam et al. 2013; Rai et al. 2009), hence it is logical to hypothesise that they may have anti-mycobacterial properties also. The mechanisms by which they exert antimicrobial properties are discussed in depth in the following chapters (4 and 5). Delivering an effective concentration of anti-TB drugs to sites where *Mtb* resides in the immune cells, deep within the lungs, is a huge feat, as often drugs dissolve rapidly and are absorbed by the blood (Mizoe et al. 2008). Cells take up molecules/particles through phagocytosis and pinocytosis: ‘cell drinking’, processes generally defined as endocytosis. By engulfing NPs, particularly in the case of macrophages where *Mtb* resides, the particles may be co-localised with the microorganism. This would allow for very accurate targeting, for both anti-microbial NPs, as well as drug delivery. Furthermore, it is accepted that smaller NPs are efficient at crossing epithelial barriers following oral administration, hence the branching of nanotechnology into TB research (Hussain et al. 2001). As such, nanomedicine has led to an original path of research undertaken within the therapeutic field of TB.

Recent literature on using nanomedicines to target TB is predominantly based on the use of polymers or liposomes with drugs such as RIF (Ohashi et al. 2009; Aboutaleb et al. 2012; Raj et al. 2012; Chuan et al. 2013; Pandey & Khuller 2006; Pandey & Khuller 2005; Dube et al. 2013; Hirota et al. 2010). Studies have highlighted the possibilities of encapsulating anti-TB drugs within biodegradable polymer NPs thus offering assistance in increasing the concentration of drugs at specific sites (e.g. infected macrophages) through targeting. NPs containing anti-TB drugs are usually made from biodegradable materials (e.g alginate or solid lipids) and most TB research focuses on the use of PLGA synthetic polymers (Gelperina et al. 2005; Onoshita et al. 2010; Ohashi et al. 2009; Hirota et al. 2010; Kalluru et al. 2013). Hirota *et al.*, carried out a study to determine the uptake and cytotoxicity of PLGA microspheres (MS) loaded with RIF on NR8383 cells derived from rat alveolar macrophages (Hirota et al. 2010). It was determined that RIF PLGA

MS had little/no cytotoxicity against the NR8383 cells (at 5 µg/mL for 48 hours) and were readily taken up by the cells, significantly more than when compared with RIF in a non-nano form (native drug). Additionally, they reported that high concentrations of RIF were detected within phagosomes, suggesting that RIF entrapped in PLGA MS can enter membranes of macrophages (probably through phagocytosis) more readily than native RIF. NR8383 cells were then infected with *M. bovis*-BCG and exposed to the RIF PLGA MS. The RIF PLGA MS were found to be bactericidal against intracellular *M. bovis*-BCG, significantly more so than native RIF at both concentrations tested (0.25, 2.50 µg/mL) over a period of 7 days incubation (Hirota et al. 2010). Comparing RIF administered via a nano-carrier compared to a solution in an *in vitro* setting offered very encouraging results, and could be very useful in the treatment of LTBI.

Aboutaleb *et al.*, created RIF loaded solid lipid NPs (SLNs [NPs with a solid hydrophobic core coated with a phospholipid monolayer]) for intravenous administration. The aim was to create spherical, stable RIF SLNs <100 nm in diameter. They found that RIF was released over a 120 hour period *in vitro* in a biphasic pattern when in SLNs form, thus indicating that the drug release was controlled and did not occur instantaneously (Aboutaleb et al. 2012). The anti-mycobacterial properties of the SLNs were tested against a surrogate strain of *M. fortuitum* and results show an 8-fold higher efficacy at inhibiting growth when delivered in the SLNs compared with native RIF solution. Controlled release could offer potential to lowering dosages therefore these were promising results. However, the SLNs were prepared with 2 g of Tween 80. Tween 80 (a detergent) can have a toxic effect on some mycobacterial species and at high concentrations an effect would be expected (Van Boxtel et al. 1990). A suitable control measure was not in place, which may have altered the results on the mycobacterial growth observed.

Dube *et al.*, have designed a 1,3- $\beta$ -glucan (Glu) functionalised chitosan shell (CS), PLGA core NPs loaded with RIF drug (Glu-CS-PLGA+RIF [Fig 1.11]) with the aim of both stimulating some antimicrobial responses which *Mtb* suppress within the host macrophage, and delivering RIF intracellularly (Dube et al. 2013). The spherical Glu-CS-PLGA+RIF NPs created were approximately 280 nm in size with a zeta potential of  $+12.47 \pm 8.49\text{mV}$ .

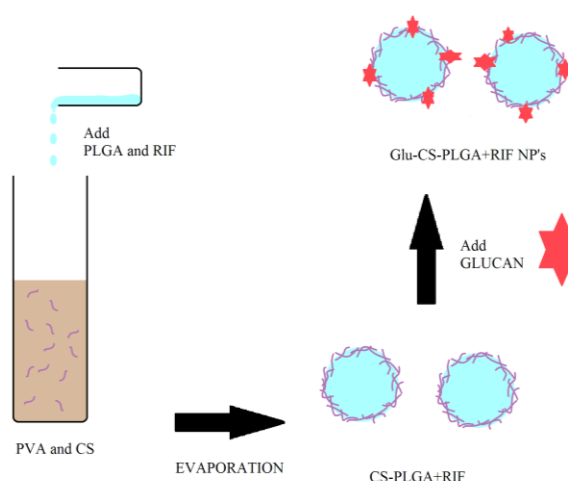


**Figure 1.11 Preparation of Glu-CS-PLGA+RIF NPs**  
(created using Dube *et al.*, 2013)

Using human alveolar-like-macrophages (ALM), NP uptake was achieved through incubation (6 hours) and confirmed by confocal microscopy. Cytotoxicity testing proved no significant change in macrophage viability when incubated with Glu-CS-PLGA NPs (at 0.1% v/v nanoparticle suspension in water) for 2 hours (although there was great variation in the data) (Dube et al. 2013). The focus was on *Mtb*'s ability to prevent the host cell (macrophage) from producing bactericidal ROS and reactive nitrogen species (RNS) and pro-inflammatory cytokines (eg: IL-12 and IFN- $\gamma$ ). This suppression aids in *Mtb*'s intracellular survival. In the design of Glu-CS-PLGA+RIF NPs, 1,3- $\beta$ -glucan was selected as it can interact with Dectin-1 macrophage surface receptors which promote both pro-inflammatory cytokine production, ROS/RNS generation and also enhance the

process of phagocytosis (Dube et al. 2013). Results suggest that CS-PLGA+RIF NPs successfully increased the anti-microbial activities of macrophages; TNF- $\alpha$ , IFN- $\gamma$  and IL-12 secretion were all enhanced by the NPs. Interestingly, it was reported that this work confirmed that RIF could be delivered 4 times faster when delivered as a NP construct rather than as a free RIF solution (*in vitro*), however the efficacy of the drug in this NP formulation is not known as no tests with *Mtb* infected macrophages were carried out (Dube et al. 2013). Also, this study utilised human monocytes that differentiated *in vitro* to alveolar-like-macrophages. As such, alveolar macrophages have not yet been tested and would require an *in vivo* study to confirm the preliminary cytotoxicity data.

In a more recent study, Edagwa *et al.*, demonstrated that PLGA NPs encapsulating RIF and a modified INH drug (INHP), localised in subcellular organelles within phagosomes in monocyte derived macrophages (MDMs) (MDMs) (Edagwa et al. 2014). Their results display confocal microscopy images of PLGA RIF and INHP in endosomal compartments. To determine whether these NPs were trafficked to the same compartment as mycobacteria, the MDMs were infected with *M. smegmatis* and then treated with the NPs. Imaging suggested that co-localisation also occurred for the particles and the mycobacteria within the MDM cells (Edagwa et al. 2014). To assess their anti-mycobacterial activities, MDMs were exposed to RIF PLGAs (loaded with approximately 10% drug) and INHP PLGAs (loaded with approximately 5% drug) for 24 hours, then MDMs were infected with *M. smegmatis* for 1-10 days. The same experiment was carried out for RIF and INHP in native forms. Comparing the results between the 2 types, the PLGA NPs exerted over 1.3-fold greater toxicity after 1 day incubation with *M. smegmatis* at 300  $\mu$ M (Edagwa et al. 2014). It was found that when MDMs were infected with mycobacteria following 10 days of exposure to the PLGAs or native drugs, the PLGA NPs inhibited mycobacterial growth by 50%, whereas the native drugs had no effect on mycobacterial growth in macrophages. This suggesting that in the nano-form,

drugs are retained for extended periods inside macrophage cells. It must be noted however, that this was a somewhat unorthodox means of measuring anti-mycobacterial activity, as the macrophage cells were first treated with the drug (in both nano and native forms) before being infected with mycobacteria. It is unclear whether this is a means to prevent infection rather than clearing an infection. Additionally, for an *in vitro* experiment, the authors tested relatively high concentrations of drugs (up to 300  $\mu$ M). Overall however, these results were encouraging from a nano-medicine perspective.

With published reports demonstrating PLGA NPs carrying anti-TB drugs being engulfed by macrophages, the possibility of targeting granulomas has begun to be investigated. Granulomas are concentrated masses of *Mtb* infected macrophages (section 1.5) and are poorly accessed by drugs, thus they harbour mycobacteria which could cause reactivation to a diseased state or lead to the development of MDR TB. Grobler *et al.*, have reported that delivering NPs to granulomas is possible (Grobler et al. 2016). Using colloidal Pheroids (NPs with an oil, gas and water phase that are filled with RIF [dissimilar to PLGAs]) and an *in vitro* granuloma model, it was possible to target NPs to the macrophages. Pheroids are a patented drug delivery system, with the ability to control the rate of drug clearance and offer protection to drugs (e.g. from enzyme degradation) *in vivo* (Steyn et al. 2010). The analytical model presented by Grobler *et al.*, demonstrate that when RIF was delivered using Pheroids, there was a significantly higher concentration of RIF in the macrophages than in the blood (of 16 patients following their fourth daily dose of drug) when compared to native RIF. This suggesting that RIF can be targeted to macrophages when delivered in this form (Grobler et al. 2016). Additionally, using the delivery system, higher drug concentrations were measured at several positions in the granuloma model when compared with the native RIF. This work correlated nicely with the previous reports; when RIF was administered in a nano-

formulation (loaded on either PLGAs, SLNs or packaged in Pheroids) a higher concentration of drug reached the desired site compared to a solution of native RIF.

### **1.13 Summary**

The effective treatment of TB remains one of the world's biggest challenges. This primitive disease has killed more than 100 million people, and even with tremendous advances in medicine, it is still evading eradication. The rise of MDR and XDR TB is extremely concerning and the problems facing medical practitioners are only set to increase with the growing population. Any advance in reducing TB treatment time and the number of different drugs administered would be advantageous. As the use of NPs in the management of other human diseases increases, including infectious diseases, it is hoped that they will be found to be equally useful in the fight against TB. Nanomedicines may be the alternative to current drug regimes, but thorough investigations into their use is required first.

## 1.14 PhD Proposal

Given the global situation of TB and the advances offered by nanomedicine, this project had four main aims:

1. To develop, optimise and validate an *in vitro* screening procedure for the identification of effective anti-TB drugs or NPs.
2. Using the above assay, screen for anti-mycobacterial properties of a range of NPs.
3. To utilise an *in vitro* macrophage infection model to investigate the uptake of SDNs by infected macrophages and the relative intracellular localisation of SDNs in comparison to mycobacteria.
4. To assess the ability of SDNs to kill or inhibit the growth of mycobacteria within infected macrophage models *in vitro*.



# **CHAPTER II**

## **GENERAL METHODS AND MATERIALS**

## **2.1 Culture of mycobacteria (using aseptic techniques in a microbiological safety cabinet [class 2])**

### ***2.1.1 Growth conditions***

*Mycobacterium avium*. subsp *paratuberculosis* (*Map*) was supplied by Raul Barletta, University of Nebraska, Lincoln (Harris et al. 2002). *Map* strain K10 was supplied transformed with a plasmid carrying the *gfp* gene and a kanamycin resistance gene (*Map* K10/GFP). *Map* K10/GFP from agar stock was cultured in 10 mL of Middlebrook 7H9 broth medium (see 6.2.1) supplemented with 10% (vol/vol), Middlebrook ADC enrichment (albumin/dextrose/catalase [Becton Dickinson, UK]), with 0.2% (vol/vol) glycerol, 0.05% (vol/vol) Tween 80 (+ [Sigma-Aldrich<sup>®</sup>, UK]), 2 µg/mL mycobactin J (Allied Monitor, France) and 25 µg/mL of kanamycin (K) (hereafter named 7H9K<sup>+</sup>) in sterile universals at 37°C gently stirred continuously with magnetic stirrers.

### ***2.1.2 Sub-culturing: broth cultures***

To produce mycobacterial liquid stocks, *Map* K10/GFP was grown in sterile plastic universals containing 10 mL of 7H9K<sup>+</sup> as outlined in 2.1.1. Growth was monitored by McFarland (McF) standards using a Densimat<sup>®</sup> (Peñuelas-Urquides et al. 2013). Cells were harvested in the log phase of growth (McF 3-5); 2 mL of the bacterial suspension was pelleted by centrifugation at 3080 g for 20 minutes at 20°C. The pellet was then re-suspended in the appropriate volume of 7H9K<sup>+</sup> to give McF standard 3, from which 100 µL was sub-cultured into 10 mL of 7H9K<sup>+</sup> and allowed to grow for 7 days, in the dark at 37°C, gently stirred continuously with magnetic stirrers, before the sub-culturing process was repeated. Universals were only seeded from liquid broths as above or directly from 7H11 slopes (2.1.3).

### ***2.1.3 Sub-culturing: slopes***

To maintain mycobacterial stocks, *Map* K10/GFP was grown in sterile plastic universals containing 10 mL of 7H9K<sup>+</sup> as outlined in 2.1.1, 2 mL of the bacterial suspension was pelleted by centrifugation at 3080 g for 20 minutes at 20°C. The pellet was then re-suspended in the appropriate volume of sterile PBS to give a McF standard > 3, from which 100 uL was sub-cultured onto 10 mL 7H11 agar slopes (see 2.6.3 [in glass McCartney bottles]). The cell suspension was evenly spread over the slopes (bottle lids loosened for 7-10 days to allow drying). Slopes were left for a minimum of 8 weeks (or until good visible coverage of cells) incubated at 37°C in the dark.

### ***2.1.4 Preparation of glycerol stocks***

To freeze down stocks at low passage numbers, using a sterile swab, colonies were removed from a 7H11 slope and added to 30% glycerol and mixed well. Cell density was monitored using a Densimat<sup>®</sup> (wanted McF >5). From this, 1 mL was added to a cryovial for storage at -80°C. Later, these stocks could be defrosted at room temperature and inoculated onto 7H11 agar slopes.

### ***2.1.5 Retrospective colony counts***

Following inoculation of 100 µL of a serial dilution onto 7H11 (90 mm petri dishes) the dishes were inverted, placed in airtight containers and incubated at 37°C. Colony counts (colony forming units [cfu]/mL) were performed after 12 weeks. Plates were checked regularly for contamination. To calculate CFU from counts, dilution factors were

accounted for and numbers were multiplied by 10 to determine CFU/mL (not per 100  $\mu$ L).

## **2.2 Nanoparticles (NPs)**

### ***2.2.1 Preparation***

All NPs were sub sampled under sterile conditions and kept in the dark at ambient temperature until use. NPs were weighed into sterile bijoux using a Sartorius balance (ME36S [Sartorius, UK]) to 3-6 mg per sample. NPs were suspended in sterile fetal calf serum (FCS [2% (vol/vol) prepared in sterile distilled water]) at a concentration of 1 mg/mL and sonicated for 16 minutes at 400 W in a bath sonicator from Ultrawave<sup>®</sup> (Cardiff, UK) and then placed on ice prior to use following the ENPRA (Risk Assessment of Engineered Nanoparticles) protocol ([www.enpra.eu](http://www.enpra.eu)) (Jacobsen et al. 2010; Kermanizadeh et al. 2013). NPs were then diluted in Middlebrook 7H9 medium supplemented with 10% (vol/vol) Middlebrook ADC enrichment (albumin/dextrose/catalase [Becton Dickinson, UK]), 0.2% (vol/vol) glycerol, 2  $\mu$ g/mL mycobactin J (hereafter named 7H9) or RPMI (1640 [Thermo Fisher Scientific, UK] supplemented with 10% heat inactivated FCS, 100  $\mu$ g/mL STR, 100 IU/mL penicillin, 0.1 mM non-essential amino acid and 1 mM sodium pyruvate solution [hereafter named complete medium]). Concentrations were achieved by further serial dilutions in the appropriate medium.

### ***2.2.2 Dynamic light scattering (DLS)***

Agglomeration/aggregation status, zeta potential, hydrodynamic size and polydispersity

index (PdI) of all NPs were analysed by dynamic light scattering (DLS) at a concentration of 100 µg/mL in 7H9 (NPs were prepared as outlined in 2.2.1) at a temperature of 25°C using a Zetasizer Nano-ZS instrument with a 4 mW He–Ne, 633 nm laser (Malvern Instruments Ltd., UK). Samples were first vortexed for 10 seconds and slowly (to avoid air bubbles) syringed into disposable capillary zeta cells. Malvern Zetasizer software (version 7.03) was used for data analysis. Averages were obtained from a minimum of three individual measurements and were obtained using the instrument's automatic optimisation settings. Generally, agglomerates are defined as NPs held together by weak bond and can be dispersed (e.g. by ultrasonication) whereas aggregates are NPs held by much stronger bonds (e.g. covalent bonds) (Müller et al. 2014).

## **2.3 Macrophage (J774A.1) cells**

### ***2.3.1 Macrophage cell culture conditions***

J774A.1 murine mouse 'macrophage-like' cell lines were obtained from the European Collection of Cell Cultures (ECACC). J774A.1 cells (hereafter referred to as 'macrophages') were cultured in complete medium in 75cm<sup>2</sup> T5 flasks (Corning, canting neck [Sigma-Aldrich®, UK]) and incubated at 37°C, 5% CO<sub>2</sub> until confluent. Sub-culture was achieved using a gentle scraping method in sterile conditions to remove adhered cells which were re-suspended in fresh complete medium in sterile 75cm<sup>2</sup> T5 flasks.

### ***2.3.2 Macrophage stocks (storage)***

Macrophage stocks were maintained by culturing them in complete medium in 75 cm<sup>2</sup> T5 flasks and incubating at 37°C, 5% CO<sub>2</sub> until confluent. Cells were detached from flasks using TrypLE™ Express Gibco® (Thermo Fisher Scientific, UK) and centrifuged at 850

g for 5 minutes. The supernatant was removed and the pellet was resuspended in complete medium (1 or 2 mL depending on pellet size) and at a density of  $2.4 \times 10^7/\text{mL}$  (using trypan blue [section 2.5] for accurate cell counts) added to 0.5 mL of DMSO and 0.5 mL of FCS (heat inactivated) in a cryovial then stored at  $-80^\circ\text{C}$  for 24 hours (in a Nalgene box with 250 mL isopropanol) before transferring to liquid nitrogen for longer term storage.

### ***2.3.3 Macrophage stocks (revival)***

Pre-warmed complete medium (30 mL) was added to macrophage stocks from liquid nitrogen storage and the semi-frozen solution was added to 30 mL of complete medium and centrifuged at 850 g for 5 minutes. The supernatant was removed and the pellet was resuspended in 5 mL of complete medium and added to  $25 \text{ cm}^2$  T5 flasks incubated at  $37^\circ\text{C}$ , 5%  $\text{CO}_2$ . Growth was monitored daily and once confluent, cells were re-seeded into  $75 \text{ cm}^2$  T5 flasks for use.

## **2.4 Alamar blue assay**

Macrophages were grown as outlined in section 2.3 until confluent. The alamar blue assay set up was achieved by using a gentle scraping method in sterile conditions to retrieve the cells which were re-suspended in 6 mL of complete medium and centrifuged at 850 g for 5 minutes. The supernatant was removed and the pellet was resuspended in complete medium (1 or 2 mL depending on pellet size) and then seeded into the wells of flat-bottomed, cell culture 96 well plates at a density of  $5 \times 10^5/\text{mL}$  (using trypan blue [section 2.5] for accurate cell counts) at a total volume of 100  $\mu\text{L}$  per well and incubated at  $37^\circ\text{C}$ , 5%  $\text{CO}_2$  for 24 hours to allow adherence. The supernatant was removed from

the wells after 24 hours incubation. NPs/drugs at pre-determined concentrations (each concentration was prepared in triplicate treatment groups) were prepared as outlined in 2.2.1 (in an appropriate volume of complete medium) and were added to the wells and incubated at 37°C, 5% CO<sub>2</sub> for a further 24 hours. Positive (macrophages and 0.1% Triton [to indicate 100% of lysis of cells]) and negative (macrophages and medium only) controls were included in each plate. The supernatant was removed and cells were washed twice with PBS, 0.1 mg/mL of alamar blue cell proliferation reagent (Sigma-Aldrich®, UK) was added to each well (1:10 dilution in complete medium) and incubated for an additional (and final) 4 hours at 37°C, 5% CO<sub>2</sub>. Fluorescence was then read at an excitation wavelength of 560 nm and an emission wavelength of 590 nm using a SpectraMax M5 plate reader (USA). To account for NP interference, the 96 well plate was centrifuged at 850 g for 2 minutes and the supernatant was removed from each well and transferred into a fresh plate to be re-read at an excitation wavelength of 560 nm and an emission wavelength of 590 nm.

## **2.5 Cell counts**

### ***2.5.1 Macrophage counts***

Macrophages were cultured in complete medium in 75cm<sup>2</sup> T5 flasks and incubated at 37°C, 5% CO<sub>2</sub> until confluent. As above, using a gentle scraping method in sterile conditions, cells were resuspended in 6 mL of complete medium and centrifuged at 850 g for 5 minutes then resuspended in 1 or 2 mL of complete medium. To obtain a homogenous suspension with evenly distributed cells, using a 1000 µL Gilson tip the pellet was gently extracted and expelled in complete medium. Using Trypan Blue Reagent (Sigma-Aldrich®, UK) at a 1:20 dilution with suspended cells, approximately 10 µL of the cell solution was added to a Neubauer chamber (when adding the coverslip to

the counting slide, ensured Newton rings were present confirming the coverslip was firmly adhered). Trypan blue is a vital stain therefore it is excluded from live cells. To gain an average number of cells, the colourless/bright cells (under phase contrast) in the four larger corner squares were counted on both sides and averaged, disregarding any dark stained cells (indicating dead cells) and taking into account the dilution factor and the conversion factor ( $\times 10^4$ ), the number of cells were determined per 1 mL of medium. K10/GFP using microscopy.

### ***2.5.2 Mycobacteria counts***

*Map* K10/GFP cultured in 10 mL 7H9K<sup>+</sup> was centrifuged at 3080 g at 20°C for 20 minutes to pellet the bacterial suspension. The pellet was re-suspended in the appropriate volume of PBS to give a McF standard 2. As above, to obtain a homogenous suspension with evenly distributed mycobacteria, using a 1000  $\mu$ L Gilson tip the pellet was extracted and expelled in PBS and approximately 10  $\mu$ L of the solution was added to a Helber (Thoma grid) bacteria counting chamber (when adding the coverslip to the counting slide, ensured Newton rings were present confirming the coverslip was firmly adhered) and left for 10 minutes to settle (otherwise cell counting was difficult). The 80 small squares (5 large squares with 16 internalised squares) were counted and the total number was divided by 80 to give the average number of cells per square. Using the conversion factor ( $2 \times 10^7$ ) and taking into account the dilution factor, the number of cells was determined per 1 mL of PBS.



## **2.6 Medium preparation**

### ***2.6.1 Middlebrooks 7H9 (+ Tween 80) broth (7H9K<sup>+</sup>)***

Into a large Duran bottle 4.7 g of Middlebrooks broth (7H9) powder (Becton Dickinson, UK), 2 mL glycerol (Sigma-Aldrich<sup>®</sup>, UK), 0.5 mL Tween 80 (Sigma-Aldrich<sup>®</sup>, UK) and 1 vial of mycobactin J (dissolved in 2 mL ethanol) was added to 900 mL distilled water and repeatedly inverted until no visible powder remained. This solution was autoclaved at 121°C for 10 minutes. Broth was stored at -5°C (for up to 6 months) until use. Prior to culturing, 100 mL of Middlebrook ADC enrichment (albumin/dextrose/catalase) and 25 µL of kanamycin (Sigma-Aldrich<sup>®</sup>, UK) was added aseptically.

### ***2.6.2 Middlebrooks 7H9 (- Tween 80) broth (7H9K)***

As above, but without addition of Tween 80.

### ***2.6.3 Middlebrooks 7H11 agar***

Into a large Duran bottle 21 g of Middlebrooks agar (7H11) powder (Becton Dickinson, UK), 0.3 g L-Asparagine (BDH lab supplies, UK), 25 mL glycerol, and 1 vial of mycobactin J (dissolved in 2 mL ethanol) was added to 700 mL distilled water and repeatedly inverted until no visible powder remained. This solution was autoclaved at 121°C for 15 minutes. Prior to decanting, 200 mL newborn calf serum (heat inactivated at 56°C), 100 mL OADC (oleic acid/ albumin/dextrose/catalase enrichment) enrichment medium (Becton Dickinson, UK) and 2 Kirchnew Selectatabs (polymyxin B, ticarcillin, amphotericin B, trimethoprim [Mast Diagnostic, France]) was added aseptically, then 33

mL was poured into sterile petri dishes (90 mm) and left to dry for 30 minutes. Agar filled petri dishes were stored at -5°C (for up to 3 months) until use.

#### ***2.6.4 RPMI***

Into the 500 mL RPMI (Roswell Park Memorial Institute) medium (1640 + L-glutamine [Thermo Fisher, UK]) bottle 5 mL of MEM non-essential Amino Acid Solution (100×) without L-glutamine (Sigma-Aldrich®, UK), 5 mL of sodium pyruvate solution (Sigma-Aldrich®, UK), 5 mL penicillin-STR solution liquid (5000 units/mL [Thermo Fisher, UK]) and 50 mL of heat inactivated FCS was added and mixed well prior to use. Medium was stored at -5°C for use up to 3 months.

### **2.7 Fixatives**

#### ***2.7.1 4% Paraformaldehyde***

In a fume hood, 10 g of paraformaldehyde powder (Sigma-Aldrich®, UK) was weighed and dissolved in 475 mL of pre-heated PBS (60-70°C) and 1-2 drops of 5 M NaOH (Thermo Fisher Scientific, UK) was added thus turning the cloudy suspension clear. This solution was allowed to cool at room temperature before use (up to 2 hours). Solution was stored at -5°C for use in up to 2 days or aliquots were stored at -20°C for up to three months.

### ***2.7.2 3% Glutaraldehyde in 0.1M sodium cacodylate***

In a fume hood 1.38 g sodium cacodylate powder (Agar Scientific, UK) was weighed into 50 mL distilled water and mixed. Glutaraldehyde (Sigma-Aldrich®, UK) was pipetted into distilled water, yielding a 6% solution and 50 mL of each of the above solutions was mixed together. Solution was stored at -5°C for use up to 1 week.

# **CHAPTER III**

## **FLUORESCENCE MICROTITER ASSAY FOR SCREENING THE ANTI-MYCOBACTERIAL PROPERTIES OF NPS**

### 3.1 Introduction

Given the global situation, novel anti-bacterial agents are urgently required to fight infections and fill the void with new substances. Nanomedicines may be the solution to this, but a novel means of screening their efficacy at killing bacterial species is required. There are great challenges associated with developing new anti-mycobacterial drugs, in particular anti-TB drugs. Pharmaceutical companies are reluctant to undertake new drug discovery, screening or development because it involves exorbitant costs with insufficient profit margins or investment return (Gumbo, Pasipanodya, et al. 2015). There are challenges in identifying new substances that can kill both actively growing and persistent or latent bacteria, in evaluating new substances and testing them in clinical trials. Generally, there has been an overall void in the discovery of novel anti-bacterial agents for the past 25 years (Boogaard et al. 2009; Silver 2011; WHO 2014a) in part attributed to the costs and problems involved in screening procedures. The continual emergence of drug resistant strains of mycobacterial species augments this problem.

Pathogenic *Mycobacterium* species are slow growing and difficult to culture *in vitro* (taking 4-16 weeks for colonies to be visible on agar plates), in fact some species like *M. leprae* cannot be propagated in the laboratory. As there are problems with their cultivation, the assessment of the anti-mycobacterial activity of therapies can take several months (Boogaard et al. 2009; Ohara 2012). Generally, pathogenic mycobacteria are very challenging to work with (Elguezal et al. 2011) which makes drug screening procedures additionally expensive and time consuming.

Historically it has been a slow path to evaluate substances which might offer some toxicity against mycobacteria. From Koch's initial identification of the infectious bacillus in 1882, it was a further 6 years until a suitable medium was created allowing its culture *in vitro* and it was not until 1940 when the first treatments became available (Franzblau et al. 2012). There are now various methods of screening for new drugs available, which can be computational (virtual screening [VS]) or real screening (preferably high throughput screening [HTS]). VS is *in silico* drug screening/design using computational models to predict the efficacy of different molecular structures against characterised targets, whereas HTS is the screening of large numbers of compounds simultaneously (e.g. using robotics) to try and find activity or affinity for a selected target (or model) of a specific disease. The ultimate goal of both is to find effective relationships between chemical structures and biological targets (Giacomotto & Segalat 2010).

### **3.1.1 Virtual screening**

The completion of the human genome project has accelerated the development of computational screening, a means to virtually search vast libraries of molecules (e.g. proteins) to find suitable drug binding targets (Meng et al. 2011). VS has a number of advantages. Compared to laboratory based experiments, VS is financially attractive, has no requirement of specialised laboratories (e.g. high containment), products, drugs or pathogens, and can be used to screen theoretical compounds, thus being a unique and very powerful feature (Bielska et al. 2011). VS can be categorised into ligand (e.g. quantitative structure-activity relationships [QSAR] and pharmacopoeia mapping) and structure (e.g. molecular docking) methods (Meng et al. 2011). QSAR and pharmacopoeia mapping are employed when active ligands are identified but there is no information on the target

structure. Molecular docking is used to predict the binding site of a ligand to a 3D protein structure (Meng et al. 2011). Adversely, VS cannot substitute real screening. Although useful for preliminary screening, VS cannot replace physical screening and the results real screening generates.

### ***3.1.2 High throughput screening***

HTS is a means to screen many compounds (large libraries can contain many thousands of compounds) via a fast and automated operation platform, ideally using microtiter plates (96 or 384 well plates) on cells in culture (Liu et al. 2004). Traditionally, HTS is based on *in vitro* cell culture, biochemical or receptor binding assays (Pandey & Nichols 2011). By screening a number of compounds (monitoring a biological modulator against specific targets), investigators are looking for a ‘hit’ to try and quickly identify biologically relevant compounds displaying promising results which can be taken to secondary validation stages (Liu et al. 2004). This system is rapid, and allows ineffective compounds to be disregarded at early investigatory stages thus significantly saving time (and money). Up to 10,000 compounds per day can be tested and if a hit is observed, half maximal inhibitory concentration (IC<sub>50</sub>) values are then calculated (Szymański et al. 2012). Unfavourably, HTS has relatively large operating costs. HTS also requires laboratory space, equipment, trained staff and the purchase, or manufacture, of all compounds for testing which quickly incurs large expenses.

The BACTEC 460 TB radiometric system revolutionised mycobacterial culture as it offered an automated, faster liquid culture system. This has now been replaced by the BACTEC MGIT 960, which is utilised for many applications including drug screening and drug susceptibility testing. The BACTEC MGIT 960 system is arguably the best

system available for screening, yet requires relatively large quantities of compounds (and mycobacteria) for drug screening, increasing costs and safety issues. There are some problems with quantifying data from the system (i.e. it is non-specific therefore can detect other bacterial species), its sensitivity is often reported to be low and there are problems with contamination (compared to the older BACTEC 460) (Lucas et al. 2002; Robbe-Austerman et al. 2013) consequently making it less desirable for HTS. As such, other screening tests have been utilised and developed, such as the luciferase, alamar blue (Ozeki et al. 2015; Collins & Franzblau 1997) and GFP assays (Primm & Franzblau 2007).

Luciferase is a class of oxidative enzymes, isolated from various organisms and animal species (e.g. click beetles and fireflies [*Photinus pyralis*]) that have inherent bioluminescence. It is a highly efficient biological reporter molecule. The luciferase assay produces a photon of light via excitation energy following an enzymatic reaction; bioluminescence is produced when luciferase uses ATP to catalyse the oxidation of luciferin (the substrate) producing oxyluciferin (Deb et al. 2000). This assay measures viability via the presence of ATP, found in live cells. As cell populations multiply, so will the bioluminescence signal due to the increased ATP available from metabolically active cells (e.g. a yellow green light [557 nm] in the case of *Photinus pyralis*). The signal produced is therefore a product of the number of cells and the viability of those cell.

Luciferase has been used successfully in drug screening for anti-malarial drugs (Che et al. 2012). This assay, which is reported to be amenable to HTS, used the ONE-Glo™ luciferase assay system (using a transgenic luciferase expressing parasite) to screen compounds from which 67 hits were found to inhibit >85% parasite growth. From these compounds, 3 hits and 3 non-hits hits were re-analysed via a fluorescence assay (SYBR green-based assay) to determine if they matched the results generated via the luciferase assay, which they did. The authors reported overall repeatability and reliability (Che et



al. 2012). However, using a transgenic parasite may differ from the hits generated using a wildtype parasite.

Andreu *et al.*, have developed a screening assay utilising luciferase expressing *Mtb* that can be used to screen for anti-mycobacterial drugs both *in vitro* and within macrophages in a 96 well format. The authors use both the firefly luciferase system and a construct with the whole operon expressing the bacterial luciferase, which rendered the *Mtb* autofluorescent and so did not require the addition of substrate (Andreu et al. 2012). MICs could be available in only 3 days. Ozek *et al.*, also developed a screening assay utilising luciferase expressing recombinant *M bovis BCG* (rBCG) to screen for compounds *in vitro* in a 96 well format (Ozeki et al. 2015). By culturing luciferase expressing rBCG and comparing the growth (via relative light intensity) to CFU following convention plate-outs, they found that the two methods correlated. The authors discovered that when anti-TB drugs were added, the decrease in the light intensity readings and CFU still correlated, thus allowing them to successfully screen compounds using a luciferase based assay (they screened 10,080 drug extracts) (Ozeki et al. 2015). From the screening, 137 drug extracts were identified to inhibit rBCG, and from this, 41 inhibited both *Mtb* (H37Rv) and an XDR TB strain (Ozeki et al. 2015). A luciferase reported mycobacteriophage system has also been used in drug susceptibility testing for *Mtb* (Banaiee et al. 2008; Banaiee et al. 2001). Results were found to be 98.4% in agreement with the BACTEC 460 system, it was semi-automated and had low costs associated with its use (Banaiee et al. 2008). These studies highlight the advantages of the use of a luciferase system.

There are a great number of commercially available luciferase assay kits and luminometers. Cell viability results can be used to determine gene expression and many cellular processes involved in gene regulation following exposure to a compound. As this assay often requires the addition of luciferin (construct dependent) (which reacts with

ATP in living cells to fluoresce) (Deb et al. 2000), it is also an endpoint assay, therefore often no MBCs or drug kinetic information is obtainable following it. Luciferase assays vary greatly and there seems to be no consensus in the literature on a set protocol (Primm & Franzblau 2007). Furthermore, luminometers are regarded as expensive laboratory equipment, luciferin is a costly substrate and often the assay lacks reproducibility between tests. Most importantly however, is a publication highlighting that some compounds (e.g. PTC124) can directly affect the reporter, leading to nonspecific but reproducible assay signal modulation, which was actually just an artefact. Auld *et al.*, demonstrated that PTC124 (a drug for cystic fibrosis in clinical trials) and its analogues were strongly associated with the luciferase reporter, this leading to increased luciferase activity (Auld et al. 2009). This association would cause a false positive, incorrectly showing a compound to have desirable drug effects.

Redox-based techniques, such as the alamar blue assay (Chapter II, [section 2.4]), have been employed for drug screening (Collins & Franzblau 1997; Hamid et al. 2004) although the assay tends to be more popular for drug susceptibility testing (Martin et al. 2003; Yajko et al. 1995b). The alamar blue assay measures metabolic activity as an indicator of cell viability. A non-fluorescent, oxidised blue dye resazurin (the alamar blue reagent [which is non-toxic and can pass through cell membranes]) is reduced by living cells to resorufin, which is a highly fluorescent pink. The alamar blue assay is generally deemed cost effective, with growth monitored visually (no equipment required but not quantitative), fluorometrically and spectrophotometrically. This assay is widely used, is simple to implement and cost effect but it is more relevant for mammalian cells. Hamid *et al.*, compared the alamar blue to the 3-[4,5-dimethylthiazol-2-yl]-2,5- diphenyl tetrazolium bromide (MTT) assay for *in vitro* screening of 117 compounds using human hepatoma cell lines. Authors reported general comparability between the two assays, but found increased sensitivity when using the alamar blue assay (Hamid et al. 2004).

This microtiter assay however is an endpoint test (following the colour change after set incubation time points) like the luciferase assay. Drug kinetics or MBCs therefore cannot be determined as bacterial growth would not be possible following the addition of a stop reagent into the wells. Additionally, there are other reductases which may be able to reduce alamar blue causing a colour change, therefore it may not necessarily detect cellular metabolism impairment (Rampersad 2012), which is important when testing potential clinical-use drugs. Due to the inducers or inhibitors of other metabolic enzymes, false positives and/or negatives could be produced (Hamid et al. 2004). Furthermore, absorbance readings will differ according to the microtiter plate utilised in the experiment and most studies only use this assay in combination with another testing means thus increasing timeframes and costs in drug screening (Rampersad 2012).

GFP found in the jellyfish *Aequorea victoria*, is a self-fluorescing (in the presence of UV or blue light) protein (Parker & Bermudez 1997). It has been described as the most widely exploited protein in cell biology, often harnessed as a marker of gene expression or protein targeting. Wildtype GFP has a 238 amino acid structure and has two excitation (ex) peaks; a major one at 396 nm (UV) and a smaller one at 475 nm (blue), with emission (em) at 509 nm (green) (Heim & Tsien 1996). By incorporating a foreign plasmid with the *gfp* gene into bacteria, it can be amplified and therefore expressed thus allowing fluorescence to be used as an indicator of cell number. Mycobacteria strains that have been successfully engineered to express GFP using plasmids include *Mtb*, *M. bovis* BCG, *M. avium*, *M. aurum*, *M. smegmatis* and *Map* (Collins et al. 1998; Srivastava et al. 1998; Parker & Bermudez 1997; Kremer et al. 1995; Blokpoel et al. 2003; Harris et al. 2002a). The use of these strains has allowed successful screening of anti-mycobacterial substances (Donnellan et al. 2015; Srivastava et al. 1998; Collins et al. 1998). As such, GFP was chosen as a reporter molecule for this PhD project.

Assays that utilise the GFP protein have many advantages associated with their use as GFP is intrinsically fluorescent, only requires oxygen for stimulation and exhibits very low toxicity, is extremely stable and allows for easy visualisation/imaging (Collins et al. 1998; Chalfie et al. 1992). GFP is encoded by a small DNA sequence thus making the construct of gene fusions possible. Natural, intrinsic fluorescence allows detection and monitoring of bacterial species without the requirement of any staining. GFP assays are generally more desirable over the alamar blue and luciferase assays as there is no requirement for a dye or substrate (disregarding recombinant luciferase constructs), which decreases the labour and increases the assays safety aspects. Additionally, repeated measures from the same cells are possible, allowing easy track proliferation over time for the same culture. GFP provides a means of tracking viable cells *in vivo*, monitoring growth, quantifying gene expression and investigating protein localisation in living cells. GFP based assays can be used for *in vitro* drug testing as well as intracellular drug testing (inside macrophages) (Parker & Bermudez 1997). Fluorescence can be monitored using a fluorometer, flow cytometry and microscopy (Blokpoel et al. 2003). Furthermore, GFP assays are amenable to HTS (Fortin et al. 2005; Collins et al. 1998; Lu et al. 2004).

### **3.1.3 Aims**

The aim of this chapter was to develop and optimise a rapid, inexpensive assay to screen and compare the anti-mycobacterial effects of NPs against mycobacteria. The approach used was adapted, modified and optimised from previous work by Collins *et al.*, (1998), employing a GFP reporter strain of *Map* K10 (Collins et al. 1998; Harris & Barletta 2001). This chapter highlights some of the technical issues which were overcome during the development stages and outlines the advantages and limitations of the assay. Some results

from this chapter have been published in ‘*A rapid screening assay for identifying mycobacteria targeted nanoparticle antibiotics*’ (Donnellan et al. 2015).

## **3.2 Materials and Methods**

### ***3.2.1 Mycobacterium avium subsp. paratuberculosis (Map) K10/GFP: the surrogate organism***

*Map* an acid-fast pathogen (see Chapter I [section 1.9.4]), strain K10, was chosen as a surrogate for *Mtb* for this study. Unlike *Mtb*, *Map* is classified as a Hazard Group 2 organism by the UK Advisory Committee for Dangerous Pathogens and therefore has the advantage that it can be handled in Containment Level 2 rather than Containment Level 3 laboratories. In addition, the reporter strain was available (Harris et al. 2002b). *Map* K10/GFP is a reporter strain of *Map* K10 capable of expressing GFP thus enabling growth to be monitored via fluorometry. This strain was kindly supplied by Dr Raul G Barletta (University of Nebraska-Lincoln, USA) (Harris et al. 2002a). *Map* K10/GFP is representative of the slow growing pathogenic mycobacteria for which survival within macrophages is a hallmark trait, akin to *Mtb* (Hostetter et al. 2002; Tan et al. 2013; Plain et al. 2011). As well as the genetic similarities it has to *Mtb*, outlined in Chapter I, it is also resistant to a similar broad spectrum of antibiotic drugs.

To engineer this reporter strain, Harris *et al.*, (2002a) transformed *Map* K10 with plasmid pWES4, containing the *gfp* gene under the control of the *M. bovis* BCG promotor *hsp60* and a kanamycin resistant gene (*kan*) for selection (Fig 3.1) (Harris et al. 2002a). (It should be noted that the antibiotic used for selection of the plasmid is not used for TB treatment, and therefore did not impinge on the drug screening).

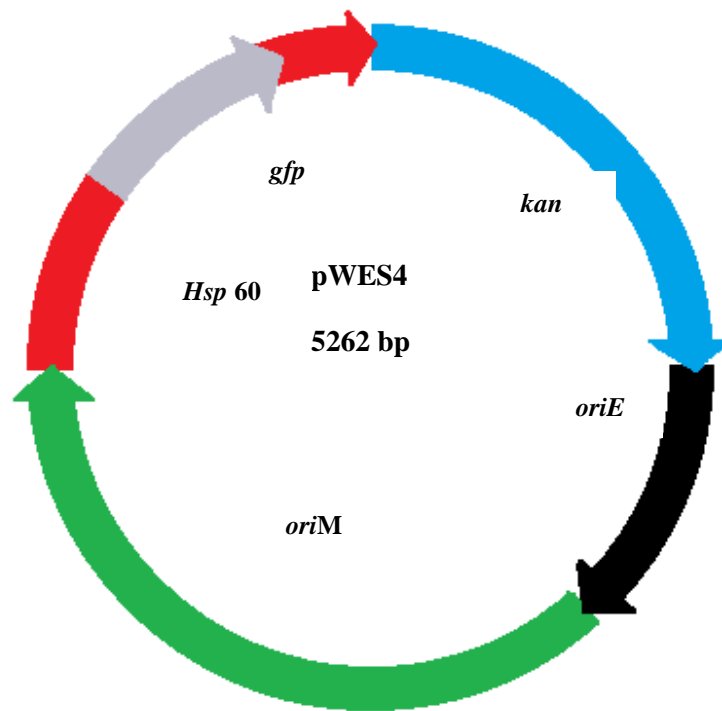


**Figure 3.1 The recombinant plasmid pWES4.** Plasmid pWES4, containing the *gfp* gene under the control of the *M. bovis* BCG promoter *hsp60* and a kanamycin resistant gene (*kan*) for selection  
(adapted from Parker and Bermudez, 1997)

### 3.2.2 A new protocol for screening the anti-mycobacterial properties of NPs

*Map* K10/GFP was grown in 7H9K<sup>+</sup> (see Chapter II [section 2.1.1]) until the exponential stage of growth was reached. Growth was monitored by McF standards using a Densimat<sup>®</sup> (Peñuelas-Urquides et al. 2013). Centrifugation at 3080 g at 20°C for 20 minutes was used to pellet 3 mL of the bacterial suspension in the exponential phase of growth. The pellet was re-suspended in the appropriate volume of 7H9 to give a McF standard 2, approximating to  $3.2 \times 10^8$  CFU per mL. *Map* K10/GFP was further diluted (1/16 in 7H9) and cells were seeded in a 96 well, sterile, black plate ( $2 \times 10^6$  CFU/well) (Nunc, Thermo Fisher) in a volume of 100  $\mu$ L per well. The outer wells were filled with 200  $\mu$ L of distilled water (DW) to prevent dehydration of the experimental wells.

Although a full working example of NP/drug screening is not given in this chapter, (this can be found in Chapters IV and V), an overview of the assay and plate set up is. Serial dilutions of NPs (or drugs) were prepared to give the desired final concentrations per well, and were added to the wells containing *Map* K10/GFP, giving a final volume of 200  $\mu$ L per well. The 96 well plates were incubated at 37°C with medium agitation (250 rpm) for 7 days and kept in the dark throughout the experimental procedure. To check for NP/drug interference in fluorescence readings, wells of medium and medium plus NPs/drugs were included. Fluorescence was measured (top read) using a GloMax® Multi<sup>+</sup> plate reader (Promega, UK) at an ex/em of 490/510-570 nm using the blue optical kit, the plate was shaken for 0.3 minutes in an orbital motion before each reading. Bacterial fluorescence was monitored immediately before and after NP addition (day 0), then at the same time each day for 7 days. Plates were incubated at 37 °C wrapped in tin-foil between readings. All screening experiments were performed at least in triplicate under sterile conditions.

### ***3.2.3 Mycobacterial growth on solid agar***

*Map* K10/GFP was grown in 7H9 with NPs/drugs or without (control) for 7 days in a 96 well plate format as described in 3.3.1. After the final fluorescence reading, 100  $\mu$ L of the mycobacterial solution was serially diluted (in 7H9<sup>+</sup>) onto 7H11 agar (see Chapter II [section 2.6.3]) and incubated at 37°C for 12 weeks. Each set of serial dilutions were performed in duplicate under sterile conditions.

### 3.3 Results

#### 3.3.1 Bacterial Growth: monitored by McF and fluorescence

The McF standard of 10 mL liquid cultures (inoculated with a defined number of cells according to McF standards) of *Map* K10/GFP and wildtype *Map* K10 (without the plasmid for GFP) was plotted against time to generate a growth curve over a period of 35 days (Fig.3.2a,b). Figure 3.2(a) demonstrates the overall biphasic growth of the *Mycobacterium*, with three distinct phases of growth; the lag phase, the exponential phase and the stationary phase. The first exponential growth stage was determined to be between days 5-11 for *Map* K10/GFP (Fig 3.2a). *Map* K10/GFP in the exponential growth phase was found to be optimal for monitoring fluorescence in the microtiter assay over a period of 7 days (taking *Map* K10/GFP between days 9-11). Figure 3.2(b) demonstrates the growth of wildtype *Map* K10. The first exponential growth stage was determined to be between days 3-7 (Fig 3.2b). As shown, the growth patterns differ between the two species with *Map* K10/GFP taking longer to reach the exponential growth phase. Additionally, wildtype *Map* K10 had a longer stationary phase (approximately 7 days) than *Map* K10/GFP (approximately 5 days) (Figs 3.2a,b). This was important for the assay optimisation. Figure 3.3 depicts the growth of *Map* at different passage numbers over a period of 11 days, passage number was found not to significantly affect the growth rate. To determine the growth pattern for *Map* K10/GFP (starting with cells in the first exponential growth phase) using the 96 well plate format,  $2 \times 10^6$  CFU/well of *Map* K10/GFP (in 200  $\mu$ L of 7H9K<sup>+</sup>) was monitored by fluorescence readings (GloMax<sup>®</sup> Multi<sup>+</sup> plate reader [Promega, UK]) (ex/em 490/510-570 nm) over a period of 7 days (Fig 3.4). Generally, mycobacterial growth increased steadily over the week long assay.



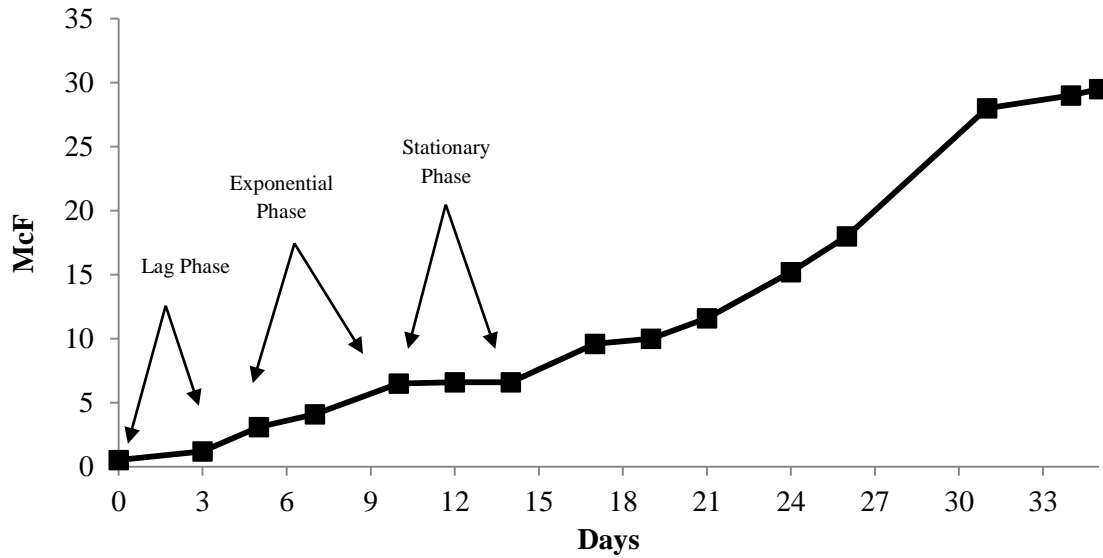


**Figure 3.2(a) Biphasic growth of *Map* K10/GFP over 35 days in 10 mL cultures in 7H9K<sup>+</sup> (using McFarland [McF] standards).** The curve displays biphasic growth of the mycobacteria, where the organism is switching between carbon sources in the 7H9K<sup>+</sup> medium. The first exponential growth phase was between days 5 and 11, the second exponential growth phase began at approximately day 16. *Map* K10/GFP was taken between days 9 and 11 for the fluorescence assay (n=2).

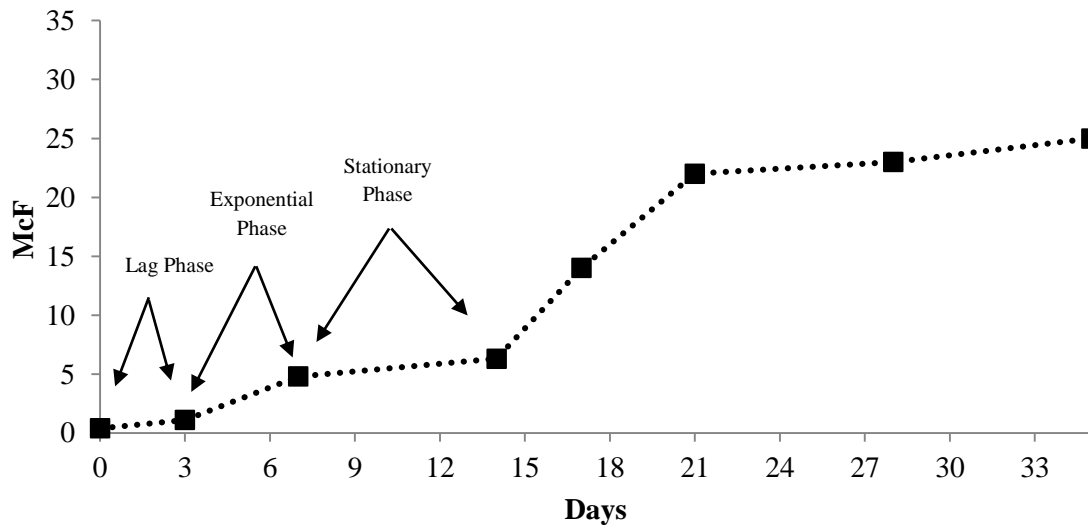


**Figure 3.2(b) Biphasic growth of wildtype *Map* K10 over 35 days in 10 mL cultures in 7H9K<sup>+</sup> (using McF standards).** The curve displays biphasic growth of the mycobacteria, where the organism is switching between carbon sources in the 7H9K<sup>+</sup> medium. The first exponential growth phase was between days 3 and 7, the second exponential growth phase began at approximately day 14 (n=2).

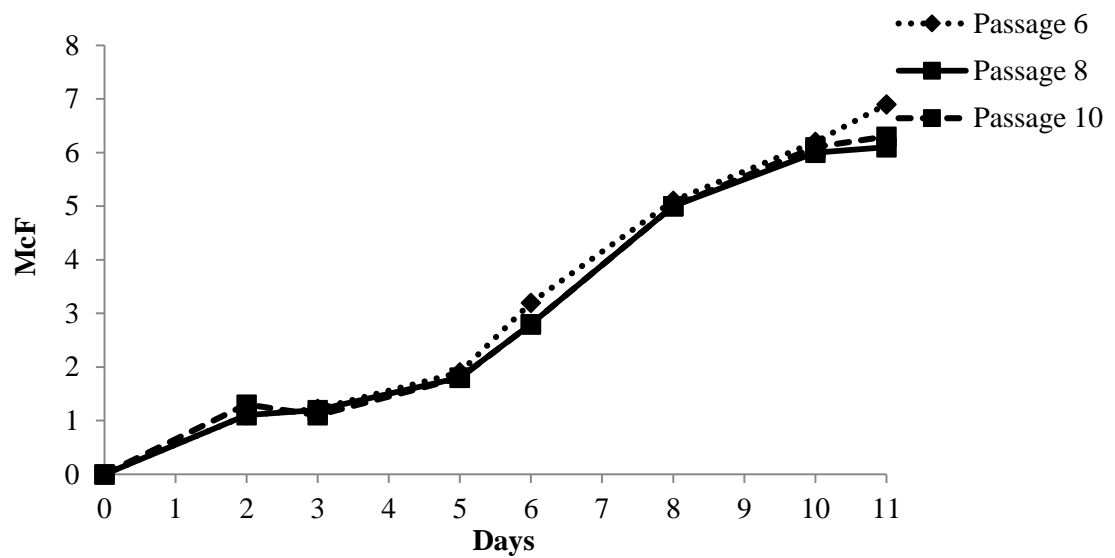


**Figure 3.3 Growth of *Map* K10/GFP over 11 days in 10 mL cultures in 7H9K<sup>+</sup> (using McF standards) at different passage numbers.** This was used to compare the first exponential growth phase (5-11) between 3 passage numbers. No significant difference between growth rates/patterns was observed (n=1).

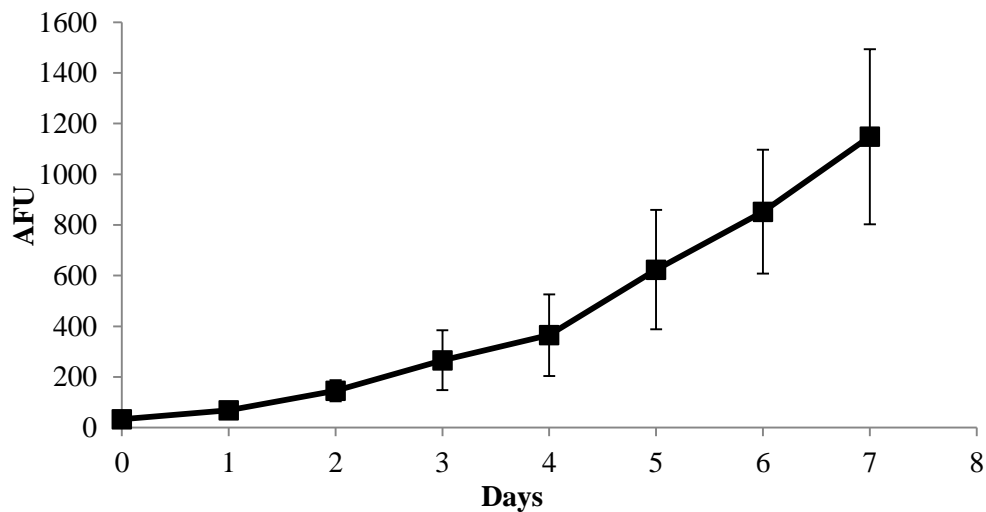


**Figure 3.4 Growth of *Map* K10/GFP over 7 days monitored by fluorescence in 7H9K<sup>+</sup>.** Growth was monitored over 7 days in a microtiter format, with each point displaying 2\* standard error of the mean (SEM) (n=12) (AFU= Arbitrary fluorescent units).

### 3.3.2 Fluorescent microtiter assay optimisation

During the microtiter assay optimisation, a number of variables were manipulated including CFU/mL and plate type. Figure 3.5 (a) shows the effect of plate type and depicts the assay performed with different numbers of CFU/mL in black versus white plates and the readings obtained via fluorometry. As shown, the white plates gave very high readings due to background fluorescence. As the CFU/mL increased, the fluorescence increased beyond a readable scale. To determine the optimum CFU/mL of *Map* K10/GFP for seeding into the black plates, to allow optimal growth over the 7 day period, various cell densities were tested using the fluorescence assay, Figure 3.5 (b) displays the results obtained. Using these results a value between the two lower numbers was selected for the assay ( $2 \times 10^6$  CFU/mL); a low CFU number was sought but not too low that a GFP signal was barely measureable. As shown above (Fig 3.2), the growth pattern of *Map* K10/GFP was an important factor to consider, as it differed from the wildtype strain. As such, the fluorescence assay was begun after cells were incubated for 9-11 days, instead of 7 days as would occur with the wildtype strain. Figure 3.6 depicts the 96 well plate set up. As illustrated, each concentration was carried out in triplicate and DW filled the outer wells. Two separate NPs/drugs could be tested at once, with each run in triplicate. Three sets of controls were included; mycobacteria only (wells B2-B7), 7H9 and 7H9<sup>+</sup> medium only (to account for any interference from tween 80 [B8-B10]) and NP/drug at each concentration with medium (rows 8,9,10 [Fig 3.6]).

Other variables that were manipulated include the sample mixing time, medium volume, evaporation/dehydration rates during incubation *etc*, many being determined through visual observations. For example, if outer wells were not filled with distilled water, by the 7<sup>th</sup> day the experimental wells began to experience evaporation. Different ex/em peaks were tested on the GloMax<sup>®</sup> Multi<sup>+</sup> plate reader (Promega, UK) (e.g. the UV optical

kit [ex/em 360/410-460 nm]) but interestingly, readings were found to be more stable and reproducible using the blue optical kit. Overall the growth stage of the mycobacteria, cell number per well and plate type were found to be particularly important factors for optimal performance.

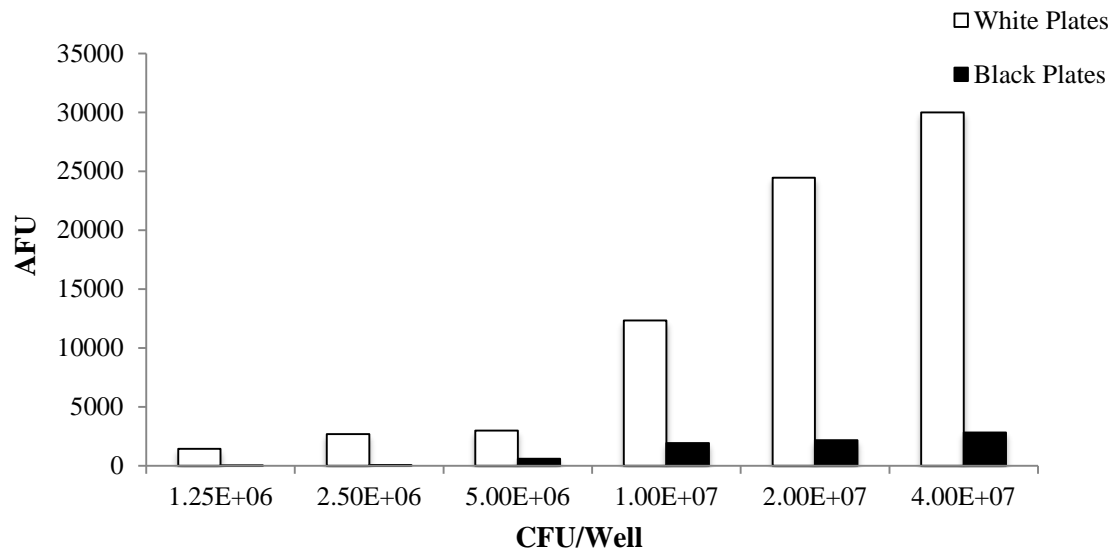


**Figure 3.5 (a) Assay Optimisation: determining plate type.** Black plates were chosen to minimise background fluorescence found when using white plates (n=1).

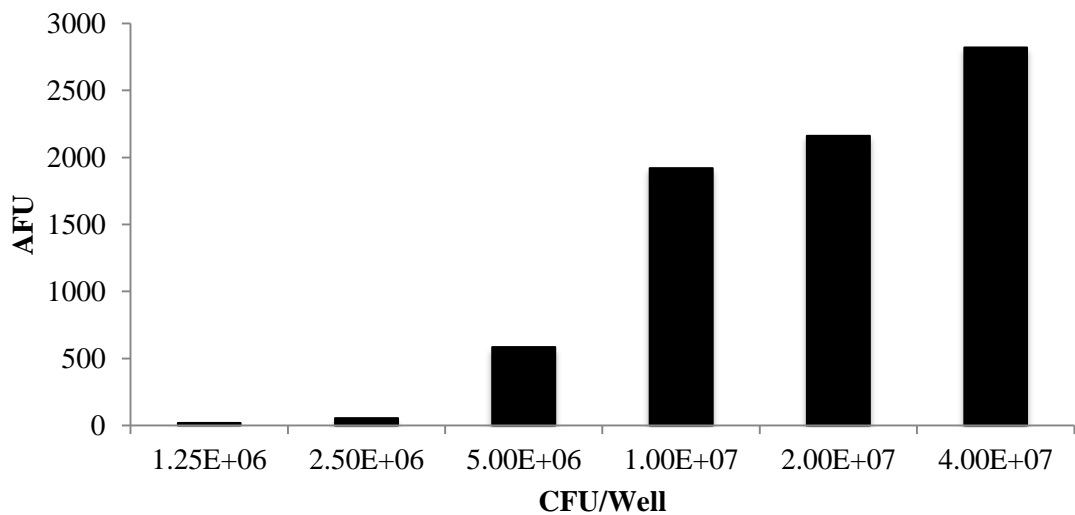


**Figure 3.5 (b) Assay Optimisation: determining colony forming units (CFU) per well.** To obtain an optimal number of cells to begin the 7 day assay  $2 \times 10^6$  CFU/mL was chosen based on these results; high enough that a signal was obtainable but keeping cell numbers low to start with (n=1).

**Experiment 1**  
(columns 2,3&4)

**Experiment 2**  
(columns 5,6&7)

**Controls**  
(Columns B and  
8,9&10)

	1	2	3	4	5	6	7	8	9	10	11	12
A	DW	DW	DW	DW	DW	DW	DW	DW	DW	DW	DW	DW
B	DW	Mycobacteria Control <i>Map</i> K10/GFP (in 7H9 <sup>+</sup> ) & 7H9	Mycobacteria Control <i>Map</i> K10/GFP (in 7H9 <sup>+</sup> ) & 7H9	Mycobacteria Control <i>Map</i> K10/GFP (in 7H9 <sup>+</sup> ) & 7H9	Mycobacteria Control <i>Map</i> K10/GFP (in 7H9 <sup>+</sup> ) & 7H9	Mycobacteria Control <i>Map</i> K10/GFP (in 7H9 <sup>+</sup> ) & 7H9	Mycobacteria Control <i>Map</i> K10/GFP (in 7H9 <sup>+</sup> ) & 7H9	Medium control 7H9 & 7H9 <sup>+</sup>	Medium control 7H9 & 7H9 <sup>+</sup>	Medium control 7H9 & 7H9 <sup>+</sup>	BLANK	DW
C	DW	<i>Map</i> K10/GFP & NP/Drug	<i>Map</i> K10/GFP & NP/Drug	<i>Map</i> K10/GFP & NP/Drug	<i>Map</i> K10/GFP & NP/Drug	<i>Map</i> K10/GFP & NP/Drug	<i>Map</i> K10/GFP & NP/Drug	NP/Drug (in 7H9) & 7H9 <sup>+</sup>	NP/Drug (in 7H9) & 7H9 <sup>+</sup>	NP/Drug (in 7H9) & 7H9 <sup>+</sup>	BLANK	DW
D	DW	<i>Map</i> K10/GFP & NP/Drug	<i>Map</i> K10/GFP & NP/Drug	<i>Map</i> K10/GFP & NP/Drug	<i>Map</i> K10/GFP & NP/Drug	<i>Map</i> K10/GFP & NP/Drug	<i>Map</i> K10/GFP & NP/Drug	NP/Drug (in 7H9) & 7H9 <sup>+</sup>	NP/Drug (in 7H9) & 7H9 <sup>+</sup>	NP/Drug (in 7H9) & 7H9 <sup>+</sup>	BLANK	DW
E	DW	<i>Map</i> K10/GFP & NP/Drug	<i>Map</i> K10/GFP & NP/Drug	<i>Map</i> K10/GFP & NP/Drug	<i>Map</i> K10/GFP & NP/Drug	<i>Map</i> K10/GFP & NP/Drug	<i>Map</i> K10/GFP & NP/Drug	NP/Drug (in 7H9) & 7H9 <sup>+</sup>	NP/Drug (in 7H9) & 7H9 <sup>+</sup>	NP/Drug (in 7H9) & 7H9 <sup>+</sup>	BLANK	DW
F	DW	<i>Map</i> K10/GFP & NP/Drug	<i>Map</i> K10/GFP & NP/Drug	<i>Map</i> K10/GFP & NP/Drug	<i>Map</i> K10/GFP & NP/Drug	<i>Map</i> K10/GFP & NP/Drug	<i>Map</i> K10/GFP & NP/Drug	NP/Drug (in 7H9) & 7H9 <sup>+</sup>	NP/Drug (in 7H9) & 7H9 <sup>+</sup>	NP/Drug (in 7H9) & 7H9 <sup>+</sup>	BLANK	DW
G	DW	<i>Map</i> K10/GFP & NP/Drug	<i>Map</i> K10/GFP & NP/Drug	<i>Map</i> K10/GFP & NP/Drug	<i>Map</i> K10/GFP & NP/Drug	<i>Map</i> K10/GFP & NP/Drug	<i>Map</i> K10/GFP & NP/Drug	NP/Drug (in 7H9) & 7H9 <sup>+</sup>	NP/Drug (in 7H9) & 7H9 <sup>+</sup>	NP/Drug (in 7H9) & 7H9 <sup>+</sup>	BLANK	DW
H	DW	DW	DW	DW	DW	DW	DW	DW	DW	DW	DW	DW

Increasing  
NP/Drug  
concentration  
↓

**Figure 3.6 The 96 well plate set up for NP/drug efficacy screening.** Drug/NP increasing (serial dilutions) from 2C-2G. Row B (2-7) are control sets (for mycobacteria and medium only) and row B (8-10) are medium only controls. Columns 8,9 & 10 (rows C-G) are NP/drug and medium controls.

\*DW=distilled water

**WILL BE NORMAL, BIG IMAGE WHEN PRINTED**

### 3.3.3 Fluorescence microtiter assay

Figure 3.7 depicts a working example of the assay after optimisation. The aminoglycoside antibiotic hygromycin was screened (6.25-100  $\mu\text{g/mL}$ ) over the 7 day period as a pilot study, to monitor the mycobacteria growth via fluorescence taking into account all the controls. *Map* K10/GFP was inhibited in a clear dose and time dependant manner by hygromycin (Fig 3.7). Hygromycin was utilised in the early stages of optimising the assay and in the initial experiments as it was available and because *Map* K10 is known to be susceptible to this drug.

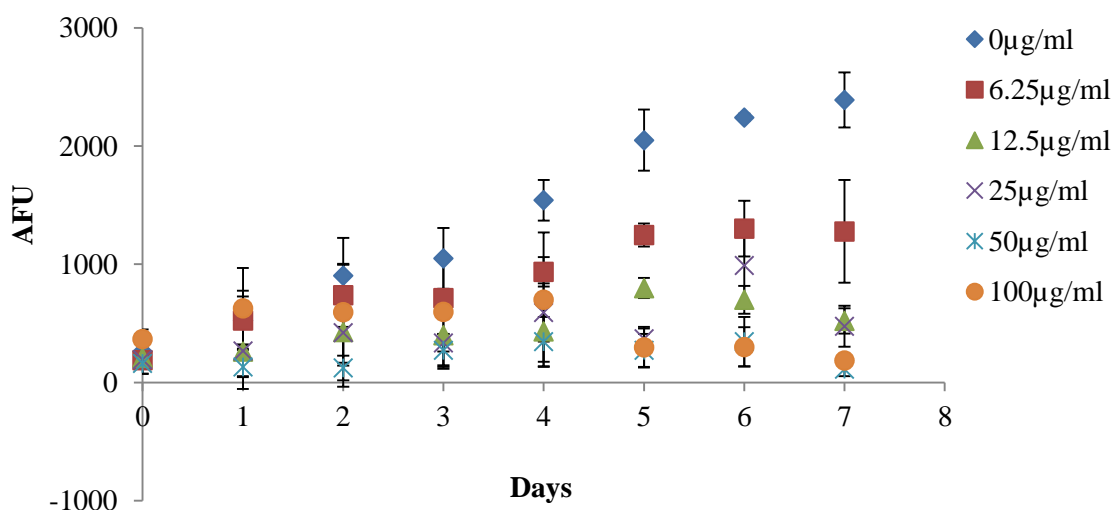


**Figure 3.7** *Map* K10/GFP growth with hygromycin in 200  $\mu\text{L}$  of 7H9 in a microtiter format. Mycobacteria were exposed to hygromycin at different concentrations (6.25-100  $\mu\text{g/mL}$ ) over a period of 7 days. Results are plotted using the raw data, with each point displaying 2\* the SEM (n=3).

### **3.3.4 Processing raw fluorescence data: novel approach**

Working with large, complex data sets can be time consuming and challenging. Therefore, it was important to devise an analytical procedure by which the data generated from the fluorescence readings in this novel assay could be analysed and easily visualised. It was important to be able to compare the effects different substances had on the mycobacterial growth at many different concentrations and several time points, as well as taking all the controls into account. Working with the raw fluorescence readings generated huge data sets that quickly became unmanageable; therefore a novel approach was designed.

Fluorescence readings obtained from the GloMax<sup>®</sup> Multi<sup>+</sup> plate reader (Promega, UK) were expressed as Arbitrary Fluorescent Units (AFU) and were plotted against time (days) (Fig 3.4). Each treatment was carried out in triplicate and the mean was calculated. From this mean value, the control triplicate mean (of medium only or medium plus NPs/drugs in experimental wells) was subtracted. This gave a true reading of the fluorescence emitting from *Map* K10/GFP and not any medium/NP/drug interference. The results expressed as AFU against time were transformed and normalised to obtain the usual dose response relationship, to compare the effects of NPs/drugs on the growth of the mycobacteria. The exponential growth of the bacteria was calculated:  **$G = G_0 \cdot \exp(\beta t)$**

(where  $G$  = fluorescent units,  $G_0$  = bacterial growth at time 0,  $\beta$  = growth rate [per day] and  $t$  = time [days]).

To estimate  $\beta$ , first the collected data was transformed by taking the log of  $G$ :  **$\text{Log } G = \text{Log } G_0 + \beta t$** , allowing  $\beta$  to be estimated by linear regression (calculated using Excel [Microsoft Office Worksheet]). The data could then be normalised to the slope of the



control (0 µg/mL) for each data set (e.g. controls, NPs/drugs) by dividing each value by the control value and 2\* the standard error for each data point using the LINEST function in Excel (Microsoft Office Worksheet). This analysis is further outlined, with working examples given, in the following chapters (IV and V).

This data was then plotted using the dose response modelling software PROAST (version 38.9 [RIVM, Bilthoven, The Netherlands]) or further explored in packages such as Minitab to obtain statistical information (Chapters IV and V).

### **3.4 Discussion**

The aim of this study was to design a low cost assay to screen NPs and/or drug toxicity against mycobacteria. The assay was adapted and refined to use a GFP modified *Map* strain. It can be successfully used to screen the relative toxicity of different NPs/drugs within just 7 days, representing a significant saving of both time and money compared with traditional bacteriological culture methods. Additionally, a novel method for analysis of the data was developed to permit easy comparisons between data sets and therefore assess the relative potency of different anti-mycobacterial agents, and it has been employed in the following chapters. It is hoped that the adoption of the technical and data analysis protocols will allow greater numbers of potential anti-mycobacterial agents to be screened (including NPs).

#### **3.4.1 Assay optimisation**

Optimisation of the assay was relatively time consuming, but the factors which had a significant impact on generating true results have been identified. The growth pattern of

*Map* K10/GFP was found to differ to the wildtype strain. If the assay began at the wrong stage of growth (e.g. the lag phase), the control wells (no treatment) may not have provided a suitable negative control, as growth would have been slowed. It was important the *Map* K10/GFP was cultured from the start of the exponential phase of growth and not the end of the lag phase or the start of the stationary phase. To prevent readings being too high, a low cell density was chosen in order to allow optimal growth of the 7 day period in a microtiter well. If too many cells were added, the mycobacteria may change the carbon source too rapidly thus altering the growth pattern, plus clumping may have occurred which would affect the GFP readings, while if too few cells were added the GFP signal may have been too weak to monitor. Finding a suitable plate manufacturer which was widely and commercially available was important to allow for standardisation and black plates were essential to ensure the fluorescence detected was from the mycobacteria and to minimise background noise. The changes made were informed by published literature (Collins et al. 1998), experimental observations over many repeats and knowledge of the exceptionally fastidious nature of this microorganism.

Developing a data analysis protocol was time consuming and took many different routes before it was optimised. Although bigger data sets can give greater significant reporting, they need to be managed accordingly to prevent loss and misinterpretation of information. Therefore, a novel method to work mycobacteria growth fluorescence data needed to be established; firstly to manage the vast quantity of numbers generated from the microtiter assay and secondly due to problems encountered when comparison were made between the controls (mycobacteria only [0 µg/mL]) from individual experiments. During the experiments there was variation between the controls, therefore normalising all the results to a mean control accommodated for this. By fitting a linear regression to the log data, it allowed an estimation of fluorescence for each of the concentrations, thus summarising the dose response curve obtained from the raw data. This allowed for different time points

(days), concentrations and fluorescence readings to be summarised into one 'line' on a graph instead of many lines for different days and/or concentrations. A full working example of this is found in Chapter IV.

### **3.4.2 Assay advantages**

The assay had many strengths associated with its use. Main advantages include, it was an *in vitro*, cell-based assay that is amenable to HTS development. The use of the reporter molecule GFP to monitor growth and viability of *Map* K10 was beneficial, as only viable mycobacteria fluoresce, hence fluorescence could be used to measure viability and cell number in the same colonies/wells over time. The preparation for this assay was relatively quick (on day '0' everything could be prepared in under 4 hours) and only 20 minutes each day over the week long period was required to read fluorescence. The assay generated data very rapidly. Two substances (NPs or drugs) could be screened at once (with each in triplicate) thus allowing repeats to be generated quickly. The assay required only small quantities of mycobacteria, thus increasing the safety aspects, as large volumes of liquid culture broths were not required. Additionally, only small quantities of NPs/drugs were required, as the volumes required for screening were very small. Hence, both these features lowered the financial costs of early stage compound screening. Unlike after the alamar blue and some luciferase assays, GFP can be repeatedly measured for fluorescence in the same cells over time and the mycobacteria can be plated onto agar following fluorescence screening which allows colony counts from the same study to be measured to determine MICs/MBCs.

### 3.4.3 Assay disadvantages

A disadvantage of exploiting GFP as a means of measuring viability is that MICs and MBCs cannot directly be calculated from the fluorescence assay, as GFP may linger (and hence be measureable) even after cell death. However, as stated, colony counts could be measured. Furthermore, this assay would not be suitable to screen all substances. As outlined in the next chapter, NPs were screened for anti-mycobacterial properties, and this included titanium dioxide (TiO<sub>2</sub>) NPs in the first screening study of metal/metal oxide NPs. TiO<sub>2</sub> NPs have been reported to have ultraviolet (UV) protective properties for skin because these NPs reflect UV light (Yang et al. 2004). As such, when screened in the assay, the fluorescence readings were off the scale and over three times greater than the control readings (mycobacteria only). Therefore, NPs with UV reflective properties cannot be screened in this assay. This may also apply for drugs with inherent fluorescent properties if the excitation and/or emission wavelengths overlap with GFP.

A technical disadvantage would include the physical reading of the 96 well plate. The protocol requires the lid of the plate to be removed before being inserted into the GloMax® Multi<sup>+</sup> plate reader (Promega, UK), which would be problematic if this was used for a Hazard Group 3 organism (e.g. *Mtb*). To be able to do this, the plate reader would be required to stay within a microbiological safety cabinet. Additionally, by the 6<sup>th</sup>/7<sup>th</sup> day of plate incubation during the assay, condensation formed on the inside of the plate lid which may have issues for contamination between wells.

### 3.4.4 Assay improvements

There were alternatives to GFP that could have been utilised for screening NPs, such as the luciferase and alamar blue assays, but overall GFP was a suitable reporter, which offered reproducible results. However, there are aspects of this assay that could be further improved. Although expression of the *gfp* gene under control of the *M. bovis* BCG *hsp60* promoter was easily detected, this is a particularly powerful promoter (hence why it was chosen) therefore GFP may have been over expressed. If it was over expressed, in time it could become insoluble due to super saturation, which may affect the metabolism of the *Mycobacterium* (although no evidence of this was found during this assay), as such, a different promoter may be more suitable. Wildtype strains of GFP have a relatively short period of high intensity fluorescence before saturation occurs. There are mutant forms of GFP available which have desirable properties; reduced saturation rates thus enhancing photo-stability, better temperature tolerance, increased signal intensity, reduced aggregation formation and increased solubility (Heim & Tsien 1996). Imaging *Map* K10/GFP (Chapter V) was often difficult due to the problems encountered with photo-bleaching therefore, a mutant strain of GFP might be worth considering. Enhanced GFP (EGFP) is a mutant of GFP, with a mutation of serine to threonine at amino acid position 65 that has the major excitation peak red-shifted to 490 nm, with emission staying at 509 nm (Cormack et al. 1996; Li et al. 1997). This mutant has a reported 35 fold fluorescence enhancement over wildtype GFP (Li et al. 1997). With the increase in fluorescence and increased photo-stability, it would be worth considering, especially as integrating the signal over time may become important for future studies.

### 3.4.5 Next steps

The next stage following on from this assay would be to determine MIC/MBCs for the substances/NPs screened. This could be done using traditional bacteriology methods. Generally, plating out broth cultures on to agar medium and the interpretation of data can give immensely varied results. There are problems with contamination, human errors, and interruptions in incubation temperatures can greatly affect results and because it can take many weeks to gain results from colony counts, this method alone can greatly hold up results. Further, bacteriological culture assays do not detect viable but non-culturable cells (Sharma et al. 2014). Therefore using this fluorescence assay and the traditional methods side by side, they could correlate and complement each other suitably.

In this project only one strain of mycobacteria was screened. Although structurally and genetically similar, *Map* K10/GFP may not have the same susceptibility/resistance to NPs/drugs that clinical *Mtb* isolates do, therefore following on from the initial screening of substances using a surrogate, such substances would need to be re-tested for *Mtb* (and ideally MDR TB strains). As described at a later stage of this thesis, the efficacy of the substances screened need to be tested on intracellular mycobacteria. This assay only allows substances to be tested against mycobacteria in liquid culture, and not within a macrophage. The doubling time of mycobacteria inside a macrophage is known to differ from liquid culture (from ~16 hours to ~24 hours for *Mtb*) (Ohara 2012; Hirota et al. 2010) which could therefore alter efficacy results, meaning a wider range of concentrations would be needed.

### 3.5 Conclusions

In this study, through the adaption and modification of previous work, an assay with an accompanying protocol that uses a GFP modified *Map* strain to allow quick, low cost screening of NP toxicity against mycobacteria has been developed. This assay permits substances to be screened rapidly, to determine which may have anti-mycobacterial potential to be taken forward for further testing and development. While this PhD project focused mainly on testing the efficacy of NPs, this protocol could be used to test a range of therapeutic types. The microtiter assay itself has proven to be reliable, robust and reproducible, producing rapid, clear results within just 7 days. The actual method ensures that the chosen ranges are robust and ensures high quality data with test/re-test reliability and reproducibility. In addition to developing the *in vitro* screening assay, a protocol for data analysis was established that allows easy comparison between the efficacies of different substances.

# **CHAPTER IV**

## **ANTI-MYCOBACTERIAL PROPERTIES OF METAL/METAL OXIDE NPS**



## 4.1 Introduction

The anti-bacterial properties of metals (e.g. silver) are well established as they have been exploited as anti-bacterial agents since antiquity. They are considered good alternatives to biocides, chemical disinfectants, toxic polishes *etc.*, as they do not pollute the environment to the same degree and some are very cost effective (Yasuyuki et al. 2010). Such anti-bacterial properties have been used in a vast array of consumer products (e.g. food packaging, textiles) and clinical applications (e.g. alternatives to antibiotics, wound dressings). The methods to which metals exert toxicity on bacterial species is not well understood, but it is reported that oxidative stress and membrane damage are key factors (Lemire et al. 2013). Metal and metal oxide NPs are well documented for killing both Gram-positive and Gram-negative bacteria (Pasquet et al. 2014; Bondarenko et al. 2012; Ruparelia et al. 2007; Dizaj et al. 2014; Azam, Ahmed, M. Oves, et al. 2012), therefore it seems feasible that they would also exhibit anti-mycobacterial properties, yet there is limited information available for mycobacteria. A small number of studies recently published on the efficacy of metal NPs against mycobacteria (e.g. *M. smegmatis* and *M. bovis*-BCG) exist (Mohanty et al. 2013; Larimer et al. 2014; Islam et al. 2013; Pati et al. 2014). Bacterial resistance to metals is rare and develops very slowly, therefore their anti-mycobacterial activity should be further explored (Pelgrift & Friedman 2013).

The physico-chemical properties of NPs (e.g. composition, solubility, morphology) are fundamental to their anti-bacterial activity (Puzyn et al. 2011) and although it is known that the properties of metal/metal oxide NPs differ to that of the bulk material, the exact mechanism of anti-bacterial action has not been well elucidated (Dizaj et al. 2014). Currently, the two main hypotheses are; toxicity is exerted from the metal ions released from the NPs and/or oxidative stress via generation of ROS on NP surfaces (Besinis et al. 2014), being a similar method to the bulk metal. As most bacteria cells are in the micron

scale, the pores in the cell membrane (which are in the nano meter range) could facilitate the passing of NPs and/or metal ions intracellularly (Azam, Ahmed, M. Oves, et al. 2012), thus allowing disruption of many cellular processes and hence the advantage NPs have over bulk forms of the same material.

Three metal/metal oxide NPs were selected to test the potential inhibition of mycobacterial growth, which could provide novel tools for aiding the fight against mycobacterial infections and be invaluable for overcoming anti-bacterial resistance associated with current therapies for TB (or other diseases such as leprosy or Johne's disease).

#### **4.1.1 NP selection**

##### **4.1.1.1 Ag NPs**

The bacterial properties of silver (Ag) were first described by Hippocrates in 400 BC (Morones-Ramirez et al. 2013). Ag is inert, but when it comes into contact with moisture (e.g. following application to the skin) it can be employed as an anti-bacterial agent for wound dressings, ulcer treatments, burn healing *etc.*, which has been the case for centuries (Kim et al. 2007; Jung et al. 2008; Bondarenko et al. 2013a). A range of Ag NPs which vary with regards to their physico-chemical properties are reported to have toxic anti-bacterial properties (Rai et al. 2009; Ansari et al. 2011; Yuan et al. 2012; Kim et al. 2007; Choi et al. 2008; Ruparelia et al. 2007; Leo et al. 2013; Sharma et al. 2009) and they are currently the most popular inorganic NPs used as anti-bacterial agents (Zinjarde 2012; Bondarenko et al. 2013b). Ag NPs (e.g. silver nanopowder [ $<100$  nm] from Sigma-Aldrich®) are reported to have anti-bacterial properties against many bacterial organisms, including Gram-positive species *Streptococcus mutans*, Methicillin-resistant *Staphylococcus aureus* (MRSA), *Listeria monocytogene*, as well as Gram-negative

bacteria *Escherichia coli* (*E.Coli*), *Salmonella* (Ansari et al. 2011; Besinis et al. 2014; Choi et al. 2008; Pal et al. 2007) and mycobacteria; *Mtb*, *M. xenopi* and *M. smegmatis* (Islam et al. 2013; Seth et al. 2011).

When Ag is in the nano-form its anti-bacterial activity is reported to increase (Rai et al. 2009). As proposed above, this may be due to the increased ability of NPs to enter through cell membranes (Fig 4.1) (Choi et al. 2008). Once inside a cell, most studies suggest that Ag NPs target proteins which protect DNA molecules thus preventing DNA replication (Feng et al. 2000). When Ag NPs come into contact with an oxygenated, aqueous environment, silver ions ( $\text{Ag}^+$ ) have been reported to be released (Park et al. 2009) and  $\text{Ag}^+$  action is assumed to be a main mediator of toxicity for NPs. The relatively large surface area of Ag NPs may further aid  $\text{Ag}^+$  release compared to bulk metal, contributing to the increased toxicity and generally it is recognised that smaller NPs (<30 nm) increase anti-bacterial activity (Dizaj et al. 2014).  $\text{Ag}^+$  exert their lethal effect by inhibiting metabolic enzyme functions through interaction with bacterial thiol (sulfhydryl) groups (affecting their shape and stability) found in a variety of proteins (Jung et al. 2008; Arai et al. 2015). Thiols (e.g. cysteine) are able to control bacterial oxidative stress and govern metal and metal ion uptake, therefore if deactivated they cannot neutralise the activity of Ag/ $\text{Ag}^+$ .  $\text{Ag}^+$  are also reported to cause structural changes and damage to bacterial cells by binding to negatively charged parts of the bacterial cell membrane (Rai et al. 2009), creating pits in the plasma membrane surface, and gaps between the cytoplasmic membrane and the cell wall (Fig 4.1) (Feng et al. 2000) thus allowing leakage of intracellular components (Dizaj et al. 2014). In addition,  $\text{Ag}^+$  can also interfere with membrane permeability and modulate signal transduction, leading to cell death (Park et al. 2009; Rai et al. 2009; Choi et al. 2008).

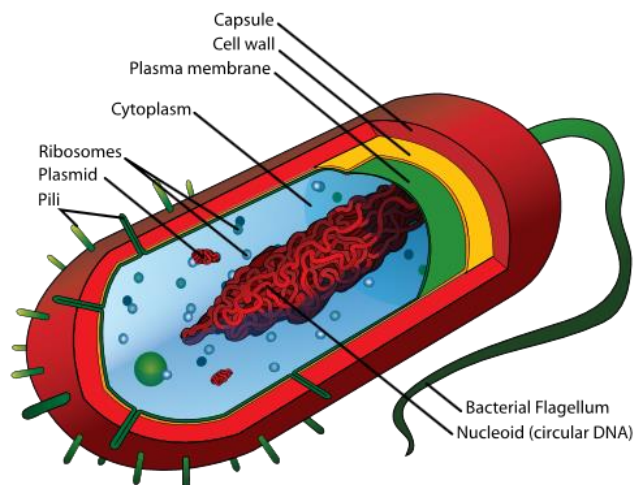


**Figure 4.1 Schematic drawing of a bacterial structure**

Taken from <https://www.boundless.com/microbiology/textbooks/boundless-microbiology-textbook/cell-structure-of-bacteria-archaea-and-eukaryotes-4/cell-walls-of-prokaryotes-34/the-cell-wall-of-bacteria-259-5681/>

#### **4.1.1.2 Cu(II)O NPs**

Copper (Cu) has properties similar to that of the noble metals (such as silver and gold) but unlike these, copper NPs are considered relatively cost effective to produce. Cu(II)O NPs are reported to be very stable when likened to other organic anti-microbial agents (Ananth et al. 2015; Das et al. 2013) and have been used in metallic coatings, batteries and paints (Chang et al. 2012). Their main uses are in the electronics and technological industries (Bondarenko et al. 2013b), but Cu(II)O NPs have recently been reported as being useful in medical applications by displaying bactericidal properties against Gram-positive species *Streptococcus iniae* and Gram-negative species *E.coli* and *Pseudomonas aeruginosa* (Ananth et al. 2015). There is evidence that Cu-coated titanium particles exhibit toxicity against *M. smegmatis* (Wu et al. 2010) but generally the anti-bacterial properties of Cu(II)O NPs are poorly covered in the literature (Ren et al. 2009). Only recently have these NPs started to gain appropriate attention, hence little is known about their mechanism(s) of action. It is known however, that Cu affects the cell wall by

interacting with amine and carboxyl groups and that Cu ions ( $\text{Cu}^{2+}$ ) promote the formation of ROS and, similarly to Ag NPs, they accumulate on bacterial plasma membranes (Fig 4.1) forming pores, negatively effecting the proton motive forces (Pelgrift & Friedman 2013; Chatterjee et al. 2014). As with Ag NPs, size and the stability of Cu(II)O NPs plays a role in their bactericidal activity (Azam, Ahmed, M. Oves, et al. 2012). Overall, limited literature was found on the anti-bacterial properties of Cu(II)O NPs, therefore it was important to try and bridge this gap.

#### **4.1.1.3 ZnO NPs**

ZnO NPs (e.g. zinc oxide nanopowder [ $<50$  nm] from Sigma-Aldrich<sup>®</sup>) are widely reported to have anti-microbial properties against many bacterial species (Gram-negative species *E.coli* and *Pseudomonas aeruginosa* and Gram-positive *Bacillus atrophaeus*, *Bacillus subtilis*) (Ramani et al. 2013; Dizaj et al. 2014; Sharma et al. 2012; Heinlaan et al. 2008; Padmavathy & Vijayaraghavan 2008). They are found in antiseptic creams, sun lotions, cosmetics and many other consumer products. Additionally they are found in food as additives, used in food packaging as anti-bacterial agents (Ramani et al. 2013; Prach et al. 2013; Sharma et al. 2012) and have even been utilised as a fungicide (Wong et al. 2010; Allen et al. 1956). ZnO are one of the most widely produced and utilised NPs with production of 550 tons per annum worldwide (Merdzan et al. 2014). It is reported that ZnO NPs exert toxicity through production of ROS on the particle surface and via damage to the bacterial cell wall (Fig 4.1) leading to leakage of cellular contents which affects membrane permeability (Ramani et al. 2013). Oxidative stress leads to protein and lipid damage (e.g. peroxidation) affecting the membrane and therefore disrupting many other cellular processes (Heinlaan et al. 2008). Other reports include toxicity resulting from ion release ( $\text{Zn}^{2+}$ ) which bind to cellular membranes causing severe

disorganisation/leakage and/or through the formation of aggregates (Chapter 2 [section 2.2.2]) that attach directly to pathogens (Li et al. 2011; Ramani et al. 2013). It has also been suggested that ZnO NPs generate toxic ROS (e.g. hydrogen peroxide) and disrupt transmembrane electron transport in bacterial cells (Dizaj et al. 2014). As with both Cu(II)O and Ag NPs, ZnO NPs bactericidal activity is enhanced when particles are smaller thus increasing bioavailability (Padmavathy & Vijayaraghavan 2008).

**Table 4.1 Mechanisms and the attributes of metal/metal oxide NPs toxicity to bacterial species**

MECHANISMS		ATTRIBUTES
Production of ROS	<b>TOXICITY OF METAL/METAL OXIDE NPS TO GRAM POSITIVE AND NEGATIVE BACTERIAL SPECIES</b>	Size
Inhibiting enzyme function		Dissolution rate
Oxidative stress		Shape
Disruption of cell membrane		Concentration
Disruption of membrane potential		Charge
Damage to cell wall		Exposure duration
Genotoxicity		Dispersion medium (formation of aggregates/ agglomerates)
Other		Other

#### **4.1.2 Aims**

Ag, ZnO and Cu(II)O NPs were selected for investigation due to the reported effects on many bacterial species and for their different physico-chemical properties, highlighted in Figure 4.2. It was hypothesised that the three NPs tested would differ in their potency against the mycobacteria and that the relative toxicity of the NPs would relate to their physico-chemical properties, mainly their composition and dissolution rates in the bacterial growth culture medium (7H9). Using the newly developed fluorescence assay (Chapter 3), the aim of this chapter was to assess the relative efficacy of these three NPs in terms of anti-microbial impacts on *Map* K10/GFP. Results from this chapter have been

published in Nanotoxicology ‘*A rapid screening assay for identifying mycobacteria targeted nanoparticle antibiotics*’ (Donnellan et al. 2015).

## **4.2 Methods and Materials**

### ***4.2.1 NP preparation and characterisation***

Ag (NM 300) and ZnO (NM 110) NPs were obtained from the European Commission's Joint Research Centre (JRC) repository of NPs, while the Cu(II)O NPs were obtained from Sigma-Aldrich® (UK). All NPs were kept in the dark at ambient temperature until use. NPs were diluted in sterile 2% (vol/vol) fetal calf serum (prepared in sterile distilled water) at a concentration of 1 mg/mL and sonicated for 16 minutes at 400 W in a bath sonicator (Ultrawave®, UK) and then placed on ice (following ENPRA [Risk Assessment of Engineered Nanoparticles] [www.enpra.eu]) (Jacobsen et al. 2010; Kermanizadeh et al. 2013). NPs were then diluted (1 mg/mL) in 7H9 medium (see Chapter 2 [section 2.6.1] for medium details).

#### ***4.2.1.1 Transmission electron microscopy (TEM)***

Imaging of NP morphology was performed using a Philips CM120 Transmission Electron Microscope (FEI, UK). Images were taken on a Gatan Orius CCD camera. For all particle types, they were prepared as outlined above (at 25 and 100 µg/mL) and 10 µL of each suspension was pipetted onto the surface of formvar/carbon coated 200 mesh copper grid and allowed to dry at room temperature for 40 minutes prior to imaging.

#### ***4.2.1.2 DLS***

Agglomeration/aggregation status, zeta potential and hydrodynamic sizes were analysed by DLS (Pecora 2000) at a concentration of 100 µg/mL using a Zetasizer Nano-ZS instrument (Malvern Instruments Ltd., UK) as outlined in Chapter 2 (section 2.2.2). For all particle types, they were prepared as outlined above (section 4.2.1).

#### ***4.2.2 Metal salt controls***

For each metal/metal oxide particle utilised, a metal salt control was run alongside each experiment (in triplicate); silver nitrate (AgNO<sub>3</sub>), copper sulphate (CuSO<sub>4</sub>) and zinc chloride (ZnCl<sub>2</sub>) (Sigma-Aldrich<sup>®</sup>, UK). Salts were weighed and diluted in distilled water then serial diluted in 7H9, at a metal concentration matching the NPs.

#### ***4.2.3 Inductively coupled plasma optical emission spectrometry (ICP-OES)***

Inductively coupled plasma optical emission spectrometry (ICP-OES), a branch of atomic spectroscopy, was utilised to determine metal concentrations in the broth medium. ICP-OES works to determine trace levels of metals in aqueous medium (providing the materials of interest can be solvated) by spraying the solution on to plasma whereby elements present are detected from the specific wavelengths and intensities emitted from the excited atoms/ions. Initially several wavelengths were selected for each element and the following wavelengths were selected for reporting results based on the shape of the peaks at that wavelength, background interferences, wavelength sensitivity and the linearity of the calibration lines: Ag 328.068 nm, Cu 324.700 nm and Zn 334.501 nm. ICP-OES was carried out on a Perkin Elmer Optima 5300 DV (Llantrisant, UK)



employing an RF forward power of 1400 W, with argon gas flows of 15, 0.2 and 0.75 L/min for plasma, auxiliary, and nebuliser flows, respectively (standard ICP-OES set up).

#### ***4.2.3.1 Ionic fraction analysis***

A 10 mL aliquot of each NP type and metal salt control, prepared at concentrations 25 µg/mL and 100 µg/mL in 7H9 medium, as outlined above (section 4.2.4), was centrifuged for 30 minutes at 1,320 g at room temperature in order to deposit the NP content. Following centrifugation, 5 mL of supernatant (without the NP pellet) from each solution was carefully transferred to a glass screw neck tube with 5 mL of 4% nitric acid (99.999% purity, trace metal basis [Sigma-Aldrich®, UK]) giving a final acid concentration of 2% and a final volume of 10 mL. This analysis was done at two time points; immediately after addition of NPs to 7H9 (day 0) and 7 days post addition of NPs into 7H9, during which time the NPs and medium had been incubated at 37°C on a plate shaker (250 rpm). Each acidified sample was vortexed (no further dilutions were carried out) and loaded into a peristaltic pump where sample solutions were taken up into a Gem Tip cross-Flow nebuliser and Scotts spray chamber at a rate of 1.50 mL/min (assisted by laboratory technician Dr Lorna Eades, School of Chemistry, University of Edinburgh).

#### ***4.2.3.2 Total concentrations analysis***

A 10 mL aliquot of each NP type and salt control, prepared as outlined above (at concentrations 25 µg/mL and 100 µg/mL in 7H9), was added to 10 mL of 68% nitric acid (trace metal grade [Sigma-Aldrich®, UK]), giving a final acid concentration of 34%. This analysis was done at two time points, as above; immediately after addition of NPs to 7H9 (day 0) and 7 days post addition of NPs into 7H9, during which time the NPs and medium

had been incubated at 37°C on a plate shaker (250 rpm). For analysis, each sample was diluted 10 fold and vortexed prior to analysis.

The instrument was operated in axial mode for all samples and a range of calibration standards for each element were prepared using single element 1000 mg/L standards (Fisher Scientific, UK), diluted with 18.2  $\Omega$  deionised water. A 10 fold dilution of Merck ICP Multi element standard solution VI CertiPUR® was employed as a reference standard for each of the elements. The wavelengths were selected for each element and analysed in fully quant mode (three points per unit wavelength). Three replicate runs per sample were employed (laboratory technician Dr Lorna Eades, School of Chemistry, University of Edinburgh, carried out the analysis whilst I carried out all sample preparation and monitoring in all cases).

#### ***4.2.4 Metal/Metal Oxide NP 96 well Plate setup for toxicity assessment***

*Map* K10/GFP was cultured in 7H9K<sup>+</sup> (see Chapter 2 [section 2.1.1]) until the exponential stage of growth (see Chapter 3 [section 3.1.4]) was reached and cells were seeded in a 96 well at 2x10<sup>6</sup> CFU/mL (in 100  $\mu$ L of 7H9). Serial dilutions of NPs were made in 7H9 to give final concentrations per well ranging from 0 (control) to 100  $\mu$ g/mL and were added to the wells containing *Map* K10/GFP, giving a final volume of 200  $\mu$ L per well. The samples were incubated at 37°C with medium agitation (250 rpm) and kept in the dark throughout the experimental procedure. To check for NP interference, wells of medium only (no bacteria, no NPs) and NPs and medium (no bacteria) were included. Fluorescence was measured using a GloMax® Multi<sup>+</sup> plate reader (Promega, UK) at an excitation of 490 nm and emission of 510-570 nm (see Chapter 3 [section 3.3.1]). Bacterial fluorescence was monitored immediately before and after NP addition (day 0),

then at the same time each day for 7 days. The same steps were taken for the three salt controls. All experiments were performed in triplicate under sterile conditions.

#### ***4.2.5 Data Analysis for fluorescence assay***

Results expressed in Arbitrary Fluorescent Units (AFU) against time (days) were transformed and normalised to obtain a dose response relationship, to compare the effects of the NPs and salt controls on the growth of the mycobacteria as outlined in Chapter 3 (section 3.3.4). This data was then plotted using the dose response modelling software PROAST (version 38.9 [RIVM, The Netherlands]) in the R software (version 3.1.0, [R Foundation for Statistical Computing, Austria]). By setting the critical effect size (CES) to 50% it was possible to obtain the half maximal effective concentration ( $EC_{50}$  [the critical effect dose [CED]]) and lower/upper 90% confidence intervals [CEDL/CEDU] to allow for statistical comparison to determine if the NP differed significantly from each other, and/or their corresponding salt controls.

#### ***4.2.6 Colony counts***

Following 7 days of *Map* K10/GFP incubation with NPs in 7H9, 100  $\mu$ L of the cultures at each concentration were serial diluted and inoculated onto 7H11 agar in petri dishes for 12 weeks and incubated at 37°C. Using conventional colony counts (see Chapter 2 [section 2.1.2]) NP toxicity was ranked.

#### ***4.2.7 Cytotoxicity of NPs to macrophages***

Macrophages (J774A.1 cells) were cultured until confluent and counted as outlined in Chapter 2 (section 2.3.1) and NPs were prepared as described in 4.2.1. Using the alamar blue assay (see Chapter 2 [section 2.4]), cytotoxicity to macrophages was tested for the 3 NP types (over a 24 hour period, at a concentration range of 0.146-150  $\mu\text{g/mL}$ ).

#### ***4.2.8 Imaging***

##### ***4.2.8.1 Infected macrophages treated with metal/metal oxide NPs for TEM imaging***

Macrophages were cultured until confluent and counted as outlined in Chapter 2 (section 2.3.1). Cells were detached from flasks using TrypLE<sup>TM</sup> and centrifuged at 850 g for 2 minutes before being resuspended in complete medium (without antibiotic) and added on to Nunc<sup>TM</sup> Thermanox<sup>TM</sup> Coverslip slides in sterile 24 well plates at a density of  $2 \times 10^5$  cells/well (determined using Trypan blue [see Chapter 2 [section 2.5.1])). The cells were then incubated for 24 hours at 37°C, 5% CO<sub>2</sub>. Supernatant was removed from the chambers and cells were washed twice with 400  $\mu\text{L}$  PBS. *Map* K10/GFP was cultured as described previously (see Chapter 2 [section 2.1.1]) and 10 mL of bacterial culture was centrifuged at 3090 g for 20 minutes and resuspended in 1 mL of PBS. The 1 mL culture was centrifuged for 5 minutes at 670 g to remove any residual antibiotic, resuspended in 1 mL of PBS and passed through a Gilson tip several times to break apart any clumping. After accurate cell counts (see Chapter 2 [section 2.5.2]) at a 30:1 multiplicity of infection (MOI) the macrophages were infected with mycobacteria in complete medium (without streptomycin or penicillin) at a final volume of 400  $\mu\text{L}$  per well and incubated for 30 minutes at 37°C, 5% CO<sub>2</sub>. During this time, each NP type was prepared as described

above (at a concentration of 12.5 µg/mL), then added to the wells with *Map* K10/GFP infected macrophages and incubated for a further 4 hours at 37°C, 5% CO<sub>2</sub>.

Fixation was performed using 3% glutaraldehyde in 0.1 M sodium solution in cacodylate for 2 hours then stored in a 0.1 M sodium solution in cacodylate buffer prior to TEM imaging (see Chapter 2 [section 2.7.2]). Sample preparation for TEM was carried out by Mr Stephen Mitchell (Bio-Imaging Facility, The University of Edinburgh). Briefly, the samples were dehydrated in 50%, 70% and 100% normal grade acetone for 10 minutes, followed by 2 x 10 minute washes in analar acetone before embedding in araldite resin. Sections of 1 µm thickness were cut with a Reichert OMU4 ultramicrotome (Leica Microsystems, UK) stained with toluidine blue and viewed under a light microscope (Olympus BX40) to select suitable areas for imaging. Sections (60 nm thickness) were stained in uranyl acetate and lead citrate and the infected macrophages (treated with NPs) were viewed using a JEM-1400 Plus TEM\* (JEOL Ltd, Tokyo, Japan).

*\*please note this was a different transmission electron microscope from previous NP imaging; the equipment was updated in September 2015.*

#### ***4.2.8.2 Macrophages treated with metal/metal oxide NPs for fluorescence imaging***

As above, excluding the *Map* K10/GFP infection of the macrophages. Uninfected cells were treated with all the NP types. Cells were fixed using 4% paraformaldehyde (see Chapter 2 [section 2.7.1]) and imaged using a Zeiss Axiovert 200M inverted Epi fluorescence microscope (Zeiss, Cambridge, UK)\*\*.

*\*\*please refer to Chapter 5 for detailed methods on fluorescent microscopy.*

## 4.3 Results

### 4.3.1 NP Characterisation

The NP supplier information is outlined in Table 4.2. Ag and ZnO NPs have been extensively characterised previously (Table 4.3) (Kermanizadeh et al. 2013), whereas there is scarce literature on the characterisation of Cu(II)O NPs. Characterisation for the Ag, Cu(II)O and ZnO NPs was conducted in this study using the 7H9 growth medium.

**Table 4.2 NP Information. The nominal sizes and properties as provided by the supplier**

NP	Supplier Name	NP Diameter (supplier)	Surface Area (m <sup>2</sup> /g)	Additional Information
Ag (NM 300)	JRC Repository	<20 nm	N/A*	Polyoxylaurat Tween 20 capped
Cu(II)O	Sigma-Aldrich®	<50 nm	29	Uncoated
ZnO (NM 110)	JRC Repository	100 nm	13	Uncoated

\*Supplied as an aqueous suspension of nano Ag with stabilising agents

**Table 4.3 Kermanizadeh *et al.*, (2013) Characterisation Data**  
(used with permission from the author)

NP	Phase	TEM Size (nm)	Surface area (m <sup>2</sup> /g)	Size (nm) in MEM* (DLS)**	Primary characteristics by TEM analysis
Ag (NM 300)	Ag	8-47 (av: 17.5)	N/A	51	Mainly euhedral NP; minor fractions have either elongated or sub-spherical morphology
ZnO (NM 110)	Zincite	20-250/ 50-350	14	306	Mainly 2 euhedral morphologies: 20 - 250 nm range and few particles of approx. 400 nm. OR 50-350 nm with minor amounts of particles with irregular morphologies observed.

\* Minimum Essential Media

\*\* Intensity based size average in biological media after 15 minutes

#### **4.3.1.1 DLS**

DLS measures hydrodynamic diameter; the size of primary particles if dispersed, or agglomerates along with the shell of ions/water molecules associated with the surface, by measuring the scattered light that passes through a solution. The larger the NP or aggregate/agglomerate (see Chapter 2 [section 2.2.2]), the slower light will diffuse thus allowing hydrodynamic diameter of particles to be determined via a measure of time. The size of all the tested NPs is provided in Table 4.4. The zeta potential, a measure of the charge carried by NPs when suspended in an aqueous environment, gives an indication of the stability of NPs in a solution. The zeta potential for all the tested NPs is provided in Table 4.4.

The average hydrodynamic diameter for Ag NPs obtained by DLS was 46.47 nm, thus being akin to suppliers' information (Table 4.2). This suggests DLS detected individual NPs and/or 2 NPs and there was little spread in the data as shown by the intensity graph (Fig 4.3a). The zeta potential was -9.37 mV thus suggesting the NPs were unstable in the 7H9 medium (the zeta potential distribution graphs are provided in Appendix A).

The average hydrodynamic diameter for Cu(II)O NPs was 408.46 nm, suggesting that DLS was detecting agglomerates rather than individual NPs as suppliers' report NPs <50 nm (Table 4.2). The intensity graph (Fig 4.2b) displays a spread in the sizes detected by this method. The zeta potential was -11.40 mV again suggesting instability in 7H9 (Appendix A).

The average hydrodynamic diameter for ZnO NPs was 190.61 nm, again suggesting that DLS was detecting agglomerates (maybe 2 NPs) (Table 4.4). The intensity graph (Fig 4.2c) displays 3 main peaks, showing that both smaller and larger agglomerates were detected in the solution and there was high variation. The zeta potential was -8.22 mV,

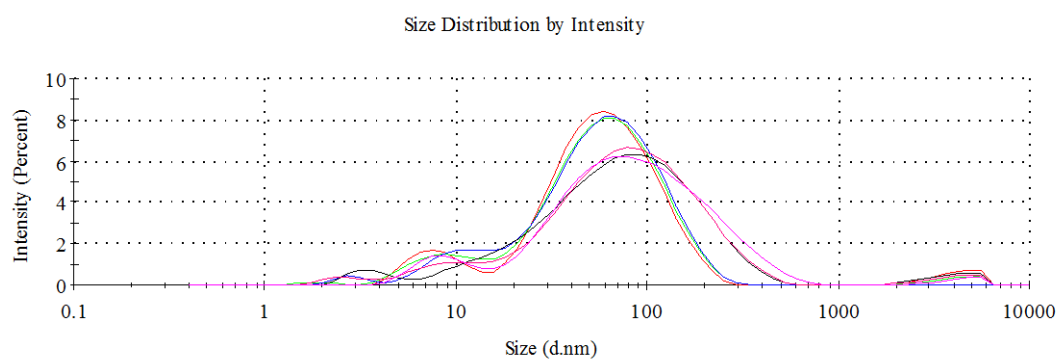
and being very low these NPs were also unstable when dispersed in 7H9 (Appendix A). Overall, DLS results suggest that NP agglomeration/aggregation occurred in the growth medium of *Map* K10/GFP (7H9), particularly for Cu(II)O and ZnO NPs and that the NPs exhibited a very small negative charge in the aqueous environment.

**Table 4.4 DLS Results.** Z-average (Hydrodynamic diameter), zeta potential (an estimate of NP surface charge) and polydispersity index (PdI [a measure of size variation]) of the NP panel was assessed using dynamic light scattering (DLS). Data expressed as mean  $\pm$  SEM (n=6). Temp: 25°C, dispersant: Middlebrooks 7H9 (100  $\mu$ g/mL), pH 6.9, equilibrium time: 30 seconds.

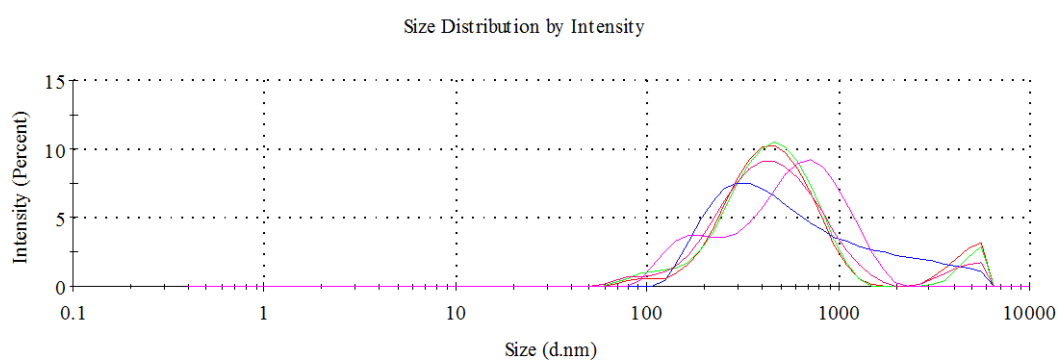
NP	Z-Average (d.nm) DLS	Zeta Potential (mV) DLS	PdI DLS	NP Diameter (TEM in 7H9)
Ag (NM 300)	46.47 $\pm$ 3.3	-9.37 $\pm$ 1.3	0.465 $\pm$ 0.01	<50 nm
Cu(II)O	408.46 $\pm$ 10.13	-11.40 $\pm$ 0.26	0.365 $\pm$ 0.02	Unknown*
ZnO (NM 110)	190.61 $\pm$ 25.3	-8.22 $\pm$ 0.48	0.55 $\pm$ 0.1	Unknown*

\*TEM showed NP agglomeration/aggregation in 7H9 therefore an accurate diameter measurement was unobtainable from TEM

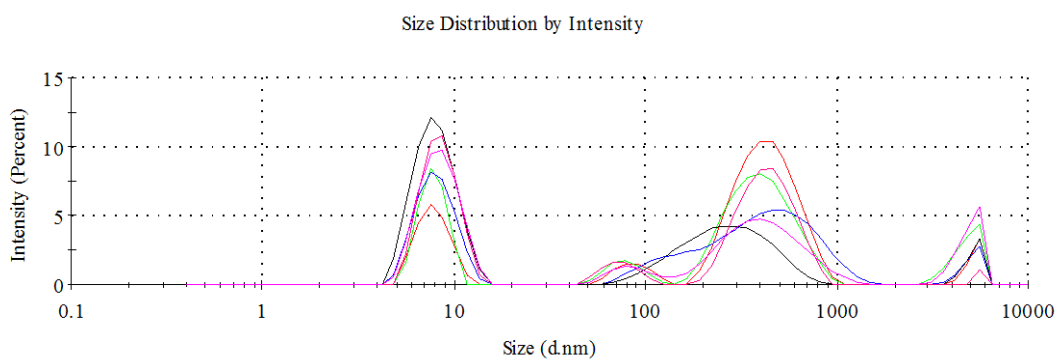




a)



b)



c)

**Figure 4.2 Size intensity graphs (DLS) (n=6)**

- (a) Ag NPs in 7H9
- (b) Cu(II)O NPs in 7H9
- (c) ZnO NPs in 7H9

#### 4.3.1.2 TEM

TEM analysis was performed to determine the size, morphology and dispersion patterns of the NPs in 7H9 and distilled water. It provides primary particle size and/or agglomerate size. This does not include the surface associated water and ions. Micrographs from TEM analysis suggest that Ag NPs were well dispersed in 7H9 at both concentrations imaged (Figs 4.3a,b). Figure 4.3 (a) depicts Ag NPs at 25  $\mu\text{g/mL}$  in 7H9, NPs are well dispersed and primary particle size was found to be  $<50$  nm. No agglomeration was evident, although slight clustering was observed but the spherical shape of the NPs was clearly visible. Figure 4.3 (b) depicts Ag NPs at 100  $\mu\text{g/mL}$  in 7H9. Overall the NPs display limited agglomeration and smaller particles were observed surrounding larger particles, which may have been generated via precipitation of dissolved  $\text{Ag}^+$  ions as silver salts. When dispersed in distilled water (at 100  $\mu\text{g/mL}$ ) Ag NPs were found to be well dispersed, evenly spread, spherical in shape and primary particle size was  $<50$  nm (Figs 4.3c,d). Smaller particles can be seen surrounding a larger particle, again possibly caused via precipitation of dissolved  $\text{Ag}^+$  ions (Figs 4.3b,d).

$\text{Cu(II)O}$  were agglomerated/aggregated in 7H9 at both concentrations tested. Figure 4.3 (e) depicts agglomerates/aggregates of  $\text{Cu(II)O}$  NPs at 25  $\mu\text{g/mL}$  in 7H9, where individual NPs were barely visible. At 100  $\mu\text{g/mL}$  (Fig 4.3 f)  $\text{Cu(II)O}$  NPs were highly agglomerated/aggregated and only masses of NPs were visible and so no information on individual NP size/shape could be obtained. When dispersed in distilled water (at 100  $\mu\text{g/mL}$ )  $\text{Cu(II)O}$  NPs were agglomerated/aggregated, although to a much lesser extent than when dispersed in 7H9 medium, thus allowing mixed shaped particles to be seen (Fig 4.3 g,h). Figure 4.3 (h) shows that it was possible to see individual  $\text{Cu(II)O}$  NPs in distilled water, but these images were difficult to obtain.

ZnO NPs were also agglomerated/aggregated in 7H9 at both concentrations tested (Figs 4.3 i,j). Figure 4.3 (i) depicts ZnO NPs at 25  $\mu\text{g/mL}$  in 7H9 where agglomeration/aggregation was evident and mixes of different shaped/sized NPs were present. As such, information on individual particle size/shape was not possible to acquire. When at 100  $\mu\text{g/mL}$  in 7H9 (Fig 4.3j), miscellaneous shapes were visible amongst large dark masses of agglomerates/aggregates. Again individual NP size/shape was not possible to view when dispersed in 7H9. The same pattern was observed when ZnO NPs were dispersed in distilled water (Figs 4.3 k,l). As they behaved similarly when in both aqueous environments, it indicates that that ZnO NPs tend to form agglomerates/aggregates readily when dispersed. Overall TEM micrographs concur with the DLS results, that Ag NPs were well dispersed in 7H9 at the concentrations tested, unlike Cu(II)O and ZnO NPs.

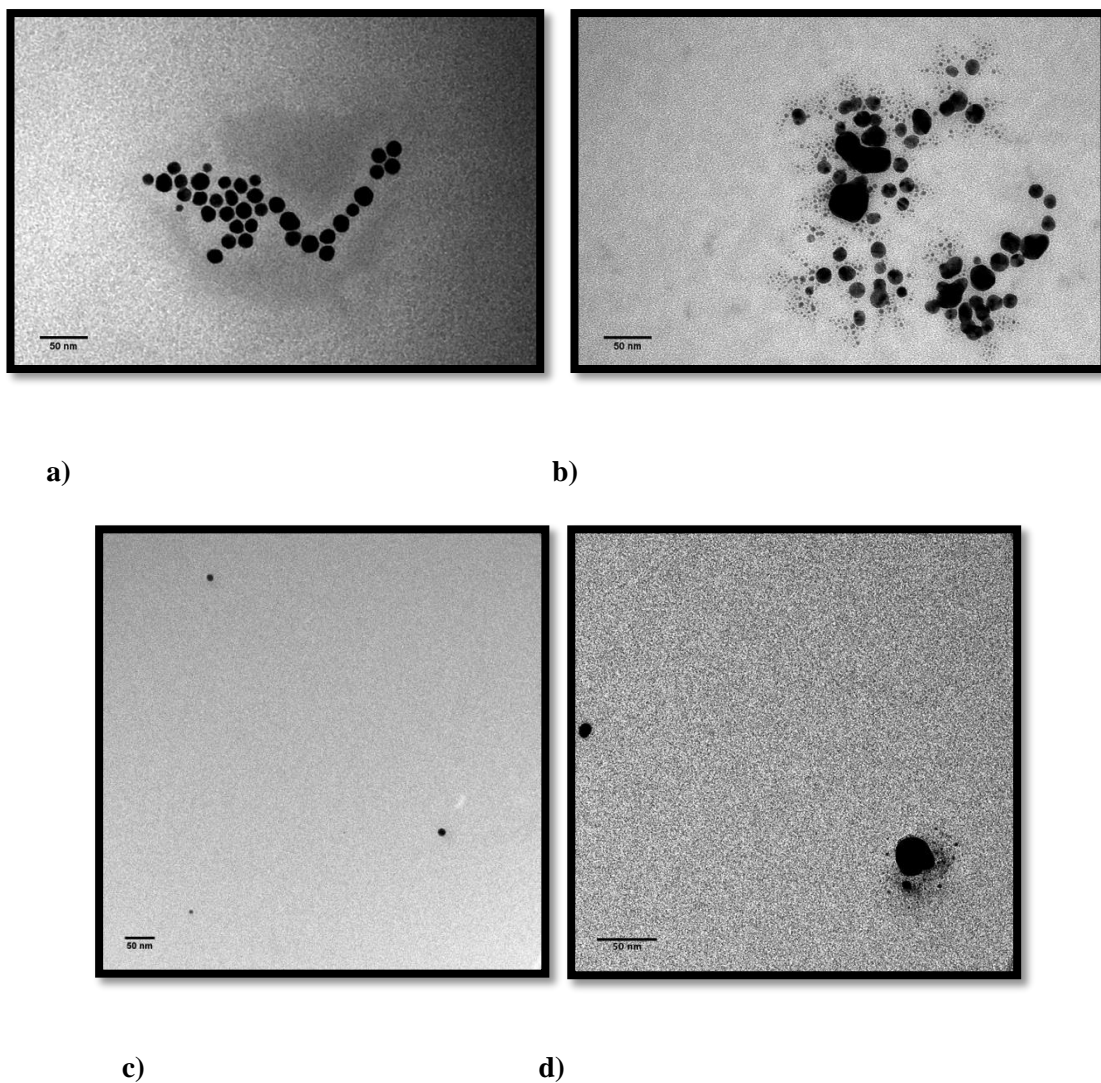
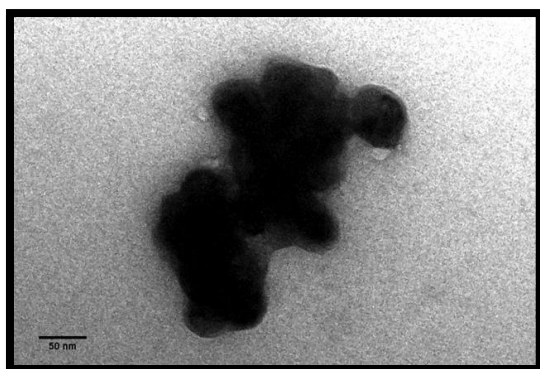
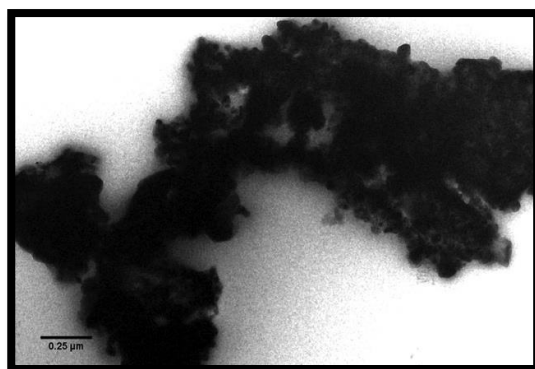


**Figure 4.3 (a-d) TEM-images of Ag NP suspensions in 7H9 medium (a,b) and distilled water (c,d) (magnification ranging from 30-52K) (scale bars all represent 50 nm).**

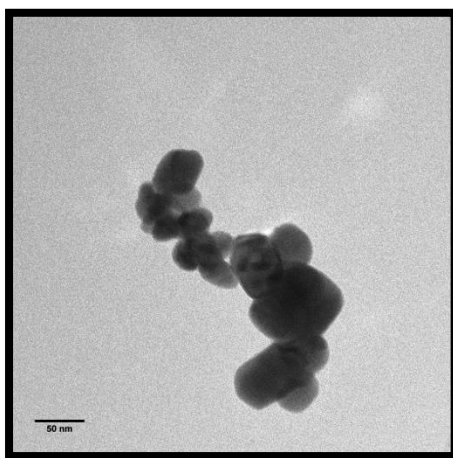
- a) Ag NPs at 25 µg/mL in 7H9. NPs were well dispersed with individual particle size <50 nm.
- b) Ag NPs at 100 µg/mL in 7H9. NPs were well dispersed with different sized NPs visible, generally NPs were ≤50 nm.
- c) Ag NPs at 100 µg/mL in distilled water. NP were very evenly dispersed, with particle size <50 nm.
- d) Ag NPs at 100 µg/mL in distilled water. NPs were evenly dispersed, different sized NPs were visible and average particle size <50 nm.



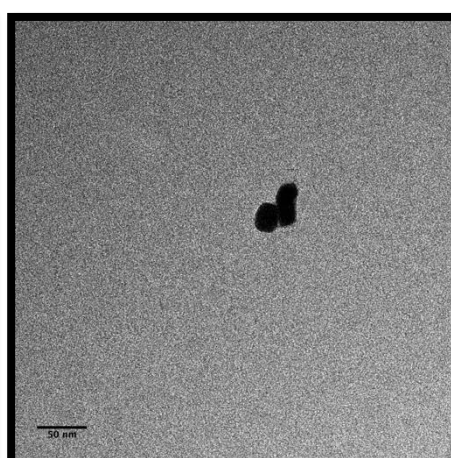
e)



f)



g)



h)

**Figure 4.3 (e-h) TEM-images of Cu(II)O NP suspensions in 7H9 medium (e,f) and distilled water (g,h) (magnification ranging from 30-52K) (note the different scale bars).**

- e) Cu(II)O NPs at 25 µg/mL in 7H9. Only agglomerates were visible.
- f) Cu(II)O NPs at 100 µg/mL in 7H9. Mass agglomeration/aggregation occurred with individual NPs not visible.
- g) Cu(II)O NPs at 100 µg/mL in distilled water. NPs were agglomerating, but individual NP shapes can be visualised.
- h) Cu(II)O NPs at 100 µg/mL in distilled water. Individual NPs both <50 nm.

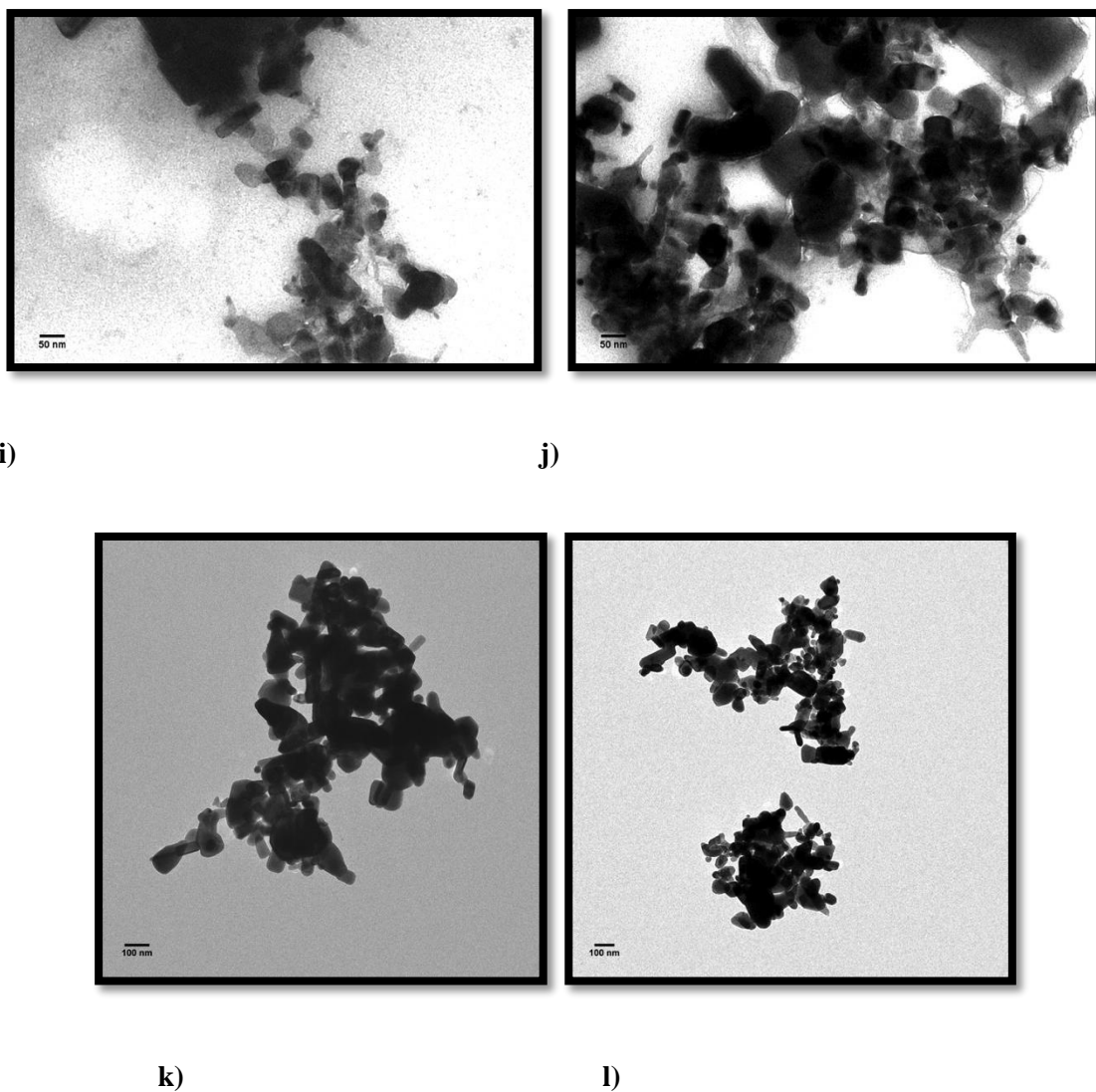


**Figure 4.3 (i-l) TEM-images of ZnO NP suspensions in 7H9 medium (i,j) and distilled water (k,l) (magnification ranging from 30-52K) (note the different scale bars).**

- i) ZnO NPs at 25 µg/mL in 7H9. Agglomeration/aggregation was occurring, NP size was not possible to obtain
- j) ZnO NPs at 100 µg/mL in 7H9. Mass agglomeration/aggregation was occurring.
- k) ZnO NPs at 100 µg/mL in distilled water. NPs were highly agglomerated; a mix of varied shapes and sizes was visible.
- l) ZnO NPs at 100 µg/mL in distilled water. NPs were highly agglomerated, forming masses throughout the field of view.

### 4.3.2 Assessment of NP Dissolution (ICP-OES)

NP dissolution in 7H9 medium was assessed at day 0 and 7 using ICP-OES. It is difficult to have confidence in this data, due to the large spread in the data and the problems encountered trying to detect Ag in the medium. The data for all NPs suggested low solubility (Fig 4.4). Cu(II)O NP solubility was low at day 0 but a small increase in solubility was observed by day 7, whereas CuSO<sub>4</sub> dissolution was generally high in 7H9, suggesting that for the copper salt Cu<sup>2+</sup> ions played a significant role in the toxicity to *Map* K10/GFP (Fig 4.4). The solubility of ZnO NPs did not change over time, in-fact it slightly decreased by day 7, but the solubility of these NPs was generally very low (Fig 4.4). ZnCl<sub>2</sub> solubility on day 0 was relatively high, but this did not change over time (Fig 4.4). It is possible that components of complex 7H9 medium (see Chapter 2 [section 2.6.1]) interfered in this assay.

In order to check the ability of the ICP-OES technique to accurately measure the metal content of both the NP and metal salt suspensions, the total amount of metal in each of these solutions was analysed. For Cu(II)O and ZnO NPs (and salts), at day 0 and 7, the concentration of Cu and Zn detected generally reflected the concentration of metal added to the 7H9 medium, suggesting that this analysis worked (Fig 4.5). In contrast Ag NPs and AgNO<sub>3</sub> was not detected using the protocol applied in this study, suggesting that it was not possible to accurately determine the extent of Ag dissolution in the 7H9 medium (Fig 4.5).

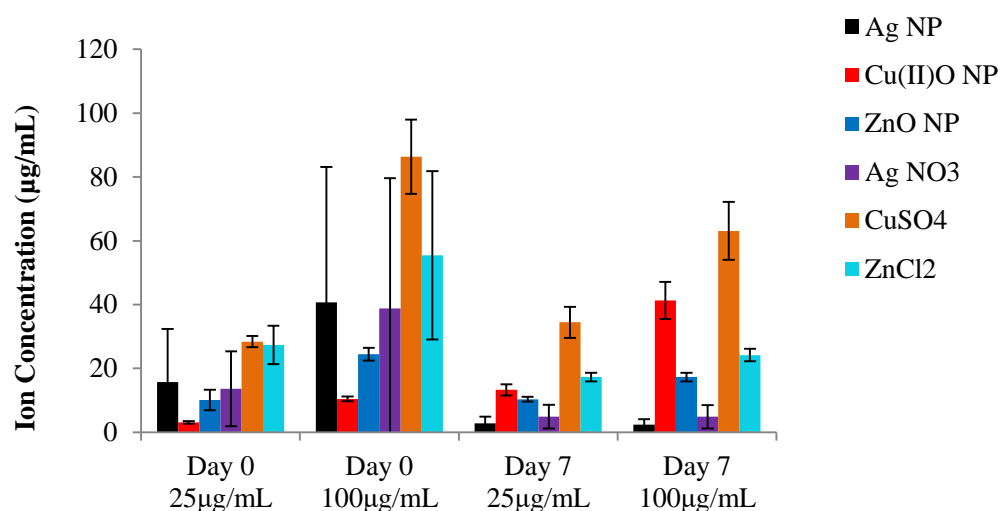


**Figure 4.4 Ionic analysis using ICP-OES: Assessment of dissolution of the NPs and salts in 7H9.** The solubility of ZnO and Cu(II)O NPs did not change over time and ion release was very low for all NPs. Data for Ag NPs was very variable and therefore not reliable. Overall, the results shown for the metal ion concentrations for Ag NPs, AgNO<sub>3</sub> and ZnCl<sub>2</sub> cast this method into doubt. Each point displaying SEM (n=4).

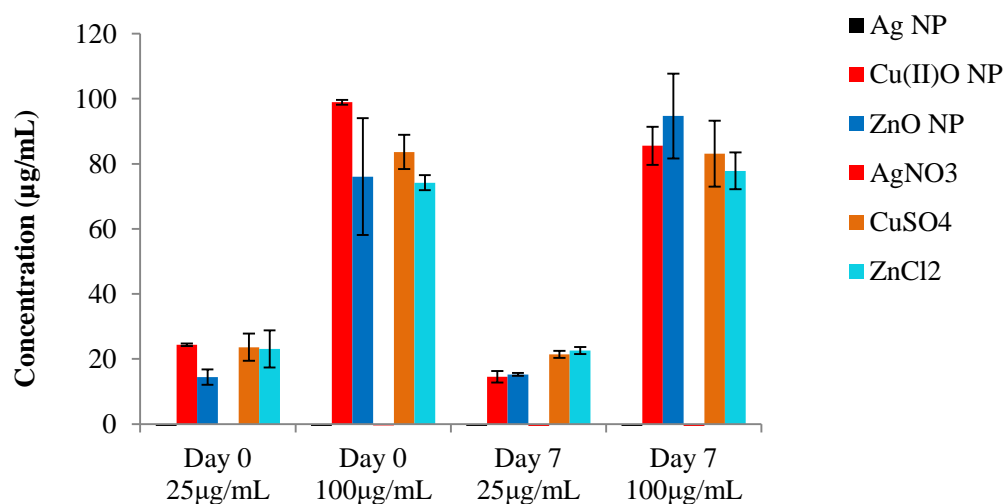


**Figure 4.5 A measure of the total amount of metal in each solution using ICP-OES.** The amount of metal detected for Cu(II)O and ZnO particle types generally reflects the concentration of NPs/metal salt added to 7H9. However, this method did not yield results for Ag NPs or AgNO<sub>3</sub>. Each point displaying SEM (n=4).



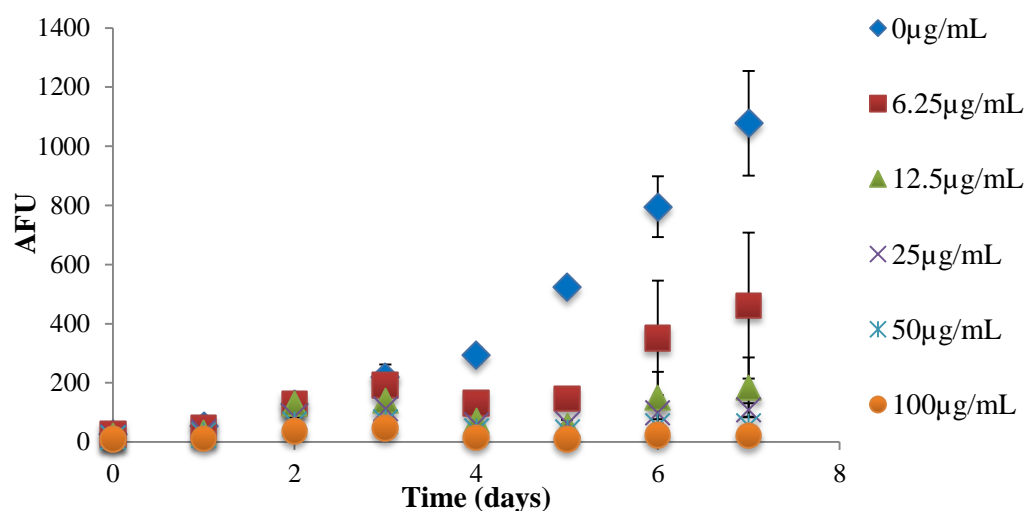
### 4.3.3 Anti-mycobacterial properties of NP

Following exposure to Ag, Cu(II)O or ZnO NPs, the growth of *Map* K10/GFP was inhibited in a dose and time dependent manner. The different stages of the data analysis for Ag NPs are presented in Figures 4.6 a-d, Table 4.5 and in Appendix A for Cu(II)O and ZnO NPs. The results are firstly presented as AFU plotted against time obtained on the GloMax® Multi<sup>+</sup> (Promega, UK) and presented using Excel (Microsoft Office Worksheet) as  $G = G_0 \cdot \exp(\beta t)$  (as previously described in Chapter 3 [section 3.3.4]) (Fig 4.6 a). The control well values (medium with NP but no bacteria) were subtracted from the experimental well values to exclude any NP interference in fluorescence readings.

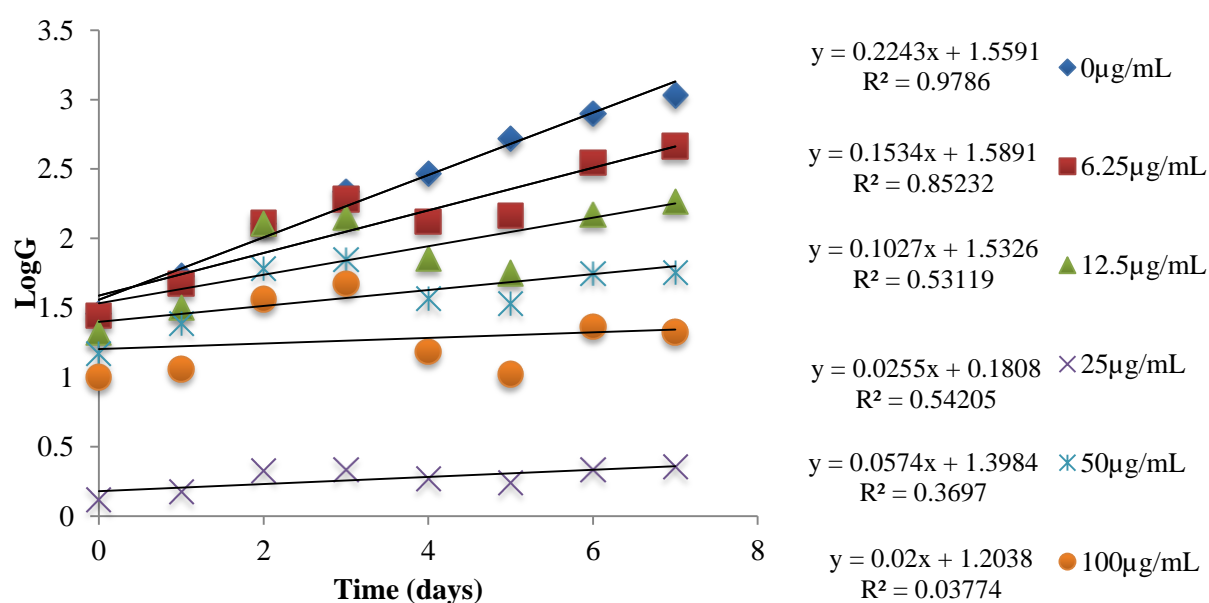
There was a clear dose dependent inhibition of the *Map* K10/GFP growth, observable within 3-4 days of exposure at concentrations as low as 6.25 µg/mL for Ag NPs (Figs 4.6 a-c). The raw data (Fig 4.6 a) indicates that at the highest concentration tested (100 µg/mL), Ag NPs affected mycobacterial viability after only 48 hours of incubation. This inhibition was also reflected in the log data, which displays the linear relationship from which  $\beta$  was calculated ( $\text{Log}G = \text{Log}G_0 + \beta t$ ) (Fig 4.6 b, Table 4.5). Figure 4.6 (c) depicts the transformed and normalised change in fluorescence data for Ag NP, allowing development of a dose response curve for Ag NP in this case, which could be replicated to allow comparison between all NPs.

Figure 4.7 depicts the 3 different NPs and their efficacy against *Map* K10/GFP over a 7 day period. Ag NPs were the most toxic, there was an obvious inhibition of growth even at the lowest concentration tested (6.25 µg/mL) and toxicity generally increased with concentration over time. Cu(II)O NPs seemed to enhance mycobacterial growth at the lowest concentration, toxicity slightly increased with concentration but fluorescence (the indicator of viability) was not inhibited below 50% by 100 µg/mL, unlike Ag NPs (Fig 4.7). ZnO NPs overall displayed little toxicity over the 7 day period, although these

particles were more toxic than Cu(II)O NPs at 6.25  $\mu\text{g/mL}$ , toxicity did not increase with concentration and fluorescence was not inhibited below 50% at any time point (Fig 4.7).



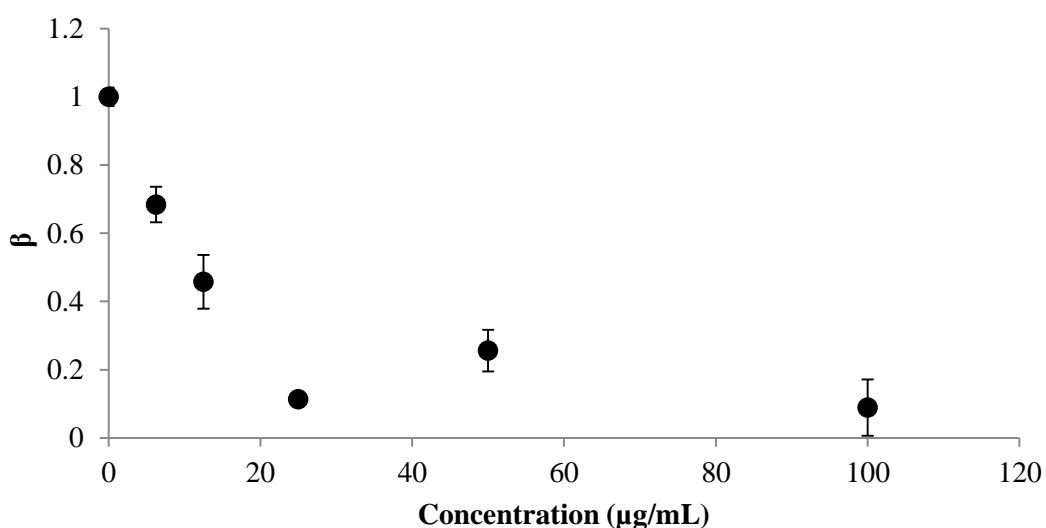
**Figure 4.6 (a) Viability Testing: Growth of *Map* K10/GFP with Ag NP (raw data).** *Map* K10/GFP grown in 200  $\mu$ L of 7H9 in a microplate format, with Ag NP at different concentrations (6.25-100  $\mu$ g/mL) over a period of 7 days, represented in the form:  $G = G_0 \cdot \exp(\beta t)$  (where  $\beta$  represents the change in fluorescence [representing mycobacterial growth] per day) using the raw data with each point displaying 2\* the SEM (n=6).



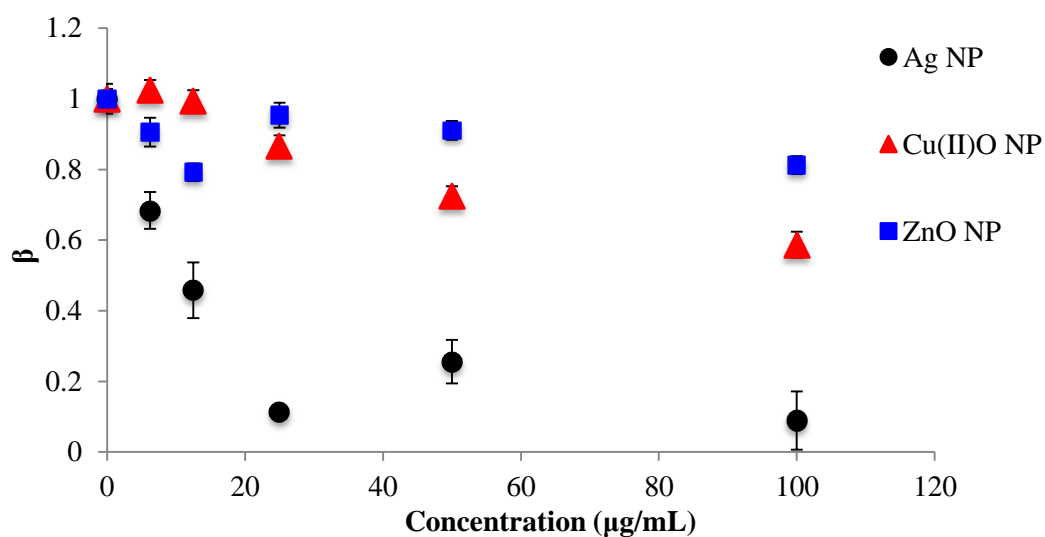
**Figure 4.6 (b) Data Transformation 1: plot of the Log data to determine  $\beta$ .** Linear regression analysis of *Map* K10/GFP growth with Ag NPs in the form  $\text{Log}G = \text{Log}G_0 + \beta t$  to calculate  $\beta$  (where  $\beta$  represents the change in fluorescence [representing mycobacterial growth] per day) (see Table 4.4).

**Table 4.5  $\beta$  Values calculated from the linear regression of the Log data from Figure 4.7 (b) normalised to the slope of the control (0  $\mu\text{g/mL}$ ) to plot Figure 4.7 (c).**

Concentration ( $\mu\text{g/mL}$ )	Slope of the line ( $\beta$ )	$\beta$ (Normalised)
0	0.2243	1
6.25	0.1534	0.683905
12.5	0.1027	0.457869
25	0.0255	0.113687
50	0.0574	0.255907
100	0.02	0.089166



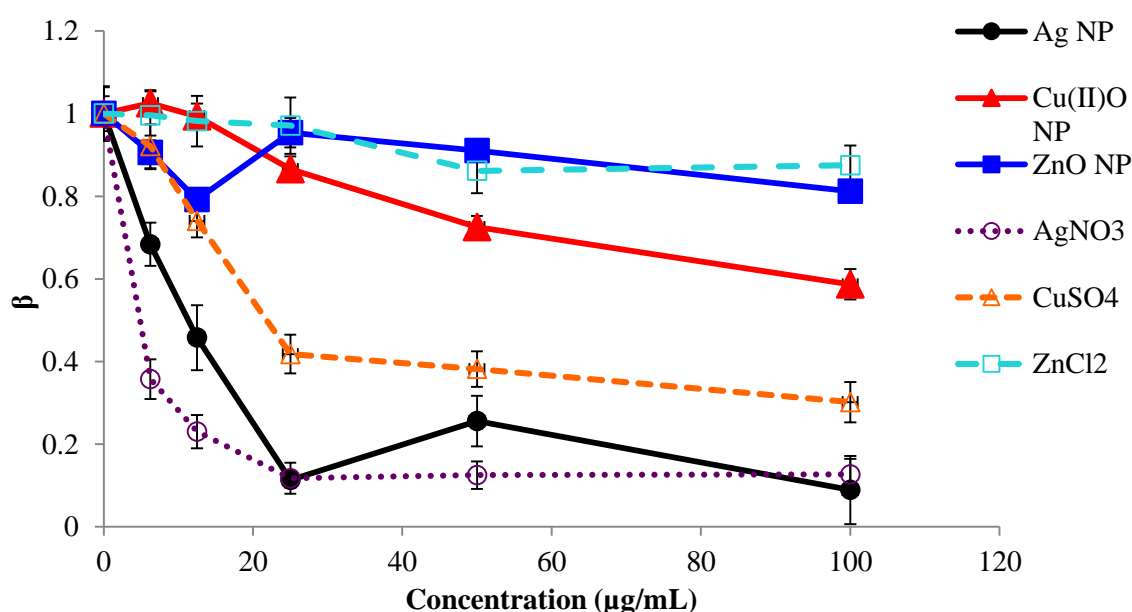
**Figure 4.6 (c) Data Transformation 2: Growth of *Map* K10/GFP with Ag NP normalised to the control.** Normalised, transformed data showing the growth of *Map* K10/GFP grown in 200  $\mu\text{L}$  of 7H9, in a microplate format, with Ag NP at different concentrations (6.25-100  $\mu\text{g/mL}$ ), normalised to the slope of the control (where  $\beta$  represents the change in fluorescence [representing mycobacterial growth] per day).  $\beta$  was calculated through linear regression analysis of the Log data (Figs 4.6 a, b, Table 4.4). Each point displaying 2\* the standard error calculated using LINEST function Excel (Microsoft Office Word) (n=6).



**Figure 4.7 Growth of *Map* K10/GFP with 3 NPs normalised to the control.** *Map* K10/GFP grown in 200 μL of 7H9 in a microplate format, with Ag, Cu(II)O and ZnO NPs at different concentrations (6.25-100 μg/mL) normalised to the slope of the control where  $\beta$  represents the change in fluorescence (representing mycobacterial growth) per day, with each point displaying 2\* the standard error, calculated using LINEST function Excel (Microsoft Office Word) (n=min of 3 for each NP type).

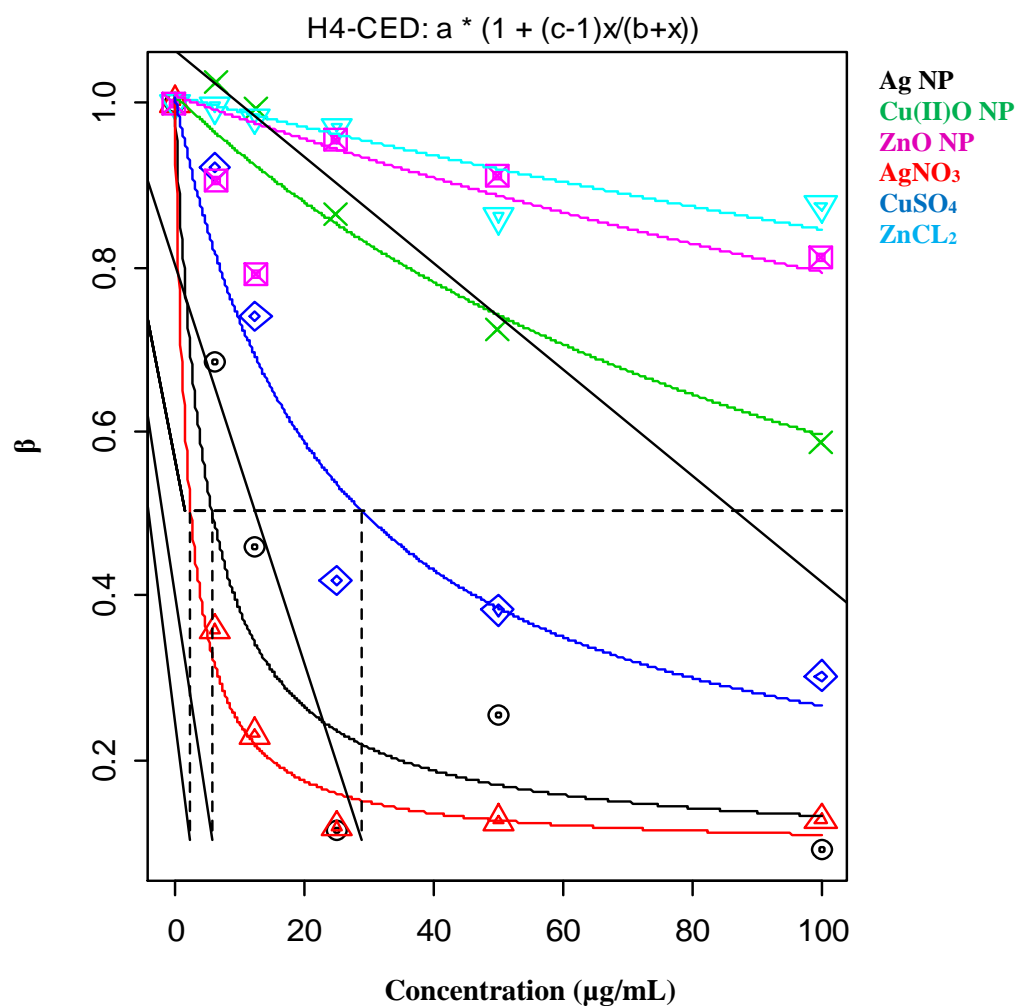
#### 4.3.4 Anti-mycobacterial properties of NPs compared with salt controls

Figure 4.8 depicts the efficacy of the 3 different NPs and their corresponding salt controls at inhibiting the growth of *Map* K10/GFP and it shows that there was a dose dependent inhibition of growth, with an obvious difference in efficacy between the different NPs and salt controls. Ag NP and AgNO<sub>3</sub> were highly toxic to the mycobacteria and very similar to each other in terms of their toxicity, whereas ZnO NP and ZnCl<sub>2</sub> both induced no significant toxicity over the 7 day period. Cu(II)O NP were less toxic to the mycobacteria than its salt control, as CuSO<sub>4</sub> inhibited growth at nearly all concentrations tested and was similar in toxicity to Ag NP/AgNO<sub>3</sub> by day 7 (Fig 4.9).



**Figure 4.8 NP v Metal Salt Efficacy against *Map* K10/GFP.** *Map* K10/GFP grown in 200 µL of 7H9 in a microplate format, with salts or NP at different concentrations (6.25-100 µg/mL) normalised to the slope of the control where  $\beta$  represents the change in fluorescence (representing mycobacterial growth) per day, with each point displaying 2\* the standard error, using LINEST function Excel (Microsoft Office Word) (n=min of 3 for each substance).

Figure 4.9 illustrates the relative growth rate of the mycobacteria (the  $\beta$  data plotted in PROAST [38.9]) on treatment with each of the NP (and salt controls) re-plotted in PROAST (38.9). This plot allowed the estimation of the  $EC_{50}$  for each substance and to determine whether the NPs and the salt controls differed significantly from each other (Fig 4.10, Table 4.6). Figure 4.10 shows the  $EC_{50}$  values with confidence intervals for each NP/salt control, plotted from Table 4.6. Comparing the confidence intervals for the 3 NPs it was clear that they did not overlap, therefore we could be reasonably confident that there was a significant difference between the 3 NPs and the 3 salt controls tested (Fig 4.10, Table 4.6). There was no significant difference between the Ag/ZnO NPs and both their corresponding salts however, which were very similar (Figs 4.9 & 4.10). The  $EC_{50}$  values for Cu(II)O NPs and CuSO<sub>4</sub> were significantly different, with the copper salt being more toxic (Figs 4.9 & 4.10). Using this analysis, the toxicity of the different NPs was ranked in the following order: Ag>Cu(II)O>ZnO.



**Figure 4.9 NP v Salt efficacy: comparison between NP and salt controls on the growth of *Map* K10/GFP NP normalised to the control, re-plotted in PROAST 38.9.** *Map* K10/GFP grown in 200  $\mu\text{L}$  of 7H9 in a microplate format, with salts or NP at different concentrations (6.25-100  $\mu\text{g/mL}$ ).  $\beta$  data obtained as described (Fig 4.7 a,b) and all substances were plotted using PROAST 38.9\* to allow comparison between NP and salts.

*\*please note PROAST 38.9 does not allow allocation of figure legend or choice of colours/symbols*



**Table 4.6** EC<sub>50</sub> value for each substance with the lower (CEDL) and upper (CEDU) 90% confidence intervals to plot Figure 4.11, derived from Figure 4.10.

Treatment	Ag NP	Cu(II)O NP	ZnO NP	AgNO <sub>3</sub>	CuSO <sub>4</sub>	ZnCl <sub>2</sub>
EC <sub>50</sub>	5.71	149	399	2.45	28.8	566
CEDL	3.11	22.5	180.3	0.75	7.2	184.1
CEDU	5.99	36.9	761	0.95	10.3	333

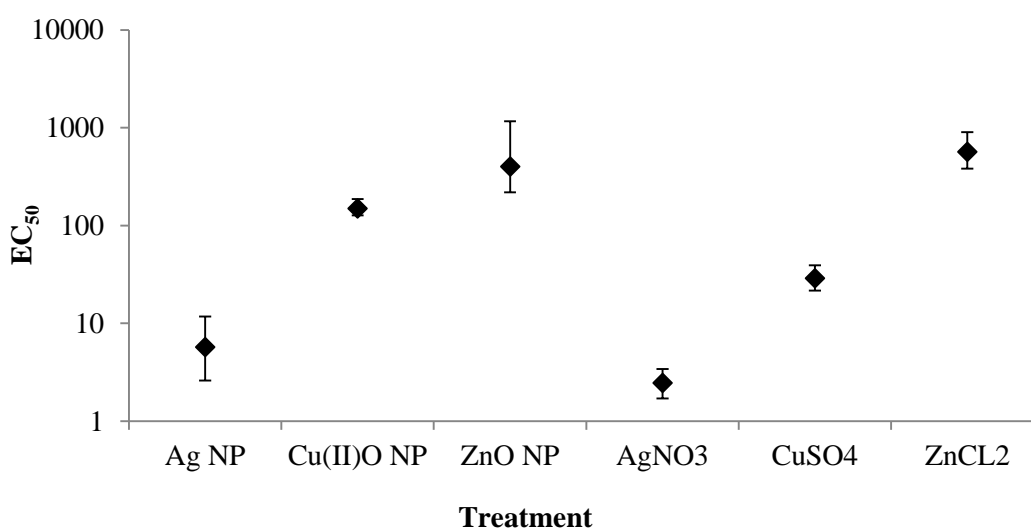


**Figure 4.10** The half maximal effective concentration (EC<sub>50</sub>) for each compound with the upper and lower 90% confidence intervals. Plot of the mean EC<sub>50</sub> values and corresponding confidence intervals (on the common logarithmic scale) for each treatment on the rate of mycobacterial growth.

#### 4.3.5 Colony Counts

Figure 4.11 depicts the growth of *Map* K10/GFP on solid agar after incubation for 12 weeks, following 7 day exposure to the NPs/salt controls. This experiment was conducted as a control alongside the fluorescence assay, as it is the conventional approach to assessing the impact of substances on mycobacterial growth. These results were in general variable and some were completely disregarded (e.g. due to signs of contamination or where counting individual colonies wasn't possible). From this data, Ag NPs and AgNO<sub>3</sub> have exerted the most toxicity against *Map* K10/GFP. Cu(II)O NPs and CuSO<sub>4</sub> were similar in their effects, unlike what was observed in the 7 day fluorescence assay. Interestingly ZnO NPs had an effect on mycobacterial growth after 12 weeks incubation on agar, whereas ZnCl<sub>2</sub> had very little effect on growth. Compared to the control plates, morphological differences were observed in colonies treated with NPs/salt controls. Generally colonies tended to be much smaller and less well defined, probably caused by stress, but this phenomenon did increase the variability when cell counting, as a 'pinpoint' colony was still counted as 1 along with a 'healthy' colony. Using the conventional method of toxicity testing it was clear that toxicity could be ranked in the same order, where: Ag>Cu(II)O>ZnO.

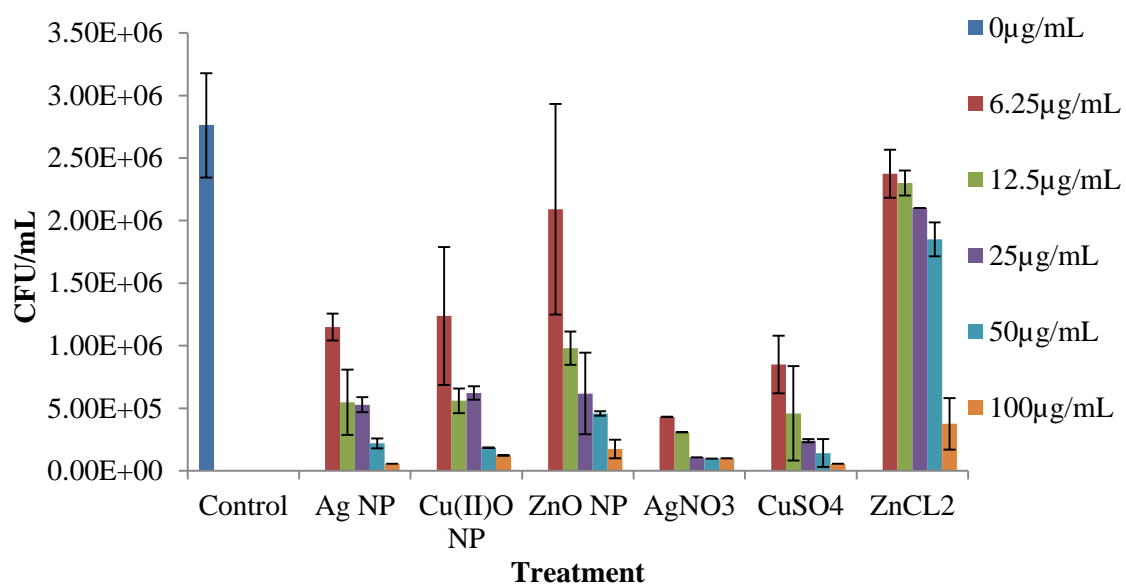
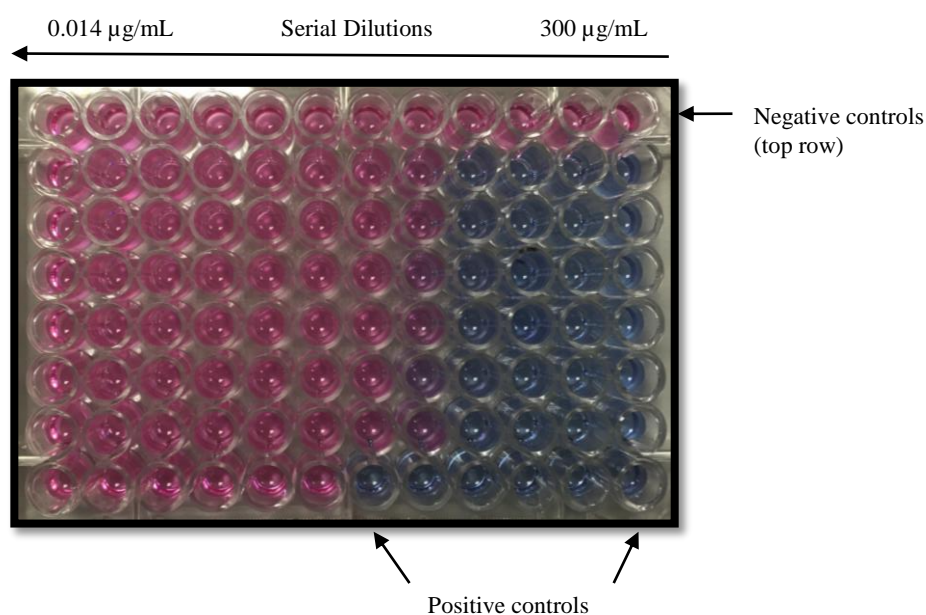


**Figure 4.11 Colony counts after 12 weeks culture on 7H11 agar.** Using conventional colony counts, the toxicity of the different NPs can be ranked in the following order: Ag>Cu(II)O>ZnO. Each concentration displaying the SEM (n=min of 3 repeats).

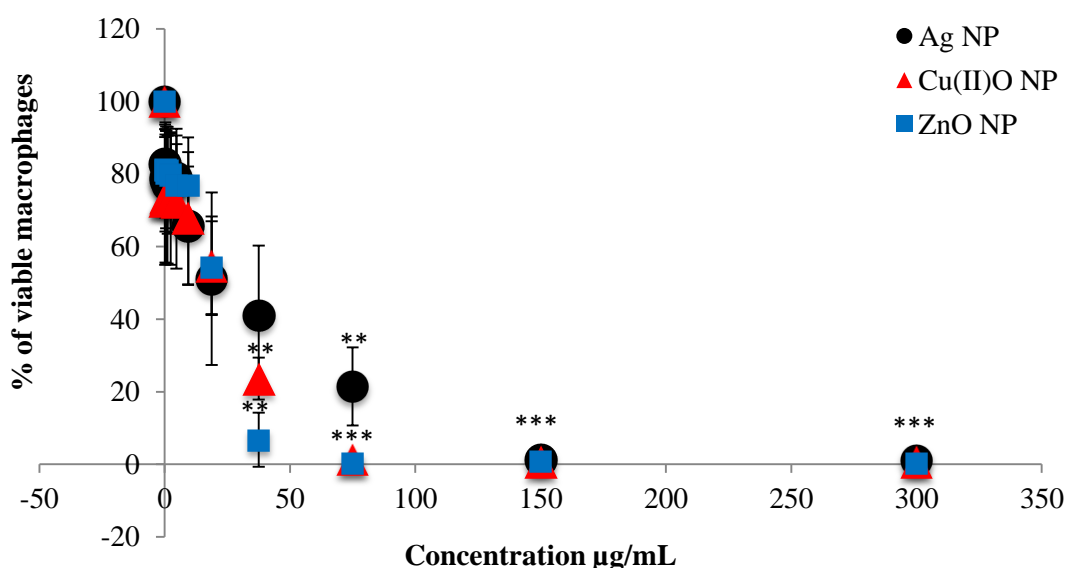
#### 4.3.6 Cytotoxicity of NPs to macrophages

Cytotoxicity was tested over a concentration range of 0.14 - 300  $\mu\text{g/mL}$ , by serial dilutions (plate set up, with controls, displayed in Fig 4.12) using the alamar blue assay (Chapter 2 [section 2.4]). Results were expressed by determining the mean value of the positive controls (0.1% triton) and subtracting this from the mean value of the negative controls (medium only [giving an overall mean control,  $n = \text{min of } 3$ ]). All readings were then divided by the overall mean control (negative control minus the positive control) and  $\times 100$ , to show toxicity by the % of cells viable at each concentration of NP/salt tested after 24 hours incubation. Figure 4.13 illustrates that cytotoxicity of the three NPs was relatively cytotoxic and very similar. Statistical significance was first determined using an analysis of variance (ANOVA) test, which found an overall high level of significance ( $p < 0.001$ ), therefore, each NP was considered separately to compare each concentration between particle types via a student's t-test (2 sample t-test) (MINITAB®, version 17). Results were considered significant if  $p < 0.05$  (significance level was denoted by:  $p < 0.001$  [\*\*\*],  $< 0.01$  [\*\*] and  $< 0.05$  [\*]).

All three NPs were found to be cytotoxic to the macrophages. Concentrations  $> 37.5 \mu\text{g/mL}$  decreased cell viability to below 50% and differed significantly from the control (0  $\mu\text{g/mL}$ ) for Cu(II)O and ZnO NPs. There was an obvious colour change (from blue to pink) in the highest four concentrations tested (300, 150, 75 and 37.5  $\mu\text{g/mL}$ ), then the colour change became more subtle as the concentrations decreased (Fig 4.13).



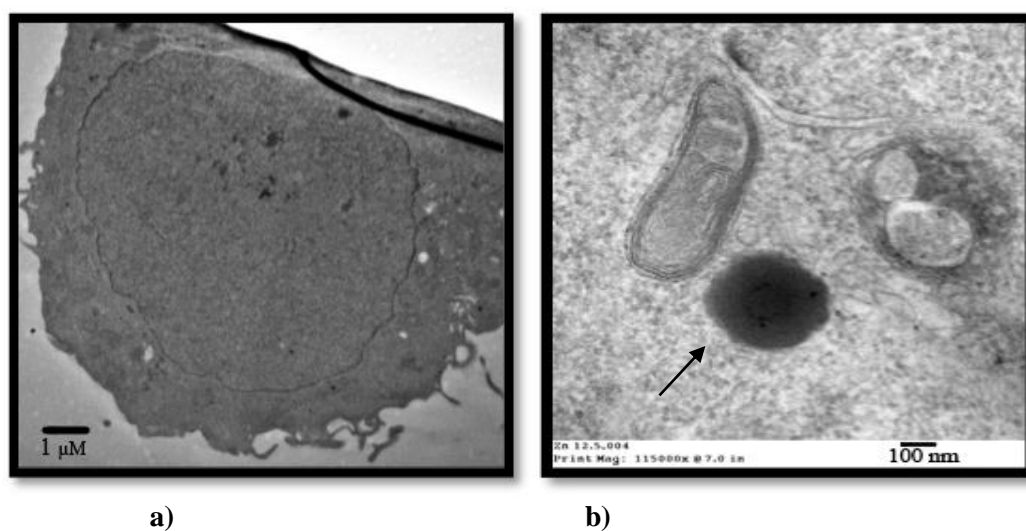
**Figure 4.12 NP cytotoxicity 96 well plate following 24-hour incubation with ZnO NPs (alamar blue assay).** Where the blue colour is visible, cells were no longer viable thus representing cell death, detected upon fluorescence readings. As shown in the negative control and lowest NP concentration wells, a strong colour change is evident, from blue to pink.



**Figure 4.13 NP cytotoxicity to macrophages after 24-hour incubation.** All NPs display a similar level of cytotoxicity, decreasing cell viability below 50% from 37.5 µg/mL of each NP type. Significance level is denoted by:  $p < 0.001$  (\*\*\*),  $p < 0.01$  (\*\*) and  $p < 0.05$  (\*). Each concentration displaying the SEM (n=3).

#### 4.3.7 Imaging macrophages following treatment with metal/metal oxide NPs

High-resolution TEM images were obtained of *Map* K10/GFP infected macrophages, treated with NPs. In each case, cells were infected and treated for 4 hours with NPs at a concentration of 12.5  $\mu\text{g/mL}$ . Figure 4.14 (a) illustrates the control; untreated and non-infected macrophages by TEM, and (b) highlights a common problem when imaging macrophages treated with NPs by TEM, the precipitation of heavy metals in the staining process creating dark stains which can be misinterpreted. Please note the difference in scales.



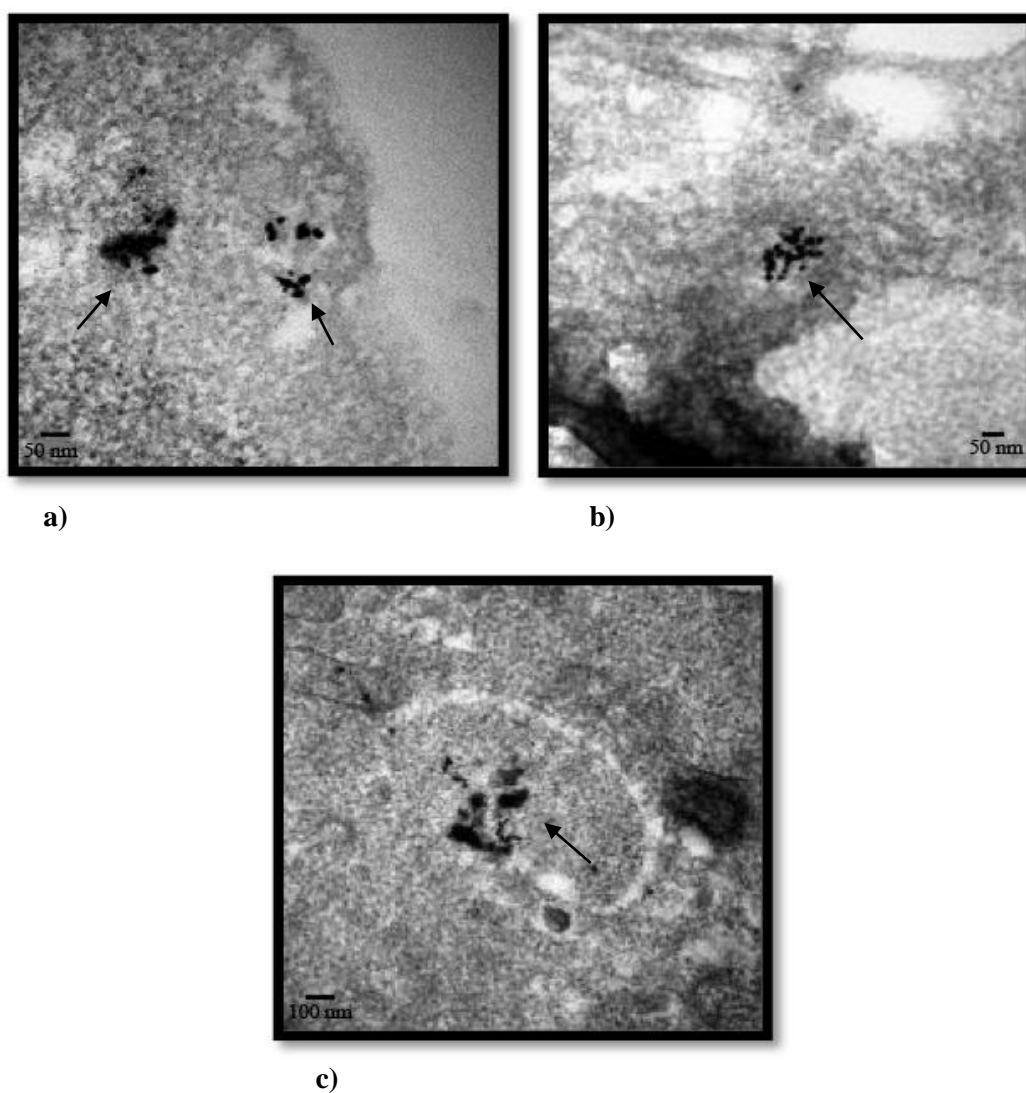
**Figure 4.14 Macrophages by TEM (TEM magnification ranging from 30-90K) (note the different scale bars).** (a) depicts a macrophage and (b) the staining process for TEM uses heavy metals (e.g. lead, uranium) that can precipitate out, which can be wrongly interpreted as NPs as indicated by the arrow.

Figure 4.15 (a-c) illustrate *Map* K10/GFP infected macrophages following 4 hour treatment with Ag NPs at 12.5  $\mu\text{g/mL}$ . It appears that the NPs (of different sizes [possibly metal ions]) were engulfed by the macrophages, as shown in Figure 4.15 (a-c). Figure 4.15 (e) shows the NPs within a cellular organelle, possibly a lysosome.

Figure 4.15 (d-f) illustrate *Map* K10/GFP infected macrophages following 4 hour treatment with Cu(II)O NPs at 12.5  $\mu\text{g/mL}$ . The TEM images (d-f) illustrate what looked to be engulfed NPs, and their location throughout the cell. Figure 4.15 (f) shows a structure that could be associated with cell damage (possible evidence of cellular contacts seeping out). This was a common pattern observed for macrophages treated with Cu(II)O NPs.

Figure 4.15 (g-i) illustrate *Map* K10/GFP infected macrophages following 4 hour treatment with ZnO NPs at 12.5  $\mu\text{g/mL}$ . TEM indicates that the ZnO NPs had no toxic effect on macrophages. No pits, or damage to the cytoplasm was observed. Figure 4.15 (h-i) illustrate what is possibly a lysosome, with internalised ZnO NPs. By increasing the magnification, a black mass of possible ZnO NPs was observed inside the cellular organelle (Fig 4.15 i).

Unfortunately in all cases, mycobacteria were not detected within NP treated macrophages. It also must be considered that what was assumed to be damage to the macrophages could actually be cellular uptake, whereby the membrane is forming around NPs to internalise them. This was deemed unlikely as many cellular fragments were imaged thus suggesting cell death, but should be considered.



**Figure 4.15 (a-c) Macrophages following treatment with Ag NPs (12.5  $\mu\text{g/mL}$ ) (TEM magnification ranging from 50-90K) (note the different scale bars). From these images, it is assumed that it is Ag NPs which are visible, but as Energy Dispersive X-Ray (EDX) Spectroscopy analysis was not carried out, this could not be confirmed.**

- a) Macrophage with possible intracellular Ag NPs (see arrows), showing the likely precipitation of  $\text{Ag}^+$  from NPs.
- b) Macrophage with intracellular Ag NPs (see arrow), NPs appeared to be slightly agglomerated, although individual structures can be viewed.
- c) Macrophage with intracellular Ag NPs inside a vacuole, possibly a lysosome (see arrow).



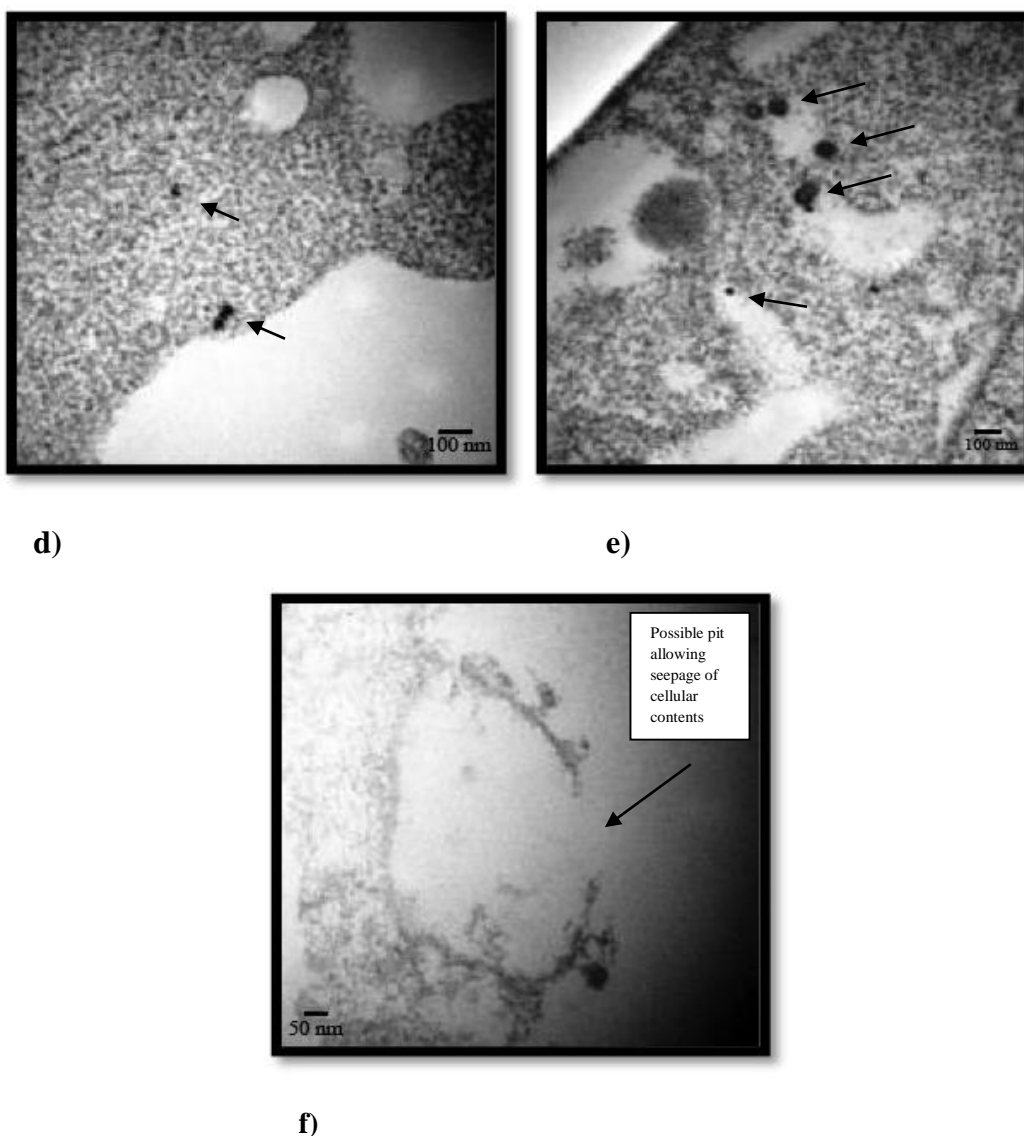


**Figure 4.15 (f-h) Macrophages following treatment with Cu(II)O NPs (12.5  $\mu\text{g/mL}$ ) (TEM magnification ranging from 50-90K) (note the different scale bars). From these images, it is assumed that it is Cu(II)O NPs which are visible, but as EDX Spectroscopy analysis was not carried out, this could not be confirmed.**

- d) Macrophage with possible intracellular Cu(II)O NPs (see arrows). The NPs are much smaller than previous TEM images (of NPs in medium), thus suggesting these were precipitated  $\text{Cu}^{2+}$  rather than NPs.
- e) Macrophage with intracellular Cu(II)O NPs (see arrows), where NPs appeared to be internalised within a vacuole or were causing structural damage to the cell by creating pits/holes.
- f) Macrophage with structural damage (to the cellular cytoplasm [see arrow]), likely caused by the Cu(II)O NPs. Conversely, this could be a membrane forming around particles to make a phagosome. Additionally, this could be the formation of an extracellular trap by NETosis.

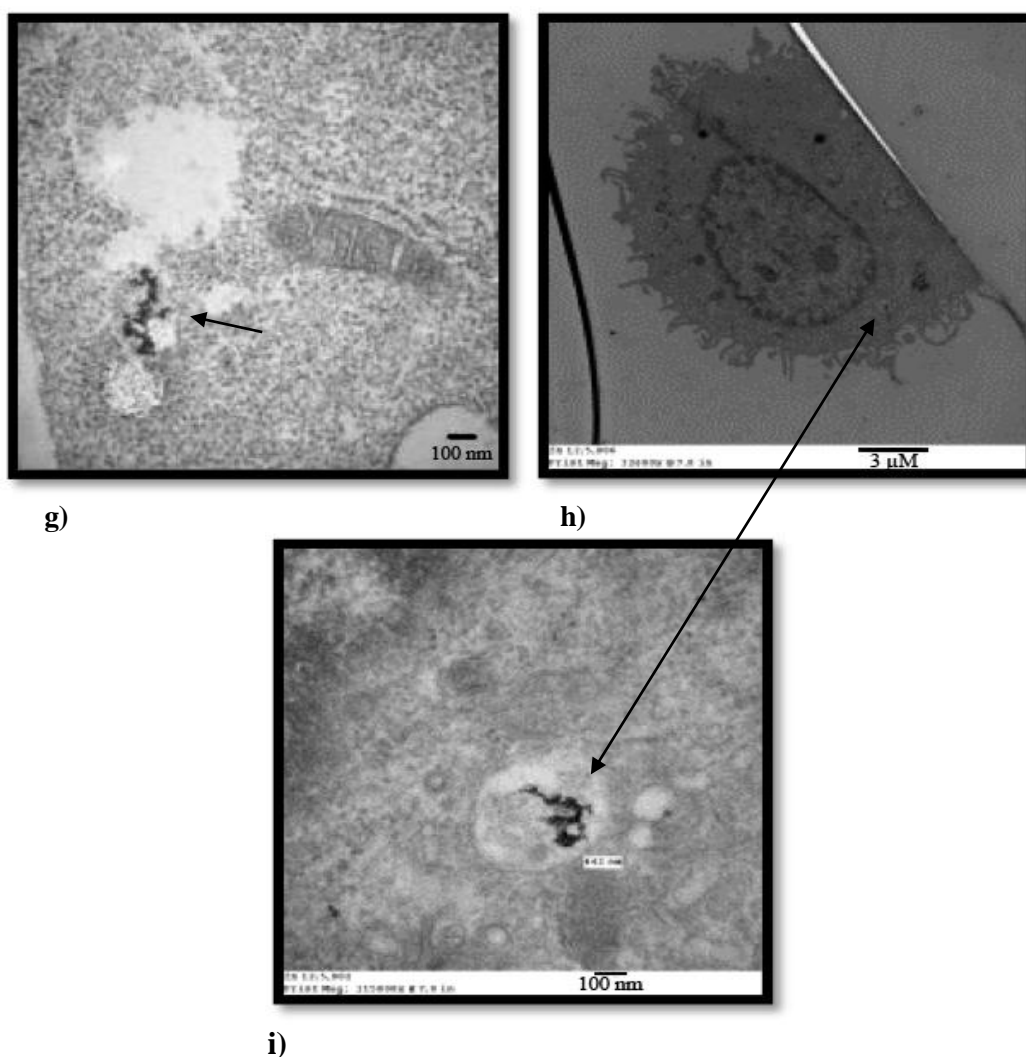


**Figure 4.15 (i-k) Macrophages cells following treatment with ZnO NPs (12.5  $\mu\text{g/mL}$ ) (magnification ranging from 30-90K) (note the different scale bars). From these images, it is assumed that it is ZnO NPs which are visible, but as EDX Spectroscopy analysis was not carried out, this could not be confirmed.**

- g) Macrophage with possible intracellular ZnO NPs (see arrows), again depicting NPs within a cellular vacuole.
- h) Macrophage with intracellular ZnO NPs. The nucleus and other cellular organelle are visible. The arrow indicates to a vacuole, which was possibly a lysosome.
- i) A magnified view of (j), with the arrow indicating what looks to be internalised, agglomerated ZnO NPs within a vacuole, possibly a lysosome.

DIC channel images (DAPI stained) taken on a Zeiss Axiovert 200M inverted Epi fluorescence microscope (Zeiss, Cambridge, UK) to display information on the macrophage surface morphology (see Chapter 5 for further details on this type of imaging) are displayed below (Fig 4.16 a-c). The fluorescent microscope images depict uninfected cells treated with NPs. These NPs were not labelled therefore they were not detectable by fluorescent microscopy, and what was observed appears to be damage to the macrophage cytoskeleton or ‘shadows’ created by agglomerates.

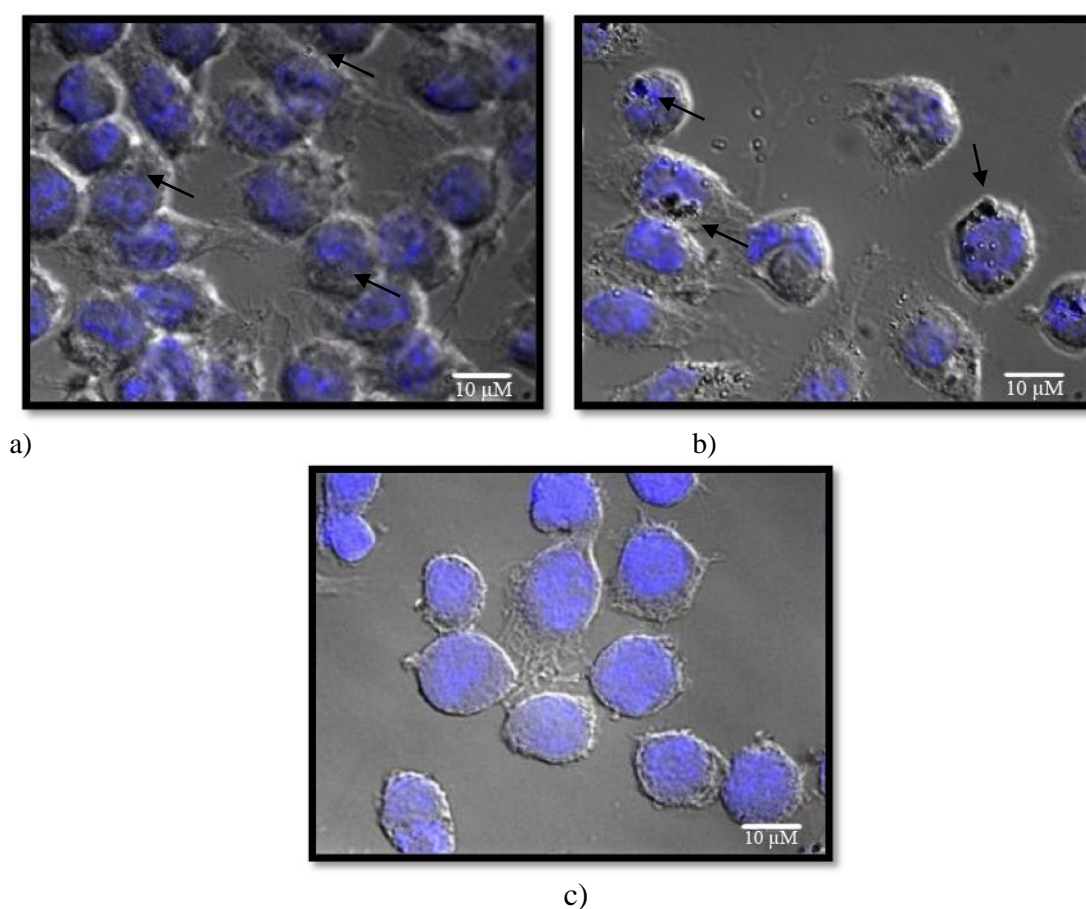


**Figure 4.16 NP treated (12.5 μg/mL) macrophage by fluorescence microscopy (63 X magnification)**

- a) Macrophage with arrows indicating possible cytoskeleton damage (pit formation) or agglomerated Ag NPs.
- b) Macrophage with arrows indicating either possible cytoskeleton damage (pit formation) or agglomerated Cu(II)O NPs.
- c) Macrophages with no visible signs of cytoskeleton damage following treatment with ZnO NPs.

Figure 4.17 (a) depicts TEM images of *Map* K10/GFP. The mycobacteria were not detected intracellularly, but were found adhered to macrophage fragments, possibly following macrophage lysis. Figure 4.17 (a) clearly showed the waxy, rough cell wall structure of *Map* and intracellular vacuoles or inclusions were evident. Interestingly, one of the *Mycobacterium* cells had small, dark masses, which were comparable to the Cu(II)O NPs (below images were obtained from Cu(II)O NP treated macrophage slides). These dark spherical structures were easily detected by TEM and were suggestive of metal NPs, all being <100 nm in diameter, and very solid entities.

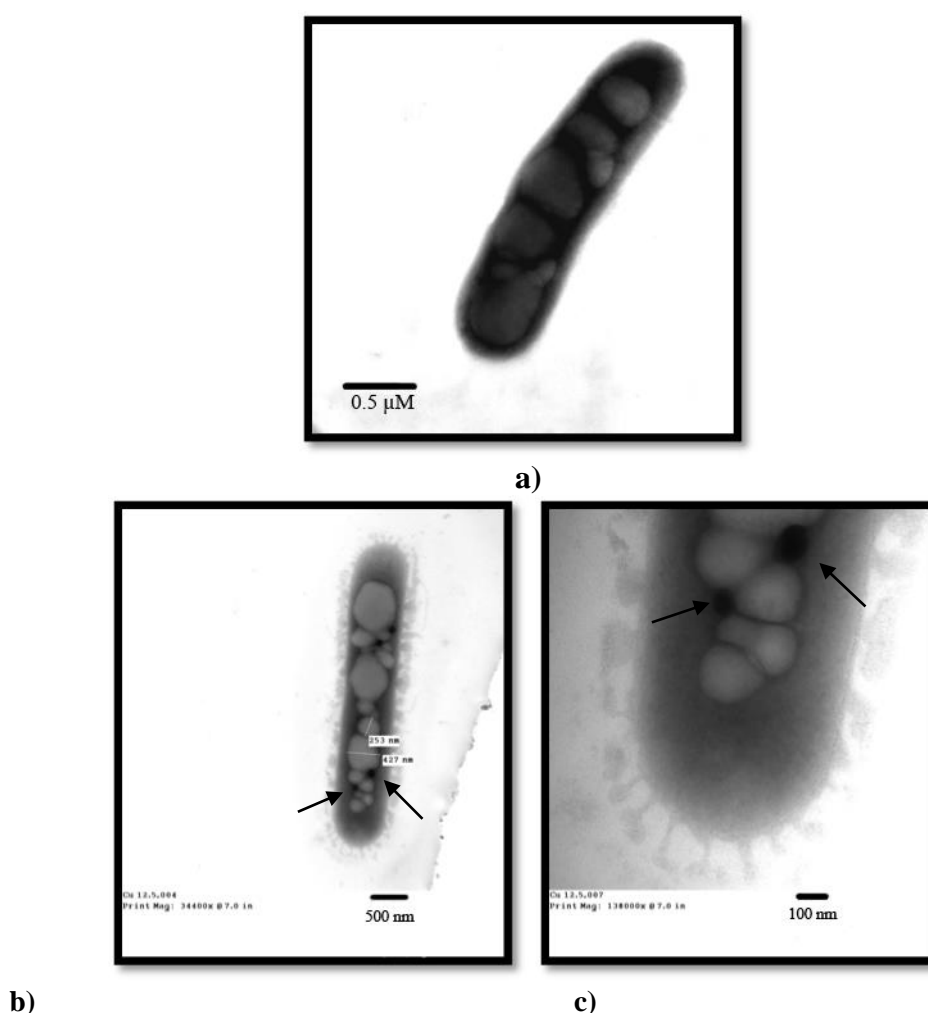


**Figure 4.17 *Map* K10/GFP by TEM (magnification ranging from 35-38K)**

- (a) A clear picture of *Map* with internal vacuoles visible.
- (b) Black areas indicated by arrows are possibly intracellular Cu(II)O NPs.
- (c) Magnified view of (b) where possible NPs are indicated by arrows.

#### 4.4 Discussion

The anti-microbial properties of NPs, resulting from unique characteristics are well documented (Mohanty et al. 2013; Morones-Ramirez et al. 2013; Chatterjee et al. 2014; Pandey & Khuller 2006; Park et al. 2009) yet this knowledge base is limited regarding the impact of metal/metal oxide NPs on pathogenic mycobacteria (Larimer et al. 2014; Islam et al. 2013). Therefore, it was important to test their effects. Based on results, the NPs tested in this study varied in their toxicity against *Map* K10/GFP and could be ranked in the following order: Ag>Cu(II)O>ZnO. As expected Ag NPs (and corresponding salt control [AgNO<sub>3</sub>]) were the most toxic to the mycobacteria. Cu and Zn are essential elements for biological systems, playing pivotal roles in cell physiology (Pasquet et al. 2014), therefore their uptake into cells is relatively well regulated. At higher concentrations they act as toxicants, observed at concentrations 25 µg/mL and above, where growth was inhibited. These 3 NPs all have similarities; reported anti-bacterial properties, negative surface charges and solubility in aqueous environments (to some extent). The differences in anti-mycobacterial activities for each particle type were interesting and will be discussed relating to the results obtained and the experimental conditions of this study.

The toxicity of NPs is often related to particle size, as uptake and distribution are size dependent (as well as surface reactivity) (Ruparelia et al. 2007; Johnston et al. 2012). The TEM images illustrated well-dispersed, spherical Ag NPs in 7H9, measuring <50nm in diameter. Imaging the Ag NPs in distilled water further supported this result which agrees with other studies (Johnston et al. 2015). The images suggest a wide range of Ag NP sizes, and perhaps two populations of particles. The difference in appearance of the smallest particles observed in the Ag NPs suspension suggests they may have been generated via precipitation of dissolved Ag<sup>+</sup> ions as silver salts, as was observed in both

7H9 and distilled water. This would further contribute to the toxicity exhibited by the Ag NPs.

In contrast to the Ag NP, TEM illustrated that both Cu(II)O NP and ZnO NP were agglomerated and/or aggregated in 7H9. This could be an artefact of the drying procedure prior to TEM analysis; however, this observation was further supported by the DLS measurements of hydrodynamic diameter. TEM of NPs in 7H9 was originally carried out at two concentrations (25 and 100 µg/mL) only in 7H9. However, as individual particle size/shape was not visible for both Cu(II)O and ZnO NPs due to agglomeration, this was repeated at 100 µg/mL in DW. Micrographs of Cu(II)O NPs in DW displayed less agglomerated particles, thus suggesting that components of the 7H9 medium caused this phenomenon, whereas ZnO NPs were found to be highly agglomerated in both water and media. ZnO NPs are reported to have very fast agglomeration rates in aqueous environments (Odzak et al. 2014), as found in this study. One potential explanation for the relatively high toxicity of Ag NPs compared to the Cu(II)O and ZnO NPs, might be their better dispersion and hence smaller agglomerate size. For Cu(II)O and ZnO NPs their agglomeration could reduce the interaction with mycobacteria in terms of uptake and surface area available to interact with the mycobacteria in the medium, thus being a possible contributing factor to the relatively low toxic effects exerted by these NPs (particularly ZnO) over the 7 day period. TEM and DLS data generally complement each other, but DLS tends to give a clearer view of what is happening to NPs in any given solution.

Overall, the ICP-OES data yielded results that make it difficult to have confidence in them. The results suggest that there was no Ag in the solutions and there was little ion release from all NPs tested in the experimental conditions. It is possible that the NPs were interacting with organic material in 7H9 (e.g. proteins) preventing analysis, as well-established protocols were employed in this process. It seems likely that the 7H9 medium

interfered with the procedure by either preventing accurate detection of the NPs, or the NPs were not fully dissolved in the nitric acid. These studies could have been repeated in DW; however as the NPs were added to the mycobacteria in the 7H9, such results would not have given any further insight to ion release/metal content in the assay conditions. Furthermore, it was hard to compare these results to those in the literature as most studies prepare NPs in distilled or deionised water and not a complex growth medium such as 7H9. The following text draws some limited suggestions, rather than conclusions, from the data obtained here.

When NP are in an aqueous environment one factor that can influence the rate of ion release is the pH of the medium/liquid (Mumper et al. 2013) (other factors [e.g. temperature] will also play a role). As the pH of an aqueous solution becomes more acidic, the dissolution rate has been reported to increase (Mumper et al. 2013). The pH of 7H9 is  $6.9 \pm 0.2$ , the medium thus being a very weak acidic/neutral solution, and would likely not affect ion release from the NPs significantly. All the NPs types used in this study were reported to be soluble (Bondarenko et al. 2013b) but using the protocols employed in this study it was not possible to accurately assess Ag NP dissolution in these experimental conditions. The problems in analysis could be accounted for by the fact that Ag has a long wash out time, as it tends to be retained in the pump of the ICP-OES (personal communication with laboratory technician Dr Lorna Eades, School of Chemistry, University of Edinburgh). Alternatively it is possible that the medium interfered with the analysis. Due to this, it was not feasible to ascertain whether  $\text{Ag}^+$  ions contributed to the toxicity of the Ag NP. However, the relative toxicity of the Ag NP and the  $\text{AgNO}_3$  were comparable, suggesting that either the NPs completely dissolved during the exposure or that neither would dominate the mechanism of Ag NP induced toxicity. Previous studies have ascertained that solubility of the NM300 Ag NP to be less than 1%

(Kermanizadeh et al. 2012), whereas others reported that bacterial toxicity of Ag NPs is related directly to the amount of soluble Ag released from the NPs (Zhao & Wang 2012).

The ICP-OES data suggested that the Cu(II)O NP were the most soluble NP tested in the conditions used for this study. The CuSO<sub>4</sub> was more toxic than the Cu(II)O NP over 7 days, suggesting that Cu<sup>2+</sup> are toxic to *Map* K10/GFP cultures. Dissolution has also been reported to play an important role in the toxicity of ZnO NPs (Brunner et al. 2006; Pasquet et al. 2014) with ZnO usually having a very fast dissolution rate, releasing Zn ions (Zn<sup>2+</sup>) and leaving few to no particles detectable after 2 hours in aqueous medium (Odzak et al. 2014). A relatively slow dissolution rate in 7H9 was observed; possibly contributing to the low toxicity of the ZnO NP, yet dissolution cannot be attributed to toxicity alone. Another report found that the NP was the mediator of toxicity (to THP-1 cells) and released metal ions were not solely responsible (Prach et al. 2013). The ZnO NP and the ZnCl<sub>2</sub> salt solution were remarkably similar in terms of their toxicity to the *Map* K10/GFP cultures. Taken together, this data would suggest that the NPs alone or both the NPs and the metal ions contribute to the low levels of toxicity exerted by ZnO NP, possibly with neither inducing a dominant effect.

The alamar blue assay demonstrated that all three NPs were cytotoxic to the macrophages from concentrations >30 µg/mL. The overall cytotoxicity, including the nature of the dose response curves were very similar in respect to each other. Results for the Ag NPs were akin to another project, where macrophage viability was reduced by 50% at the higher concentrations for similar sized particles (from 50 µg/mL) (Arai et al. 2015). Gaiser *et al.*, (2013) reported an EC<sub>50</sub> of 20 µg/mL for Ag NPs (NM 300) via the alamar blue assay, again similar to the results generated in this project. It was surprising that the ZnO NPs were so cytotoxic to these cells after 24 hours treatment if compared to the effect they had after 7 days incubation with the mycobacteria and a previously published data set (Prach et al. 2013). These results are important to consider if these NPs were



ever to be incorporated into clinical use (primary cell lines should be investigated and *in vivo* testing would be the next steps).

Following 4 hour treatment with the NPs, TEM was used to determine whether the NPs were engulfed by infected macrophages and if so, where the NPs were localised within the macrophages and if they co-localised with mycobacteria. Fluorescent microscopy was utilised to determine whether NP agglomerates could be observed intracellularly. Both methods were used to gain a better insight into the behaviour of the NPs in an intracellular environment and to determine whether any damage to the macrophages was visible (to compliment the alamar blue results).

Unfortunately, the TEM methods employed did not produce visualisation of mycobacteria within a macrophage. This may have been caused by a number of factors. Firstly the mycobacteria may have been damaged beyond recognition following close contact with the NPs within an intracellular environment or they were already within a phagolysosome complex and undetectable. As control slides (with only macrophage infected with *Map* K10/GFP) also did not offer any results (only macrophages were visible), it is likely that the sample fixation and preparation processes rendered the mycobacteria impossible to view by this means. As discussed later in Chapter V, macrophage infected with mycobacteria were imaged successfully using fluorescence microscopy therefore it suggests that this was caused by the sample processing, and mycobacteria were present but unable to be visualised. Only images of extracellular mycobacteria were identified. As stated in the results, it appears that a *Mycobacterium* may have had internalised Cu(II)O NPs, which would concur with speculation that NPs are toxic through their internalisation of bacterial cells. As only one image of this was obtained, it does not hold any statistical significance, but it was exciting to observe and may offer more of an insight into how NPs might be toxic to mycobacteria.

The fluorescent microscopy yielded interesting images. It is possible that the dark masses observed on and around some of the macrophages were a shadow effect created by NPs or NPs were agglomerating enough to be detected, but individual NPs would not be visible as the microscope utilised had a plan apochromat 63 X lens with a numerical aperture of 1.4, thus preventing resolution for anything below 0.3  $\mu\text{m}$ , or more. Apparently something impacting on the macrophage cytoskeleton/membrane was detected, such as pits and burrows, caused by the NPs as previously observed (Yuan et al. 2012; Feng et al. 2000). Thus, it was hard to conclude what was observed in these images.

In the case of treatment of NPs on macrophage, images of what seemed to be engulfed NPs were obtained, particularly for the Ag and ZnO NPs. These could have been intact NPs or partially dissolved NPs. In each case, they seem to be internalised within a cellular organelle, possibly a lysosome; the organelle where mycobacteria reside, thus being a desirable site for the toxic Ag NPs to be trafficked to by macrophage cells. EDX analysis would be useful to confirm this.

Counting colonies of *Map* K10/GFP was difficult as clumping occurred readily and therefore it was very hard to distinguish between a single colony or a clump of colonies. Additionally, colonies from cultures which had been exposed to NPs/salt controls were generally very small. This was probably because the cells were sub-lethally stressed and/or damaged and they may have had trouble multiplying, resulting in pinpoint-like colonies, but 1 of these colonies counted the same as 1 'healthy' colony from the control plates (which was much larger and morphologically different). This data did agree with results from the fluorescence assay however, even with the variation in colony size/morphology observed.

#### 4.4.1 Ag and AgNO<sub>3</sub>

Ag NP are reported to have anti-bacterial properties against many bacterial species (Park et al. 2009; Ansari et al. 2011; Islam et al. 2013) and as shown, exhibited a very potent effect on this *Mycobacterium* species. Most Ag NPs studies use AgNO<sub>3</sub> as a control when testing toxicity against bacterial species, and some found the salt control less toxic to bacterial species (Lok et al. 2007; Pal et al. 2007) whereas some found the salt more toxic than the NPs (Besinis et al. 2014; Jiang et al. 2012) and/or the difference in toxicity was related to exposure length (Völker et al. 2013). In this study, the Ag NPs and salt were not statistically different in terms of their toxicity against *Map* K10/GFP. ICP-OES data did not offer information on the dissolution of silver, and as there are mixed reports in the literature on its solubility, we can only assume that toxicity could include either ion and/or particle mediated mechanisms. It is known that Ag<sup>+</sup> (from NP or salt) damage bacterial cell walls, and as anti-mycobacterial drugs target the cell wall, it is likely that Ag<sup>+</sup> causes structural damage to cell wall components (e.g. mycolic acids), either through entering the cell or by adhering to the outer structure causing rupturing. Ag<sup>+</sup> may also cause protein misfolding and aggregation through interaction with sulphhydryl groups, as aforementioned, which are present in many proteins and hence disrupt multiple cellular processes including disruption of internal iron homeostasis (Morones-Ramirez et al. 2013).

As NM 300 Ag NPs were supplied in dispersion before serial dilutions in 7H9 were made, it is feasible that the amount of individual Ag NPs in the different concentrations would have varied between experiments, thus adding variation to the data sets (e.g. DLS, toxicity testing) as observed in some of the raw data. Furthermore, ion release from these NPs could have been hampered due to the Polyoxylaurat Tween 20 cap, as another study found that any coatings could directly affect ion release (Zhao & Wang 2012). Some coatings

can prevent aggregation of NPs, therefore increasing the surface area exposure (Sharma et al. 2009). Additionally, these were spherical NPs, but many reports state that variable and truncated NPs are more toxic (Pal et al. 2007; Zhao & Wang 2012), therefore it would be interesting to test different shaped and uncoated or capped NPs against *Map* K10/GFP to determine whether they are more or less toxic.

Unlike Cu and Zn, Ag is not an essential element in biological systems and it is not required for any cellular processes. It is known that Ag NPs can be engulfed by macrophages and localised in the lysosome, giving an advantage over bulk Ag and Ag salt (Fig 4.18). Therefore these are very interesting NPs to consider for mycobacterial infections. A Nature news publication titled '*Silver makes antibiotics thousands of times more effective*' briefly discusses the benefits of the metal's use and the advantages it offers in combating antibiotic resistance (Owens 2013a). Ag has the potential to become common place in clinical medicine, however, the use of Ag as a treatment against infections need to be used with caution as there would be implications for toxicity against mammalian cells, genotoxicity and the accumulation of Ag in non-target organs such as the liver (Gaiser et al. 2013; Pinto et al. 2013).

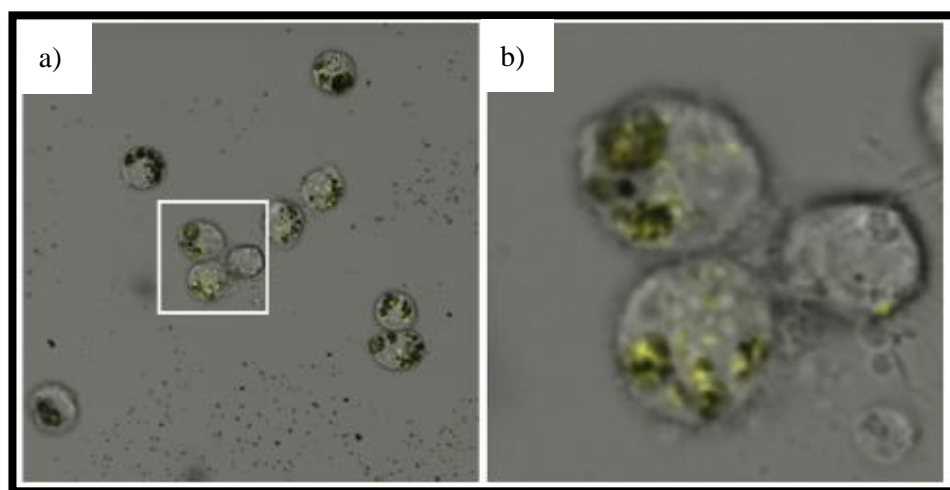


**Figure 4.18** DIC light microscopy overlaid with fluorescent image obtained by confocal microscopy of J774.1 cells incubated with 10  $\mu\text{g/mL}$  Ag NPs depicting likely co-localisation with lysosomes (where the square in image [a] is enlarged to image [b]). Taken from (Arai et al. 2015).

#### 4.4.2 Cu(II)O and CuSO<sub>4</sub>

Literature on the anti-bacterial properties of Cu(II)O NPs was difficult to obtain and it is acknowledged that such information is scarce (Bondarenko et al. 2013b). Over the 7 day fluorescence assay, CuSO<sub>4</sub> exerted greater inhibitory properties than Cu(II)O NPs against *Map* K10/GFP. In the salt form, soluble Cu could have been readily released in the medium and directly available to the mycobacteria, whereas solubility for the NPs appeared relatively low. Another study found that CuSO<sub>4</sub> was more effective at inducing DNA damage and ROS than CuO NPs against *E.coli* over a relatively short period of time (Bondarenko et al. 2012), and again this could relate to metal dissolution. The colony count data in this study surprisingly showed the CuO NPs to be relatively more toxic than first assumed (from the 7 day fluorescence assay), and toxicity was more comparable to the salt control following 12 weeks growth. Over the 7 day period *Map* K10/GFP would have replicated approximately 7 times (the doubling time for *Map* is estimated as 22-26 hours under optimum conditions) and the mycobacteria and the NPs were constantly moving (at 250 rpm) to prevent clumping in the 96 well plate format. However, when the mycobacterial solution and NPs were inoculated onto agar for 12 weeks, they may have been in direct contact if all the Cu(II)O NPs had not dissolved so allowing the NPs to exert increased toxicity by adhering to the mycobacterial cell wall or by entering mycobacterial cells as possibly imaged via TEM.

Overall, Cu(II)O NPs could offer a potential toxicant against mycobacteria at higher concentrations. It is assumed they can be engulfed by macrophages, yet they are cytotoxic to macrophages at concentrations >35 µg/mL therefore their use in clinical applications should also be with caution as Cu(II)O NPs may exhibit toxicity to mammalian cells which is difficult to predict *in vitro* (Bondarenko et al. 2013b). Toxicity to epithelial cell

lines has been reported (Thit et al. 2013). What is clear, is that the anti-bacterial properties of Cu(II)O NPs are under reported in the literature and should be further investigated.

#### 4.4.3 Zn and ZnCl<sub>2</sub>

Zn NP and ZnCl<sub>2</sub> did not exert significant toxicity to *Map* K10/GFP over the 7 day fluorescence assay, and both were very similar in their effects. Zn<sup>2+</sup> are essential in cellular growth, required for many catalytic reactions and structural activities. The concentration of Zn in cells is tightly controlled by many transporters which regulate the metals intracellular levels (Pasquet et al. 2014). It therefore seems at the low concentrations of NPs and salt tested in the assay, that *Map* K10/GFP either utilised the ions to aid cellular growth, or was able to metabolise Zn<sup>2+</sup>, so that no anti-mycobacterial effect was observed over the 7 day period. When concentrations were increased to 50-100 µg/mL, some toxicity (although minor) was observed. Generally, Zn<sup>2+</sup> are considered to be more toxic than Zn NPs or bulk metal against bacteria (Li et al. 2011), therefore if ZnO (NM100) NPs had very low solubility it could explain the results observed for the NPs. Importantly, it is reported that the size of ZnO NPs significantly affect their anti-bacterial activity (Padmavathy & Vijayaraghavan 2008), and as only agglomerates were detected in 7H9 by TEM it could further add to poor efficacy observed. Another study reported that the anti-bacterial effects of Zn take longer than Cu to be observed (Allen et al. 1956), which could account for the difference observed between the 7 day fluorescence assay and the 12 week colony count data, especially with the slow growth of the mycobacteria. It may take longer for the NPs to exert toxicity by adhering to the cell wall as reported previously (Li et al. 2011), yet a recent report carried out toxicity studies on ZnO NPs against *M. bovis*-BCG and like this work, found it ineffective at killing *Mycobacterium* (Pati et al. 2014); *M. bovis*-BCG and ZnO NPs were

incubated for 24 hours with little affect on the CFU recorded. Through scanning electron microscopy it was evident that no morphological damage had occurred to *M. bovis*-BCG rods, thus suggesting that the NPs were unable to disrupt the cell wall, likely because of the resilient mycolic acids, during this time period. In this study, no morphological changes to the ZnO NP treated macrophages was detected.

Although Zn did not exhibit remarkable anti-mycobacterial properties, it would be worth further investigating the metal based on the colony count data, as their use is vast in consumer products and foods. They do not exhibit high levels of cytotoxicity to cell lines and the NPs are known to be up taken by macrophages where mycobacteria reside (Pati et al. 2014). Many ZnO NPs are considered safe by the FDA as vigorous testing on their safety has been carried out (Pati et al. 2014). ZnO NPs could be used as a drug carrier or drug excipient for example, however ZnCl<sub>2</sub> displayed very poor anti-mycobacterial affects shown by both the fluorescence assay and the colony counts, thus ZnCl<sub>2</sub> do not offer results that warrant further investigation into properties against mycobacterial strains.

The mechanisms underlying NP toxicity to bacterial species has been shown to involve disruption of the cell wall through direct NP contact and plasma membrane leakage and production of ROS (Pasquet et al. 2014; Kim et al. 2007; Theophel et al. 2014; Ruparelia et al. 2007). The mechanisms of toxicity were not investigated in this study, but it was hypothesised they would be similar.

## 4.5 Conclusions

Each of the metal/metal oxide NPs tested here displayed interesting results, particularly the very high toxicity of the Ag NPs and the relatively lower toxicity displayed by ZnO NPs over the 7 day period. Ag NPs and the AgNO<sub>3</sub> control were the most toxic, thus suggesting that for this NP toxicity against *Map* K10/GFP could be either particle and ion mediated. The ZnO NPs and ZnCl<sub>2</sub> control were very similar in their effects whereas Cu(II)O NPs were significantly less toxic compared with the CuSO<sub>4</sub> control over the 7 day assay. These results suggest that dissolution was not the only factor that mediates toxicity of metal/metal oxide NPs, and that there are likely to be many factors influencing this (e.g. composition, size, agglomeration status in medium). Further work is clearly required to determine the dissolution of Ag in 7H9, and the overall solubility of this NP as the literature gives very mixed reports. The TEM offered a small insight into how metal/metal oxide NPs might behave intracellularly for both macrophages and bacteria, and had time allowed this work would have been repeated. Ag showed the most promising results in terms of anti-mycobacterial properties and its use in clinical applications should be considered, possibly as an antibiotic drug carrier or drug excipient. Finally, these results demonstrate that the newly developed florescence assay gives a good insight into which NPs show anti-mycobacterial properties.



# **CHAPTER V**

## **SOLID DRUG NANOPARTICLES: SCREENING THEIR EFFICACY AND UPTAKE INTO MACROPHAGES**

## 5.1 Introduction

Robert Koch (1882) stated *“If the importance of a disease for mankind is measured by the number of fatalities it causes, then tuberculosis must be considered much more important than those most feared infectious diseases...One in seven of all human beings dies from tuberculosis...tuberculosis carries away one-third, and often more.”* (cited from (Jain et al. 2008)). Remarkably, even with tremendous medical advancements, superior knowledge of the causes and screening/development of anti-TB drugs, 134 years later TB remains a leading cause of human mortality throughout the world. Today’s TB treatments are constructed to attempt to either: cure patients, to prevent relapse (thus minimising death) or to stop disease transmission (Pham et al. 2015). The primary aims of current anti-TB drug development are: to simplify and shorten treatment periods, to eliminate problems with drug-drug interactions (particularly for HIV patients), to identify novel, safe, anti-mycobacterial substances and to reduce side effects (Ginsberg & Spigelman 2007; WHO 2015b; Boogaard et al. 2009). New treatments are sorely needed because of the complexity and toxicity of current drug programmes and emergence of MDR/XDR TB. Drug development is always an immense undertaking, involving highly complex, often risky and lengthy pre-clinical and clinical trials at large expense. Despite so many advances in bio-medical science and technology, the aim of bringing out a novel treatment for TB has proved elusive.

### ***5.1.1 Current treatments: the costs and complications***

The first line TB treatment regimen involves multiple drugs over 6-9 months. MDR TB treatment, relies on the use of second line drugs, is highly complex, taking 18-24 months

of multi-drug therapy which is both very expensive (up to 200 times more expensive than drug susceptible strains), and very demanding on both the patient and health professionals (Ginsberg & Spigelman 2007; WHO 2015b). Drugs used to treat MDR TB are found to be less well tolerated (with more serious side effects) and up to 50% of those diagnosed with MDR TB die from the infection (190,000 deaths in 2014) (WHO 2015b). Current literature suggests only 10 new drug candidates are in the pipeline, with only BDQ and Delamanid recently being approved by the FDA, the first drugs in over 40 years to be introduced (Chapter 1 [section 1.8]) (Goel 2014; WHO 2014b; WHO 2015b). BDQ is only recommended for MDR TB, its safety and efficacy are still under investigation in Phase III clinical trials (WHO 2015b). Delamanid is only recommended for adults with MDR TB who are HIV positive, as little is known about its effects on specific populations (e.g. infants and the elderly) and it too is being further investigated. There have been recent human trials testing a variety of novel substances (e.g. Pretomanid) or piloting different combinations of first line drugs and/or changing drug dosages (Boeree et al. 2015; Dawson et al. 2015; Hurdle et al. 2008; Grosset & Ammerman 2013). Pretomanid, developed by the Global Alliance for TB drug development, is being investigated for its properties against both drug susceptible and MDR TB with results reported as being promising (Grosset et al. 2012).

There is debate about whether clinicians are prescribing patients with the correct dose of first line antibiotics, such as RIF (van Ingen et al. 2011). Currently patients are dosed with 10 mg/kg up to a maximum of 600 mg per day of RIF, yet little literature exists on how or why this concentration was established. Boeree *et al.*, explain that from 3000 published papers, extracting information on this accepted dose was difficult to find and that the only explanation discovered was that it loosely related to pharmacokinetics, drug toxicity and financial costs (Boeree et al. 2015). It has been suggested that this dose is not optimal, it certainly requires fresh investigation and should possibly be increased (van

Ingen et al. 2011; Boeree et al. 2015). An increase in RIF however, could lead to further side effects already reported by patients (e.g. increase the severity already reported or lead to new side effects not observed at lower doses). Along with all the side effects listed in Chapter 1, hepatotoxicity is frequently reported following administration of RIF (Hest et al. 2004; Shu et al. 2013), which is a matter of great concern and makes the proposed increase in RIF concentration perturbing. Overall it is clear from much of the literature, that anti TB drugs and/or the correct concentration of drugs are not getting to exactly where they are needed in the patient. The pharmacokinetic data is poorly understood, hence why RIF (and INH) is not being dosed accordingly (Longo et al. 2015). Anti-microbial pharmacokinetic/ pharmacodynamic data is highly important for drug development, and should be integrated when determining optimal clinical doses (Gumbo, Angulo-Barturen, et al. 2015).

As well as drug dosing being a problem which limits the effectiveness of currently available drugs, up to 49% of patients are thought not to complete the recommended dosing regimen due to; side effects, costs associated with treatment (e.g. purchasing drugs, travelling to clinics, time required off work *etc*), the stigma linked with TB, and the feeling of ‘being better’ following the initial treatment phase (Longo et al. 2015). The practicalities in taking multiple drugs daily is a burden on patients therefore studies have investigated how to ‘fix’ dose treatment plans to reduce this (Lienhardt et al. 2011). By reducing table numbers of the first line drugs to 3-4 (from 9-16) per day during the intensive phase, the authors found that patient compliance improved, and their results supported the WHO recommendations for use of fixed-dose combinations of drugs, although an improved efficacy from using these drugs was not demonstrated (Lienhardt et al. 2011).

The financial cost of treating TB is staggering when considering a third of the world’s population are thought to be latently infected. An estimated \$100-500 (USD) per patient

for drug susceptible TB is required, increasing to \$10,000-50,000 per patient for MDR that can escalate to \$250,000 (WHO 2015b). As most TB cases are in the developing world, it brings with it a huge financial burden to many poor countries that often have both a fragile economy and weak infrastructure. The cost of identifying a new anti-mycobacterial substance and bringing it into commercial circulation is estimated at \$2.5 billion (Global Business Intelligence, retrieved from <http://gbiresearch.com/media-center/press-releases/pharmaceutical-deals-crucial-to-offsetting-25-billion-cost-of-developing-a-novel-drug>, accessed 04/02/2016), a staggering figure, but as it's associated with a disease that primarily affects developing countries, where there is little return to be gained from treatments, the lack of investment is unsurprising.

If it was possible to find a means to lower the drug dose yet keep drug efficacy the same, this would be advantageous, yet if efficacy could be increased with a *lower dosage* this could be an extraordinary achievement in the TB field, hugely beneficial both medically and financially when considering the global scale of the problem.

### ***5.1.2 The intracellular pathogen***

Macrophages are mononuclear cells of the innate immune system. Reaching *Mtb* inside infected immune cells (e.g. alveolar macrophages) and killing it is difficult as there are great challenges in getting enough drugs to the intracellular mycobacteria. Once engulfed by the immune cells, bacilli cause the activation of multiple microbiocidal mechanisms, including the fusion of the phagosome and generation of pro-inflammatory cytokines. Macrophages aim to remove *Mtb* through rapid acidification, by presenting pathogen antigens to the adaptive immune system, and fusion with lysosomes, containing proteolytic and lipolytic enzymes (Podinovskaia et al. 2013). Phagocytosis is a process by which pathogens are trafficked within a macrophage into fluid-filled, double-

membrane vesicles to be killed (Manivannan et al. 2012). *Mtb* manipulates this process, preventing phagosomal maturation. These infected macrophages, which are unable to kill the bacilli, recruit uninfected macrophages to ultimately form a granuloma (Flynn et al. 2011).

Caseous granulomas are well-organised, dynamic structures, and are typical of an *Mtb* infection. They may be described as the *meeting* of innate and adaptive immunity and are classic to active, latent and reactivated TB (Flynn et al. 2011). Granulomas are poorly vascularised, and the blood supply to the centre where *Mtb* resides is further reduced, thus restricting the delivery of drugs (Grobler et al. 2016). Therefore, in essence, granulomas protect *Mtb* from drugs, as although *Mtb* is contained and often unable to replicate, many TB treatments are unable to penetrate this immune defence and reach their target in macrophage intracellular compartments (Pham et al. 2015; Ehlers & Schaible 2012). As such, the mycobacteria in the centre of granulomas are either, not dosed at all or are under-dosed, which can lead to resistance. If these granulomas rupture, latent TB infection becomes active TB and the disease then becomes transmittable. Due to the importance of these complexes in an *Mtb* infection, the use of *in silico*, *in vitro* and *in vivo* models of intracellular *Mtb* have been used to study drug response (Guirado & Schlesinger 2013; Grobler et al. 2016; Dube et al. 2013). By modelling granulomas *in silico*, investigators have been able to compare drug concentration in the blood compared to the macrophages and found that generally, drug concentration inside macrophages was low (Grobler et al. 2016), thus suggesting that uptake of conventional antibiotics into immune cells is insufficient. Griffiths *et al.*, investigated drug concentrations inside macrophages *in vitro* when drugs were delivered via a nano-carrier and reported a greater than 20 fold increase of intracellular drug compared to the traditional, aqueous drug (Griffiths et al. 2010). *In vivo* models of *Mtb* infection largely use mice and guinea-pigs. Pandey *et al.*, encapsulated RIF, INH and PZA in PLG NPs and administered these orally to mice to

measure biodistribution (RIF 12 mg/kg, INH 10 mg/kg and PZA 25 mg/kg) (Pandey et al. 2003). The mice were euthanised at different time points and various tissues were examined. They reported therapeutic concentrations (MIC levels) for up to 11 days in the lungs, liver and spleen of the mice following administration from the PLG NP, whereas the aqueous drugs were cleared after only 24 hours following oral administration (Pandey et al. 2003).

Nanomedicines may be suitable for treating problematic, intracellular pathogens such as *Mtb*. Studies demonstrate that macrophage cells engulf NPs and internalise NPs by endocytic mechanisms (Clift et al. 2008). The physical advantages include the reported ability to pass through fine capillary vessels, uptake by macrophages, increased circulation time in the blood stream and surface modifications allowing specific targeting (Onoue et al. 2014; Clift et al. 2008; Navalakhe & Nandedkar 2007). Furthermore, NPs can be targeted to specific sites using surface modifications (Hirota et al. 2010; Byrne et al. 2011). With this knowledge, the adaption of anti-TB drugs into nano-formulations will mean better targeting, reduced dosage, and thus possibly decreasing side effects and increasing patient compliance. This could in-turn decrease MDR cases, and has opened up many new avenues for TB medical research to follow. Smith stated *“Using current anti-TB drugs, nanoparticle-based formulations may shorten drug regimen duration, reduce frequency, and deliver medications more efficaciously, ultimately reducing patient default and improving completion rates. In turn, this holds significant potential in the reduction of DR (drug resistant)-TB cases...”* (Smith 2011). This proposal is now a reality, as SDNs are a novel and exciting development in nanotechnology.

### 5.1.3 Solid drug nanoparticles (SDNs)

SDNs are excipient stabilised nanoparticulate versions of FDA approved therapeutics (Fig 5.1) (McDonald et al. 2014). Drugs are rarely administered in an unformulated condition, they are composed of two (or more) components, the Active Pharmaceutical Ingredient (API, the chemically active substance [e.g. RIF]) which is delivered with excipients. Excipients are inactive substances which act as carriers for the medication, allowing for accurate dosage. They also enhance the release and prevent the degradation of some drugs (Pandey & Ahmad 2011). SDNs were synthesised by the University of Liverpool (Professor Andrew Owen, Dr Marco Giardiello [Department of Chemistry]) for this PhD project. The technique involved the preparation of an oil-in-water emulsion in which the drug (e.g. RIF) was present in a volatile organic oil phase while the aqueous phase contained a mixture of stabilisers (e.g. water-soluble polymers, Hyamine®). The emulsified mixture was then cryogenically frozen and both the drug and water solvent were removed via freeze-drying. Upon addition of water the drug was released, yielding nano-suspensions. The process employed a large number of screening systems in which a range of active pharmaceutical ingredients, polymers and surfactants were studied to optimise the formulation and NP dispersion production (personal correspondence with Dr Marco Giardiello [Department of Chemistry, University of Liverpool]). This technique allowed SDN size, surface charge and drug loading to be controlled and pre-determined, to enhance SDN stability. SDNs for the treatment of HIV by the same group are currently undergoing clinical trials and preliminary results are very promising (results are not yet published [see EudraCT 2013-004913-41 <https://clinicaltrials.gov/ct2/show/NCT02631473>]).



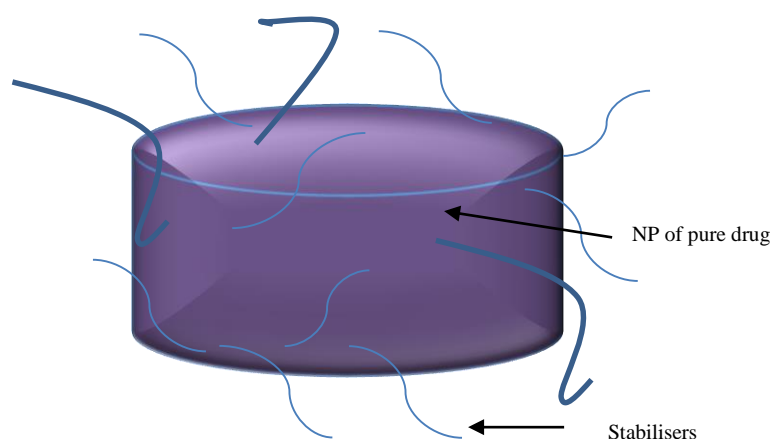


**Figure 5.1 Schematic diagram of an SDN (e.g. RIF) with stabilising excipients.**

There are many advantages to developing SDNs. One, for example, is that by using existing FDA approved pharmaceutical ingredients it saves time and the inordinate cost involved in novel drug development and testing. As SDN drugs are produced at the nano-scale they increase drug bioavailability and may offer an opportunity to lower treatment dose as well as improve targeting (Mcdonald et al. 2014; Bawa 2008). These attributes are essential when considering novel TB treatments. If the correct dose of anti-TB drugs could reach intracellular *Mtb*, the problem of latent infections could be decreased, and further, as resistance often occurs due to patient noncompliance, if drugs were administered over a shorter time period it would likely decrease the levels of MDR/XDR TB currently reported.

#### **5.1.4 Aims**

The aim of this chapter is to compare the ability of the novel SDNs to kill mycobacteria with traditional aqueous antibiotics, using the newly developed screening assay (Chapter

3). The ability of SDNs and traditional aqueous antibiotics to kill intracellular mycobacteria (within a macrophage) was also compared. It was hypothesised that a lower concentration of SDNs would be required to kill mycobacteria, using the screening assay. In addition, it was hypothesised that macrophages would uptake SDNs to enhance killing of intracellular *Map* K10/GFP. Results from this chapter are currently in preparation for a joint publication between the Moredun Research Institute, the University of Liverpool, the University of Nottingham, and Heriot Watt University.

## **5.2 Methods and Materials**

### ***5.2.1 SDN development***

SDNs (RIF, INH and PZA) were developed and supplied by project collaborators at the Institute of Translational Medicine, Department of Chemistry, University of Liverpool (Professor Andrew Owen and Dr Marco Giardiello). Please see Appendix B for information on their manufacture.

### ***5.2.2 SDN Preparation and characterisation***

All SDNs were sub sampled under sterile conditions and kept in the dark at ambient temperature until use. A stock concentration of SDNs (1 mg/mL) in sterile 2% (vol/vol) FCS (prepared in sterile DW) was prepared and sonicated for 16 minutes at 400 W in a bath sonicator from Ultrawave<sup>®</sup> (Cardiff, UK) and then placed on ice as previously outlined in Chapter 4 (section 4.2.1). NPs were then diluted in 7H9 (see Chapter 2 [2.6.1]).

### ***5.2.3 Aqueous drug preparation***

RIF and INH were purchased from Sigma-Aldrich® (UK) and prepared (and stored) following product documentation. Briefly, 150 mg of RIF was solubilised in 6 mL methanol yielding a stock solution of 25 mg/mL and vortexed for one minute prior to use. INH was solubilised in 2 mL DW yielding a 1 mg/mL solution and vortexed for one minute prior to use. Stock solutions were stored in tin-foil wrapped bottles at 4°C. From these stock solutions, appropriate serial dilutions were made in 7H9 for the desired concentrations.

### ***5.2.4 Dynamic light scattering***

Agglomeration status, zeta potential and hydrodynamic sizes were analysed by DLS at a concentration of 100 µg/mL (in 7H9 medium) using a Zetasizer Nano-ZS instrument (Malvern Instruments Ltd., UK). SDNs were prepared as outlined above (5.2.2).

### ***5.2.5 SDN 96 well plate setup***

The antimicrobial properties of SDNs and aqueous drugs were screened using the previously described assay (Chapter 3), with all optimisation parameters and data analysis carried out as in Chapter 4. Briefly, *Map* K10/GFP was cultured in 7H9K<sup>+</sup> until the exponential stage of growth, at which point they were seeded (2x10<sup>6</sup> CFU/100 µL/well) into a 96 well, sterile, black plates (Nunc, Thermo Fisher) at a turbidity to match McF standard 2. SDN and aqueous drugs in 7H9 were exposed to *Map* K10/GFP at

concentrations ranging from 0.001875 to 4  $\mu\text{g/mL}$  (final volume per well of 200  $\mu\text{L}$ ). The samples were incubated at 37°C with medium agitation (250 rpm) and kept in the dark throughout the experimental procedure. Medium only (no bacteria, no SDN/drug) and SDN/drug and medium (no bacteria) were included to check for SDN/drug interference. Fluorescence was measured using a GloMax® Multi<sup>+</sup> plate reader (Promega, UK) (ex/em 490/510-570 nm). Bacterial fluorescence was monitored immediately after SDN/drug addition (day 0), then at the same time each day for 7 days. All experiments were performed in triplicate, a minimum of three times, under sterile conditions.

#### ***5.2.6 Colony counts***

Following 7 days of *Map* K10/GFP incubation with SDNs/drugs in 7H9, 100  $\mu\text{L}$  of the cultures at each concentration were serially diluted and inoculated onto 7H11 agar in bacteriological plates (as outlined in Chapter 2) for 12 weeks, incubated at 37°C allowing for conventional colony counts (see Chapter 2.1.5).

#### ***5.2.7 Cytotoxicity of substances to macrophages***

Macrophages were cultured as described in Chapter 2 (section 2.3). Cytotoxicity to macrophages of the SDNs and aqueous drugs was evaluated using the alamar blue assay (Chapter 2, section 2.4).

## **5.2.8 Macrophage infections and drug treatments**

### **5.2.8.1 Infection**

Macrophages were cultured as described in Chapter 2 (section 2.3). Cells were detached from flasks using TrypLE™ and centrifuged at 850 g for 2 minutes before resuspension into 8 well chambered Permanox® slides at a density of  $1 \times 10^5$  cells/well (final volume of 200  $\mu$ L) and incubated for 24 hours at 37°C, 5% CO<sub>2</sub>. Supernatant was removed from chambers and cells were washed twice with 200  $\mu$ L PBS. *Map* K10/GFP was cultured as described in Chapter 2 (section 2.1.1) and 10 mL of bacterial culture (in the exponential phase of growth) was centrifuged at 3090 g for 20 minutes and resuspended in 1 mL of PBS. The bacterial cell suspension was then centrifuged for 5 minutes at 670 g to remove any residual antibiotic (from the 7H9), and resuspended in 1 mL of PBS and passed through a Gilson tip several times to break apart any clumping. At a 30:1, 10:1 and 5:1 multiplicity of infection (MOI [bacilli counts see Chapter 2, section 2.5.2]) the macrophages were infected with mycobacteria in complete medium (without streptomycin or penicillin) at a final volume of 200  $\mu$ L per chamber (each MOI was done in triplicate) and incubated for 4 hours at 37°C, 5% CO<sub>2</sub>. Supernatant was removed and each chamber was washed twice with 200  $\mu$ L of PBS to remove any residual/surface bound mycobacteria before fixing using 4% paraformaldehyde (Chapter 2, section 2.7.1). Control chambers were subject to the same procedures and contained macrophages and medium only.

### 5.2.8.2 Macrophage uptake of SDNs

To investigate uptake of SDNs by infected and uninfected macrophages, a label was required to allow visualisation of the SDNs by fluorescent microscopy. To achieve this 1,1'-Diocadecyl-3,3,3',3'-Tetramethylindodicarbocyanine, 4-Chlorobenzenesulfonate salt (DiD [ex/em: 596/670 nm]) was incorporated into the DCM phase of SDN production (see Appendix B).

Macrophages were seeded in 8 well chambered Permax<sup>®</sup> slides at a density of  $1 \times 10^5$  cells/well and incubated for 24 hours at 37°C, 5% CO<sub>2</sub>. Cells were then infected with *Map* K10/GFP as described in section 5.2.8.1. SDNs (with DiD) were prepared as described previously (section 5.2.2) and diluted in complete medium (without streptomycin or penicillin) to concentrations of a concentration range of 10 µg/mL- 20 µg/mL and added to the chambers (final volume of 200 µL) in triplicate. Infected macrophages were incubated for 4 hours with the SDNs at 37°C, 5% CO<sub>2</sub>. The supernatant was removed and each chamber was washed twice with 200 µL of PBS to remove any residual/surface bound SDNs and/or mycobacteria before fixing using 4% paraformaldehyde (2.7.1). Control chambers contained macrophages and medium only, macrophages with 1 mM 10 mM or 100 mM DiD dye (stocks prepared in DMSO) and macrophages and 20 nm fluorescent carboxylated polyester NP beads (NP beads [Molecular Probes, USA], ex/em: 580/605 nm).

### ***5.2.9 Staining and fixed cell imaging***

Following fixation (using 4% paraformaldehyde, Chapter 2 [section 2.7.1]), macrophages were stained with 4',6-diamidino-2-phenylindole dihydrochloride (DAPI) nuclear stain (1:10 dilution in PBS [ex/em: 358/461 nm]) and/or Alexa Fluor®568 (phalloidin [Thermo Fisher Scientific, UK], ex/em: 578/600 nm) an F-actin stain. After 15 minutes the slides were washed twice with distilled water before being mounted onto slides with Fluoro-Gel Mounting Medium with TES Buffer solution (EMS, USA).

Cellular uptake was imaged using a Zeiss Axiovert 200M inverted Epi fluorescence microscope with an AxioCam MR3 camera using objective magnifications of X10, X40, X63 and X100. Cy3, Cy5, DAPI, GFP and DIC (differential interference contrast) or phase contrast channels (depending on objective) were used. Images were processed using Image-J (Fiji) software (Schindelin et al. 2012) and Zeiss Axio vision Rel 4.8 software (Z-stacks) thus showing the DIC (grey), DiD control dye (yellow) and DiD incorporated SDNs (red [RIF] and yellow [TRIPLE]), polyester beads (pink), *Map* K10/GFP (green), macrophage nucleus (blue) and actin (cyan).

### ***5.2.10 Phage amplification assay to quantify viable mycobacteria following drug contact***

A phage-PCR amplification assay was utilised to compare the killing of RIF SDN to that of aqueous RIF intracellularly (within a macrophage). The FASTPlaqueTB™ assay is a rapid test which uses bacteriophage amplification technology to detect viable mycobacteria. Originally developed for detecting *Mtb*, it has also been successfully used

to detect viable *Map* (Botsaris et al. 2010; Altic et al. 2007). Bacteriophages are viruses that infect and kill bacterial cells. When added to a sample containing live and dead bacteria, the bacteriophages will infect only viable cells where they attach to cell surface receptors (a process termed adsorption) and inject their genetic material into the cell to be replicated (a process termed penetration). Replication occurs and phage are released following lysis of the bacterial cells. In the phage amplification assay, the sample-containing *Map* is mixed with the phage and incubated to permit adsorption and penetration. Before lysis of the infected *Map* cells, a virucide is added to kill any extracellular phage and the sample then mixed with fast growing *M smegmatis* mc<sup>2</sup>155 and plated out in agar. Products of phage amplification can then be viewed as lysed areas (plaques) on a lawn of *M smegmatis*. Each plaque formed represents one *Map* cell from the original sample. The assay was performed using a modification of the method described by Swift *et al.*, 2013.

Macrophages (seeded into the wells of flat-bottomed, cell culture 96 well plates at a density of  $5 \times 10^5$ /mL) were infected with *Map* K10/GFP (at an MOI 1, 10 and 30) and incubated for 30 minutes at 37°C, 5% CO<sub>2</sub> as previously described (section 5.2.8). Aqueous and SDN RIF were added at a concentration of 4 µg/mL. Control wells were included that contained infected macrophages only and no SDN or drug. The infected cells were incubated for a further 24 hours at 37°C, 5% CO<sub>2</sub>. Following 24 hours incubation, the supernatant was removed and cells were washed twice with 200 µL of PBS to remove any residual/surface bound drug/SDN and/or mycobacteria. Macrophages were lysed by adding 400 µL of 7H9 (for 10 minutes) to the wells thus releasing intracellular *Map* K10/GFP. The 400 µL of 7H9 (with lysed macrophages and *Map* K10/GFP) was then added to 600 µL of 7H9, which was mixed with  $1 \times 10^8$  mycobacteriophage D29 (100 µL) and incubated for 1 hour. After this time, remaining extracellular phage were inactivated using 100 µL of 10 mM ferrous ammonium sulphate



[virucide] for 5 minutes. The virucide was then neutralised by dilution in 7H9 and the phage-infected cells were mixed with growing *M. smegmatis* (1 mL,  $10^7$  CFU/mL) using soft agar (FASTPlaqueTB™ agar [BIOTEC Laboratories Ltd, UK]) (0.8% w/v) and incubated at 37°C for 24 hours. Positive (*M. smegmatis*) and negative (no mycobacteria) controls were included (standard FASTPlaqueTB™ assay controls). This assay was carried out only once (due to project time restraints). *M. smegmatis*, soft agar, virucide and mycobacteriophage D29 were provided by Dr Benjamin Swift (Faculty of Medicine & Health Sciences, The University of Nottingham), who also provided training for this assay.

#### **5.2.11 Data analysis**

For the fluorescence assay, results expressed in AFU against time were transformed and normalised to obtain the usual dose response relationship, to compare the effects of the SDNs and aqueous drugs on the growth of the mycobacteria as outlined in Chapter 3 (novel method of data analysis). Some results were also plotted using the common Log scale to allow easier visualisation of data close points and other results were plotted using the dose response modelling software PROAST (version 38.9) in the R software (version 3.1.0). By setting the critical CES to 50% it was possible to obtain the EC<sub>50</sub> and 90% CEDL/CEDU to allow for statistical comparisons, as carried out in Chapter 4. Statistical testing varied between different experiments depending on the data type. See results section for further details. Results were considered significant if  $p < 0.05$ .

## **5.3 Results**

### ***5.3.1 SDN characterisation***

#### ***5.3.1.1 Particle drug loading***

The aqueous drug and SDN drug loading information and concentration is presented in Table 5.1. The difference loading of each drug is an important factor to consider when interpreting the results. Each SDN had a different drug loading, RIF had 30% drug, TRIPLE had 53.3% drug and DUAL had 30% drug (Table 5.1).

#### ***5.3.1.2 DLS***

Characterisation of the SDNs was carried out in 7H9 growth medium by DLS. The average hydrodynamic diameter for RIF SDNs was found to be <50 nm (Table 5.2), thus being the smallest of all the SDNs analysed. DUAL SDNs on average were found to be 93.78 nm (Table 5.2). The TRIPLE SDNs were either larger NPs or were agglomerating in the medium as the primary particle size was 161.78 nm (Table 5.2) thus being considerably larger than the RIF SDNs. SDNs with the incorporation of the DiD increased in size, RIF SDN increased in size to 70 nm and TRIPLE SDNs increased in size to 253.53 nm (Table 5.2).

The size distribution graphs (Appendix B) display a spread in the sizes detected by DLS. As shown in all figures, there was quite a spread in primary particle size, suggesting that agglomerates were being detected in some cases, rather than individual particles. Like the metal/metal oxide NPs the zeta potentials were all low, negative values, thus suggesting that they were unstable in 7H9 (Table 5.1).

**Table 5.1 Drug types and drug loading (%)**  
(partly supplied by the University of Liverpool)

SDN/DRUG	TOTAL DRUG LOADING	FORMULATION
RIF aqueous (Rifampicin aqueous drug)	$\geq 97\%$	Powder* (Stock solution prepared with methanol to 25 mg/mL)
INH aqueous (Isoniazid aqueous drug)	$\geq 99\%$	Powder** (Stock solution prepared with distilled water to 1 mg/mL)
RIF SDN (Rifampicin solid drug nanoparticle)	30%	30% RIF/55% F68 <sup>®</sup> Protect/ 15% Hyamine <sup>®</sup>
TRIPLE SDN (Rifampin, isoniazid, and pyrazinamide solid drug nanoparticle )	53.3%	34% PZA/ 13% RIF/6% INZ/ 40% Kollicoat <sup>®</sup> Protect/ 7% Hyamine <sup>®</sup>
DUAL SDN (Rifampin, isoniazid solid drug nanoparticle)	30%	20% RIF/ 10% INZ/ 60% Kollicoat <sup>®</sup> Protect/ 10% Hyamine <sup>®</sup>

\*Sigma-Aldrich<sup>®</sup> Product number R8883

\*\* Sigma-Aldrich<sup>®</sup> Product number I3377

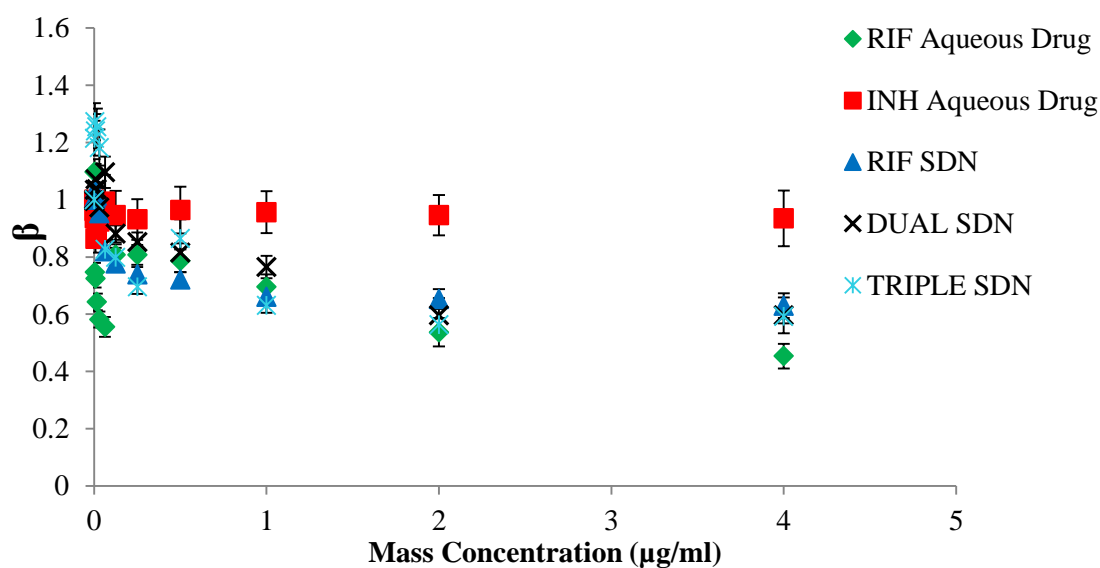
**Table 5.2 DLS Results.** Hydrodynamic diameter (Z-average), zeta potential and polydispersity index (PdI) of SDN panel was assessed using DLS. Data expressed as mean  $\pm$  SEM (n=4). With or without 1,1'-Dioctadecyl-3,3,3',3'-Tetramethylindodicarbocyanine, 4-Chlorobenzenesulfonate Salt (DiD). Temp: 25°C, dispersant: Middlebrooks 7H9 (100  $\mu$ g/mL), pH 6.9, equilibrium time: 30 secs.

SDN	Z-Average (d.nm)	Zeta Potential (mV)	PdI
RIF SDN	36.75 $\pm$ 6.34	-9.71 $\pm$ 0.38	0.77 $\pm$ 0.07
DUAL SDN	93.78 $\pm$ 17.92	-7.49 $\pm$ 0.49	0.37 $\pm$ 0.01
TRIPLE SDN	161.78 $\pm$ 8.56	-6.31 $\pm$ 0.86	0.31 $\pm$ 0.07
RIF SDN (+ DiD)	107.27 $\pm$ 32.93	-10.46 $\pm$ 0.47	0.56 $\pm$ 0.09
TRIPLE SDN (+ DiD)	415.3 $\pm$ 64.81	-10.43 $\pm$ 0.81	0.42 $\pm$ 0.03

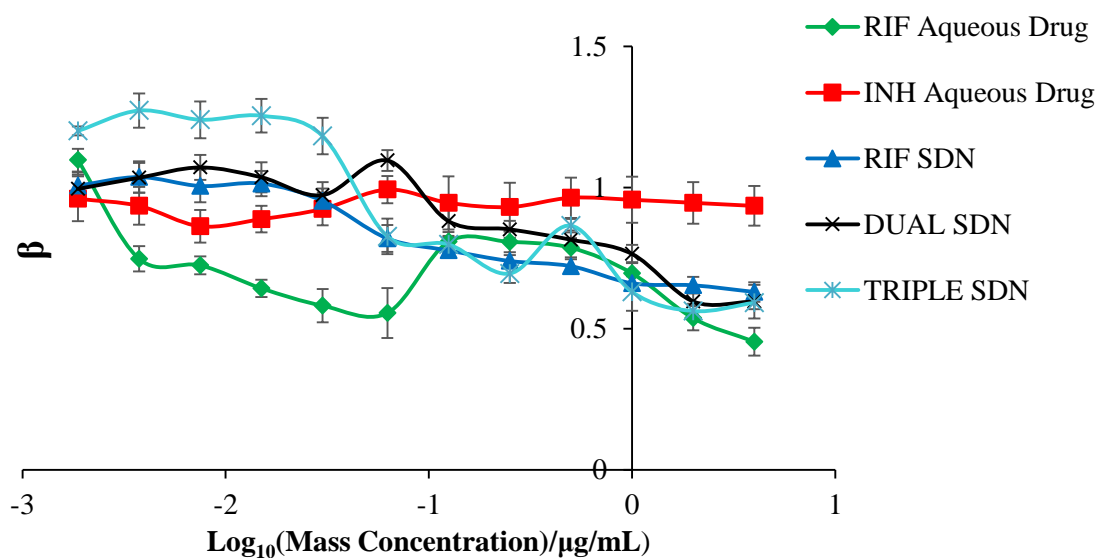
### 5.3.2 Screening the anti-mycobacterial properties of SDNs and aqueous drugs against *Map* K10/GFP

The anti-mycobacterial properties of aqueous drugs and SDNs were screened against *Map* K10/GFP using the fluorescence assay developed and described in Chapter 3. The results are first displayed similarly to the results in Chapter 4, where the raw data was transformed using the novel data analysis protocol (Chapter 3, section 3.3.4) depicting fluorescence ( $\beta$ ) against concentration for each substance. The results were then analysed for statistical significance. Significance level was denoted by:  $p < 0.001$  (\*\*\*),  $< 0.01$  (\*\*) and  $< 0.05$  (\*) (MINITAB<sup>®</sup>, version 17). Figure 5.2 (a) depicts the effect of each substance on the growth of *Map* K10/GFP (the different analysis steps can be found in Appendix B). There was a dose dependent inhibition of *Map* K10/GFP when treated with RIF SDN, RIF aqueous, TRIPLE and DUAL SDNs. However, INH aqueous did not have a great effect at inhibiting the growth of *Map* K10/GFP over the 7 day fluorescence assay (Fig 5.2 a). Interestingly, RIF aqueous appeared to be more toxic to the mycobacteria at lower concentrations (e.g. 0.015  $\mu\text{g/mL}$ ) than at some of the higher concentrations screened (e.g. 0.5  $\mu\text{g/mL}$ ) (Fig 5.2 a-b). Figure 5.2 (a) was re-plotted (Figure 5.2 b) using the common Logarithmic scale to better display the spread in the data points at the lower concentrations and then again in PROAST (version 38.9) (Figure 5.3) (which included only the higher concentrations [0.125 - 4  $\mu\text{g/mL}$ ]) to allow statistical analysis (to determine the  $\text{EC}_{50}$  values).

Four main questions were asked when analysing this data for statistical significance: 1) did the substances tested differ significantly from each other? 2) did the toxicity of the treatments differ to the controls (no treatment [0  $\mu\text{g/mL}$ ])? 3) was there a significant difference between the two RIF treatment types (SDN and aqueous) and 4) was there a difference in mycobacterial growth between days with the different treatment types?



a)



b)

**Figure 5.2 (a) Growth of *Map* K10/GFP with different substances normalised to the control.** Normalised, transformed data showing the growth of *Map* K10/GFP grown in 200 μL of 7H9, in a microplate format, with SDNs and aqueous antibiotics at different concentrations (0.001875 - 4 μg/mL), normalised to the slope of the control (0 μg/mL) (where β represents the change in fluorescence [representing mycobacterial growth] per day). β was calculated through linear regression analysis of the Log data. Each point displaying 2\* the standard error calculated using LINEST function Excel (Microsoft Office Word) (n= min of 3). **Figure 5.2 (b)** As above (concentration plotted on the log scale to display the data at the lower concentrations and with data lines to better show the data pattern).

### 5.3.2.1 Statistical Analysis 1

#### **Did the efficacy of all the substances differ significantly from each other?**

Each substance was compared to determine whether they had a significantly different effect on the growth of *Map* K10/GFP. This was achieved by estimating the EC<sub>50</sub> (calculated using PROAST [version 38.9]) when plotting the fluorescence data (indicative of bacterial growth) from the concentration range 0.125 – 4 µg/mL. Figure 5.3 presents the dose response curves for all substances screened (yielding the EC<sub>50</sub> values and 95% confidence intervals for all the substances [obtained from the software package PROAST [version 38.9] [outlined in Chapter 4, section 4.3.4]). The EC<sub>50</sub> values generated from this analysis were 2.98 µg/mL (RIF aqueous), 1380 µg/mL (INH aqueous), 40.2 µg/mL (RIF SDN), 17.3 µg/mL (DUAL SDN) and 7.17 µg/mL (TRIPLE SDN) (Table 5.3) therefore the substances toxicity could be ranked RIF aqueous> TRIPLE SDN> RIF SDN> DUAL SDN> INH aqueous. This same method of analysis was utilised for the metal NPs (Chapter 4, section 4.3.4) and the method was more suitable for that data set (where mycobacterial growth was greatly inhibited). In this case, the EC<sub>50</sub> values were estimated by the software via extrapolation. As shown in Figure 5.3, the only EC<sub>50</sub> obtained directly from the plot was for RIF aqueous, and the others were made via an estimation of when the 50% mark would be reached. A reason for this was possibly the significant difference of INH to all the other substances, which may have skewed the data.

Table 5.3 displays the confidence interval values, which were plotted in Figure 5.4 to allow a visual comparison between the 95% confidence intervals. RIF in the SDN and aqueous form differed significantly from each other in terms of toxicity to the

mycobacterium with the aqueous being more toxic (Fig 5.4, Table 5.3). However, the confidence intervals for RIF aqueous overlapped TRIPLE and DUAL SDNs suggesting no significant difference, (Fig 5.4, Table 5.3). The confidence intervals for INH aqueous did not overlap with any other substance, suggesting that INH aqueous was statistically less toxic, compared to the other treatments. In contrast, the confidence intervals for RIF SDN, DUAL SDN and TRIPLE SDN overlapped with each other (Fig 5.4, Table 5.3) suggesting no significant difference in the relative toxicity of each of the SDN on an total mass dose basis.

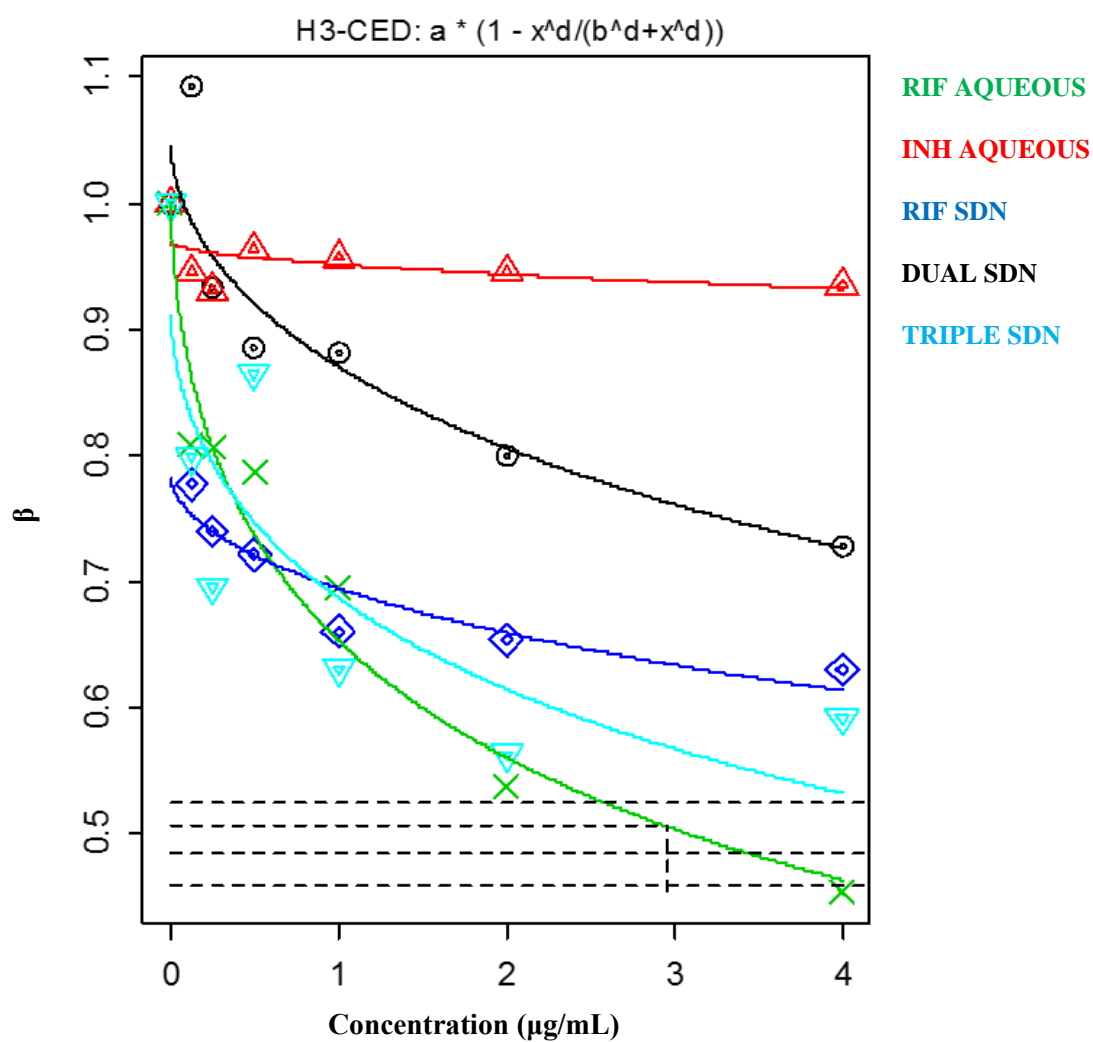


**Figure 5.3 Comparison between the substances on the growth of *Map* K10/GFP normalised to the control and re-plotted in PROAST 38.9.** *Map* K10/GFP grown in 200  $\mu\text{L}$  of 7H9 in a microplate format, with substances at different concentrations (0.125 - 4  $\mu\text{g/mL}$ ).

*\*please note PROAST 38.9 does not allow allocation of figure legend or choice of colours/symbols*



**Table 5.3**  $EC_{50}$  value for each substance with the lower (CEDL) and upper (CEDU) 95% confidence intervals to plot Figure 5.4 (derived from Figure 5.3).

Treatment	RIF AQUEOUS	INH AQUEOUS	RIF SDN	DUAL SDN	TRIPLE SDN
$EC_{50}$	2.98	1370	40.2	17.3	7.17
CEDL	1.193	1110.9	17.99	7.393	4.259
CEDU	3.016	110.9	70.19	35.817	20.341

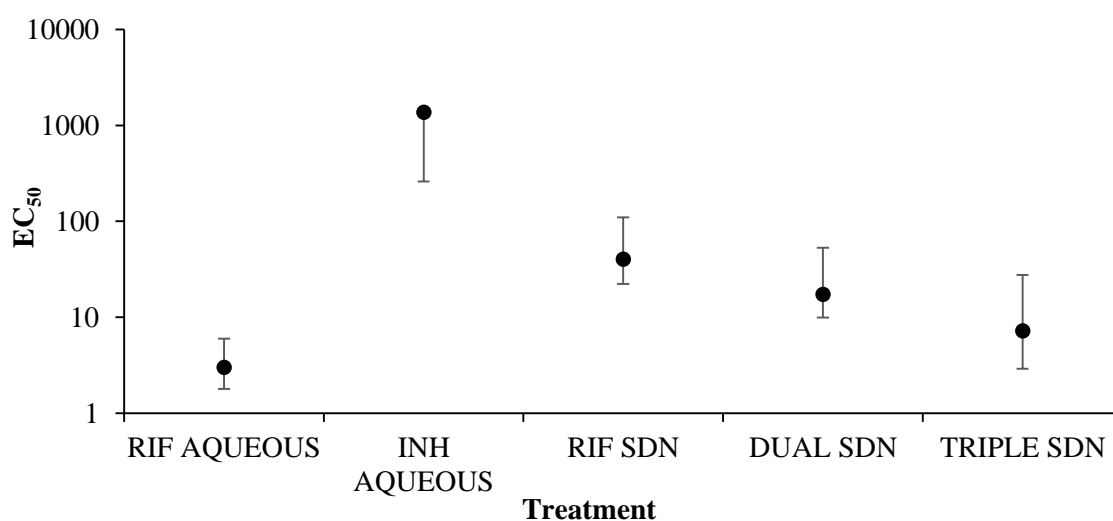


**Figure 5.4** The half maximal effective concentration ( $EC_{50}$ ) for each treatment with the upper and lower 95% confidence intervals. Plot of the mean  $EC_{50}$  values and corresponding confidence intervals (on the common logarithmic scale) for each treatment on the rate of mycobacterial growth. INH was the only substance significantly different from all the others on its effect on the growth of *Map* K10/GFP. It was the least effective substance screened.

The graphs above (Fig 5.2(a-b), 5.3) display the data for the ‘mass’ concentration of SDNs and aqueous drugs in each case. For example, RIF SDN contained only 30% rifampicin whereas RIF aqueous contained >97% rifampicin at each concentration tested. By comparing the mass concentrations, the EC<sub>50</sub> value for RIF SDN was calculated as 40.2 µg/mL via extrapolation by the PROAST (39.8) software (Table 5.3). In an attempt to account for this difference in concentration and obtain a more accurate RIF SDN EC<sub>50</sub> to allow a direct comparison between the two forms of the antibiotic, the data modelling software GraphPad Prism (version 5, GraphPad software, Inc, USA) was utilised. By plotting the whole  $\beta$  data range (0.001875 – 4 µg/mL) using a 3 parameter Emax model, but considering the API content for RIF SDN, it was possible to obtain a more effective EC<sub>50</sub> for the RIF API. Figures 5.5 (a-b) display the two data sets obtained. The RIF SDN displayed a ‘typical’ dose response curve, as RIF concentration increased, the fluorescence of *Map* K10/GFP ( $\beta$ ) decreased (Fig 5.5 a,b). When analysing the mass concentration of the SDN, the EC<sub>50</sub> for RIF SDN on the growth of *Map* K10/GFP was calculated as 0.075 µg/mL. This data was then re-plotted, but the concentrations were divided by three to represent that the had particle only 1/3 drug (e.g. 4 µg/mL became 1.33 µg/mL) and by doing so, the EC<sub>50</sub> for RIF SDN on the growth of *Map* K10/GFP was calculated as 0.025 µg/mL (Fig 5.5b)

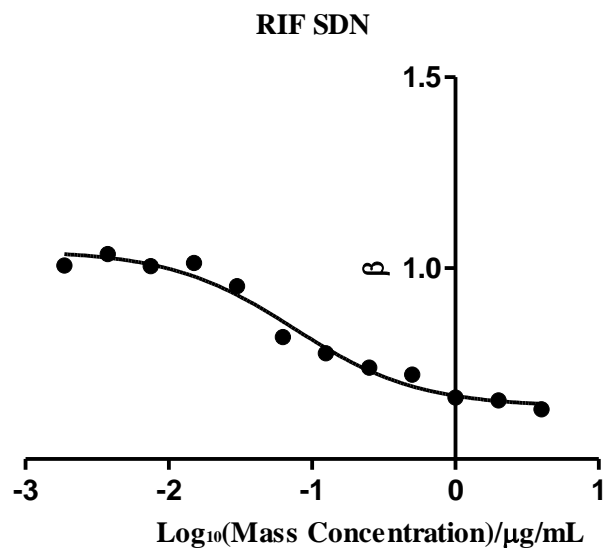


**Figure 5.5 (a) Calculating the  $\text{EC}_{50}$ .** Efficacy of RIF SDN on the growth of *Map* K10/GFP, considering 'mass' concentration of the SDN (excipient and SDN) (where  $\beta$  represents the change in fluorescence [representing mycobacterial growth] per day) and  $\text{EC}_{50} = 0.075 \mu\text{g/mL}$  ( $n=9$ ). Concentration plotted on the log scale.

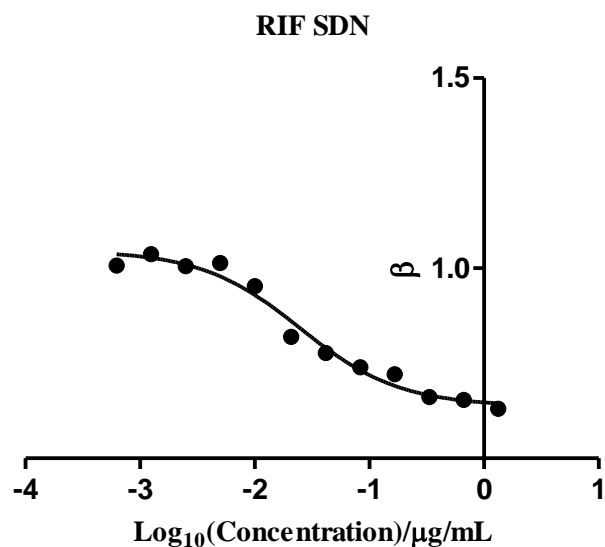


**Figure 5.5 (b) Calculating the  $\text{EC}_{50}$ .** Efficacy of RIF SDN on the growth of *Map* K10/GFP, considering effective concentration of the SDN (RIF loading only) (where  $\beta$  represents the change in fluorescence [representing mycobacterial growth] per day) and  $\text{EC}_{50} = 0.025 \mu\text{g/mL}$  ( $n=9$ ). Concentration plotted on the log scale.

### 5.3.2.2 Statistical Analysis 2

**Did the different concentrations screened differ significantly from the control (0 µg/mL) for both RIF treatment types (RIF SDN and RIF aqueous)?**

It was important to determine whether the different concentrations of RIF in each form (SDN and aqueous) differed significantly from the control (0 µg/mL). The raw data, fluorescence (AFU) against time (days), was checked for a normal distribution by plotting a histogram (MINITAB®, version 17). As the data was not normally distributed (see Appendix C), the Log data was utilised to run an ANOVA test (using a general linear model with Tukey post-test [allowing pairwise comparisons, comparing all mean values]).

In both cases (RIF SDN and RIF aqueous), there was an overall difference ( $p < 0.001$ ) between the different concentrations and the control (0 µg/mL) indicating significant toxicity for both treatments (Figs 5.6 and 5.7). For RIF SDN, concentrations 0.125, 0.25, 0.5, 1, 2 and 4 µg/mL significantly reduced the growth of *Map* K10/GFP compared with the control ( $p < 0.001$ ) (Fig 5.6), whereas concentrations 0.00375, 0.0075, 0.015, 0.03, 0.0625, 1, 2 and 4 µg/mL for RIF aqueous all significantly reduced the growth of *Map* K10/GFP compared with the control ( $p < 0.001$ ) (Fig 5.7). As shown in Figure 5.6, four (in the low range) of the twelve concentrations tested did not differ significantly from the control for RIF SDNs, whereas only one (0.001875 µg/mL) concentration did not differ significantly from the control for RIF aqueous (Fig 5.7).

From these results, it seems that the aqueous form of RIF had greater anti-mycobacterial than RIF SDN did, as it was able to significantly inhibit mycobacterial growth at lower concentrations. It must be noted however, that at each concentration for both treatment

types, only 30% of this concentration was drug for RIF SDN, unlike RIF aqueous which was >97% drug, thus making direct comparisons problematic.

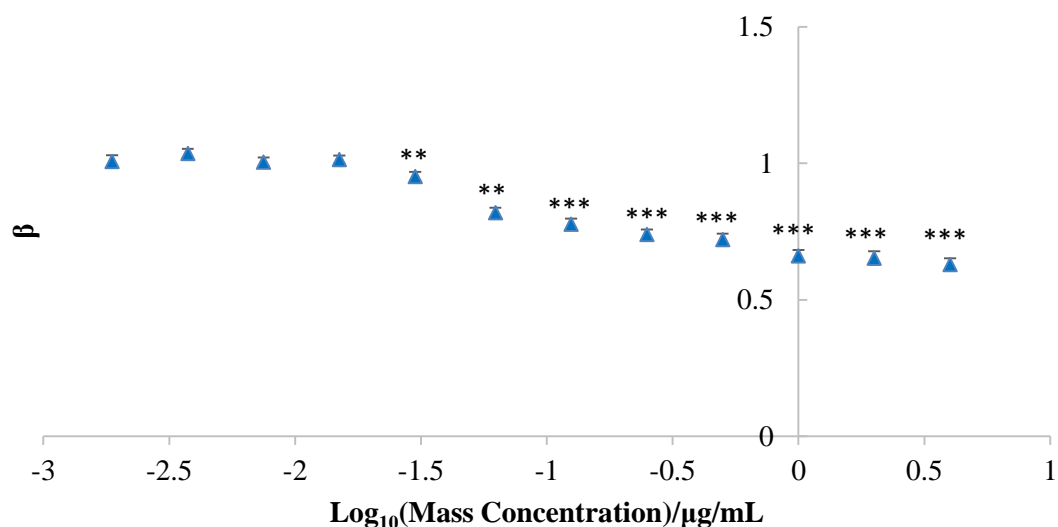


**Figure 5.6 Impact of RIF SDN on mycobacterial growth.** Comparing the control (0 μg/mL) to each concentration of RIF SDN using an ANOVA test (using general linear model with Tukey post test). Bar chart plot of fluorescence data ( $\beta$ ), showing where there is a significant difference between each RIF SDN concentration on the growth of *Map* K10/GFP and the control (0 μg/mL). (Significance level is denoted by: <0.001 (\*\*\*), <0.01 (\*\*) and <0.05% (\*)). Each bar showing 2\* the SEM. Concentration plotted on the log scale.

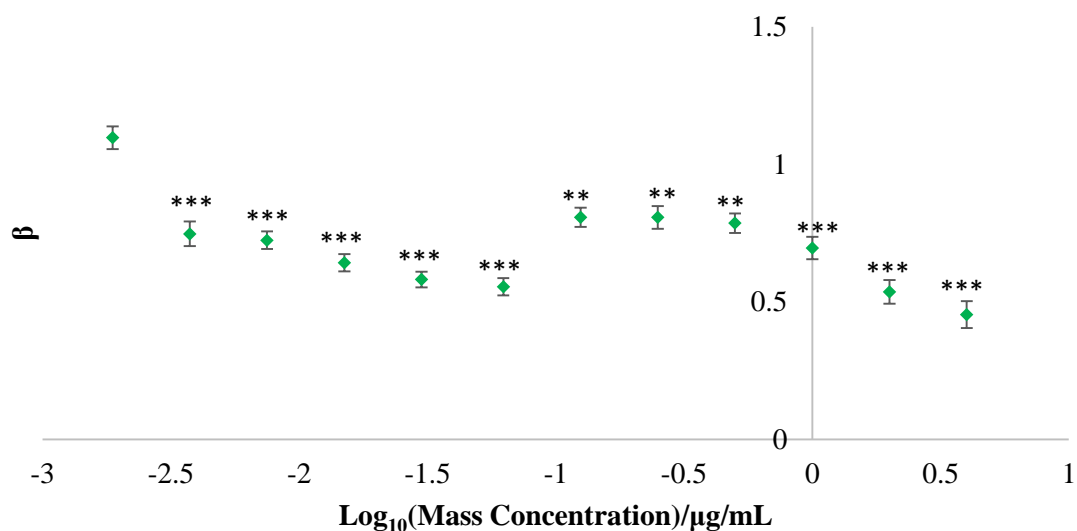


**Figure 5.7 Impact of RIF aqueous on mycobacterial growth.** Comparing the control (0 μg/mL) to each concentration of RIF aqueous using an ANOVA test (using general linear model with Tukey post test). Bar chart plot of fluorescence data ( $\beta$ ), showing where there is a significant difference between each RIF aqueous concentration on the growth of *Map* K10/GFP and the control (0 μg/mL). (Significance level is denoted by: <0.001 (\*\*\*), <0.01 (\*\*) and <0.05% (\*)). Each bar showing 2\* the SEM. Concentration plotted on the log scale.

### 5.3.2.3 Statistical Analysis 3

**Did the two forms of RIF (SDN and aqueous) differ significantly from each other on their overall (at all concentrations/times) inhibition of the growth of *Map* K10/GFP?**

To determine whether there was an overall significant difference between the growth inhibition of *Map* K10/GFP over the 7 day fluorescence assay when treated with RIF SDN or RIF aqueous, an ANOVA (using a general linear model with Tukey post-test) was employed. The log data (of the fluorescence readings) was utilised in the analysis and compared for the 2 forms of RIF (SDN and aqueous) and all the different concentrations and time points (i.e. the two mass data sets were compared). Overall, the treatments were found to be highly significantly different ( $p < 0.001$ ). Although the two forms of the drug differed significantly from each other in their effect on *Map* K10/GFP, at the higher concentrations the two treatment types had very similar effects on the mycobacterial growth (Fig 5.2 [a-b]) and as RIF SDN has excipients and stabilisers, they could have been enhancing or inhibiting the SDNs action on *Map* K10/GFP therefore a direct comparison is not possible by this means. Overall, a significant difference would be expected when one treatment type had 30% drug whereas the other had >97% drug.

These results were plotted in a boxplot (Fig 5.8) to allow a visualisation between the treatment types, with the interquartile range box displaying 50% of the data, the extending lines (whiskers) representing the upper and lower distribution in the data points and where \* represented data outliers.

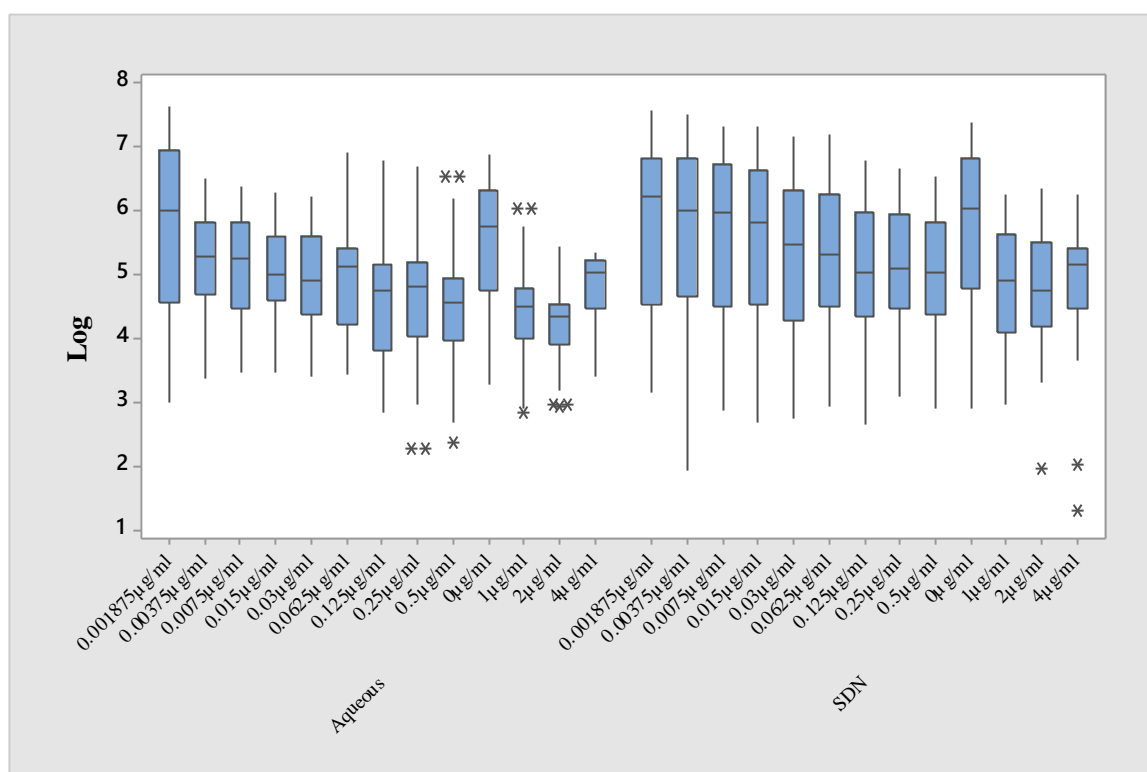


**Figure 5.8 Treatment data summary.** Boxplot displaying the data spread between RIF in an aqueous form and an SDN form, where the log has been calculated from the raw data of mycobacterial growth over 7 days. (\* denotes outliers in the data sets). These two data sets were highly significantly different from each other ( $p < 0.001$ ). The RIF SDN data from each concentration appears to be more spread than when in the aqueous form with longer whiskers and further placed outliers.

Please note the concentration is a mass concentration, where aqueous Rif = >97% drug and SDN = 30% drug.



#### 5.3.2.4 Statistical Analysis 4

**Was there a significant difference on the growth of *Map* K10/GFP between days when treated with the different forms of RIF?**

The substances were screened over 7 days, therefore it was important to see the affects of each substance between days, and how they compared between treatment types. To compare between different days for the different treatments, an ANOVA (using a general linear model with Tukey post-test) and 95% confidence interval for each treatment type (RIF SDN/aqueous) was utilised. There was an overall highly significant difference in mycobacterial growth between days for both treatment types (RIF SDN and RIF aqueous) ( $p < 0.001$ ) (where N= sample size and grouping represented statistical difference via a letter overlap). As shown in Figure 5.9 and 5.10, means that did not share a letter (or colour) were significantly different from each other, thus showing which days differed significantly.

For both treatments, via a measure of confidence intervals, day 0 did not overlap with any other day, suggesting that for all days tested, significant toxicity was observed (Tables 5.4 and 5.5). There was a significant difference for all days for RIF SDN with two exceptions (days 6 & 7 overlapped and 3 & 4 overlapped) whereas for RIF aqueous all days overlapped (groups of days that overlapped included 5, 7 & 4, 6 & 5, 7, 4 & 3, and 1 & 2) for RIF aqueous, except day 0 (Tables 5.4 and 5.5). From these results, it seems that there was less of an overlap (and therefore greater difference) between days when RIF was in the SDN form than when in the aqueous form, thus suggesting that RIF aqueous has a slower kill rate compared to RIF SDN. Additionally, the difference in R-Squared predicated (R-Sq pred) values further support this data. R-Sq pred indicates how well a model fits any given data set, the higher the value (0-100), the higher the accuracy

of the predictions made. For RIF SDN R-Sq pred was 80.24%, while for aqueous it was 51.01%, suggesting that there was greater significance between days when mycobacteria was treated with RIF as an SDN than in the aqueous form (Tables 5.4 and 5.5).

**Table 5.4 Difference in bacteria growth between days when treated with RIF SDN.**

Overall the significant difference of bacterial growth between days (ANOVA, Tukeys test) was highly significant ( $p < 0.001$ ) when treated with RIF SDN. Means that did not share a letter (or colour) were significantly different from each other. As shown, days 3 & 4 and days 6 & 7 were not significantly different from each other. Day 0 was significantly different from all other days.

Treatment	Day	N	Mean	Grouping
RIF SDN	7	63	6.53	A
RIF SDN	6	63	6.36	A
RIF SDN	5	54	6.04	B
RIF SDN	4	62	5.57	C
RIF SDN	3	58	5.39	C
RIF SDN	2	58	4.41	D
RIF SDN	1	59	4.11	E
RIF SDN	0	62	3.18	F

**Table 5.5 Difference in bacteria growth between days when treated with RIF aqueous.**

Overall the significant difference of bacterial growth between days (ANOVA, Tukeys test) was highly significant ( $p < 0.001$ ) when treated with RIF Aqueous. Means that did not share a letter (or colour) were significantly different from each other. As shown, there was some overlap between days (e.g. 4, 5 and 7). Day 0 was significantly different from all other days.

Treatment	Day	N	Mean	Grouping
RIF Aqueous	6	57	5.84	A
RIF Aqueous	5	57	5.54	A B
RIF Aqueous	7	62	5.38	B C
RIF Aqueous	4	60	5.37	B C
RIF Aqueous	3	62	5.12	C
RIF Aqueous	2	62	4.54	D
RIF Aqueous	1	59	4.19	D
RIF Aqueous	0	62	3.56	E

### 5.3.3 Colony Counts

Colony counts were measured following the growth of *Map* K10/GFP on solid agar after incubation for 12 weeks (from plating out at the end of the fluorescence assay following 7 the day exposure to the SDNs and aqueous drugs [control = 0 µg/mL]) as described in Chapter 2 (section 2.1.5). This experiment was conducted as a control alongside the fluorescence assay, as it is the conventional approach to assessing the impact of substances on mycobacterial growth.

Similarly to the metal/metal oxide NPs (Chapter 4), there was considerable variability in the data. Obtained data allow the toxicity of the test substances to be ranked RIF aqueous > RIF SDN > TRIPLE > DUAL SDN > INH aqueous (Fig. 5.9). Results for RIF in both forms, were quite comparable, akin to what was observed in the fluorescence assay results. However, the colony count data for TRIPLE SDN was unusual, particularly for concentrations 0.25 and 0.5 µg/mL where a very limited level of inhibition was observed (Fig 5.9). The results for INH were also comparable to the fluorescence assay results, where very little anti-mycobacterial properties were observed, however only 2 repeats were included for INH aqueous.

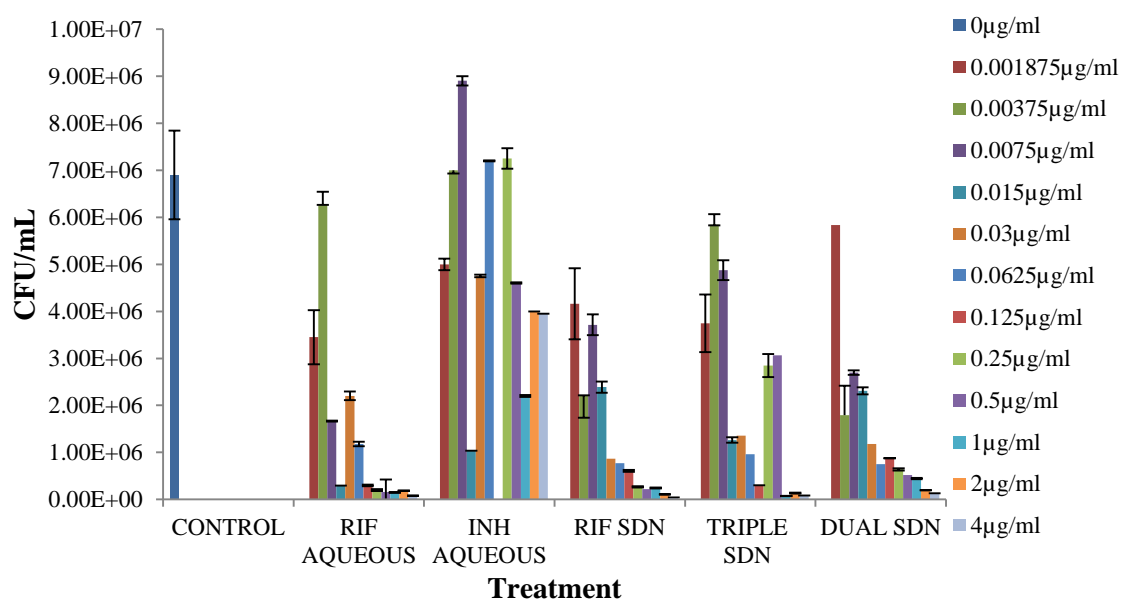


**Figure 5.9 Colony counts after 12 weeks culture on 7H11 agar.** Using conventional colony counts, the toxicity of the different treatments can be ranked in the following order: RIF aqueous> RIF SDN> TRIPLE> DUAL SDN> INH aqueous (although there is some ambiguity with the two of the TRIPLE SDN concentrations). Drug loading for each treatment differs (see Table 5.1). Each concentration displaying the SEM (n=min of 3 repeats, except INH where n=2).

### 5.3.4 Cytotoxicity of substances to macrophages

Cytotoxicity was tested over a concentration range of 0.0039 - 8  $\mu\text{g/mL}$ , by serial dilutions, using the alamar blue assay (Chapter 2, section 2.4). Results are expressed as in Chapter 4 (section 4.3.6) (Fig 5.10). Statistical significance to the control (no treatment [0  $\mu\text{g/mL}$ ]) was determined via an ANOVA (using a general linear model with Tukey post-test) (MINITAB<sup>®</sup>, version 17). Results were considered significant if  $p < 0.05$  (significance level was denoted by:  $p < 0.001$  [\*\*\*],  $< 0.01$  [\*\*] and  $< 0.05$  [\*]). No significant changes were observed in the cell viability for each substance at all concentrations tested,  $p > 0.05$  (Fig 5.10). At the lower concentrations, INH reduced cell viability more than the other substances, yet this was not significant from the control (Fig 5.10).

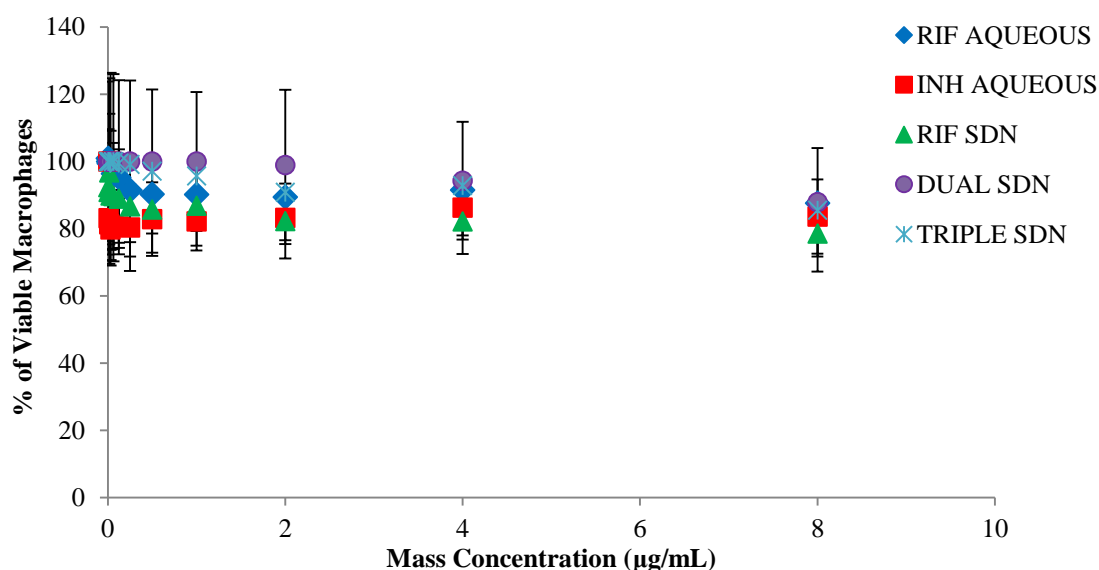


**Figure 5.10 SDN/drug cytotoxicity to macrophages after 24-hour incubation.** As shown, very little cytotoxicity was observed from the different substances, the cytotoxicity exerted was not found to be statistically significant ( $p > 0.05$ ) Each concentration displaying the SEM ( $n=3$ ).

### 5.3.5 *Map K10/GFP macrophage infection*

Using macrophage cells an infection model was designed to image the infection of macrophages by *Map K10/GFP*. All imaging was achieved using a Zeiss Axiovert 200M inverted Epi fluorescence microscope with an AxioCam MR3 camera. Optimisation of the protocol for the development of an *in vitro* macrophage infection model was required. It was important to firstly determine the optimal number of macrophages per chamber, the length of incubation period the macrophage cells required to successfully engulf foreign bodies under these experimental conditions, what MOI of mycobacteria (mycobacteria per macrophage) was suitable for imaging but minimised clumping, and finally the optimal lens resolution for these experiments. The overall aim was to image the uptake of SDNs into *Map K10/GFP* infected macrophages.

In each experiment undertaken, macrophage cells were grown in complete medium [without streptomycin or penicillin] for 24 hours prior to any infections/treatments at 37°C, 5% CO<sub>2</sub>. Infection/treatment were for 3 - 24 hour incubation periods (during optimisation experiments) at 37°C, 5% CO<sub>2</sub>. In all experiments, macrophages were seeded at a density of 5 x10<sup>5</sup>/mL in chambered slides at a final volume of 200 µL per chamber, the DIC was grey, DiD labelled SDNs (RIF [red] and TRIPLE [yellow]), NP beads (pink), *Map K10/GFP* (green), macrophage nucleus ([DAPI] blue) and F-actin ([phalloidin] cyan). Appropriate controls were included in each experiment (e.g. macrophage cells only [no infection or treatment]).

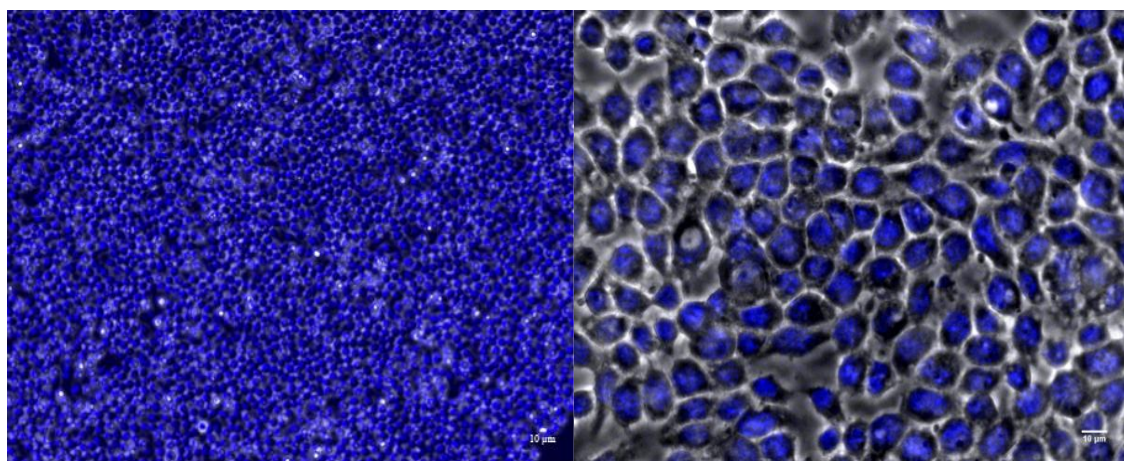
Figure 5.11 (a-d) illustrates control macrophages, showing healthy cells grown in complete medium, stained with DAPI. The four images (a-d) demonstrate the difference between the magnifications employed ([a] 10X, [b] 40X, [c] 63X, [d] 100X), with the DAPI and DIC channels in use to show the cell nuclei and the cell edges with some

structural detail. Magnification 63X (Fig 5.11 c) was found to give optimal information; displaying enough cells to give a general representation of any infection/treatment.

Figure 5.12 (a-b) illustrates control macrophages, showing healthy cells grown in complete medium, stained with DAPI and phalloidin. As displayed, the F-actin was stained to give information on the cytoskeleton. Although it gave a clearer portrayal of the control cells, it was not used in experimental conditions due to a crossover between its wavelength and the far-red wavelength of the DiD SDNs (CY5 channel). As shown in Figure 5.12 (b) in some instances, the DIC channel was removed to display only the stained cellular components of interest. This made interpretation of some images easier and allowed a clearer visualisation.

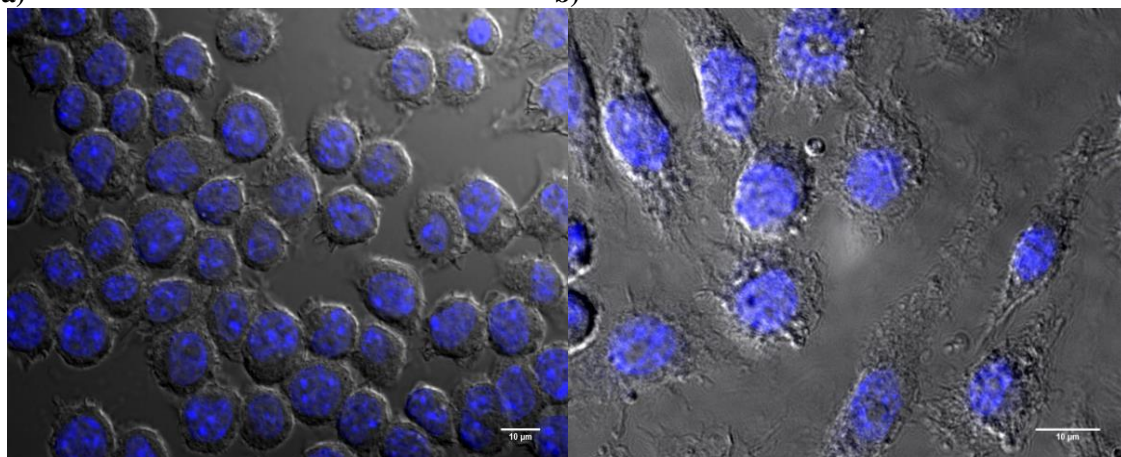
Figure 5.13 (a-c) illustrates macrophages with different MOIs of *Map* K10/GFP (5, 10 and 30). Mycobacteria were internalised by the macrophage cells and there was little/no residual GFP detected out with the cell cytoskeleton. Figure 5.13 (c[ii]) has had the DIC removed to allow a clearer visualisation of *Map* K10/GFP engulfed by the cells, although not all macrophages had mycobacteria. The rod-like structures could be visualised, and at an MOI of 30 mycobacterial clumping had occurred (Fig 5.14). Although engulfed by the macrophages, the mycobacteria were still readily detectable at all magnifications tested.





a)

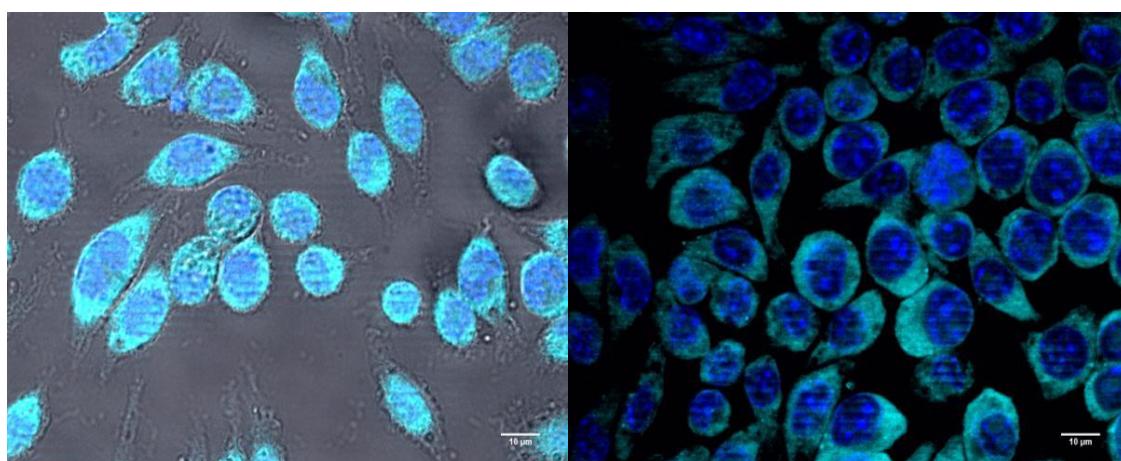
b)



c)

d)

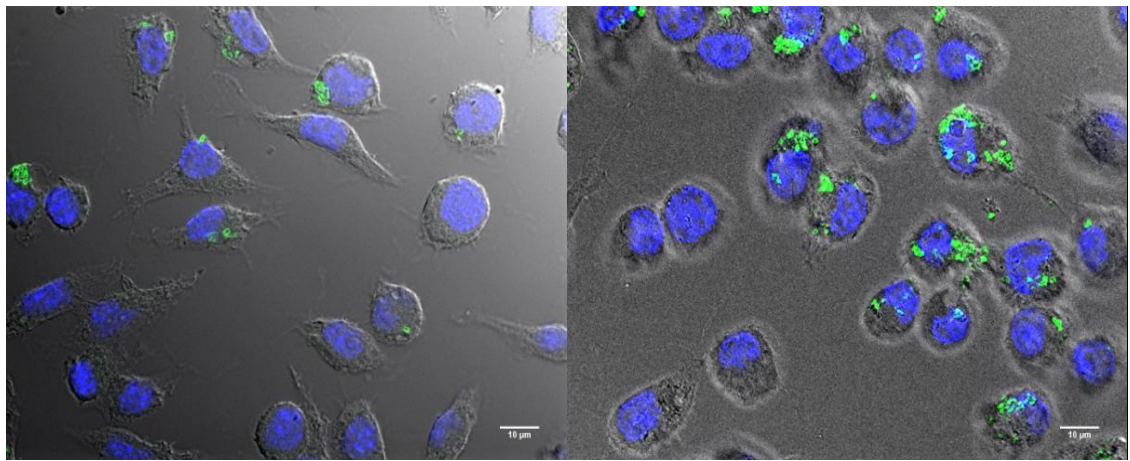
**Figure 5.11 (a-d) Controls for optimisation: macrophages with nuclei stain.** Macrophages, after 24 hours incubation, at magnifications 10X (a), 40X (b), 63X (c) and 100X (d). The intense DAPI nuclei stain (blue) was utilised as a marker for focusing in all images (scale bars all 10 µM). From these images, the 63X magnification was found to be most informative. DIC: grey, DAPI: blue.



a

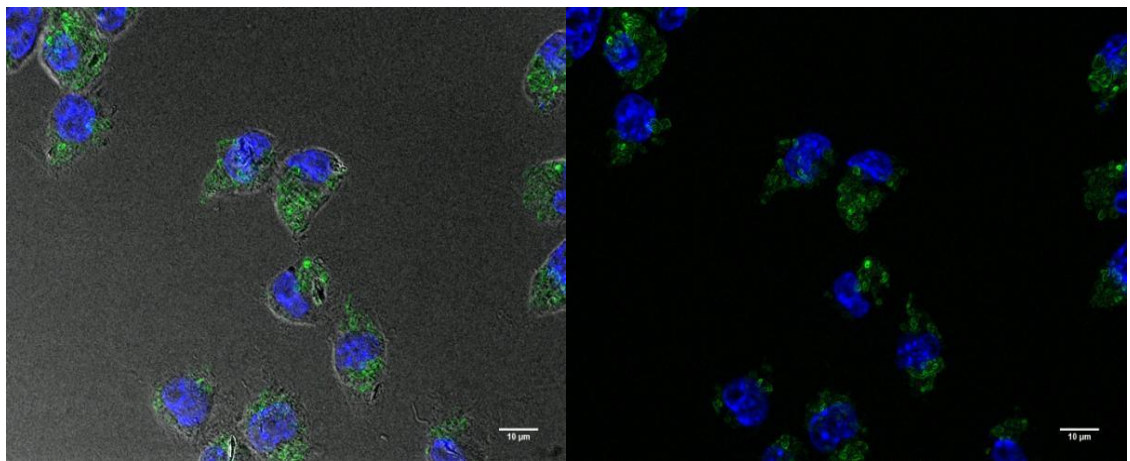
b

**Figure 5.12 (a-b) Controls for optimisation: macrophages with nuclei and F-actin stain.** Macrophages after 24 hour incubation at 63X, stained with DAPI (blue) and F-actin stain phalloidin (cyan) (DIC, DAPI & CY5 channels). Image (b) has had the DIC channel removed to show the cellular cytoskeleton. Some elongated, stretching cells were observed. DIC: grey, DAPI (nuclei): blue, phalloidin (F-actin): cyan (scale bars all 10 µM).



a)

b)



c) (i)

(ii)

**Figure 5.13 Infected macrophages.** Macrophages infected with *Map* K10/GFP at a MOI 5 (a), MOI 10 (b) and MOI 30 (c[i]) (4 hour infection) at 63X (DIC, DAPI & GFP) where (c[ii]) has had the DIC channel deleted). DIC: grey, DAPI (nuclei): blue, GFP (*Map*): green (scale bars all 10 μM).



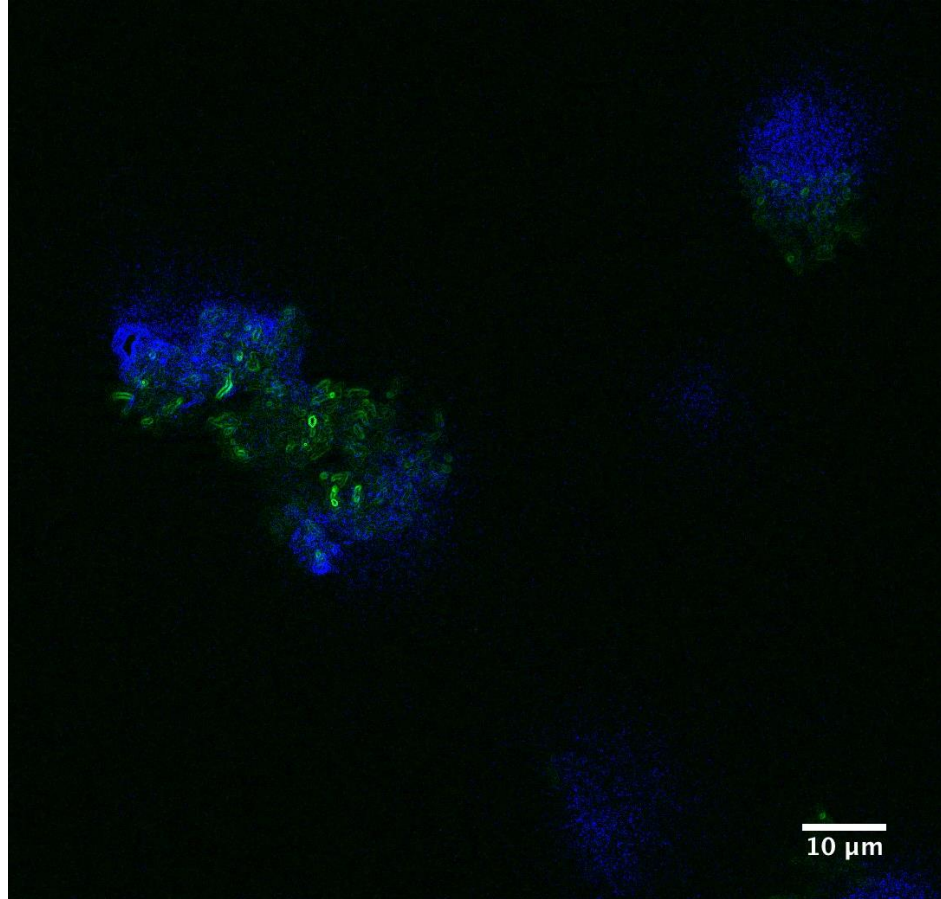


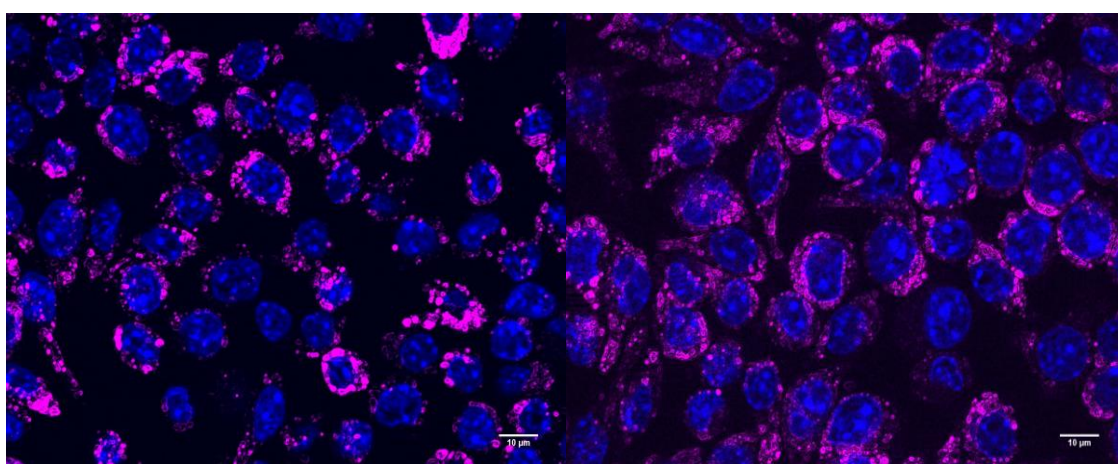
**Figure 5.14 *Map* K10/GFP infected macrophage.** Two macrophages engulfing a clump of *Map* (MOI 30) with DIC removed 100X. Individual bacilli are visible. DAPI (nuclei): blue, GFP (*Map*): green (scale bar 10 μM).

### ***5.3.6 Uptake of SDNs by macrophages***

#### ***5.3.6.1 Macrophages and 20 nm carboxylated polyester NP beads***

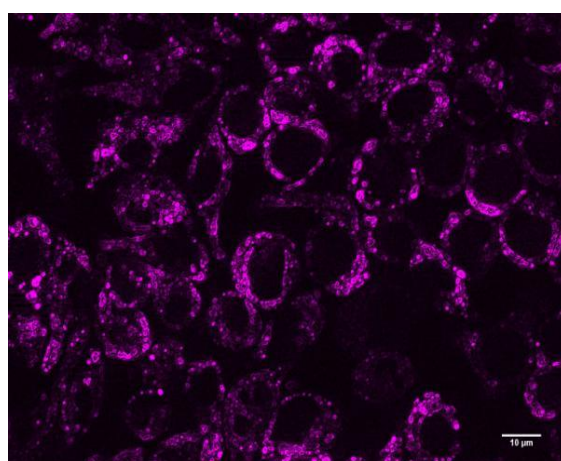
Using J774A.1 (macrophage-like) cells an infection model was designed to image the uptake of NPs by macrophages. As a control, non-toxic, fluorescent 20 nm NP beads (NP beads) (section 5.2.8) were initially used to ensure the macrophages would engulf NPs in these conditions, and to identify an appropriate incubation period which allow NP uptake to be visualised in studies with SDNs and thirdly to determine a suitable concentration of SDNs to treat the macrophages with for imaging purposes.

Figure 5.15 (a,b) illustrates macrophages engulfed NP beads 3 and 24 hours post exposure. From these initial experiments, it was determined 3 hours (possibly less) would be a suitable incubation period to allow uptake of NP by these macrophage cells to be investigated. Figure 5.15 (c) is a replication of Figure 5.15 (b) but has had the DAPI channel removed from the image to show the sub-cellular location of the NPs. As shown, the NPs, which had high intensity fluorescence, look to have been readily engulfed by the macrophages at a concentration of 20  $\mu\text{g/mL}$ , and are localised around the cell nuclei (blue) and are located throughout the cytoplasm. Based on these findings it was decided that a lower concentration of NPs (10  $\mu\text{g/mL}$ ) would be tested in future experiments.



a)

b)



(c)

**Figure 5.15 (a-c) Control for optimisation: macrophages exposed to NP beads.** Macrophages following 3 hour (a), 24 hour (b) incubation with 20  $\mu\text{g/mL}$  NP beads 63X (DIC, DAPI & CY3) where (c) has had the DAPI filter removed from (b) to allow a clearer representation of the NP beads around the nuclei. DAPI (nuclei): blue, NP beads: pink (scale bars all 10  $\mu\text{M}$ ).

Figure 5.16 illustrates macrophages which were infected with *Map* K10/GFP (MOI 5) and then exposed to NP beads at a concentration of 10  $\mu\text{g/mL}$ . Mycobacteria and NP were internalised by the macrophages. It was difficult to determine whether co-localisation was occurring or whether the NP beads were associated with the mycobacteria or not, as the GFP and CY3 signals were found throughout the field of view, suggesting good dispersion of NPs and mycobacteria.

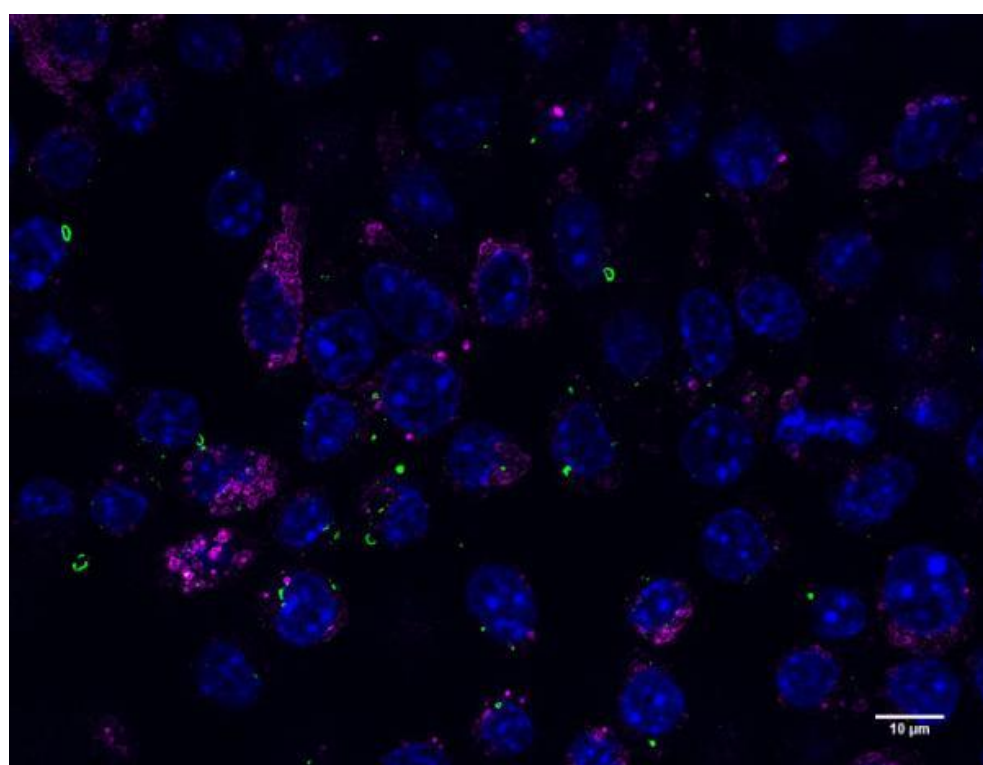


**Figure 5.16 Control for optimisation: infected macrophages exposed to NP beads.** *Map* K10/GFP (MOI 5) infected macrophages following 4 hour incubation with 10  $\mu\text{g/ml}$  NP beads 63X. DAPI (nuclei): blue, GFP (*Map*): green, NP beads: pink (scale bars all 10  $\mu\text{M}$ ).

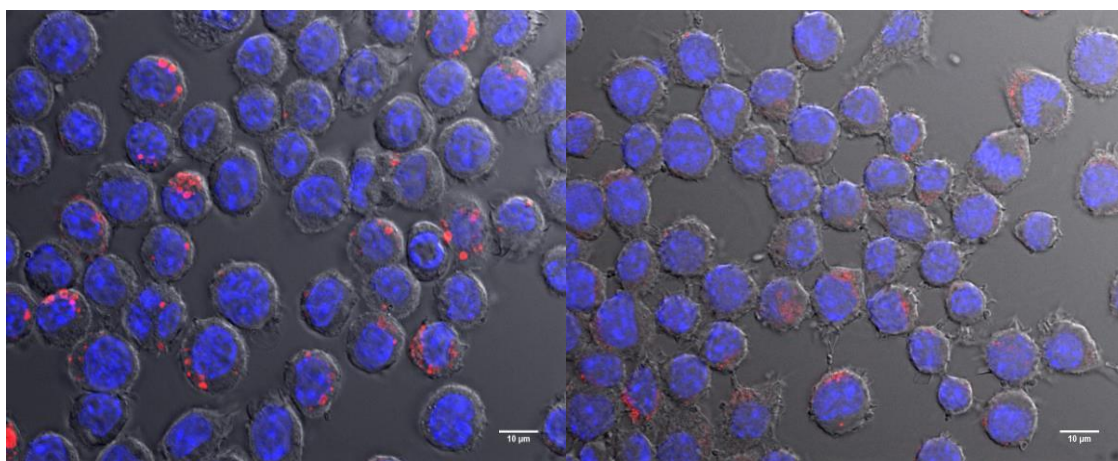
### ***5.3.6.2 Macrophages and uptake of SDNs***

Following the successful imaging of internalised NP polystyrene beads, macrophages were then treated with the DiD labelled SDNs and incubated for 4 hours. Figure 5.17 (a-c) and 5.18 (a-c) illustrates macrophages and DiD labelled RIF and TRIPLE SDNs at a concentration of 10  $\mu\text{g/mL}$ . The RIF SDNs (Fig 5.17 a-c) were not agglomerated throughout the field of view, when imaged at 63 X. In Figure 5.17 (c) the DIC channel has been removed (from b) to try and better display the sub-cellular location of SDNs. Overall, RIF SDNs were relatively well dispersed, where approximately 50% of macrophages had internalised (or surface bound) RIF SDNs. Figure 5.17 (a) suggests that SDNs were engulfed as small agglomerates by the macrophages. TRIPLE SDNs look to be quite agglomerated in (or on) the macrophages (Fig 5.18) thus concurring with DLS results for these SDNs (where average particle size was  $> 415.3 \text{ nm}$ ). Figure 5.18 (a) has only a weak CY5 signal emitting from the macrophage cells, and the concentration of SDN looked to be low. Figure 5.18 (b) depicts 2 large agglomerates, within (or surface bound) a macrophage cell. The SDNs may have been engulfed as an agglomerate or they may have compartmentalised intracellularly. Figure 5.18 (c) has had the DIC channel has been removed to try and better display the SDN agglomerates.

The RIF SDNs were the smaller of the two SDNs with DiD incorporated into their manufacture, therefore it seems that they dispersed evenly in the medium thus affecting their (possible) uptake by macrophages. It is possible that the macrophages did not engulf the TRIPLE SDNs as readily. As weaker CY5 signal was emitted for the TRIPLE SDN experimental chambers, during the cell wash prior to staining extracellular SDN may have been removed hence was less visible. Overall, there appeared to be no residual

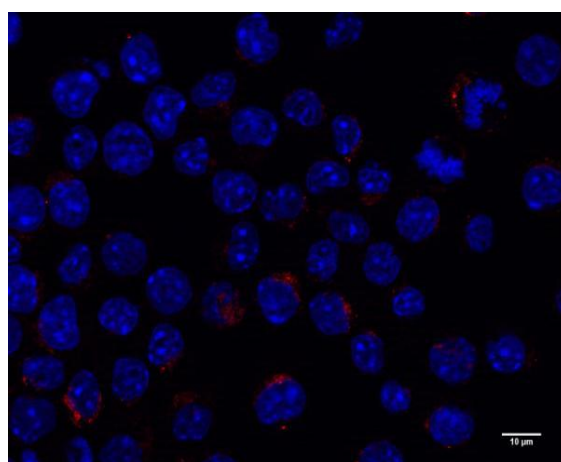
antibiotic, and it appeared that the SDNs were engulfed by the macrophages and not attaching to the cell surfaces, although this needed to be confirmed.





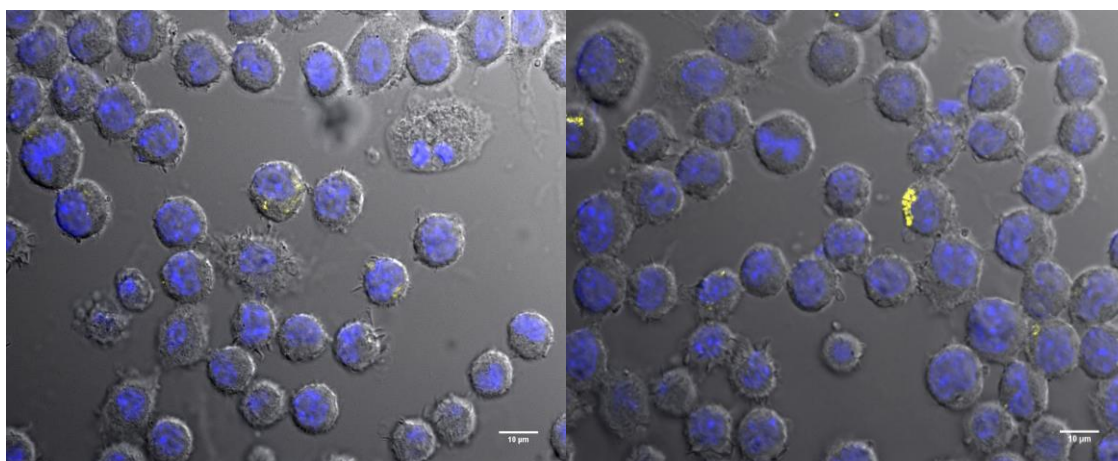
a)

b)



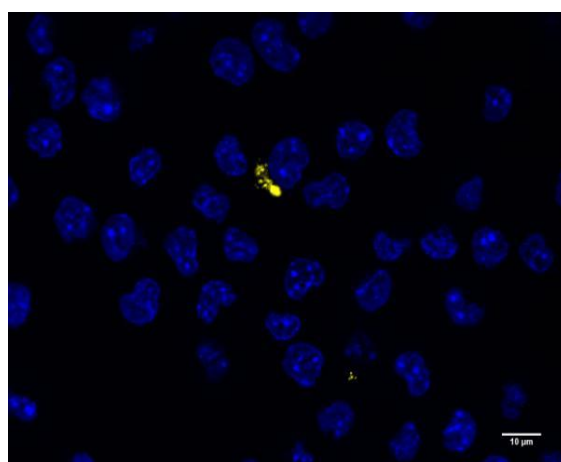
(c)

**Figure 5.17 (a-b) RIF SDN treatment to macrophages.** Macrophages following 4 hour incubation with 10  $\mu\text{g/mL}$  RIF SDN 63X where (c) has had the DAPI filter removed from (b) to allow a clearer representation of the SDNs orientation around the cell nuclei. RIF SDNs have either formed small agglomerates or cellular uptake and trafficking caused this mass formation in certain areas. DIC: grey, DAPI (nuclei): blue, CY5 (RIF SDN): red (scale bars all 10  $\mu\text{M}$ ).



a)

b)



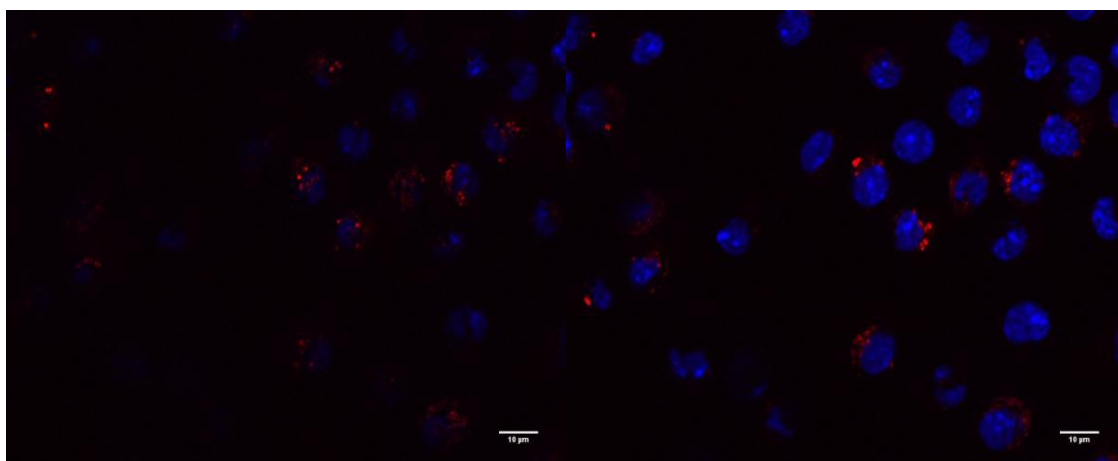
(c)

**Figure 5.18 (a-c) TRIPLE SDN treatment to macrophages.** Macrophages following 4 hour incubation with 10  $\mu\text{g/mL}$  TRIPLE SDN 63X where (c) has had the DIC filter removed to allow a clearer representation of the SDNs orientation around the cell nuclei. TRIPLE SDN look to have formed small agglomerates, and were not dispersed as well as RIF SDNs. At 10  $\mu\text{g/mL}$  TRIPLE SDNs are not as well distributed as the NP beads or the RIF SDNs. DIC: grey, DAPI (nuclei): blue, CY5 (TRIPLE SDN): yellow (scale bars all 10  $\mu\text{M}$ ).

### ***5.3.6.3 Macrophages and SDNs: 3D images***

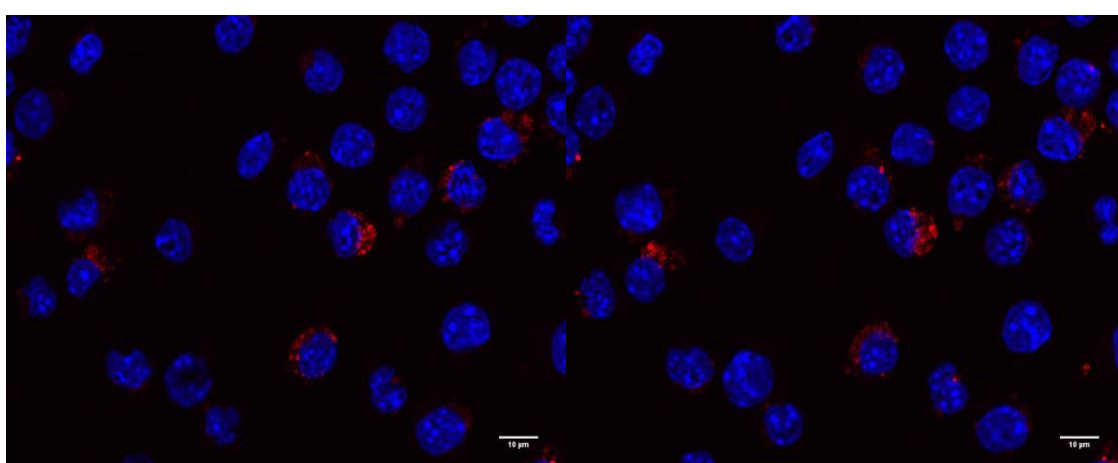
Following the successful imaging of DiD incorporated SDNs with macrophages, it was important to determine whether the SDNs were internalised by the macrophages, or if they were surface bound (e.g. if they weren't removed following cell washing) and to visualise the drugs location throughout the macrophage. This was achieved by using Z-stacks to examine individual layers of the macrophage cells. Optimisation for Z-stacks was achieved using the microscopes internalised software, with stack depth approximately 0.25-0.5  $\mu\text{M}$  in each case.

RIF SDN at 10  $\mu\text{g/mL}$  (4 hours incubation) treated macrophages were imaged using Z-stacks. Figure 5.19 (a-f) illustrates a 20 image Z-stack of SDN treated macrophages and Figure 5.20 (a-b) illustrates the condensed image of all the stacks. Figure 5.19 (a-f) and Figure 5.20 (a-b) were strongly suggestive that RIF SDNs were internalised by the macrophages, and were not surface bound. Figure 5.19 (a-f) displays RIF SDNs throughout the layers, orientated around the cell nuclei as with the NP beads previously. Small agglomerates were visible of the SDNs throughout the cells. Figure 5.20 (a) displays the condensed stack, in a 2D image, whereas 5.20 (b) displays the 3D image to show the spread and depth of the RIF SDNs compared to the cell nuclei.



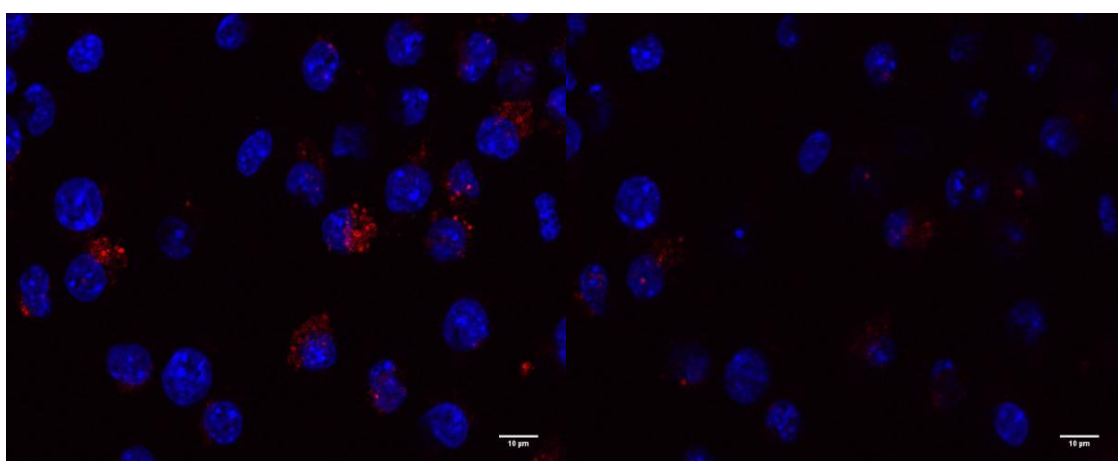
(a) Stack 1

(b) Stack 5



(c) Stack 8

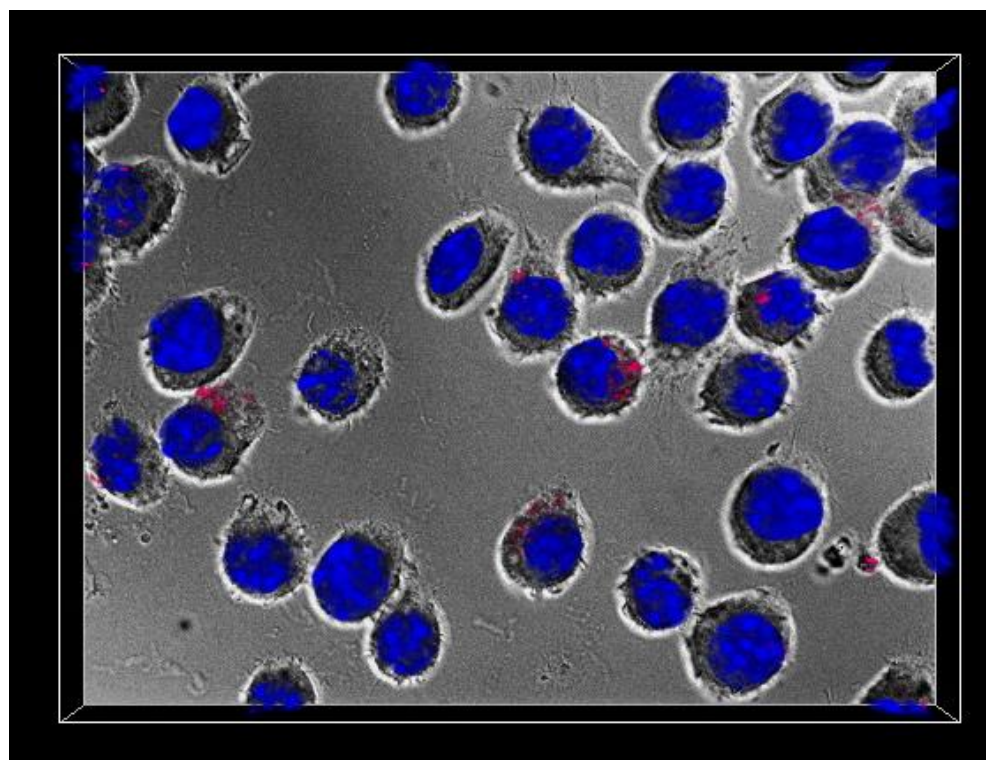
(d) Stack 12



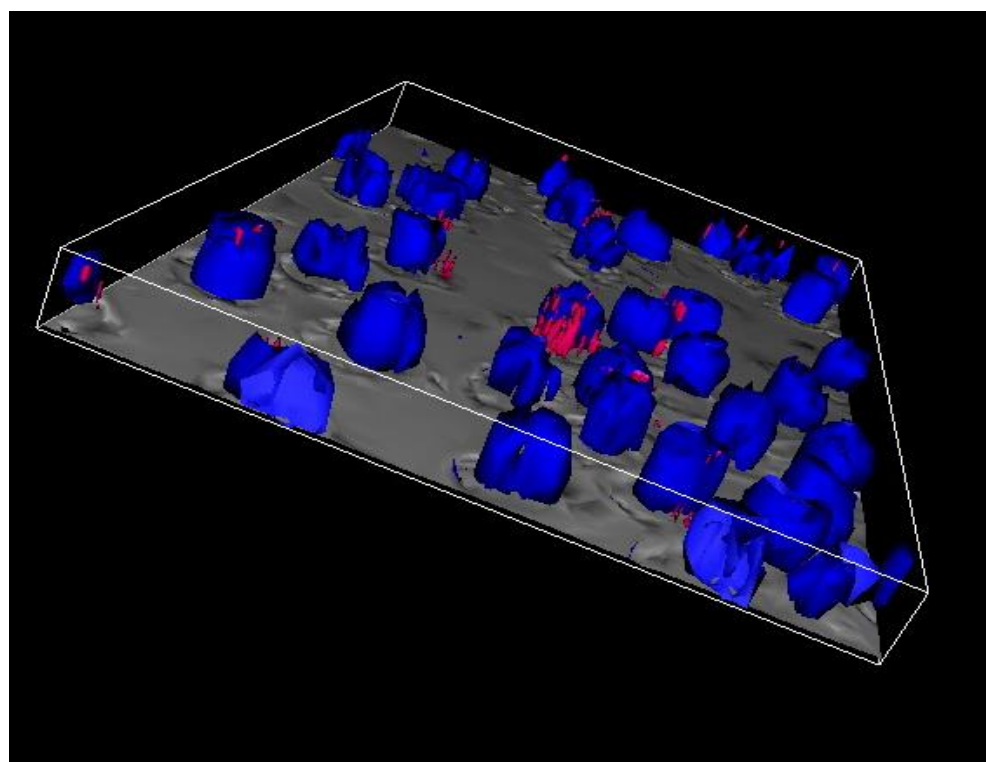
(e) Stack 17

(f) Stack 20

**Figure 5.19 Separated Z-stacks of macrophages following 4 hour incubation with 10 µg/mL RIF SND.** The Z-stacks illustrate the internalisation of RIF SDN throughout the macrophage and that the antibiotic was not only surface bound (all scale bars 10 µM). DAPI (nuclei): blue, CY5 (RIF SDN): red (scale bars all 10 µM).



a)



b)

**Figure 5.20 (a-b) 3D images.** Z-stacks (from Fig 5.19) resorted using Zeiss Axio vision Rel 4.8 of macrophages following 4 hour incubation with 10  $\mu\text{g/mL}$  RIF SND where (b) displays a different orientation of the Z-stack (created using Zeiss Axio vision Rel 4.8). DIC: grey, DAPI (nuclei): blue, CY5 (RIF SDN): red.



### 5.3.7 *Map K10/GFP infected macrophages and SDNs*

#### 5.3.7.1 *RIF SDNs and infected macrophages*

Next, the ability of *Map K10/GFP* infected macrophages to internalise SDNs (as with the NP beads) was investigated. To do so, macrophages were infected with *Map K10/GFP* (MOI 10) and then incubated with RIF SDNs (20 µg/mL) for 4 hours. Figure 5.21 depicts the detection of mycobacteria and RIF SDN in the cell cytoplasm. Although both mycobacteria and SDNs were detected from initial imaging, it was unclear whether they were both internalised by the macrophages and whether they were co-localising or not. Therefore Z-stacks were utilised again. Figure 5.22 illustrates a resorted Z-stack following RIF SDN (10 µg/mL) treatment to a *Map K10/GFP* (MOI 10) infected macrophage. This suggests possible co-localisation within the macrophage, as both the CY5 and GFP signals were emitting from a close (or same) cellular region. Figure 5.23 (a) illustrates *Map K10/GFP* (MOI 10) infected macrophage with RIF SDNs at a concentration of 10 µg/mL. As shown, mycobacteria and SDNs appeared to be enclosed within a cellular vacuole (possibly a lysosome). When the images from each channel were opened individually (Fig 5.23 c-d), it was clear that the structure the mycobacteria were held within was a very contained compartment, such as a vacuole. The same image was also imaged as a Z-stack. As illustrated in Figure 5.24 (a) from the Z-stack it was evident that both GFP and CY5 were detected throughout the cell. Using the Zeiss Axio vision Rel 4.8 software, the 3-D image was manipulated to an angle where the orientation within the cell was visible (Fig 5.24 b).

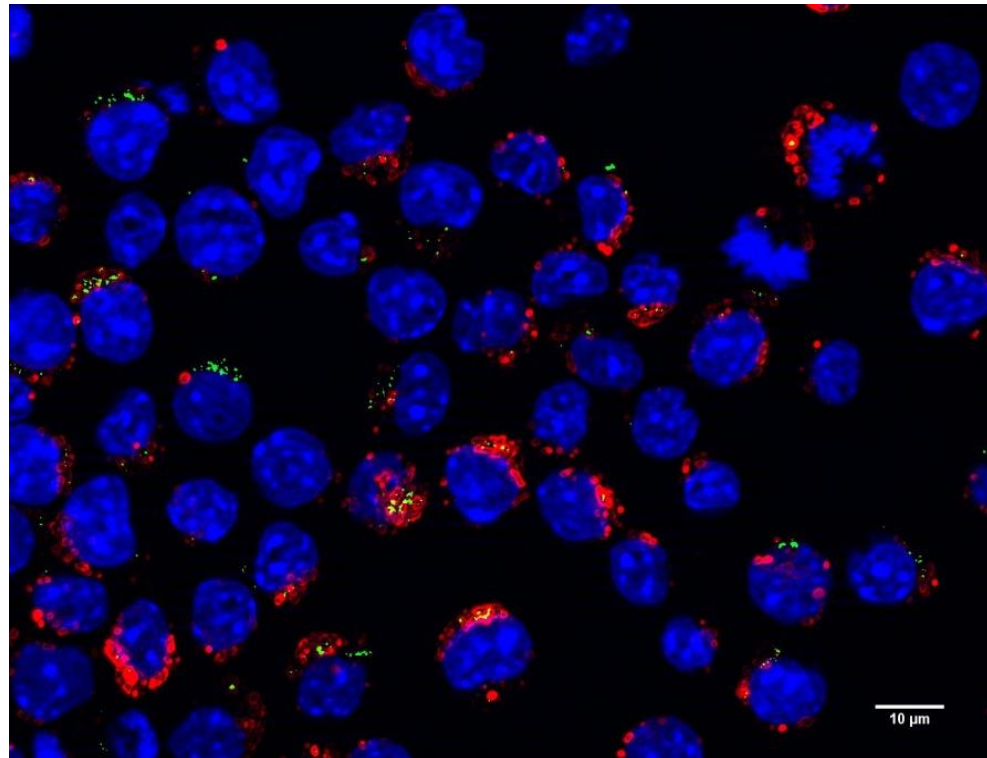


**Figure 5.21 Infected macrophages treated with RIF SDNs.** *Map* K10 GFP (MOI 10) infected macrophages following 4 hour incubation with 20  $\mu\text{g/mL}$  RIF SDN and 63X. DIC: grey, DAPI (nuclei): blue, GFP (*Map*): green, CY5 (RIF SDN): red (scale bars all 10  $\mu\text{M}$ ).

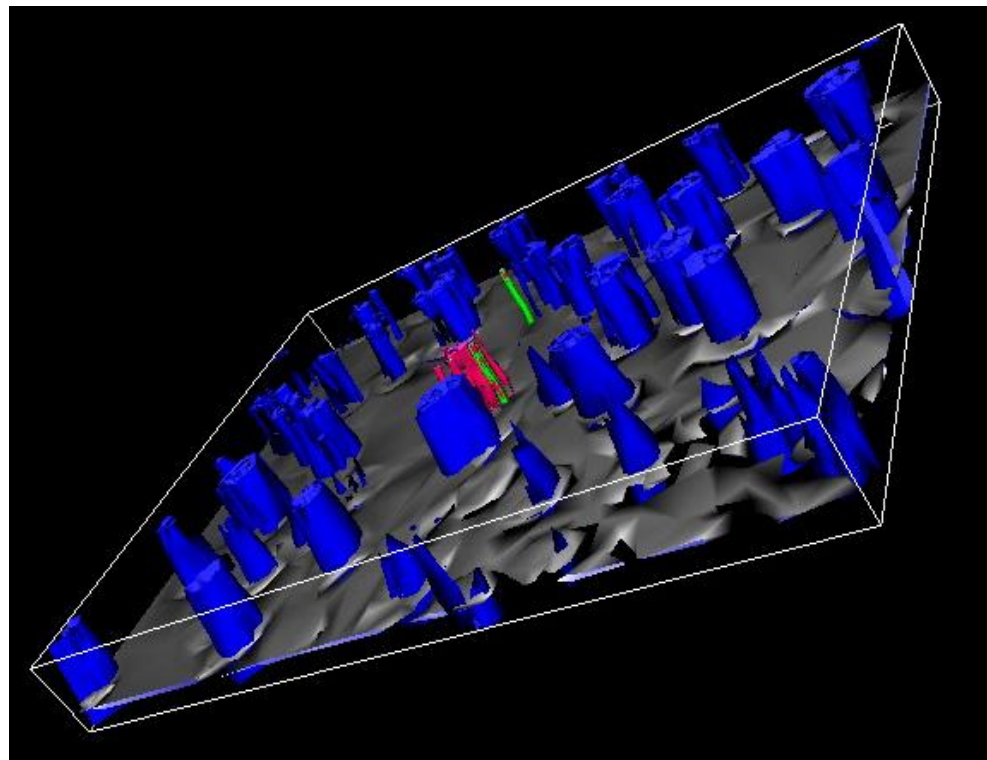
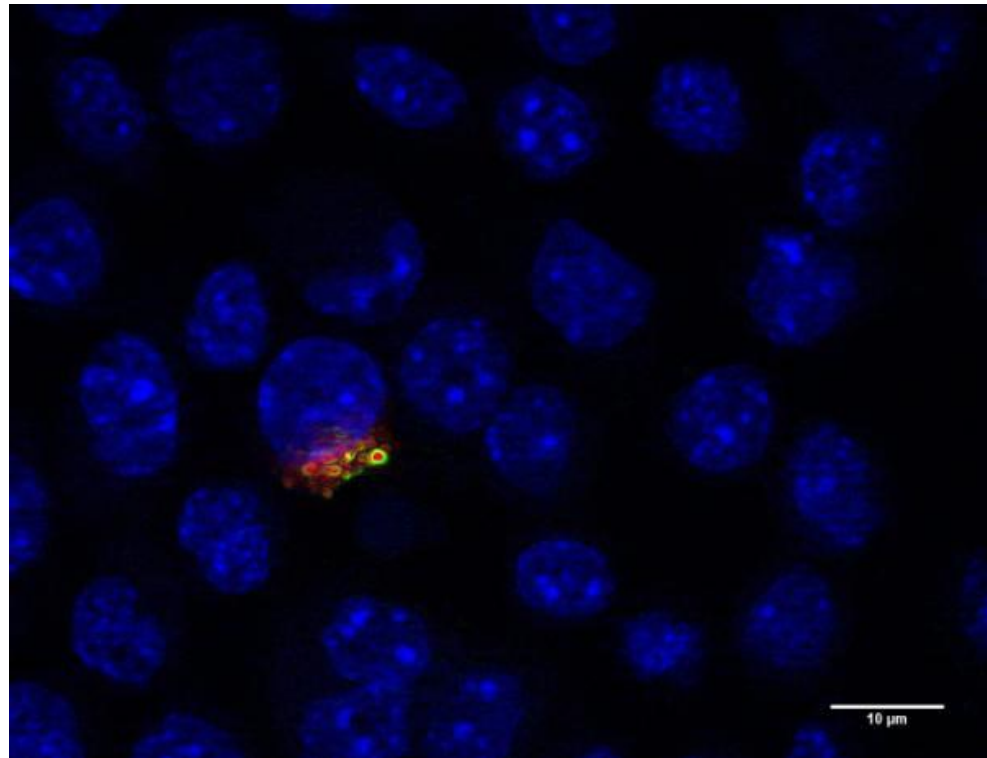
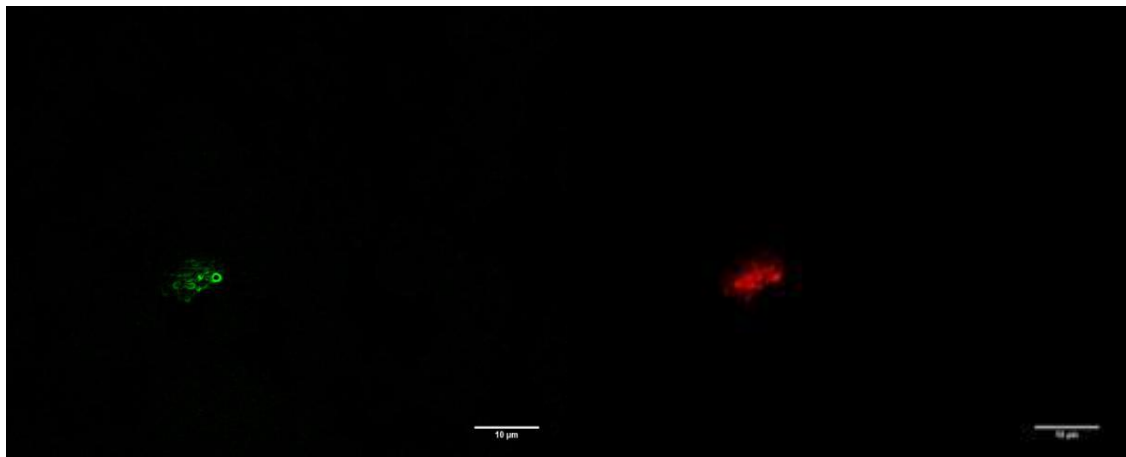


**Figure 5.22 3D image of infected macrophages.** *Map* K10 GFP (MOI 10) infected macrophages following 4 hour incubation with 10  $\mu\text{g/mL}$  RIF SND 63X. Z-stacks resorted using Zeiss Axio vision Rel 4.8. DIC: grey, DAPI (nuclei): blue, GFP (*Map*): green, CY5 (RIF SDN): red.



a)

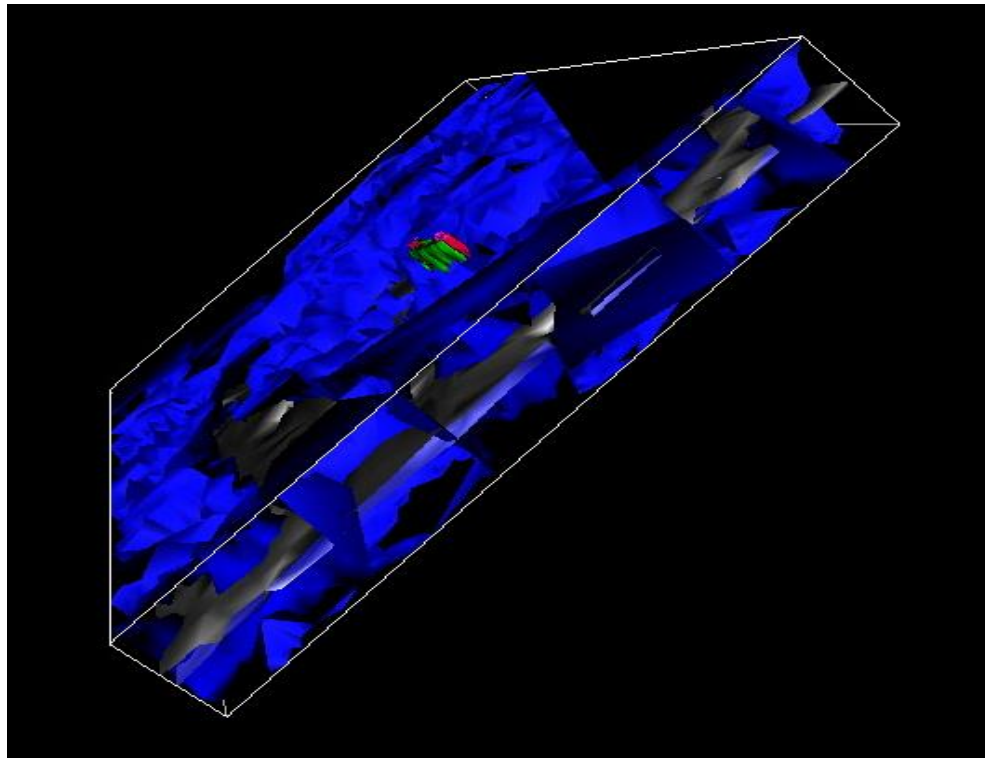


b)

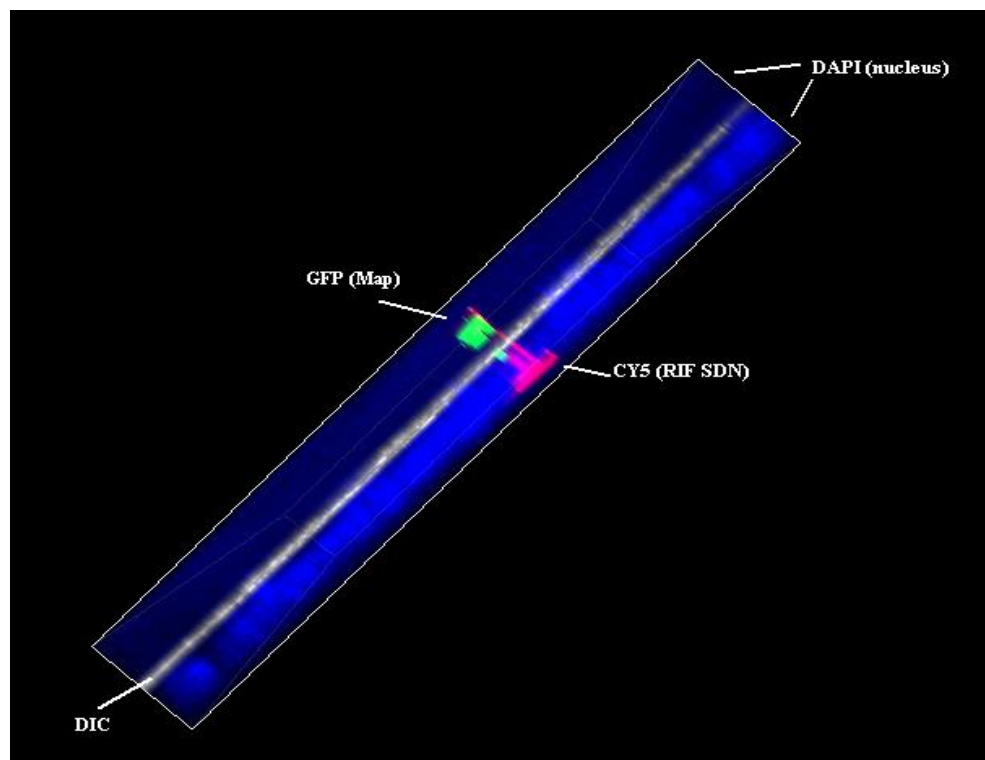
c)

**Figure 5.23 (a-c) Infected macrophages with RIF SDN.** *Map* K10 GFP (MOI 10) infected macrophages following 4 hour incubation with 10 µg/ml RIF SND 63X. The yellow signal is indicative of two overlapping fluoresce signals thus being indicative of co-localisation of mycobacteria and SNDs. (b) depicts the GFP (*Map* K10/GFP) signal only (c) depicts the CY5 (SDN) signal only, with DAPI and DIC removed. DIC: grey, DAPI (nuclei): blue, GFP (*Map*): green, CY5 (RIF SDN): red (scale bars all 10 µM).





a)

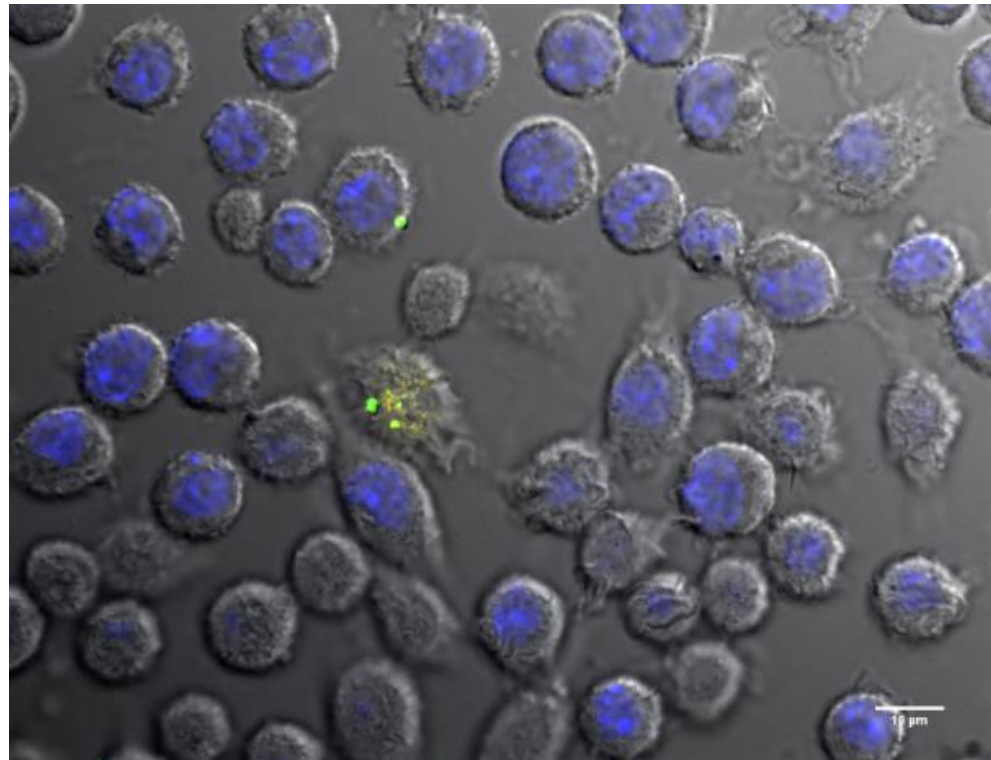


b)

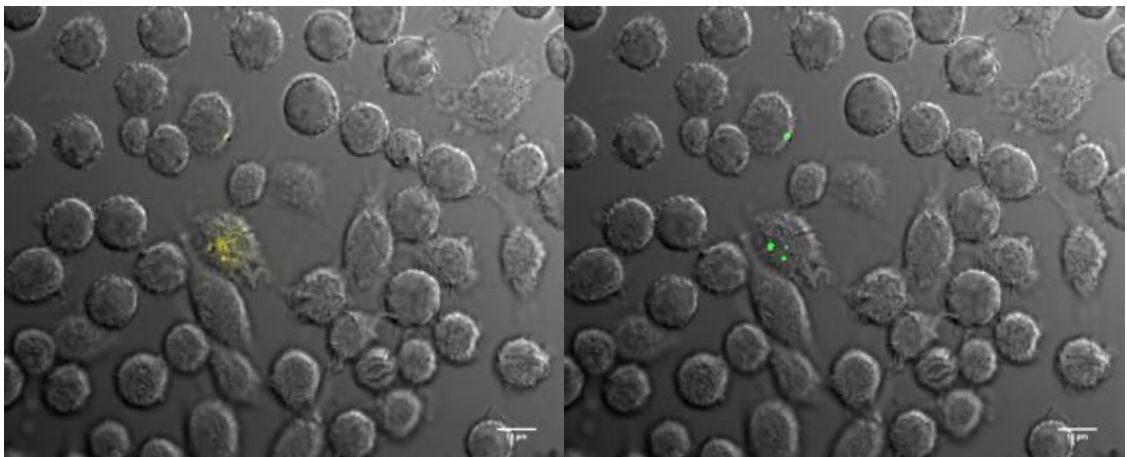
**Figure 5.24 (a-b) Infected macrophages with RIF SDN.** Z-stack resorted of Figure 5.23 using Zeiss Axio vision Rel 4.8. The different angles of the Z-stacks display the orientation of *Map* K10/GFP and depicts SDN throughout the macrophage. An overlap in the two signals was indicative of co-localisation. DIC: grey, DAPI (nuclei): blue, GFP (*Map*): green, CY5 (RIF SDN): red.

#### ***5.3.7.2 TRIPLE SDNs and infected macrophages***

Although the TRIPLE SDNs did not appear to be so readily engulfed by the macrophages compared to the RIF SDNs, a similar intracellular phenomenon was detected for the TRIPLE SDNs and *Map* K10/GFP. As shown in Figure 5.25 the mycobacteria and TRIPLE SDN were possibly co-localising within the same macrophage organelle. The green GFP (*Map* K10/GFP) and the yellow CY5 (SDN) signals were very intense from the same cellular area, and another signal was not detected elsewhere within the field of vision. This overlap in signals was indicative of co-localisation.



a)



b)

c)

**Figure 5.25 (a-c) Infected macrophages with TRIPLE SDN.** *Map* K10 GFP (MOI 10) infected macrophages following 4 hour incubation with 10  $\mu\text{g/mL}$  TRIPLE SDN 63X. The intense yellow signal (a) was indicative of two overlapping fluorescence signals thus suggesting co-localisation of mycobacteria and SNDs. (b) depicts the GFP (*Map* K10 GFP) signal only (c) depicts the CY5 (SDN) signal only with DAPI removed. Although and MOI of 10 was infected, a low proportion of macrophages have engulfed mycobacteria. DIC: grey, DAPI (nuclei): blue, GFP (*Map*): green, CY5 (TRIPLE SDN): yellow (scale bars all 10  $\mu\text{m}$ ).

### 5.3.8 Excitation/emission crosstalk

It was important to determine whether there was any level of crosstalk between the excitation and emission wavelengths of the mycobacteria and SDNs. Figure 5.26 (a) illustrates macrophages treated with SDNs at a concentration of 10  $\mu\text{g/mL}$ . Using this same field of view, the GFP filter was turned 'on' to see if GFP was detected. As shown in Figure 5.26 (b) the GFP was overexposed and gives the entire image a green covering, but it does not focus on the areas where the SDNs were in the macrophages. This control measure supported the hypothesis that when two signals (e.g. GFP and CY5) were emitting from the same cellular area, the likely co-localisation of mycobacteria and SDN within an organelle, such as a lysosome was occurring and it was not an artefact of ex/em crosstalk. This is further explained in the discussion.

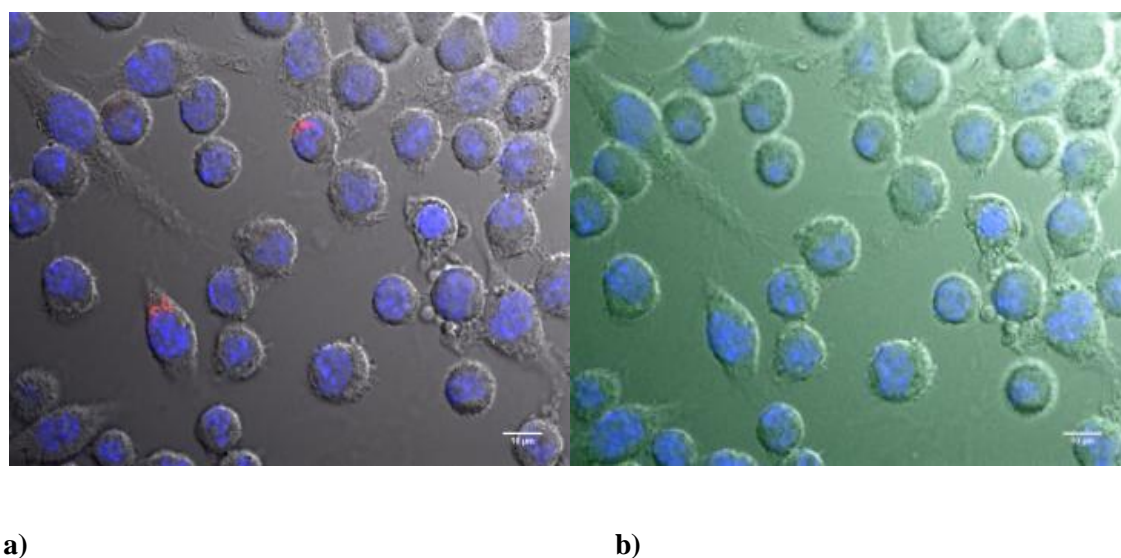


**Figure 5.26 (a-b) Crosstalk test:** Macrophages following 4 hour incubation with 10  $\mu\text{g/mL}$  RIF SDN 63 X (a) DAPI, DIC and CY5 filters and (b) DAPI, DIC, CY5 and GFP filters to determine whether there was any crosstalk between the two channels. As observed, GFP did not fluoresce where the SDNs were present within the cell, suggesting crosstalk was not occurring for the two wavelengths (all scale bars 10  $\mu\text{M}$ ). DIC: grey, DAPI (nuclei): blue, GFP (*Map*): green, CY5 (RIF SDN): red (scale bars all 10  $\mu\text{M}$ ).

### 5.3.9 Intracellular fluorescence intensity

One of the main observations from the fluorescence microscopy was the difference in the intensity of the GFP signal from macrophages with and without the SDNs. Although this was not quantified in this project, it was notable. At an MOI 10, in the cells without SDNs the green fluorescence from the *Map* K10/GFP was very intense, unlike when engulfed by cells and localised with SDNs. An example is given in Figure 5.27. It was likely that the mycobacteria were sub-lethally stressed due to the presence of the high concentration of antibiotic (this was a reproducible result) and therefore unable to emit fluorescence as intensely when macrophages were not treated with SDNs. Although this would need to be further tested.

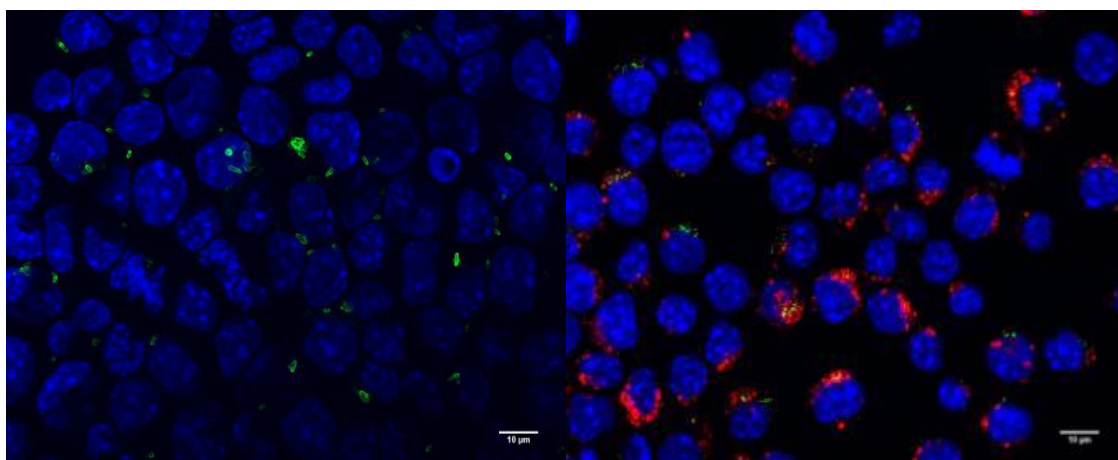


**Figure 5.27 (a-b) Control test: GFP intensity.** (a) *Map* K10 GFP (MOI 10) infected macrophages and (b) *Map* K10/GFP (MOI 10) infected macrophages treated with 10 µg/mL RIF SDN to compare fluorescence intensity. DAPI (nuclei): blue, GFP (*Map*): green, CY5 (RIF SDN): red (scale bars all 10 µm).

### 5.3.10 Phage amplification assay to quantify viable mycobacteria following drug contact

A preliminary study using the phage-PCR amplification assay was carried out to compare the killing of *Map* K10/GFP by RIF SDN to aqueous RIF, within a macrophage, after a 4 hour incubation. The assay was carried out at three MOIs (1,10 and 30) of *Map* K10/GFP (per macrophage). Control plates were macrophages infected with *Map* K10/GFP and not treated with any drug. Following 24 hour incubation with treatment then lysing of the macrophages to carry out the phage-PCR assay, confluent plaques formed on the soft agar and each plaque represented one *Map* K10/GFP cell. 'Neat' positive control plates (no treatment) had plaques which were too numerous to count (TNTC [often due to the merging of plaques]) and data was obtained from the serial dilutions of the same sample. Negative control plates (no mycobacteria) had no plaques. An example of a positive control plate is given in Figure 5.28, displaying TNTC plaques.

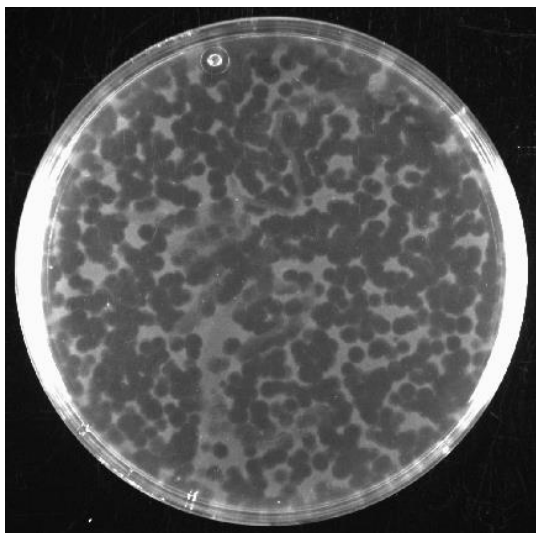


**Figure 5.28 Positive control (*Map* K10/GFP with no treatment following lysing of macrophage cells).** As shown, the confluent plaques (where one plaque represents one *Map* cell from the original sample) were TNTC and the merging of plaques was occurring.

The FASTPlaqueTB™ assay was only performed once; therefore no statistical analysis was possible on the data obtained. However, preliminary results were obtainable from the assay, which are displayed in the following figures. Results were calculated by counting the number of plaques visible on the agar, multiplying this by the dilution factor (e.g. 1 or 10 [depending on the serial dilution]) then dividing this by the volume of *Map* K10/GFP added to the phage assay (100 µL) (i.e. number of plaques\* dilution factor/volume of culture plates).

Figure 5.29 (a-c) displays the results for both treatment types (RIF SDN and RIF aqueous) at the three different MOIs of mycobacteria. Figure 5.29 (b-c) suggests that RIF SDN was more toxic to *Map* K10/GFP following contact within an intracellular environment. The data from this pilot study suggests that an MOI of 1 (1 mycobacteria per macrophage) was too low a number, as no counts were found in either of the experimental plates (Fig 5.29a). Figure 5.29 (b) shows that at an MOI 10, plaques for both treatment types were visible (although less plaques were visible following RIF SDN treatment), whereas at an MOI 30 in Figure 5.29 (c) compared to the control (no treatment), there was an approximate 2 log reduction in killing when RIF was in the aqueous form, whereas there was a complete 4 log reduction in killing in the SDN form. Although this assay was only carried out once, at three different MOIs (1, 10 and 30) and with three different serial dilutions for each MOI, it does suggest that RIF as a SDN was more toxic (at only 30% drug) compared to RIF in the aqueous form (at >97% drug).

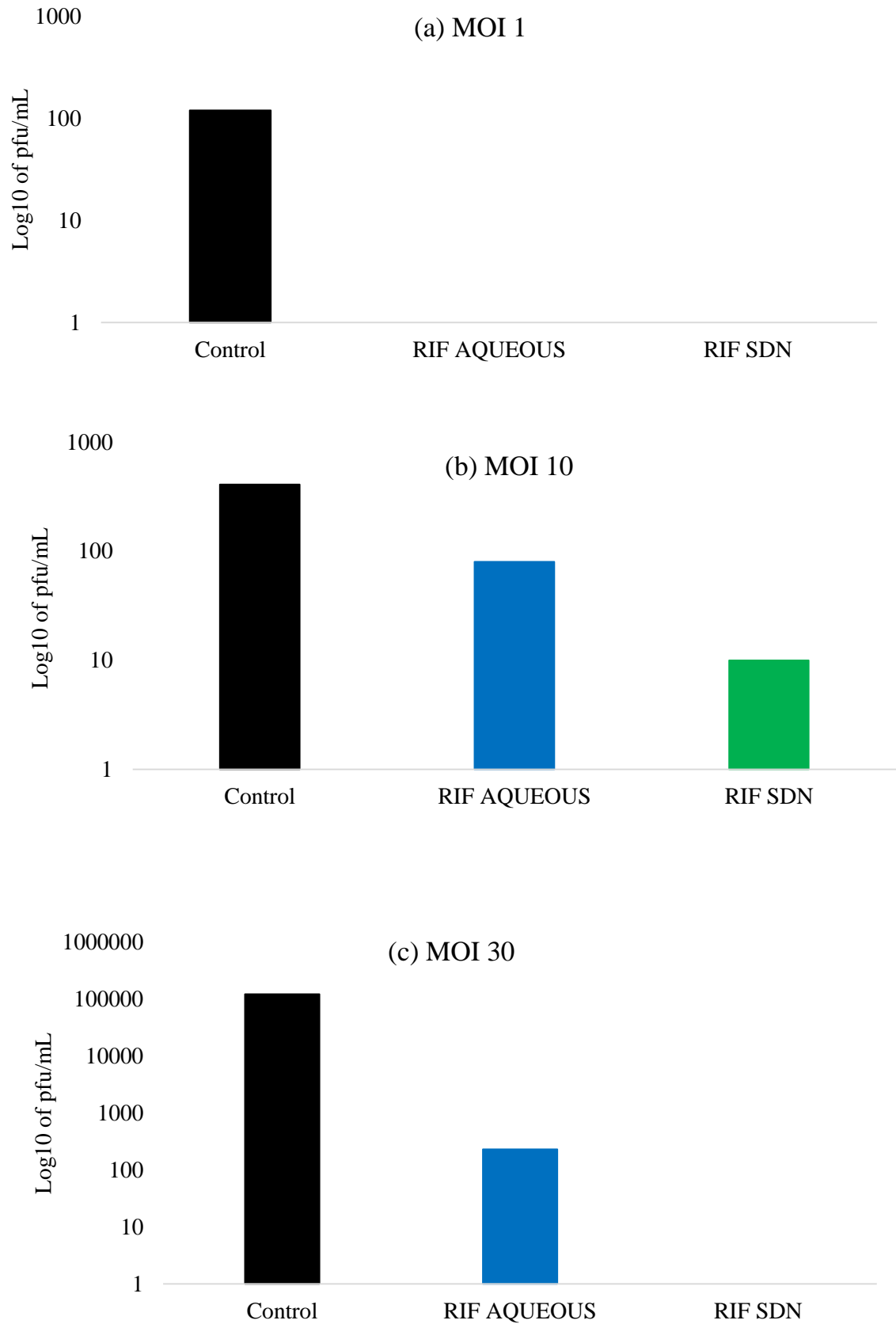


**Figure 5.29** Plaque forming units (pfu/mL) counted for each treatment (RIF SDN or RIF aqueous). Different MOIs of *Map* K10/GFP (a) MOI 1, (b) MOI 10 (c) MOI 30 per  $5 \times 10^5$ /mL macrophages (control = 0  $\mu$ g/mL [no treatment]).



## 5.4 Discussion

The main aims of novel drug discovery for TB are to lower effective drug dose and shorten the treatment period, which will consequently decrease costs and likelihood of resistance. This work aimed to address these factors. By working with FDA approved drugs (RIF, INZ and PZA), excipients from the Inactive Ingredients Database (Kollicoat<sup>®</sup> protect, Hyamine<sup>®</sup>, F68<sup>®</sup> Protect) and synthesising formulations of these drugs at the nano-scale, this approach may avoid the vast costs and timescales normally associated with novel drug development. Yet these SDNs essentially were novel drugs. Although the SDNs would have had the same target and would kill the mycobacteria by the same means, the nano-form offers many advantages, primarily the potential to enable targeted treatment (highlighted in Chapter I [section 1.10.1]).

By comparing the efficacy of the SDNs and the aqueous drugs on the growth of *Map* K10/GFP via the fluorescence assay it was clear to see all substances, except INH, inhibited mycobacterial growth over the 7 day period. As displayed in the screening assay results, there was much data generated from this analysis and there were many ways to interpret it. Using statistical means, the data was analysed to try to determine where the substances differed from each other (and to see whether it was time and/or concentration dependent). An important factor was the difference between the concentrations in the two forms of RIF. The API for each substance needed to be considered, to allow a direct comparison between the two data sets. Through expressing the concentration of the API (and not the mass of the treatment), comparing the difference in mycobacterial growth over days and the EC<sub>50</sub> values, RIF in the SDN form was the most anti-mycobacterial substance tested. The fluorescence assay results also correlated with the colony count and the phage assay results, thus strongly advocating the highly toxic properties to mycobacteria of RIF as an SDN. There were high levels of variation in the colony count

data, but again a distinct pattern was observed for nearly all substances and concentrations. More specifically, as with the metal/metal oxide NPs, the colony counts related to the fluorescence assay results on the toxicity of the substances. The phage assay (which was unfortunately only performed once) demonstrated the potential potency of nano-RIF at killing intracellular pathogens and when presented with the microscopy images demonstrating co-localisation, presents strong evidence for the highly potent nature of the SDNs.

#### **5.4.1 SDNs: an overall summary**

Overall, results from the screening assay suggest that all substances, except for INH, significantly inhibited the growth of *Map* K10/GFP over the 7-day fluorescence assay. By comparing the results from RIF SDN and RIF aqueous, initial conclusions are suggestive that both substances significantly inhibited *Map* K10/GFP growth at the time points and concentrations screened, but their overall effects were relatively similar. The EC<sub>50</sub> value calculated for the SDN was 0.075 µg/mL whereas aqueous was 2.98 µg/mL against *Map* K10/GFP. However, the API of each substance differed greatly, as RIF SDN was only 30% drug, whereas RIF aqueous was >97% drug, and when this was considered, the EC<sub>50</sub> for RIF SDN was calculated at 0.025 µg/mL (this being almost a 100-fold difference to RIF aqueous) and results were therefore more indicative that RIF SDN had greater anti-mycobacterial properties.

#### **5.4.1.1 DLS**

DLS revealed a mix of SDN sizes in 7H9 medium. RIF SDN and TRIPLE SDN were significantly larger when they had DiD added (DiD was incorporated for imaging purposes). With the addition of a further substance on to the SDNs, this increase in size was expected, but additionally, agglomeration could have increased giving a larger hydrodynamic diameter measured by DLS. As it was not possible to carry out TEM on these organic samples, DLS was the only available means to determine particulate size. Overall, DLS results suggest that RIF SDN were very small and well dispersed NPs, the DUAL SDNs were <100 nm on average, whereas the TRIPLE SDNs were >100 nm. Both particle types with DiD incorporated were >100 nm. The zeta potentials for all SDNs had low, negative values. The greater the charge (negative or positive) the more stable a suspension is assumed to be, the lower the values, the higher the chance of agglomeration, where +/- 30 mV is usually considered sufficient charge to allow repulsion between NP to prevent agglomeration (Kalbassi et al. 2013). However, in regards to the RIF SDNs, agglomeration did not seem to be occurring when measured by DLS and imaged using microscopy.

#### **5.4.1.2 TRIPLE SDNs**

The efficacy of the TRIPLE SDN was not as potent as anticipated, where an EC<sub>50</sub> of 7.17 µg/mL was calculated, but this was considering the total mass concentration of the NP. TRIPLE SDNs were composed of three first line antibiotics, RIF, INH and PZA. The loading of each drug differed from each other, (13% RIF, 6% INH and 34% PZA). Interestingly INH (aqueous) was found to have little/no effect against a *Map* K10/GFP

strain. INH is a bactericidal prodrug requiring activation from a catalase-peroxidase KatG, encoded by the *katG* gene in *Mtb* (Zhang & Yew 2009). Although *Mtb* and *M. bovis* are known to be very sensitive to INH, *Map* is known to have much greater levels of resistance to this antibiotic (Williams et al. 1999) therefore these results were not unexpected. As such, toxicity exerted would need to have been derived from either PZA and/or RIF. PZA kills non-replicating bacilli which is the opposite of many antibiotics and it disrupts the membrane potential of *Mtb*. PZA works in an unusual manner against *Mtb* and its mechanism is not well elucidated. The drug needs to be converted into pyrazinoic acid by pyrazinamidase to confer anti-TB properties, it is only effective in acidic pHs in anaerobic conditions during active inflammation and is not active against *Mtb* in ‘normal’ culture conditions at neutral pH levels (Zhang & Yew 2009; Zhang et al. 2003; Lanoix et al. 2015) which would have been the conditions of these experiments. Due to a mutation in the *pncA* gene (which codes for pyrazinoic acid), *M. bovis* is resistant to PZA (Zhang & Yew 2009) and *M. avium* is known to be non-susceptible due to a problem with pyrazinoic acid transport (Sun et al. 1997). Therefore, it is reasonable to conclude that RIF was the predominantly active API in this triple-drug NP. Even at a loading of only 13%, RIF still exerted considerable anti-mycobacterial properties against *Map* K10/GFP.

#### **5.4.1.3 DUAL SDN**

The DUAL SDN displayed the weakest anti-mycobacterial effect to *Map* K10/GFP compared to the other SDNs, screened under these experimental conditions with an EC<sub>50</sub> of 17.3 µg/mL. These SDNs were composed of two first line antibiotics, (20% RIF and 10% INH), and as aforementioned, INH did not display potent anti-mycobacterial effects

against this strain of mycobacteria, therefore RIF was likely the predominantly active API in this dual-drug NP. However, it was surprising that the DUAL SDN with 20% RIF were less potent than the TRIPLE SDN with only 13% RIF. DUAL SDNs were smaller particles and the colony count data suggests they were considerably toxic when compared to the control (no treatment). Overall, this was a difficult result to comment on, and another factor may have influenced the fluorescence assay results (e.g. their stability in medium).

#### **5.4.1.4 RIF SDNs and aqueous drug**

RIF is a bactericidal antibiotic that works by inhibiting the RNA synthesis of *Mtb* by binding the  $\beta$  subunit of the RNA polymerase thus preventing elongation of the RNA chain and it is active against bacilli in both growth and stationary log phases (Zhang & Yew 2009). There is scarce published literature on the efficacy of RIF against *Map* strains. One report suggests an MIC of 0.5-4  $\mu\text{g/mL}$  and Rifabutin (a structural analogue of RIF) was found to be highly toxic against a *Map* K10 strain (MIC 0.03-0.5  $\mu\text{g/mL}$ ) (Zanetti et al. 2006). Results obtained from this study concur with others, that *Map* is a highly sensitive *Mycobacterium* to RIF, where an  $\text{EC}_{50}$  of 2.98  $\mu\text{g/mL}$  was calculated from the screening assay. Its mode of action against *Map* is likely to be very similar to its action against *Mtb*, although this was not verified. The aqueous form of RIF was screened to allow comparisons between the SDN and the conventional form of the antibiotic, but due to the differences in the API it made data analysis more challenging. To allow a direct like-for-like comparison, three fold RIF SDN would need to have been diluted in 2% FCS, but this would have increased agglomeration of the NPs and created a very viscous solution, which was not ideal for the 96 well plate screening assay,

therefore mass concentration was utilised. Furthermore, mass concentration was more reflective in clinical terms, as SDNs require excipients.

#### ***5.4.1.5 SDN drug loading***

The drug/drug ratio of the loading was chosen to try and reflect what is used clinically (TRIPLE SDN) but with respect to maximising excipients wherever possible. Excipients are required to stabilise the pre-spray of freeze-drying, generally more excipient resulted in smaller particles (which was confirmed by DLS) by preventing particle growth and agglomeration. A series of drug ratios were initially produced and in essence, through trial and error, the drug combination that was the most reproducible was selected and supplied for this study. Specific excipients were chosen by the project collaborators based on their stability, and following feedback on initial SDN screening.

#### ***5.4.2 Cytotoxicity to macrophages***

There was very little toxicity observed at the concentrations the macrophages were exposed to for both SDNs and aqueous drugs, determined using the alamar blue assay. No treatments were significantly different from the control (no treatment). Although cytotoxicity from all the substances tested was very low, it was surprising that RIF SDN was more cytotoxic to the cells than the other SDNs, particularly the TRIPLE (which had a 53.3% total drug loading). In the SDN form, the NPs may possibly cause toxicity by mechanisms associated with other NPs. Such mechanism might include ROS/oxidative stress (Oberdörster et al. 2007) and pro-inflammatory responses (Gaiser et al. 2013) due

to physicochemical characteristics associated with the nano-size range of the particles (e.g. the large surface area) phagocytosed by the cells (Kermanizadeh et al. 2014).

#### ***5.4.3 Macrophage infection models***

Fluorescently labelled NPs have provided the information on how macrophages/cells take up and process NMs (Weissleder et al. 2014). In this study, the localisation of SDNs in relation to cellular structures and mycobacteria was investigated, allowing an understanding into the effectiveness of targeting. Macrophages are reported to engulf smaller particles more readily than larger (Clift et al. 2008). The RIF SDNs appeared to have been internalised by a higher proportion of macrophage cells compared to the TRIPLE SDNs, which were found in agglomerated masses, often in only 1 or 2 cells in a X63 field of view, although this was not quantified. This was probably due to the hydrodynamic diameter difference between the particle types, where the smaller RIF SDNs were more readily engulfed over the 4 hour incubation period. It is important to note such a difference, as this would be important if SDNs were to be manufactured for clinical treatment. Whether these drugs stay as intact SDNs following addition to the *Map* K10/GFP infected cells or whether they readily dissolve is hard to assert, although the microscope images suggest full or partial SDN uptake by the macrophages after 4 hours of treatment before fixing.

Z-stacks were utilised to determine whether SDNs and mycobacteria were associated with the cell surface or internalised into the cell interior and also to get an insight into whether co-localisation (of drug and mycobacteria) occurred following macrophage uptake. The minimum number of stacks taken was 15, and a maximum of 30 (although this would take approximately 1 hour to image one field of view), therefore this was a highly time

consuming process. Z-stacks indicated that internalisation of drugs (RIF and TRIPLE) was occurring as in nearly all the 3D images obtained, mycobacteria and SDNs were found throughout the cell, with fluorescent signals being detected in all layers imaged. In many instances, both signals were emitted from the same position within the cell. In many cells imaged, there was a strong (yellow) fluorescence signal emitted and the GFP (green) and CY5 (red) signal was emitting from the same position, therefore, it was important to determine whether this was just crosstalk between signals occurring. Wild type GFP has two excitation peaks, generally for viewing GFP, excitation is set at  $490\pm40$  nm and emission of 510-570 nm. Far red (the CY5 channel for SDNs) excitation is  $640\pm30$  nm and an emission of 690 nm therefore the excitation of GFP does not overlap with the emission of the CY5, thus indicating that crosstalk was not the phenomenon observed. Additionally, the Zeiss fluorescence microscope had a bandpass interference filter, which rejects frequencies outside the set range. A previous study reported that a mix of colours was indicative of co-localisation of two labelled entities (Panyam et al. 2002) therefore this intense yellow colour was likely produced by partial or full co-localisation of *Map* and SDNs (the green *Map* and red SDNs). Unfortunately it was not possible to determine whether co-localisation was occurring within a lysosome as LysoTracker Red (a fluorescent stain commonly used to visualise lysosomes in cells) requires live, viable macrophages and not fixed cells, therefore it was not possible in the microscopy facilities available to carry out such a test (they were not containment level 2).

The results generated may corroborate some of the results displayed in Chapter 4, where NPs look to have been engulfed by macrophages and trafficked to specific vacuoles (e.g. lysosomes). Macrophages are known to readily engulf *Mtb* but as outlined in Chapter 1, *Mtb* is able to arrest the normal phagosome maturation where bacteria are usually destroyed, thus allowing them to lay dormant or reproduce following disruption to the



phagosome environment (Podinovskaia et al. 2013). Further analysis would be required to confirm these results, and as stated in a previous study, the intracellular localisation of NPs should be reported with caution and backed-up wherever possible (Brandenberger et al. 2010). Yet this PhD project supports the concept that SDNs are engulfed by infected macrophage cells, and then trafficked by the immune cells. As the SDNs and *Map* looked to have been co-localising, this may suggest a specific form of trafficking.

#### **5.4.4 Intracellular killing of *Map* K10/GFP**

The phage assay displayed the potent effects of RIF SDN after 24 hours incubation with *Map* K10/GFP within a macrophage. In the nano form, RIF may have been in direct contact with the bacilli (within a phagolysosome) thus offering a direct, and targeted killing. Following infection of *Mtb* in an *in vivo* mouse study, after four weeks, up to 95% of bacilli were found to be intracellular (predominantly in alveolar macrophages) (Hoff et al. 2011). After ten weeks, the bacilli were eventually described to be largely ‘extracellular’, enclosed within the necrotic zone of a granuloma, where latent mycobacteria reside (Hoff et al. 2011). Until an acquired immune response occurs, and granuloma development occurs to contain the bacilli, it may be easier to ‘catch’ *Mtb* at the early stages of macrophage infection. There are four potential consequences following uptake of *Mtb*, it can be eliminated immediately, becomes indefinitely dormant within the host cell, causes active disease or causes disease many years later due to reactivation (Giacomini et al. 2001). Upon initial internalisation within a macrophage and following alteration of the behaviour of the phagosome formation, it allows a period of cell division and exponential growth for the bacilli (Russell et al. 2010). During this time before adaptive immunity begins granuloma construction, the bacilli are held within

an 'ineffective' phagolysosome and this could be a suitable target for anti-TB SDNs. Further to this, granulomas are highly complex and would require in-depth investigation to determine entry methods for SDNs, achieved possibly through surface modifications to allow entrance into this composite. Granuloma formation is driven by the onset of an acquired immune response following *Mtb* uptake by macrophages and the production of cytokines (e.g. TFN- $\alpha$ ), but this formation can also lead to tissue damage. Aggressive granuloma response can lead to acute disease, destroying tissues (Russell et al. 2010), thus asserting that early treatment to reach bacilli before they are trafficked into granulomas may be more beneficial.

#### **5.4.5 Other studies**

Most studies investigating nanotechnology for TB treatment, are preclinical studies using PLGA polymer therapeutics (Hirota et al. 2010; Onoshita et al. 2010; Gelperina et al. 2005) as highlighted in Chapter 1 (section 1.12). There are other avenues to explore however. Liposome based delivery systems have many advantages associated with their use (e.g. protection of drug, controlled release). Liposomes have a phospholipid bilayer, surrounding a core encapsulating either hydrophobic or hydrophilic drugs (Cukierman & Khan 2011). Gaspar *et al.*, manufactured Rifabutin encapsulated liposomes (500 nm) and compared their potency at killing *Mtb* (H37Rv) *in vivo* to free RIF drug (dose 20mg/kg) (Gaspar et al. 2008). They reported no statistical difference between the treatment types on bacilli found in the lungs however they report a statistical difference on bacilli in other sites (spleen and liver) where liposome encapsulated RIF was more effective (Gaspar et al. 2008). Additionally, they reported a lesser inflammatory response in the lungs of liposome treated mice, and the liposomes delivered a higher concentration of drug to target sites (Gaspar et al. 2008). Due to being vulnerable to intestinal degradation,

liposomes tend to require delivery via the intravenous route (Pandey & Khuller 2006), increasing the labour required in their use as a potential TB treatment. Yet further investigation into their administration via inhalation is being investigated (Pandey & Khuller 2006).

The manufacturers of the SDNs for this project have designed similar SDNs for HIV treatment that are currently undergoing clinical trials (see EudraCT 2013-004913-41 <https://clinicaltrials.gov/ct2/show/NCT02631473>). This is the first ever human clinical trial using oral delivery of a nano-medicine against an infectious disease (personal correspondence with Dr Marco Giardiello [Department of Chemistry, University of Liverpool]). Titled '*Pharmacokinetics of efavirenz and lopinavir nano-formulations in HIV negative healthy volunteers: an adaptive design study*' the trial recruited healthy volunteers to partake, and preliminary results from this trial correlate with the results generated in this PhD project, that a particle loaded with less than 50% drug, resulted in a 50% reduction in the EC<sub>50</sub> compared with the traditional drug which was approximately 100% drug (personal correspondence with Dr Marco Giardiello [Department of Chemistry, University of Liverpool]). The success of these studies in the HIV field, offer verification for the ability for this technology to be adapted to many more types of drugs, such as anti-TB drugs.

The screening of anti-TB SDNs has offered an insight into their anti-mycobacterial properties, and microscopy studies have revealed their likely co-localisation with mycobacteria within a macrophage, therefore, an interesting consideration would be their potential delivery system if these drugs were to make clinical trials, as with the HIV drugs. As pulmonary TB is the most common form of the disease, a respiratory method of drug delivery would be a very attractive means. NPs have improved adherence to the mucosal tissues of the lungs over conventional drugs (Pandey & Khuller 2006) therefore nebulisation would be an ideal way to administer antibiotic SDNs in the form of mist

aerosols via the pulmonary route (Dolovich & Dhand 2011). Atomizers, a common type of nebuliser, use compressed gas to generate high velocity drug aerosols, sprayed through a tight opening (Kleinstreuer et al. 2014). Inhalation of drugs could deliver a significant amount of drug throughout the lungs, akin to the common entry of *Mtb*. Suarez *et al.*, manufactured 1-5  $\mu$ M RIF-PLGA microspheres (particles with diameters in the micrometer range) and delivered them via the respiratory route to guinea-pigs by nebulisation. Guinea-pigs were then infected with *Mtb* (H37Rv), and authors reported that a significant (10 fold) reduction in bacilli was recovered compared with the control (animals treated with conventional RIF treatment, also delivered via nebulisation) 5 weeks post infection (Suarez et al. 2001). Additionally, animals treated with RIF-PLGA had reduced inflammatory response/tissues damage when compared to control animals upon analysis of the lung tissue (Suarez et al. 2001). It is unclear however, whether the authors propose this as prevention rather than a cure, as animals were treated prior to being infected with *Mtb*.

The use of biodegradable polymers (e.g. PLGA) and/or chitosan shells (Dube et al. 2013; Semete et al. 2010; Patel et al. 2013) as anti-TB drugs have some drawbacks. They have high costs associated with their production, therefore whether they are suitable for mass production is not yet established. Also, there are still some safety concerns in therapeutic applications, as further *in vivo* studies are required to demonstrate their safety and efficacy as drug carriers.

#### 5.4.6 Future work with SDNs

The SDNs displayed encouraging results against a pathogenic strain of mycobacteria and there are many avenues to be explored. The initial next step would be to screen these substances against a human strain of mycobacteria. Both INH and PZA displayed weak anti-mycobacterial properties, but this would likely differ against many *Mtb* strains, which are known to be more sensitive to these antibiotics. It would be interesting to screen these drugs against *Mtb*, using the screening assay with a GFP-modified strain and then intracellularly, preferably using primary macrophages. The data generated from this project could also be utilised to plan a comprehensive *in vivo* study, to compare bacilli loading within alveolar macrophages following infection (with *Mtb* or *Map*) between treatment groups of RIF aqueous and RIF SDN treated mice. Additionally, a direct comparison between the stability of the two drug types would be interesting, evaluating their stability under transportation and storage (long term), and their sensitivity to heat and light. I would hypothesis the SDN form of RIF to be significantly more stable.

As smaller particles tend to induce cytotoxicity as more molecules/atoms are exposed due to the large surface area presented to cells/molecules/bacteria (Semete et al. 2010) further analysis into the potentially adverse effects of these SDNs would be required. NPs behave differently (and are often more toxic) when compared to their bulk forms, similarly to metal NPs (Rai et al. 2015). Therefore, changing a material to fall within the nano-scale could create adverse effects to biological systems as well as the desirable effects already discussed. As the first line TB drugs have many side effects associated with their use normally, it must be considered whether in the nano-form if these drugs pose a potential hazard to patients. Results obtained here do not indicate this (macrophage cytotoxicity tests) but it should be considered. Further investigations could include the use of different assays, such as the water-soluble tetrazolium (WST) 1 assay

(a colorimetric non-radioactive assay for quantification of cell proliferation, cell viability and cytotoxicity using a microplate format) or studies to monitor cytokine production.

Another important point to consider is the stability of the SDNs compared to conventional, aqueous antibiotics. Although not formally tested in this project, the stability of the SDNs was observed. RIF solution has a shelf life of approximately 2-3 months (Sigma 1997), whereas RIF SDNs stability was monitored and they were stable for up to 6 months. DLS data suggested particle stability and through monitoring the potency of the SDNs for up to six months in the screening assay, it did not exhibit any notable differences. This may suggest that the SDNs offer greater stability and shelf life. However, the stability of these NPs is an important part of the development by Liverpool University in order to ascertain their suitability for clinical trials and large-scale manufacture, therefore data on these aspects is soon expected. SDNs do not require storage at 4°C, therefore again making them advantageous to the traditional form, as appropriate storage facilities can be problematic in some high burden TB countries.

#### **5.4.7 Conclusions**

To conclude, the screening of these SDNs has offered an insight into their anti-mycobacterial properties within an *in vitro* cell culture setting and an *in vitro* intracellular setting. The most exciting results generated are the efficacy results of the RIF SDN compared to the aqueous drug plus the likelihood of the co-localisation and the toxicity exerted to the mycobacteria by the SDN within a macrophage vacuole. Further work is clearly required to try to determine how these SDNs behave in a cell culture over time (i.e. do they dissolve or as stay intact NPs?), what roles the excipients play and whether the SDNs pose less (or more) adverse side effects. Overall, it was not known how stable

or efficacious these SDNs would be, and what concentration ranges would be suitable to show a decrease in bacterial growth, therefore these results offer a good foundation for a continued study with these particles.

# **CHAPTER VI**

## **GENERAL DISCUSSION**



## 6.1 Final Discussion

Killing approximately 1 person every twenty seconds, nearly 5000 per day, and up to 2 million per year, TB remains one of the world's greatest health threats. The WHO has called for an urgent surge in drug development and the NHS has invested significantly in the irradiation of TB in the UK, where incidents are the highest in Western Europe and five times higher than in the US (NHS 2015; WHO 2015b). TB is predominantly found in developing countries (WHO 2015b; WHO 2014b; WHO 2013). The United Nations has predicted that the world's population will reach in excess of 9.7 billion by 2050 and 11.2 billion by 2100 with the increase principally in the developing world (The UN, 2015 <https://www.un.org/development/desa/en/news/population/2015-report.html> accessed 20/02/16). This highlights the need for rapid disease control, before MDR/XDR TB escalates further. Through evasion of the host's immune surveillance, the inherently robust *Mtb* is a well-adapted pathogen. By preventing organism degradation through phagocytosis evasion and transition into a dormancy state, *Mtb* is rendered resilient to both host defence mechanisms and drug actions. Latency is characterised by the slowing down of the pathogen's metabolic machinery, allowing the organism to sit dormant in a secure environment. *Mtb* has a heterogeneous, dynamic nature, and the yin-yang model (Chapter I [section 1.9.2]) demonstrates this well, highlighting the difficulties in producing suitable treatment programmes. The intensive first phase of treatment followed by the continuation phase still has problems with disease relapse, and development of MDR/XDR TB (WHO 2015b). Nanomedicine offers huge potential in the fight against bacterial infections and this avenue of research may produce a suitable therapy to combat drug resistance strains of TB and curtail the problems with current treatments (e.g. side effects through lower doses).

Here, a review of this project is given, conclusions are drawn and gaps in the work are highlighted so that they may be addressed in future work. It is hoped this project will lead to more screening and testing of SDNs/NPs/drugs and eventually lead to clinical trials of these novel compounds.

A key objective of this thesis was the development of a rapid drug screening assay (Chapter III). The assay should ideally be HTS amenable, have relatively low costs associated, be simple and reproducible, and provide the ability to screen a variety of compounds, including nanomedicines. The assay allowed the efficacy of NPs/drugs against a pathogenic *Mycobacterium* to be screened over a period of 7 days, yielding data in replicate sets with suitable controls. The assay's success resulted in a peer-reviewed publication. However, due to the inability to commercialise this assay in its exact form for profitable gain (because of constraints by the provider of the *Map* K10/GFP reporter strain), a GFP reporter of *Mtb* would be required to bring this assay forward.

There were challenges involved in its optimisation including, cell number, cell growth stage, plate type, well dehydration and which controls were the most suitable. These optimisation steps have now been resolved by systematic repeats, monitoring and observations generating a published protocol that it can be employed by others working in the field. The assay offers a means to screen substances at the early stages of drug development, giving rapid information on whether such substances warrant further investigation or not. Being in a 96 well plate format, multiple repeats can be included and different substances can be screened in unison. Improvements for the assay have been highlighted in Chapter III, but a major drawback is the inability to calculate MIC/MBCs directly from the fluorescence readouts. Although GFP is stable, and fluorescence is independent of cofactors or substrates, a disadvantage is following cell death GFP is still detectable (as found with the highest concentrations of Ag NPs screened). It is known that the signal is significantly reduced (likely due to the redox

changes during the apoptotic process) (Steff et al. 2001). However, it would be difficult to standardise, as if a threshold of GFP signal was determined (i.e. indicating cell death), it would be hard to conclude whether this was a form of auto-fluorescence from dead cells, or a smaller population of resistant, viable cells. This requires further consideration.

The results on the metal/metal oxide NPs gave a good insight into the efficacy of the NPs and effective concentrations required to inhibit this pathogenic mycobacterial strain. Although there are many studies on the effects metal/metal oxide NPs have on *E.coli* and other bacterial strains, there is little literature on the efficacy of these NP types against mycobacteria (Larimer et al. 2014; Islam et al. 2013). It was interesting to observe the poor anti-mycobacterial effects of the ZnO NPs, as generally they are reported to be highly anti-bacterial (Azam, Ahmed, Mohammad Oves, et al. 2012; Li et al. 2011; Padmavathy & Vijayaraghavan 2008; Jiang et al. 2009). The highly potent effects from Ag NPs were expected, as silver is widely regarded as toxic, anti-bacterial agent (Zhao & Wang 2012; Kim et al. 2007; Besinis et al. 2014; Choi et al. 2008), whereas the literature on Cu(II)O NPs is limited, therefore it is hoped this study helped towards bridging this gap. Interestingly, Kim *et al.*, investigated the ability of the immune system to clear a bacterial infection when treated with Cu NPs (Kim et al. 2011). They reported that *Klebsiella pneumoniae* infected mice exposed to Cu NPs (32 µg/mouse) had impaired pulmonary bacterial clearance and more viable bacteria in their lungs compared to non-Cu NP exposed mice. The authors suggest that Cu NP exposure may in-fact increase the risk of a pulmonary infection through impairment of the host defence. This therefore warrants serious consideration if such NPs were to be considered as part of a treatment, and again highlights the potentially adverse effects of materials in the nano-scale.

Whether metals can be integrated into modern medicine or not is debatable but metals have been used in medical applications since ancient times. Hippocrates described the use of silver to treat wounds and ulcers and the ancient Egyptians sterilised water using

copper (Rai et al. 2015; Medici et al. 2015). It is therefore reasonable to contemplate the use of metals/metal oxides NP as antibiotic carriers, or as drug excipients (at suitable concentrations), to allow an enhanced anti-microbial affect (Owens 2013b; Rai et al. 2009; Morones-Ramirez et al. 2013).

By investigating the efficacy of metal/metal oxide NPs it was established that the screening assay could not accommodate NPs with inherent reflective properties, such as TiO<sub>2</sub> NPs. TiO<sub>2</sub> NPs were going to be included in the NP selection to be investigated in this study, but had to be removed following initial experiments whereby the readouts were 3-fold greater than the control well readings (*Map* K10/GFP only) demonstrating the importance of checking for interference in such light-based assays.

An integral part of this work was to use the fluorescence assay to screen the newly developed SDNs. The SDNs were manufactured for this PhD project and are an exciting development. Although comparing the efficacies of these particles to aqueous antibiotic was challenging due to the differences in drug loading, it was possible to calculate an EC<sub>50</sub> to compare RIF SDN to RIF aqueous. The results demonstrated almost a 100-fold difference between the two forms of the drug, with the SDN being more potent, thus being a very exciting result. Other studies have shown RIF in the nano-scale be more effective than ‘free’ RIF, therefore this work correlates with other studies (Suarez et al. 2001; Hirota et al. 2010; McCarron et al. 2008; Onoshita et al. 2010; Chuan et al. 2013). However, these studies have not used SDNs, which I hypothesis to offer an even greater anti-mycobacterial effect, as effective targeting is possible and drug loading is adjustable.

The microscopy aspects took some optimising, but once a protocol was established, images depicting the uptake of SDNs by infected macrophages and the possible co-localisation of SDN and mycobacteria were obtained. Other studies have shown NP uptake into macrophages (Clift et al. 2008) and lysosomes (Arai et al. 2015), by *Mtb*

infected macrophages (Chuan et al. 2013) and by *M. bovis* BCG infected macrophages (Kalluru et al. 2013), thus again correlating with the results obtained here. Through the use of Z-stacks and 3D imaging software, it was clear the SDNs were internalised by macrophages and not surface bound. If time had prevailed, it would have been interesting to have quantified the GFP signal in SDN treated macrophages, to compare to the GFP signal in untreated macrophages. This would be possible using the Zeiss Axio vision Rel 4.8 software, which measures the level of GFP per pixel in any given image and is therefore able to deduce where the signal fluctuates and thus compute a numerical difference between two images. However, this process required in-depth optimisation of standards to allow a consistent system to permit comparison between images. Another option would be flow cytometry. Additionally, an investigation to compare the uptake of RIF SDNs to TRIPLE SDNs by macrophages would have been interesting. For example, it is known macrophages (J774A.1 cells) more readily uptake smaller NPs to larger NPs (Clift et al. 2008) but other factors may have influenced the macrophages preference to RIF SDNs (e.g. the excipient used in manufacture or SDN stability), and it may have been the drug loading difference between the SDN types rather than SDN size.

Although the purpose of this project was to develop and optimise the screening assay for NPs, a limitation of this work was that an *Mtb* strain was not utilised in the screening of SDNs. This assay was developed for TB drug screening, and a surrogate organism was suitable for this purpose. Though interesting results were generated, it only offered an indication of the susceptibility for *Mtb*, rather than an absolute assessment, and there would likely be differences in susceptibility and mechanism of toxicity due to strain differences. If all the SDNs were screened against *Mtb*, the results generated would have a greater impact and more clinical relevance. Although genetically and physically similar, *Map* and *Mtb* are different species that cause different diseased states in different

mammals (although a link between *Map* infection and Crohn's disease in humans exists). Thus leading to the future work envisioned for this project.

## 6.2 Future work

As highlighted in each of the chapters, there are many aspects which could be further investigated. As both Ag and Cu(II)O NPs offered efficacious properties that kill *Map* K10/GFP at the higher concentrations, it would be interesting to determine the mechanism of action and how they compare to each other. Two of the main targets in *Mtb* treatment is the  $\beta$  subunit of the RNA polymerase and the mycolic acids of the cellular wall (Zhang & Yew 2009). From the results generated and the imaging carried out in Chapter IV, I would hypothesis that structural damage is exerted by the NPs to the bacilli. Whether the NPs are able to enter the bacilli or not is still ambiguous but intriguing results were obtained, showing dark NP-like entities within the pathogen.

The next major step would be to screen the SDNs against a drug susceptible strain of GFP modified *Mtb* and compare this to an aqueous form of the same drug to allow a like-for-like comparison. The results generated from such a test would have great clinical significance. Further, screening the same substances against an MDR TB strain would be very interesting. Using the DiD incorporated SDNs, it would be advantageous to repeat these experiments in live macrophages, using LysoTracker Red to be able to confirm whether the SDNs and mycobacteria were trafficked to the lysosome. This would require a high containment imaging facility, yet it could offer vital information on how the infected macrophages process the engulfed SDNs.

The SDNs manufactured for this project could be created for other TB drugs (e.g. EBM) and screening of these would be required. Further, the manufacture of PZA and INH

SDNs for the screening of these individually, could offer a further insight into the toxicity exerted by these individual drugs. It would be interesting to determine whether a quadruple SDN could be manufactured, including EMB for a 4-drug combination. Overall, it would be advantageous to have all first-line TB antibiotics produced as SDNs.

An important consideration is whether saving the host cell (e.g. macrophage) is important during an infection. As found with the highly anti-mycobacterial Ag NPs, they were also very toxic to macrophage cells. If cell death occurs by apoptosis, there would be no adverse effect on the surrounding tissue (except for re-exposure to Ag NPs), but if death occurs by necrosis this could cause tissue damage through an inflammatory response. Although macrophages offer host protection, in essence they also offer a form of protection to *Mtb*, and therefore if the pathogen could be killed whilst sacrificing the host, this could be significantly unfavourable in a clinical setting. Macrophages are known to have an intracellular threshold load. It is reported they can engulf ~25- 40 bacilli before ‘bursting’ occurs (Repasy et al. 2013; Wong & Jacobs 2016). An infected macrophage with an MOI of 40:1 would be an ideal target for SDNs, delivering maximal drug to maximal pathogen. Whether deliberately killing the infected host cell would be favourable or not is an interesting concept. This would likely have a big impact on overall infection control.

### **6.3 Concluding remarks**

There is much to be investigated and learned from nanomedicine and TB. This thesis tried to combine the relevant literature from the two fields to give an overview of the ongoing progress and limitations. Combining expertise from a range of disciplines is required to allow an amalgamated, coherent and thorough evaluation where the next steps

of research should be taken. A further understanding of how drugs are penetrating the lung cavities is required which may allow a more tailored nano-based regime to be designed, to exploit the unique properties NPs offer. Faster disease diagnosis and initiation into treatment programmes is paramount if TB is ever to be controlled. A cohesive effort between governments, funding bodies, scientists, clinicians and patients akin is essential to combat this disease.

In conclusion, more screening of substances is required to identify anti-mycobacterial compounds as MDR/XDR TB levels escalate. Metal/metal oxide NPs have the potential to be integrated into clinical medicine, their inherent anti-bacterial properties should be exploited. SDNs display interesting results that warrant further investigation. This PhD project has developed a novel drug screening assay to study the anti-mycobacterial properties of NPs/drugs, and further, has identified the potential of newly developed SDNs. These, delivered as nanomedicine, may offer hope for the eventual eradication of this global pathogen.



## APPENDICES

### *Appendix A*

#### **Additional metal/metal oxide NP data**

**Table A.1**  $\beta$  Values calculated from the linear regression of the Log data (growth of *Map* K10/GFP with Cu(II)O NP). These values were normalised to the slope of the control (0  $\mu\text{g/mL}$ ) to plot Fig A.1

Concentration ( $\mu\text{g/mL}$ )	Slope of the line ( $\beta$ )	$\beta$ (Normalised)
0	0.2254	1
6.25	0.2311	1.025288
12.5	0.2239	0.993345
25	0.1951	0.865572
50	0.1635	0.725377
100	0.1323	0.586957

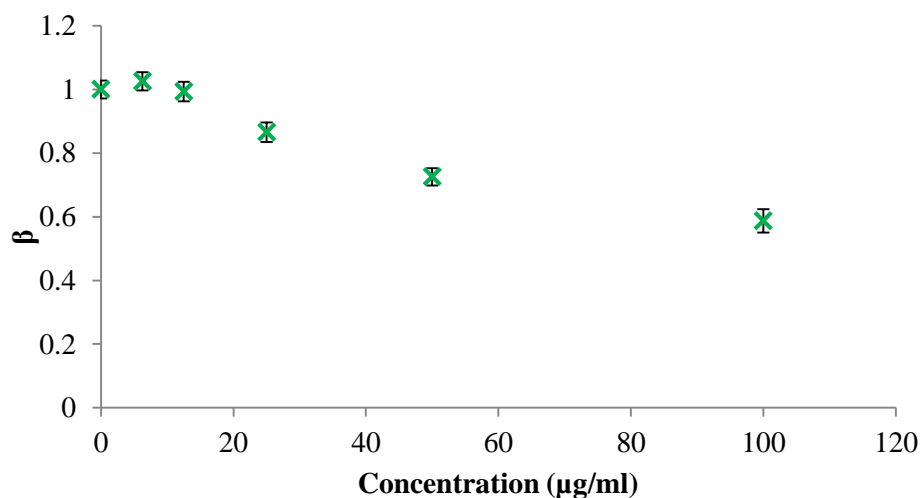


**Figure A.1** Growth of *Map* K10/GFP with Cu(II)O NP normalised to the control (where  $\beta$  represents the change in fluorescence [representing mycobacterial growth] per day). *Map* K10/GFP grown in 200  $\mu\text{L}$  of 7H9, in a microplate format, with Cu(II)O NP at different concentrations (6.25-100  $\mu\text{g/mL}$ ), normalised to the slope of the control.  $\beta$  calculated through linear regression analysis of the Log data (Table A.1). Each point displaying 2\* the standard error calculated using LINEST function Excel (Microsoft Office Word) to cover the variation of the mean (n=4).

**Table A.2  $\beta$**  Values calculated from the linear regression of the Log data (growth of *Map* K10/GFP with ZnO NP). These values were normalised to the slope of the control (0  $\mu\text{g/mL}$ ) to plot Fig.A.2

Concentration ( $\mu\text{g/mL}$ )	Slope of the line ( $\beta$ )	$\beta$ (Normalised)
0	0.1944	1
6.25	0.1761	0.905864
12.5	0.154	0.792181
25	0.1854	0.953704
50	0.177	0.910494
100	0.1579	0.812243

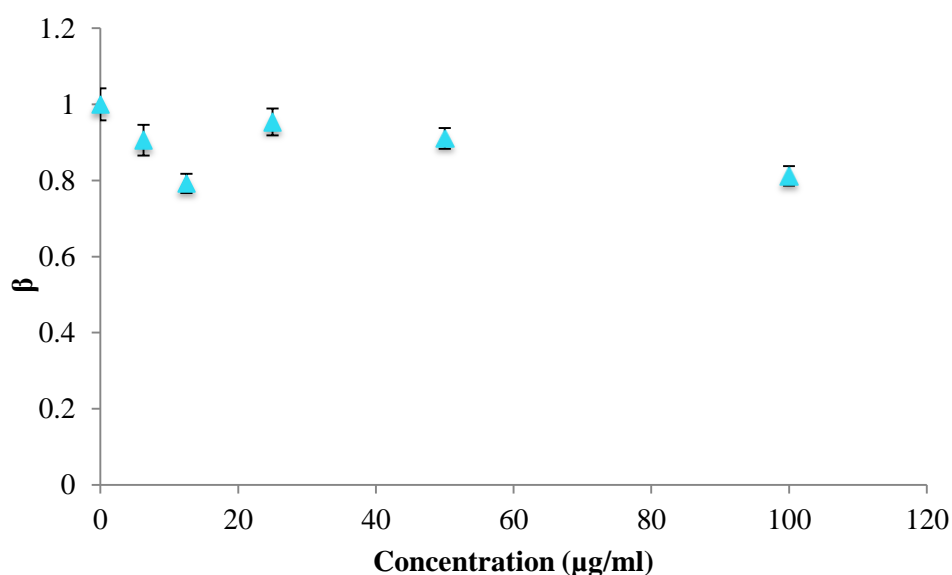
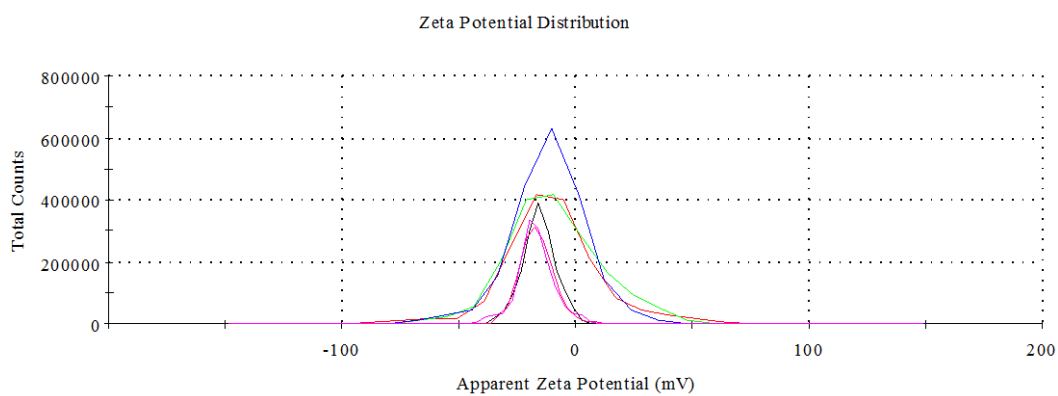
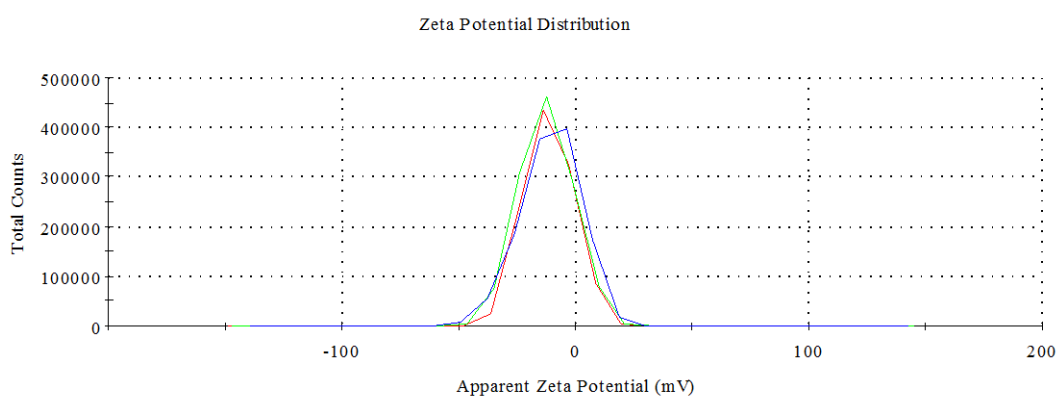


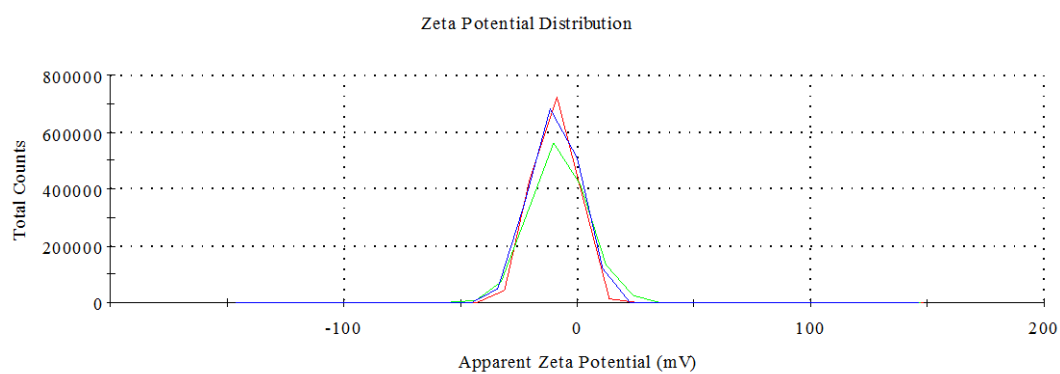
**Figure A.2 Growth of *Map* K10/GFP with ZnO NP normalised to the control** (where  $\beta$  represents the change in fluorescence [representing mycobacterial growth] per day). *Map* K10/GFP grown in 200 $\mu\text{l}$  of 7H9, in a microplate format, with ZnO NP at different concentrations (6.25-100  $\mu\text{g/mL}$ ), normalized to the slope of the control.  $\beta$  calculated through linear regression analysis of the Log data (Table A.2). Each point displaying 2\* the standard error calculated using LINEST function Excel (Microsoft Office Word) to cover the variation of the mean (n=4).



**a)**



**b)**



**c)**

**Figure A.3 Zeta potential distribution graphs (DLS) (n=6)**

(a) Ag NPs in 7H9

(b) Cu(II)O NPs in 7H9

(c) ZnP NPs in 7H9

## ***Appendix B***

### **SDN manufacture (Professor Andrew Owen and Dr Macro Giardiello, University of Liverpool)**

SDNs of first line TB drugs were prepared as outlined below. The incorporation of a fluorescent dye (1,1'-Diocetadecyl-3,3,3',3'-Tetramethylindodicarbocyanine, 4-Chlorobenzenesulfonate Salt [DiD]) to confer a fluorescent signal to each particle was included in some incidences for imaging purposes. Both freeze and spray drying methods were utilised, essentially producing the same product, while spray drying only was used to scale up the samples as freeze drying could only produce relatively small quantities (up to 10 mg).

#### ***Preparation of Emulsion-Templated Freeze-Dried Monoliths Containing 30% RIF Nanoparticles (RIF SDN).***

Stock solutions of RIF (30 mg/mL in Dichloromethane [DCM]), Pluronic F68® (22.5 mg/mL in water), and Hyamine® (22.5 mg/mL in water) were dissolved. The three stock solutions were combined in the ratio 100:245:67 (µL) (RIF : Pluronic F68®: Hyamine®) plus 88 µL water. The final solid mass ratio was therefore 30% RIF: 55% Pluronic F68®: 15% Hyamine® in a 1:4 DCM to water mixture (total volume 0.5 mL). The sample was emulsified using a Covaris S2x acoustic homogenization system for 30s with a duty cycle of 20, an intensity of 10 and 500 cycles/burst in frequency sweeping mode. Immediately after emulsification, the sample was cryogenically frozen and lyophilized using a Virtis benchtop K freeze-drier for 48 hours. The orange dry porous product was stored in the dark at room temperature.

*Preparation of Emulsion-Templated Freeze-Dried Monoliths Containing 29% RIF Nanoparticles labelled with 1% of the dye DiD (RIF SDN + DiD).*

Preparation followed the same procedure as described above, however a stock solution of 30 mg/mL DiD was prepared. The four stock solutions were added to a sample tube in the ratio 97:3: 267:133 (µl) (RIF: DiD: Pluronic F68®: Hyamine®) plus 88µl water. The final solid mass ratio was therefore 29% RIF: 1% DiD: 55% Pluronic F68®: 15% Hyamine® in a 1:4 DCM to water mixture, with a total volume of 0.5 mL.

*Preparation of Emulsion-Spray-Dried 53% TRIPLE Drug Powders Containing RIF, INH, PZA (TRIPLE SDN).*

A mass of 51.2 mg PZA, 20 mg RIF and 8.8 mg INH were weighed directly into a sample vial. A volume of 1 mL DCM was then added and the powders mixed (inverted and vortexed) [note: they did not fully dissolve]]. Stock solutions of Kollicoat Protect® (22.5 mg/mL in water), and Hyamine® (22.5 mg/mL in water) were dissolved. The aqueous stock solutions were added to the 1 mL API mix in DCM in the ratio 267:0.44 (mL) plus 0.89 mL water. The final solid mass ratio was therefore 34% PZA, 13% RIF: 6% INH: 40% Kollicoat® Protect: 7% Hyamine® in a 1:4 dichloromethane to water mixture (total volume 5 mL, 53% combined API). The sample was emulsified using a Hielscher UP400S ultrasonic processor equipped with H14 Probe at 100% output (140 W) for 300secs. Immediately after emulsification, the sample was spray dried on a benchtop spray dryer (BUCHI Mini-290) using an air-atomizing nozzle and compressed air as the drying gas. Spray drying process conditions were 5 mL/min solution flow rate and 65°C outlet temperature (120°C inlet temperature). The orange powder was collected and stored in the dark at room temperature.

*Preparation of Emulsion-Spray-Dried 52 % TRIPLE Drug Powders Containing RIF, INH, PZA labelled with 1% of the dye DiD (TRIPLE SDN + DiD)*

Preparation followed the same procedure as described above, however a stock solution of 53 mg/mL DiD was prepared. A mass of 50.7mg PZA, 19.8mg RIF and 8.7mg INH were weighed directly into a sample vial. A volume of 97ml DCM was then added and the powders mixed (note, they did not fully dissolve). To this, 0.03 mL of DiD stock was added. The aqueous stock solutions were added to the 1 mL API mix in DCM in the ratio 267:0.44 (mL) plus 0.89 mL water. The final solid mass ratio was therefore 33.7% PZA, 13% RIF: 6% IZH: 1% DiD: 40% Kollicoat® Protect: 7% Hyamine® in a 1:4 dichloromethane to water mixture (total volume 5 mL, 52% combined API, 1% DiD).

## Additional SDN data

**Figure B.1**  $\beta$  Values calculated from the linear regression of the Log data (growth of *Map* K10/GFP with RIF aqueous). These values were normalised to the slope of the control (0  $\mu\text{g/mL}$ ) to plot Figure AB.1

Concentration ( $\mu\text{g/mL}$ )	Compound	Slope of the line ( $\beta$ )	$\beta$ (Normalised)
0	RIF Aqueous	0.2151	1
0.001875 $\mu\text{g/mL}$	RIF Aqueous	0.236	1.097164
0.00375 $\mu\text{g/mL}$	RIF Aqueous	0.1608	0.747559
0.0075 $\mu\text{g/mL}$	RIF Aqueous	0.1558	0.724314
0.015 $\mu\text{g/mL}$	RIF Aqueous	0.1383	0.642957
0.03 $\mu\text{g/mL}$	RIF Aqueous	0.1251	0.58159
0.0625 $\mu\text{g/mL}$	RIF Aqueous	0.1195	0.555556
0.125 $\mu\text{g/mL}$	RIF Aqueous	0.1738	0.807996
0.25 $\mu\text{g/mL}$	RIF Aqueous	0.1737	0.807531
0.5 $\mu\text{g/mL}$	RIF Aqueous	0.1692	0.786611
1 $\mu\text{g/mL}$	RIF Aqueous	0.1497	0.695955
2 $\mu\text{g/mL}$	RIF Aqueous	0.1155	0.53696
4 $\mu\text{g/mL}$	RIF Aqueous	0.0976	0.453742

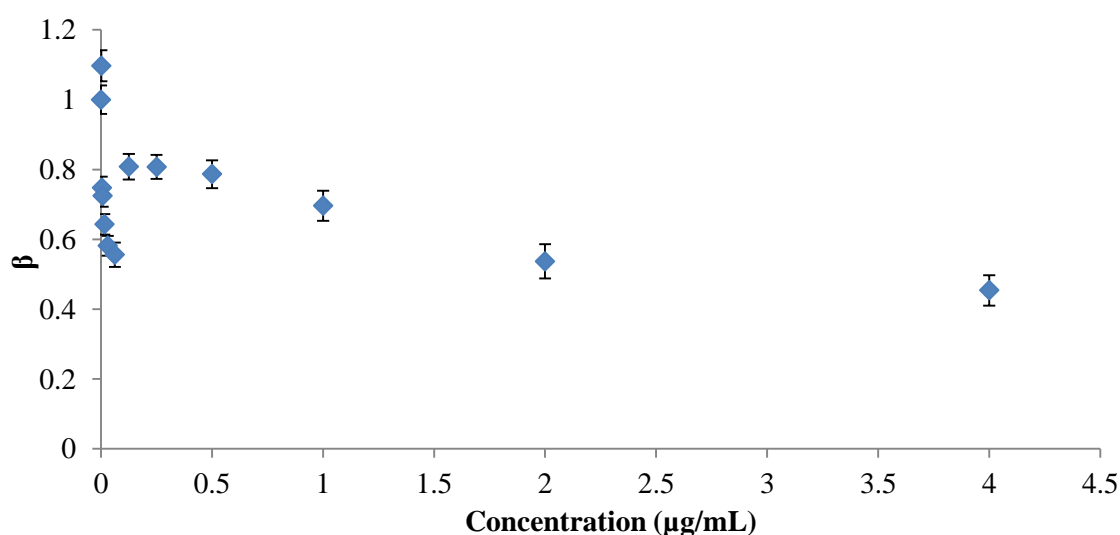


**Figure B.1 Growth of *Map* K10/GFP with RIF aqueous normalised to the control** (where  $\beta$  represents the change in fluorescence [representing mycobacterial growth] per day). *Map* K10/GFP grown in 200  $\mu\text{L}$  of 7H9, in a microplate format, RIF aqueous at different concentrations (0.001875 – 4  $\mu\text{g/mL}$ ), normalised to the slope of the control.  $\beta$  calculated through linear regression analysis of the Log data (Table B.1). Each point displaying 2\* the standard error calculated using LINEST function Excel (Microsoft Office Word) to cover the variation of the mean (n=9).

**Table B.2  $\beta$  Values** calculated from the linear regression of the Log data (growth of *Map* K10/GFP with INH aqueous). These values were normalised to the slope of the control (0  $\mu\text{g/mL}$ ) to plot Figure B.2

Concentration ( $\mu\text{g/mL}$ )	Compound	Slope of the line ( $\beta$ )	$\beta$ (Normalised)
0	RIF SDN	0.277	1
0.001875 $\mu\text{g/mL}$	RIF SDN	0.266	0.960289
0.00375 $\mu\text{g/mL}$	RIF SDN	0.259	0.935018
0.0075 $\mu\text{g/mL}$	RIF SDN	0.239	0.862816
0.015 $\mu\text{g/mL}$	RIF SDN	0.246	0.888087
0.03 $\mu\text{g/mL}$	RIF SDN	0.256	0.924188
0.0625 $\mu\text{g/mL}$	RIF SDN	0.275	0.99278
0.125 $\mu\text{g/mL}$	RIF SDN	0.262	0.945848
0.25 $\mu\text{g/mL}$	RIF SDN	0.2579	0.931047
0.5 $\mu\text{g/mL}$	RIF SDN	0.267	0.963899
1 $\mu\text{g/mL}$	RIF SDN	0.265	0.956679
2 $\mu\text{g/mL}$	RIF SDN	0.262	0.945848
4 $\mu\text{g/mL}$	RIF SDN	0.259	0.935018

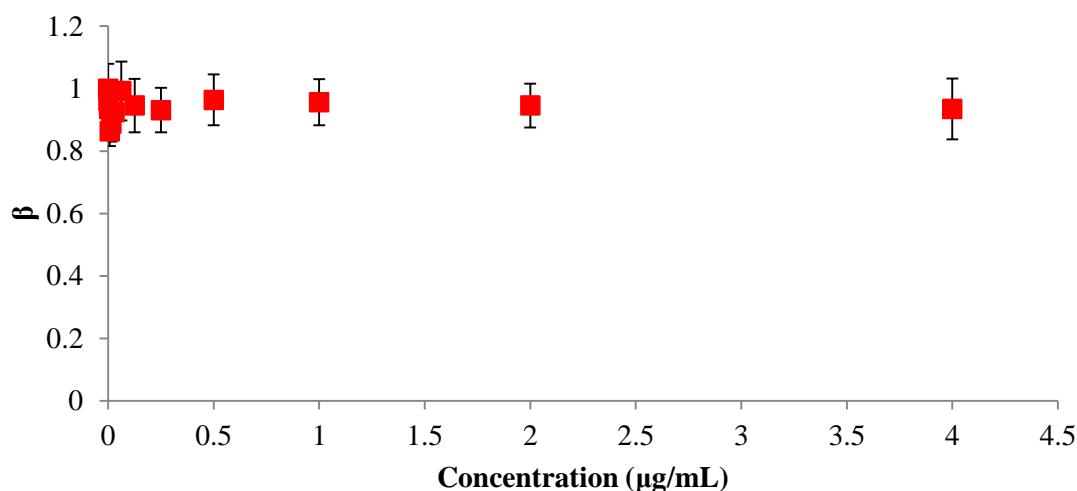


**Figure B.2 Growth of *Map* K10/GFP with INH aqueous normalised to the control** (where  $\beta$  represents the change in fluorescence [representing mycobacterial growth] per day). *Map* K10/GFP grown in 200  $\mu\text{L}$  of 7H9, in a microplate format, INH aqueous at different concentrations (0.001875 – 4  $\mu\text{g/mL}$ ), normalised to the slope of the control.  $\beta$  calculated through linear regression analysis of the Log data (Table B.2). Each point displaying 2\* the standard error calculated using LINEST function Excel (Microsoft Office Word) to cover the variation of the mean (n=2).



**Table B.3**  $\beta$  Values calculated from the linear regression of the Log data (growth of *Map* K10/GFP with RIF SDN). These values were normalised to the slope of the control (0  $\mu\text{g/mL}$ ) to plot Figures B.3.

Concentration ( $\mu\text{g/mL}$ )	Compound	Slope of the line ( $\beta$ )	$\beta$ (Normalised)
0	RIF SDN	0.2344	1
0.001875 $\mu\text{g/mL}$	RIF SDN	0.236	1.006826
0.00375 $\mu\text{g/mL}$	RIF SDN	0.2431	1.037116
0.0075 $\mu\text{g/mL}$	RIF SDN	0.2357	1.005546
0.015 $\mu\text{g/mL}$	RIF SDN	0.2377	1.014078
0.03 $\mu\text{g/mL}$	RIF SDN	0.2233	0.952645
0.0625 $\mu\text{g/mL}$	RIF SDN	0.1921	0.819539
0.125 $\mu\text{g/mL}$	RIF SDN	0.1822	0.777304
0.25 $\mu\text{g/mL}$	RIF SDN	0.1734	0.739761
0.5 $\mu\text{g/mL}$	RIF SDN	0.1691	0.721416
1 $\mu\text{g/mL}$	RIF SDN	0.1549	0.660836
2 $\mu\text{g/mL}$	RIF SDN	0.1532	0.653584
4 $\mu\text{g/mL}$	RIF SDN	0.1477	0.630119

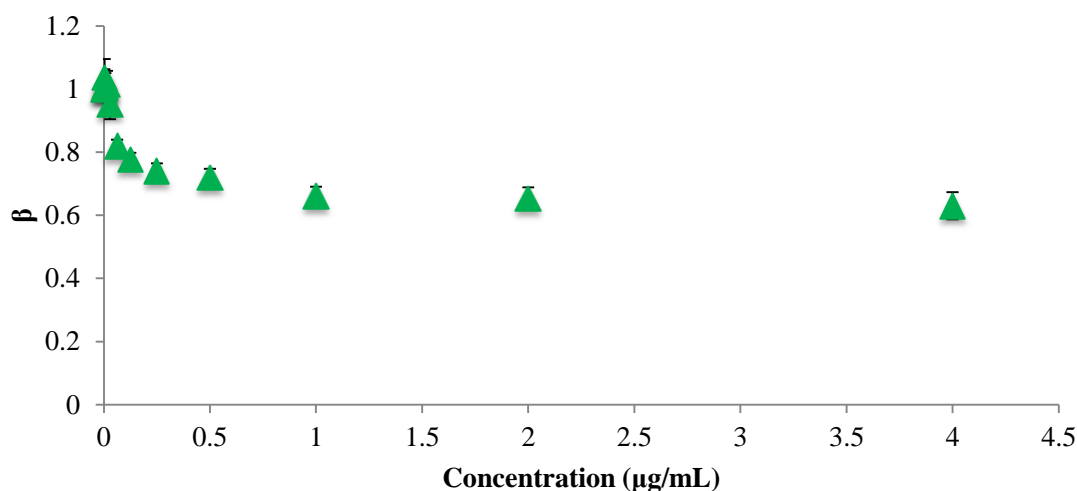


**Figure B.3** Growth of *Map* K10/GFP with RIF SDN normalised to the control (where  $\beta$  represents the change in fluorescence [representing mycobacterial growth] per day). *Map* K10/GFP grown in 200  $\mu\text{L}$  of 7H9, in a microplate format, RIF SDN at different concentrations (0.001875 – 4  $\mu\text{g/mL}$ ), normalised to the slope of the control.  $\beta$  calculated through linear regression analysis of the Log data (Table B.3). Each point displaying 2\* the standard error calculated using LINEST function Excel (Microsoft Office Word) to cover the variation of the mean (n=9).

**Table B.4  $\beta$**  Values calculated from the linear regression of the Log data (growth of *Map* K10/GFP with DUAL SDN). These values were normalised to the slope of the control (0  $\mu\text{g/mL}$ ) to plot Figures....

Concentration ( $\mu\text{g/mL}$ )	Compound	Slope of the line ( $\beta$ )	$\beta$ (Normalised)
0	RIF SDN	0.25	1
0.001875 $\mu\text{g/mL}$	RIF SDN	0.2488	0.9952
0.00375 $\mu\text{g/mL}$	RIF SDN	0.2587	1.0348
0.0075 $\mu\text{g/mL}$	RIF SDN	0.2678	1.0712
0.015 $\mu\text{g/mL}$	RIF SDN	0.2591	1.0364
0.03 $\mu\text{g/mL}$	RIF SDN	0.2433	0.9732
0.0625 $\mu\text{g/mL}$	RIF SDN	0.274	1.096
0.125 $\mu\text{g/mL}$	RIF SDN	0.2202	0.8808
0.25 $\mu\text{g/mL}$	RIF SDN	0.213	0.852
0.5 $\mu\text{g/mL}$	RIF SDN	0.2038	0.8152
1 $\mu\text{g/mL}$	RIF SDN	0.1912	0.7648
2 $\mu\text{g/mL}$	RIF SDN	0.1491	0.5964
4 $\mu\text{g/mL}$	RIF SDN	0.149	0.596

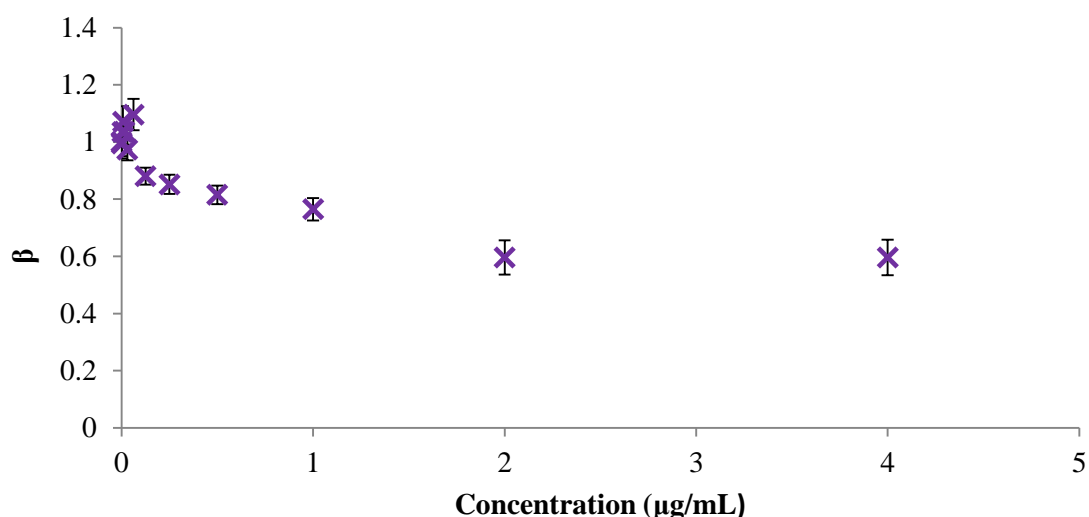


**Figure B.4 Growth of *Map* K10/GFP with DUAL SDN normalised to the control** (where  $\beta$  represents the change in fluorescence [representing mycobacterial growth] per day). *Map* K10/GFP grown in 200  $\mu\text{L}$  of 7H9, in a microplate format, DUAL SDN at different concentrations (0.001875 – 4  $\mu\text{g/mL}$ ), normalised to the slope of the control.  $\beta$  calculated through linear regression analysis of the Log data (Table B.4). Each point displaying 2\* the standard error calculated using LINEST function Excel (Microsoft Office Word) to cover the variation of the mean (n=6).

**Table B.5**  $\beta$  Values calculated from the linear regression of the Log data (growth of *Map* K10/GFP with TRIPLE SDN). These values were normalised to the slope of the control (0  $\mu\text{g/mL}$ ) to plot Figure B.5.

Concentration ( $\mu\text{g/mL}$ )	Compound	Slope of the line ( $\beta$ )	$\beta$ (Normalised)
0	RIF SDN	0.2305	1
0.001875 $\mu\text{g/mL}$	RIF SDN	0.2546	1.104555
0.00375 $\mu\text{g/mL}$	RIF SDN	0.2573	1.116269
0.0075 $\mu\text{g/mL}$	RIF SDN	0.2558	1.109761
0.015 $\mu\text{g/mL}$	RIF SDN	0.2527	1.096312
0.03 $\mu\text{g/mL}$	RIF SDN	0.2336	1.013449
0.0625 $\mu\text{g/mL}$	RIF SDN	0.1745	0.75705
0.125 $\mu\text{g/mL}$	RIF SDN	0.1685	0.73102
0.25 $\mu\text{g/mL}$	RIF SDN	0.1754	0.760954
0.5 $\mu\text{g/mL}$	RIF SDN	0.1984	0.860738
1 $\mu\text{g/mL}$	RIF SDN	0.1602	0.695011
2 $\mu\text{g/mL}$	RIF SDN	0.1576	0.683731
4 $\mu\text{g/mL}$	RIF SDN	0.156	0.67679

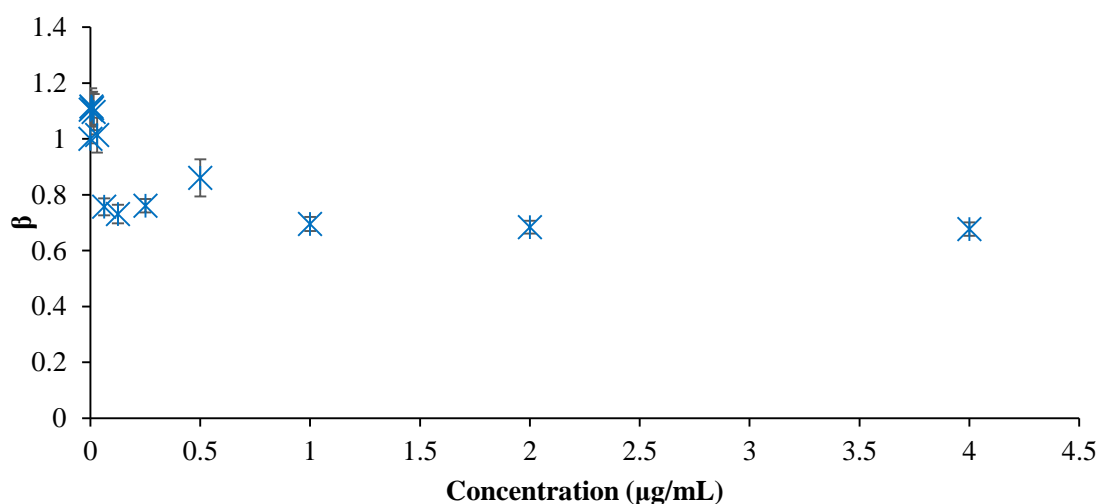
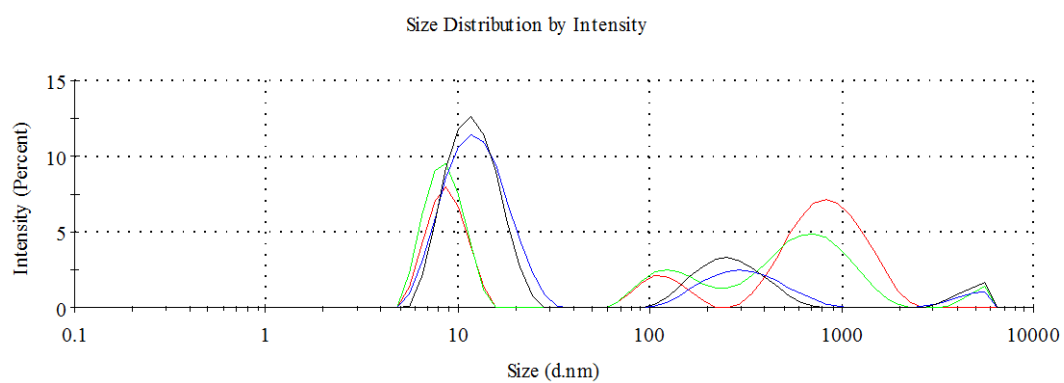
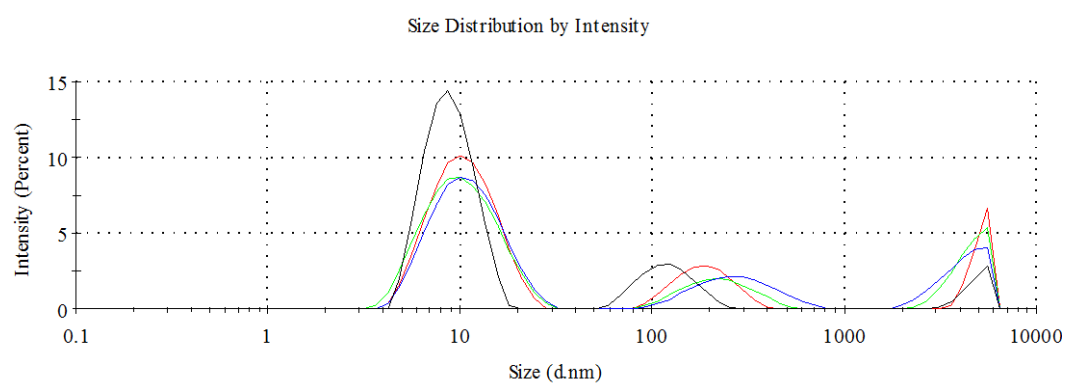


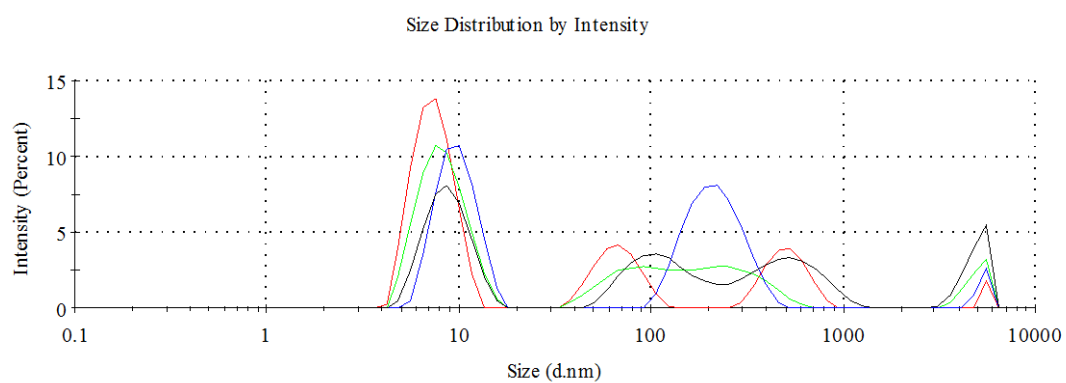
**Figure B.5 Growth of *Map* K10/GFP with TRIPLE SDN normalised to the control** (where  $\beta$  represents the change in fluorescence [representing mycobacterial growth] per day). *Map* K10/GFP grown in 200  $\mu\text{L}$  of 7H9, in a microplate format, TRIPLE SDN at different concentrations (0.001875 – 4  $\mu\text{g/mL}$ ), normalised to the slope of the control.  $\beta$  calculated through linear regression analysis of the Log data (Table B.5). Each point displaying 2\* the standard error calculated using LINEST function Excel (Microsoft Office Word) to cover the variation of the mean (n=9).



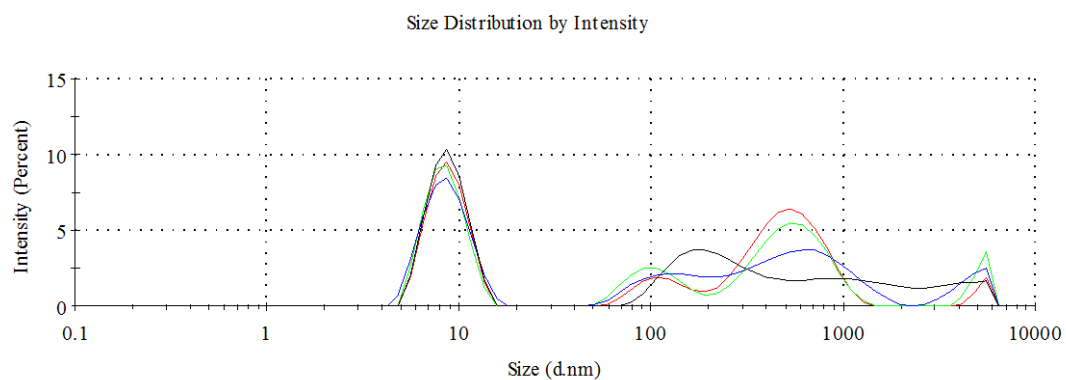
**a)**



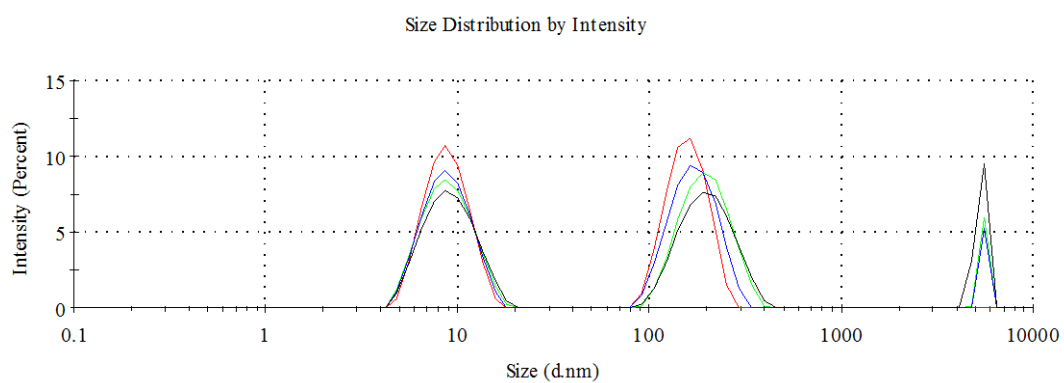
**b)**



**c)**



d)



e)

**Figure B.6 (a-e) Size intensity graphs (DLS) (n=4)**

- (a) RIF SDN 7H9
- (b) TRIPLE SDN 7H9
- (c) DUAL SDN in 7H9
- (d) RIF SDN (with DiD) 7H9
- (e) TRIPLE SDN 7H9 (with DiD) 7H9

**Appendix C**  
Statistical analysis

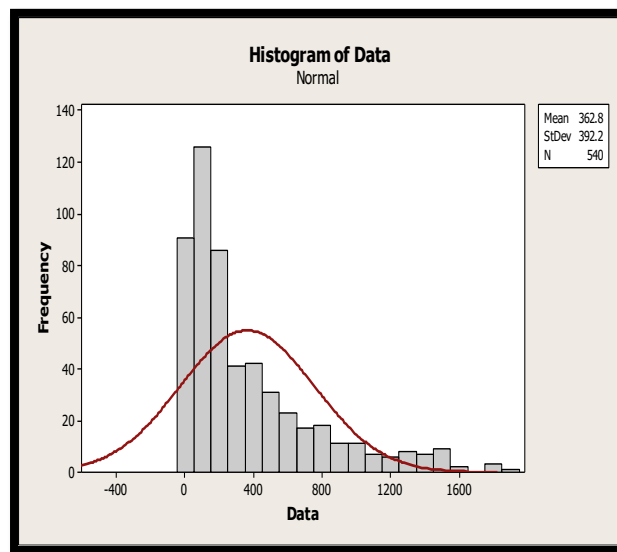


Figure C.1 Histogram of RIF SDN data (the data was skewed therefore it was normalised prior to analysis).

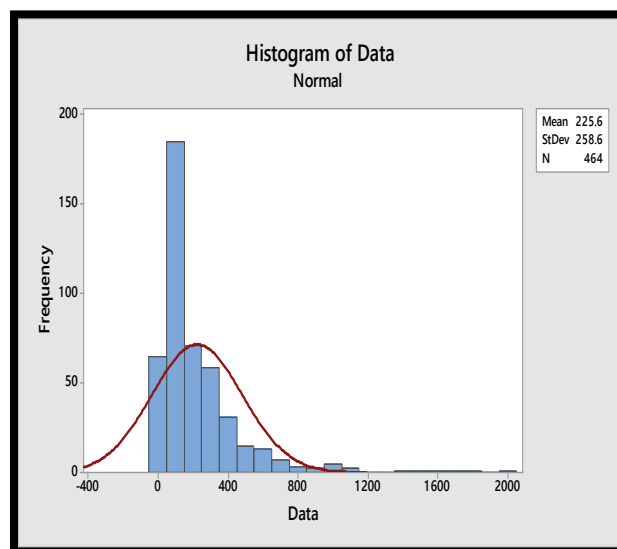


Figure C.2 Histogram of RIF aqueous data (the data was very skewed therefore it was normalised prior to analysis).

## **PUBLISHED ARTICLE AND PRESENTATIONS**























Poster Presentation, '*A rapid screening assay for TB*' **TB SUMIT, London**, March 2015.

**AWARDED FIRST PRIZE IN POSTER COMPETITION.**

Podium Presentation (invited speaker), '*Nanomedicines for the Treatment of TB*', **T-NANO, India**, Dec 2014.

Poster Presentation, '*Metal Oxide NPs used in a rapid screening assay*' **CLINAM, Basel**, July 2014.

Poster Presentation, '*Metal Oxide NPs used in a rapid screening assay*' **European Society of Mycobacteria (ESM), Vienna**, July 2014

Podium Presentation, '*Nanomedicines for the Treatment of TB*' **C.O.S.T ACTION, Marseille**, April 2014.

Podium Presentation, '*Nanomedicines for the Treatment of TB*' **Science for Life Competition, Dundee**, May 2014.

Poster Presentation, '*A Rapid Screening Assay to Compare the Effectiveness of 3 Metal Oxide Nanoparticles at Killing Mycobacteria*' **Science for Life Competition- Royal Society of Edinburgh, Edinburgh** May 2014.

## **LIST OF REFERENCES**

- Aboutaleb, E. et al., 2012. Improved antimycobacterial activity of rifampin using solid lipid nanoparticles. *International Nano Letters*, 2, p.33.
- Albrecht, M., Evans, C. & Raston, C., 2006. Green chemistry and the health implications of nanoparticles. *Green Chemistry*, 8, p.417.
- Allen, R. et al., 1956. Fungicides, Toxic Action of Metal Ions to Fungus Spores. *Journal of Agricultural and Food Chemistry*, pp.116–122.
- Altic, L., Rowe, M. & Grant, I., 2007. UV light inactivation of *Mycobacterium avium* subsp. paratuberculosis in milk as assessed by FASTPlaqueTB phage assay and culture. *Applied and Environmental Microbiology*, 73, pp.3728–3733.
- Ananth, A. et al., 2015. Copper oxide nanomaterials: Synthesis, characterization and structure-specific antibacterial performance. *Chemical Engineering Journal*, 262, pp.179–188.
- Andreu, N. et al., 2012. Rapid measurement of antituberculosis drug activity in vitro and in macrophages using bioluminescence. *Journal of Antimicrobial Chemotherapy*, 67, pp.404–414.
- Ansari, M. et al., 2011. Evaluation of antibacterial activity of silver nanoparticles against MSSA and MRSA on isolates from skin infections. *Biology and Medicine*, 3, pp.141–146.
- Arai, Y., Miyayama, T. & Hirano, S., 2015. Difference in the toxicity mechanism between ion and nanoparticle forms of silver in the mouse lung and in macrophages. *Toxicology*, 328, pp.84–92.
- Ardito, F. et al., 2001. Evaluation of BACTEC *Mycobacteria* Growth Indicator Tube (MGIT 960) Automated System for Drug Susceptibility Testing of *Mycobacterium tuberculosis*. *Journal Clinical of Microbiology*, 39, pp.4440–4444.
- Auld, D.S. et al., 2009. Mechanism of PTC124 activity in cell-based luciferase assays of nonsense codon suppression. *Proceedings of the National Academy of Sciences of the United States of America*, 106, pp.3585–3590.
- Azam, A., Ahmed, A.S., Oves, M., et al., 2012. Antimicrobial activity of metal oxide nanoparticles against Gram-positive and Gram-negative bacteria: A comparative study. *International Journal of Nanomedicine*, 7, pp.6003–6009.
- Azam, A., Ahmed, A.S., Oves, M., et al., 2012. Size-dependent antimicrobial properties of CuO nanoparticles against Gram-positive and -negative bacterial strains. *International Journal of Nanomedicine*, 7, pp.3527–3535.
- Bakula, Z. et al., 2013. Mutations in the *embB* gene and their association with ethambutol resistance in multidrug-resistant *mycobacterium tuberculosis* clinical isolates from Poland. *BioMed Research International*, (167954).
- Banaiee, N. et al., 2008. Evaluation of a Semi-Automated Reporter Phage Assay for Susceptibility Testing of *Mycobacterium tuberculosis* Isolates in South Africa. *Tuberculosis (Edinb)*, 88, pp.64–68.
- Banaiee, N. et al., 2001. Luciferase Reporter *Mycobacteriophages* for Detection , Identification , and Antibiotic Susceptibility Testing of *Mycobacterium tuberculosis* in Mexico. *Journal of Clinical Microbiology*, 39, pp.3883–3888.
- Barry, D.P. & Beaman, B.L., 2006. Modulation of eukaryotic cell apoptosis by members of the bacterial order Actinomycetales. *Apoptosis: an international journal on programmed cell*

death, 11, pp.1695–707.

Bawa, R., 2008. Nanoparticle-based therapeutics in humans: A survey. *Nanotechnology Law & Business*, 5, pp.135–155.

BBC Health News, 2013. Antibiotic “apocalypse” warning. Available at: <http://www.bbc.co.uk/news/health-21178718> [Accessed September 2, 2014].

BBC Health News, 2015. Parts of London have higher TB rates than Iraq or Rwanda. Available at: <http://www.bbc.co.uk/news/uk-england-london-34637968> [Accessed January 10, 2015].

Beard, P. et al., 2001. Paratuberculosis infection of nonruminant wildlife in Scotland. *Journal of clinical microbiology*, 39, pp.1517–21.

Behr, M. & Collins, D., 2010. Paratuberculosis and Crohn’s Disease. In *Paratuberculosis, Organism, Disease, Control*. CABI, pp. 40–49.

Benedictus, G., Dijkhuizen, A. & Stelwagen, J., 1987. Economic losses due to paratuberculosis in dairy cattle. *Veterinary Record*, 121, pp.142–146.

Besinis, A., De Peralta, T. & Handy, R.D., 2014. The antibacterial effects of Ag, TiO<sub>2</sub> and SiO<sub>2</sub> nanoparticles compared to the Dental Disinfectant Chlorhexidine on *Streptococcus mutans* Using a Suite of Bioassays. *Nanotoxicology*, 8, pp.1–45.

Bhadade, A. et al., 2015. Utility of light-emitting diode microscopy for the diagnosis of pulmonary tuberculosis in HIV infected patients. *International Journal of Mycobacteriology*, 4, pp.31–35.

Bielska, E. et al., 2011. Virtual screening strategies in drug design— methods and applications. *Journal of Biotechnology, Computational Biology and Bionanotechnology*, 92, pp.249–264.

Blokpoel, M.C.J. et al., 2003. Development and application of unstable GFP variants to kinetic studies of mycobacterial gene expression. *Journal of Microbiological Methods*, 54, pp.203–211.

Boehme, C. et al., 2011. Feasibility, diagnostic accuracy, and effectiveness of decentralised use of the Xpert MTB/RIF test for diagnosis of tuberculosis and multidrug resistance: a multicentre implementation study. *Lancet*, 377, pp.1495–505.

Boeree, M.J. et al., 2015. A dose-ranging trial to optimize the dose of rifampin in the treatment of tuberculosis. *American Journal of Respiratory and Critical Care Medicine*, 191, pp.1058–1065.

Bondarenko, O. et al., 2012. Sub-toxic effects of CuO nanoparticles on bacteria: kinetics, role of Cu ions and possible mechanisms of action. *Environmental pollution*, 169, pp.81–89.

Bondarenko, O. et al., 2013a. Toxicity of Ag, CuO and ZnO nanoparticles to selected environmentally relevant test organisms and mammalian cells in vitro: A critical review. *Archives of Toxicology*, 87, pp.1181–1200.

Bondarenko, O. et al., 2013b. Toxicity of Ag, CuO and ZnO nanoparticles to selected environmentally relevant test organisms and mammalian cells in vitro: A critical review. *Archives of Toxicology*, 87, pp.1181–1200.

Boogaard, J. et al., 2009. New drugs against tuberculosis: problems, progress, and evaluation of agents in clinical development. *Antimicrobial agents and chemotherapy*, 53, pp.849–862.

Botsaris, G. et al., 2016. Detection of viable *Mycobacterium avium* subspecies paratuberculosis

- in powdered infant formula by phage-PCR and confirmed by culture. *International Journal of Food Microbiology*, 216, pp.91–94.
- Botsaris, G. et al., 2010. Rapid detection methods for viable *Mycobacterium avium* subspecies paratuberculosis in milk and cheese. *International journal of food microbiology*, 141 Suppl , pp.S87–90. Available at: <http://www.ncbi.nlm.nih.gov/pubmed/20381185>.
- Van Boxtel, R.M., Lambrecht, R.S. & Collins, M.T., 1990. Effects of colonial morphology and tween 80 on antimicrobial susceptibility of *Mycobacterium paratuberculosis*. *Antimicrobial agents and chemotherapy*, 34, pp.2300–3.
- Brandenberger, C. et al., 2010. Intracellular imaging of nanoparticles: is it an elemental mistake to believe what you see? *Particle and fibre toxicology*, 7, p.15.
- Brites, D. & Gagneux, S., 2015. Co-evolution of *Mycobacterium tuberculosis* and *Homo sapiens*. *Immunological reviews*, 264(1), pp.6–24.
- Brosch, R. et al., 2002. A new evolutionary scenario for the *Mycobacterium tuberculosis* complex. *Proceedings of the National Academy of Sciences USA*, 6, pp.3684–9.
- Brunner, T.J. et al., 2006. In Vitro Cytotoxicity of Oxide Nanoparticles: Comparison to Asbestos, Silica, and the Effect of Particle Solubility †. *Environmental Science & Technology*, 40, pp.4374–4381.
- Burrells, C. et al., 1998. A study of immunological responses of sheep clinically-affected with paratuberculosis (Johne's disease): The relationship of blood, mesenteric lymph node and intestinal lymphocyte responses to gross and microscopic pathology. *Veterinary immunology and immunopathology*, 66, pp.343–358.
- Busquets, M.A., Estelrich, J. & Sánchez-Martín, M.J., 2015. Nanoparticles in magnetic resonance imaging: from simple to dual contrast agents. *International Journal of Nanomedicine*, 140, pp.1727–1741.
- Byrne, J. et al., 2011. More Effective Nanomedicines through Particle Design. *Small*, 7(14), pp.1919–1931.
- Byrne, J. & Baugh, J., 2008. The significance of nanoparticles in particle-induced pulmonary fibrosis. *Mcgill J Med*, 11, pp.43–50.
- Cha, K. et al., 2008. Comparison of acute responses of mice livers to short-term exposure to nano-sized or micro-sized silver particles. *Biotechnology Letters*, 30, p.1893.
- Chacon, O., Bermudez, L. & Barletta, R., 2004. Johne's disease, inflammatory bowel disease, and *Mycobacterium paratuberculosis*. *Annual Review of Microbiology*, 58, pp.329–363.
- Chalfie, M. et al., 1994. Green Fluorescent Protein as a Marker for Gene Expression. *Science*, 263, pp.802–805.
- Chang, Y.-N. et al., 2012. The Toxic Effects and Mechanisms of CuO and ZnO Nanoparticles. *Materials*, 5, pp.2850–2871.
- Chatterjee, A., Chakraborty, R. & Basu, T., 2014. Mechanism of antibacterial activity of copper nanoparticles. *Nanotechnology*, 25, p.135101.
- Che, P. et al., 2012. Validating a firefly luciferase-based high-throughput screening assay for antimalarial drug discovery. *Assay and drug development technologies*, 10, pp.61–68.
- Chen, D. et al., 2011. Effects of Cu<sub>2</sub>O nanoparticle and CuCl<sub>2</sub> on zebrafish larvae and a liver cell-line. *Aquatic Toxicology*, 105, pp.344–354.
- Cheon, S. et al., 2016. Recent tuberculosis diagnosis toward the end TB strategy. *Journal of*

*Microbiological Methods*, p.10.1016/j.mimet.2016.02.007.

- Choi, H. et al., 2010. Rapid translocation of nanoparticles from the lung airspaces to the body. *Nature Biotechnology*, 28, pp.1300–1303.
- Choi, O. et al., 2008. The inhibitory effects of silver nanoparticles, silver ions, and silver chloride colloids on microbial growth. *Water research*, 42, pp.3066–3074.
- Choudhary, S. & Kusum Devi, V., 2015. Potential of nanotechnology as a delivery platform against tuberculosis: Current research review. *Journal of Controlled Release*, 202, pp.65–75.
- Christensen, F. et al., 2010. Nano-silver - feasibility and challenges for human health risk assessment based on open literature. *Nanotoxicology*, 4, pp.284–95.
- Chuan, J. et al., 2013. Enhanced rifampicin delivery to alveolar macrophages by solid lipid nanoparticles. *Journal of Nanoparticle Research*, 15(5), pp.1–9.
- Clift, M. et al., 2008. The impact of different nanoparticle surface chemistry and size on uptake and toxicity in a murine macrophage cell line. *Toxicology and Applied Pharmacology*, 232, pp.418–427.
- Cocito, C. et al., 1994. Paratuberculosis. *Clinical Microbiology Reviews*, 7, pp.328–345.
- Cohen, R., 2005. Mycobacterium in Crohn's: Something to ruminate about? *Gastroenterology*, 128, pp.2167–2168.
- Collins, F., 1997. Tuberculosis research in a cold climate. *Tubercle and Lung Disease*, 78, pp.99–107.
- Collins, L. & Franzblau, S.G., 1997. Microplate alamar blue assay versus BACTEC 460 system for high-throughput screening of compounds against Mycobacterium tuberculosis and Mycobacterium avium. *Antimicrobial agents and chemotherapy*, 41, pp.1004–1009.
- Collins, L., Torrero, M. & Franzblau, S., 1998. Green fluorescent protein reporter microplate assay for high-throughput screening of compounds against Mycobacterium tuberculosis. *Antimicrobial agents and chemotherapy*, 42, pp.344–347.
- Comas, I. et al., 2010. Human T cell epitopes of Mycobacterium tuberculosis are evolutionarily hyperconserved. *Nature Genetics*, 42(6), pp.498–503.
- Comas, I. et al., 2013. Out-of-Africa migration and Neolithic co-expansion of Mycobacterium tuberculosis with modern humans. *Nature genetics*, 45, pp.1176–1182.
- Cooper, A., 2009. T cells in mycobacterial infection and disease. *Current opinion in immunology*, 21, pp.378–84.
- Cormack, B.P., Valdivia, R.H. & Falkow, S., 1996. FACS-optimized mutants of the green fluorescent protein (GFP). *Gene*, 173, pp.33–38.
- Crevel, R. et al., 2002. Innate Immunity to Mycobacterium tuberculosis Innate Immunity to Mycobacterium tuberculosis. *Clinical Microbiology Reviews*, 15, pp.294–309.
- Cukierman, E. & Khan, D., 2011. The Benefits and Challenges Associated with the Use of Drug Delivery Systems in Cancer Therapy. *Biochem Pharmacol*, 80, pp.762–770.
- Dalziel, K., 1913. Chronic Interstitial Enteritis. *British Medical Journal*, ii, pp.1068–1070.
- Das, D. et al., 2013. Synthesis and evaluation of antioxidant and antibacterial behavior of CuO nanoparticles. *Colloids and Surfaces B: Biointerfaces*, 101, pp.430–433.

- Davies, P., 2003. The role of DOTS in tuberculosis treatment and control. *American Journal of Respiratory Medicine: drugs, devices and other interventions*, 2, pp.203–209.
- Dawson, R. et al., 2015. Efficiency and safety of the combination of moxifloxacin, pretomanid (PA-824), and pyrazinamide during the first 8 weeks of antituberculosis treatment: a phase 2b, open-label, partly randomised trial in patients with drug-susceptible or drug-resistant pul. *Lancet*, 385, pp.1738–1747.
- Deb, D.K. et al., 2000. Bioluminescent *Mycobacterium aurum* expressing firefly luciferase for rapid and high throughput screening of antimycobacterial drugs in vitro and in infected macrophages. *Biochem Biophys Res Commun*, 279, pp.457–461.
- Degano, M. et al., 2014. *Mycobacterium tuberculosis* Pyrazinamide Resistance Determinants: A Multicenter Study. *American Society for Microbiology*, 5, pp.1–10.
- Dizaj, S.M. et al., 2014. Antimicrobial activity of the metals and metal oxide nanoparticles. *Materials Science and Engineering*, 44, pp.278–284.
- Dolovich, M.B. & Dhand, R., 2011. Aerosol drug delivery: Developments in device design and clinical use. *The Lancet*, 377, pp.1032–1045.
- Donaldson, K., Li, X.Y. & Macnee, W., 1998. Ultrafine (nm) particle mediated lung injury. *Journal of aerosol science*, 29, pp.553–560.
- Donnellan, S. et al., 2015. A rapid screening assay for identifying mycobacteria targeted nanoparticle antibiotics. *Nanotoxicology*, 5390, pp.1–9.
- Dube, A. et al., 2013. Multimodal nanoparticles that provide immunomodulation and intracellular drug delivery for infectious diseases. *Nanomedicine: nanotechnology, biology, and medicine*, 10, pp.1–8.
- Dubnau, E. & Smith, I., 2003. *Mycobacterium tuberculosis* gene expression in macrophages. *Microbes and infection / Institut Pasteur*, 5, pp.629–37.
- Ducati, R.G. et al., 2006. The resumption of consumption - A review on tuberculosis. *Memorias do Instituto Oswaldo Cruz*, 101, pp.697–714.
- Edagwa, B.J. et al., 2014. Long-acting antituberculous therapeutic nanoparticles target macrophage endosomes. *FASEB journal : official publication of the Federation of American Societies for Experimental Biology*, 12, pp.5071–5082.
- Ehlers, S. & Schaible, U.E., 2012. The granuloma in tuberculosis: Dynamics of a host-pathogen collusion. *Frontiers in Immunology*, 3, pp.1–9.
- Elguezabal, N. et al., 2011. Estimation of *Mycobacterium avium* subsp. paratuberculosis growth parameters: strain characterization and comparison of methods. *Applied and environmental microbiology*, 77, pp.8615–24.
- Ellingson, J. et al., 2005. Detection of viable *Mycobacterium avium* subsp. paratuberculosis in retail pasteurized whole milk by two culture methods and PCR. *Journal of Food Protection*, 7, pp.966–972.
- Elsaesser, A. & Howard, C.V., 2012. Toxicology of nanoparticles. *Advanced Drug Delivery Reviews*, 64(2), pp.129–137.
- Etheridge, M. et al., 2013. The big picture on nanomedicine: the state of investigational and approved nanomedicine products. *Nanomedicine*, 9, pp.1–14.
- ETP, 2015. European Technology Platform on Nanomedicine. Available at: <http://www.etp-nanomedicine.eu/public/about-nanomedicine/what-is-nanomedicine> [Accessed January 26,

2016].

- Fabre, M. et al., 2004. High genetic diversity revealed by variable-number tandem repeat genotyping and analysis of hsp65 gene polymorphism in a large collection of "Mycobacterium canettii" strains indicates that the M. tuberculosis complex is a recently emerged clone of "M. can. *Journal of Clinical Microbiology*, 42(7), pp.3248–3255.
- Farias, P., Santos, B. & Fontes, A., 2009. Semiconductor Fluorescent Quantum Dots: Efficient Biolabels in Cancer Diagnostics. *Micro and Nano Technologies in Bioanalysis*, 544, pp.407–419.
- Favrot, L. & Ronning, D., 2012. Targeting the mycobacterial envelope for Tuberculosis Drug Development. *Expert review of anti-infective therapy*, 9, pp.1023–1036.
- Feng, Q. et al., 2000. A mechanistic study of the antibacterial effect of Ag ions on E coli and Straphylococcus aureus. *Journal of biomedical materials research*, 4, pp.662–668.
- Ferin, J. et al., 2009. Pulmonary tissue access of ultrafine particles. *Journal of aerosol medicine*, 4, pp.57–68.
- Ferin, J., Oberdorster, G. & Penney, D., 1992. Pulmonary Retention of Ultrafine and Fine Particles in Rats. *American Journal of Respiratory Cell and Molecular Biology*, 6, pp.535–542.
- Fernández-Cruz, M.L. et al., 2012. Comparative cytotoxicity induced by bulk and nanoparticulated ZnO in the fish and human hepatoma cell lines PLHC-1 and Hep G2. *Nanotoxicology*, 7(August), pp.1–18.
- Flynn, J.L., Chan, J. & Lin, P.L., 2011. Macrophages and control of granulomatous inflammation in tuberculosis. *Mucosal Immunology*, 4, pp.271–278.
- Fortin, M., Steff, A. & Hüge, P., 2005. High-throughput technology: green fluorescent protein to monitor cell death. *Methods Molecular Biology*, 110, pp.121–137.
- Franzblau, S. et al., 2012. Comprehensive analysis of methods used for the evaluation of compounds against Mycobacterium tuberculosis. *Tuberculosis*, 92, pp.453–88.
- Gagneux, S., 2012. Host-pathogen coevolution in human tuberculosis. *Philosophical Transactions of the Royal Society B: Biological Sciences*, 367(1590), pp.850–859.
- Gagneux, S. et al., 2006. Variable host-pathogen compatibility in Mycobacterium tuberculosis. *Proceedings of the National Academy of Sciences of the United States of America*, 103, pp.2869–73.
- Gaiser, B.K. et al., 2013. Effects of silver nanoparticles on the liver and hepatocytes in vitro. *Toxicological Sciences*, 131, pp.537–547.
- Ganguly, N. et al., 2008. Mycobacterium tuberculosis secretory proteins CFP-10, ESAT-6 and the CFP10:ESAT6 complex inhibit lipopolysaccharide-induced NF-kappaB transactivation by downregulation of reactive oxidative species (ROS) production. *Immunology and cell biology*, 86, pp.98–106.
- Gantedia, S., Narsimha, R. & Anreddya, R., 2012. Toxicological studies of zinc oxide nanomaterials in rats. *Toxicological & Environmental Chemistry*, 94, pp.1768–1779.
- Gaspar, M. et al., 2008. Rifabutin encapsulated in liposomes exhibits increased therapeutic activity in a model of disseminated tuberculosis. *International journal of antimicrobial agents*, 31(1), pp.37–45.
- Geiser, M. et al., 2008. The Role of Macrophages in the Clearance of Inhaled Ultrafine

- Titanium Dioxide Particles. *American Journal of Respiratory Cell and Molecular Biology*, 38, pp.371–376.
- Geiser, M., 2010. Update on Macrophage Clearance of Inhaled Micro- and Nanoparticles. *Journal of aerosol medicine and pulmonary drug delivery*, 23, pp.207–217.
- Gelperina, S. et al., 2005. The Potential Advantages of Nanoparticle Drug Delivery Systems in Chemotherapy of Tuberculosis. *American Journal of Respiratory and Critical Care Medicine*, 172(12), pp.1487–1490.
- Georgioui, S. et al., 2012. Evaluation of Genetic Mutations Associated with Mycobacterium tuberculosis Resistance to Amikacin , Kanamycin and Capreomycin: A Systematic Review. *PloS One*, 7(3), p.e33275.
- Giacomini, E. et al., 2001. Infection of human macrophages and dendritic cells with Mycobacterium tuberculosis induces a differential cytokine gene expression that modulates T cell response. *Journal of immunology*, 166, pp.7033–7041.
- Giacomotto, J. & Segalat, L., 2010. High-throughput screening and small animal models, where are we? *British Journal of Pharmacology*, 160(2), pp.204–216.
- Gillespie, S.H. et al., 2014. Four-Month Moxifloxacin-Based Regimens for Drug-Sensitive Tuberculosis. *New England Journal of Medicine*, 371, pp.1577–1587.
- Ginsberg, A.M. et al., 2009. Safety, tolerability, and pharmacokinetics of PA-824 in healthy subjects. *Antimicrobial Agents and Chemotherapy*, 53(9), pp.3720–3725.
- Ginsberg, A.M. & Spigelman, M., 2007. Challenges in tuberculosis drug research and development. *Nature Medicine*, 13(3), pp.290–294.
- Gninafon, M. et al., 2014. A Four-Month Gatifloxacin-Containing Regimen for Treating Tuberculosis. *New England Journal of Medicine*, 371, pp.1588–1598. Available at: <http://dx.doi.org/10.1056/NEJMoa1315817>.
- Goel, D., 2014. Bedaquiline: A novel drug to combat multiple drug-resistant tuberculosis. *Journal of pharmacology & pharmacotherapeutics*, 5(1), pp.76–8.
- Green, K.D. & Garneau-Tsodikova, S., 2013. Resistance in tuberculosis: What do we know and where can we go? *Frontiers in Microbiology*, 4(July), pp.1–7.
- Griffiths, G. et al., 2010. Nanobead-based interventions for the treatment and prevention of tuberculosis. *Nature Reviews microbiology*, 8, pp.827–834.
- Grobler, A., Perez Sierra, Z. & Viljoen, H.J., 2016. Modeling nanoparticle delivery of TB drugs to granulomas. *Journal of Theoretical Biology*, 388, pp.85–95.
- Grosset, J. & Ammerman, N., 2013. Dose-Ranging activity of the newly registered antituberculosis drug bedaquiline (TMC207). *Expert Review of Anti-infective Therapy*, 11(7), pp.649–651.
- Grosset, J.H., Singer, T.G. & Bishai, W.R., 2012. New drugs for the treatment of tuberculosis: hope and reality. *The International Journal of Tuberculosis and Lung Disease*, 16(8), pp.1005–1014.
- Guirado, E. & Schlesinger, L.S., 2013. Modeling the Mycobacterium tuberculosis granuloma - the critical battlefield in host immunity and disease. *Frontiers in Immunology*, 4, pp.1–7.
- Gumbo, T., Pasipanodya, J.G., et al., 2015. Forecasting Accuracy of the Hollow Fiber Model of Tuberculosis for Clinical Therapeutic Outcomes. *Clinical Infectious Diseases*, 61(suppl 1), pp.S25–S31.



- Gumbo, T., Angulo-Barturen, I. & Ferrer-Bazaga, S., 2015. Pharmacokinetic-Pharmacodynamic and Dose-Response Relationships of Antituberculosis Drugs: Recommendations and Standards for Industry and Academia. *Journal of Infectious Diseases*, 211, pp.S96–S106.
- Gutierrez, C. et al., 2005. Ancient origin and gene mosaicism of the progenitor of *Mycobacterium tuberculosis*. *PLoS Pathogens*, 1(1), pp.0055–0061.
- Hamid, R. et al., 2004. Comparison of alamar blue and MTT assays for high through-put screening. *Toxicology in Vitro*, 18(5), pp.703–710.
- Harris, B. & Barletta, R., 2001. *Mycobacterium avium* subsp . paratuberculosis in Veterinary Medicine. *Clinical Microbiology Reviews*, 14, pp.489–512.
- Harris, N. et al., 2002a. Cell Sorting of Formalin- Treated Pathogenic *Mycobacterium* paratuberculosis Expressing GFP. *Biotechniques*, 32, pp.522–527.
- Harris, N. et al., 2002b. Cell sorting of formalin-treated pathogenic *Mycobacterium* paratuberculosis expressing GFP. *Biotechniques*, 32, pp.522–527.
- Hassen Ali, A. et al., 2013. Anti-tuberculosis drug induced hepatotoxicity among TB/HIV co-infected patients at Jimma University Hospital, Ethiopia: nested case-control study. *PloS one*, 8(5), p.e64622.
- Health Protection Agency, 2012. Tuberculosis in the UK: 2012 report. Available at: [http://www.hpa.org.uk/webw/HPAweb&HPAwebStandard/HPAweb\\_C/1317134916916](http://www.hpa.org.uk/webw/HPAweb&HPAwebStandard/HPAweb_C/1317134916916) [Accessed January 24, 2013].
- Health Protection Scotland, 2015. Health Protection Scotland.
- Heep, M. et al., 2000. Mutations in the beginning of the *rpoB* gene can induce resistance to rifamycins in both *Helicobacter pylori* and *Mycobacterium tuberculosis*. *Antimicrobial agents and chemotherapy*, 44(4), pp.1075–7.
- Heim, R. & Tsien, R.Y., 1996. Engineering green fluorescent protein for improved brightness, longer wavelengths and fluorescence resonance energy transfer. *Current biology*, 6(2), pp.178–182.
- Heinlaan, M. et al., 2008. Toxicity of nanosized and bulk ZnO, CuO and TiO<sub>2</sub> to bacteria *Vibrio fischeri* and crustaceans *Daphnia magna* and *Thamnocephalus platyurus*. *Chemosphere*, 71(7), pp.1308–1316.
- Hermon-Taylor, J., 2009. *Mycobacterium avium* subspecies paratuberculosis, Crohn's disease and the Doomsday scenario. *Gut pathogens*, 1(1), p.15.
- Hest, R. Van et al., 2004. Hepatotoxicity of Rifampin-Pyrazinamide and Isoniazid Preventive Therapy and Tuberculosis Treatment. *Clin Infect Dis*, 39, pp.488–96.
- Higuchi, K. et al., 2007. Use of QuantiFERON-TB Gold to investigate tuberculosis contacts in a high school. *Respirology (Carlton, Vic.)*, 12(1), pp.88–92.
- Hirota, K. et al., 2010. Delivery of rifampicin-PLGA microspheres into alveolar macrophages is promising for treatment of tuberculosis. *Journal of Controlled Release*, 142(3), pp.339–346. Available at: <http://dx.doi.org/10.1016/j.jconrel.2009.11.020>.
- Hoff, D.R. et al., 2011. Location of intra- and extracellular *M. tuberculosis* populations in lungs of mice and guinea pigs during disease progression and after drug treatment. *PLoS ONE*, 6(3).
- Hossain, M.M. & Norazmi, M.N., 2013. Pattern Recognition Receptors and Cytokines in Infection-The Double-Edged Sword? *BioMed Research International*, p.179174.

- Hostetter, J.M. et al., 2002. Cytokine effects on maturation of the phagosomes containing *Mycobacteria avium* subspecies paratuberculosis in J774 cells. *FEMS Immunol Med Microbiol*, 34, pp.127–134.
- Hughes, V. et al., 2007. Proteomic comparison of *Mycobacterium avium* subspecies paratuberculosis grown in vitro and isolated from clinical cases of ovine paratuberculosis. *Microbiology (Reading, England)*, 153(Pt 1), pp.196–205.
- Hurdle, J.G. et al., 2008. A microbiological assessment of novel nitrofuranylamides as anti-tuberculosis agents. *Journal of Antimicrobial Chemotherapy*, 62(5), pp.1037–1045.
- Hussain, M.M., Samir, T.M. & Azzazy, H.M.E., 2013. Unmodified gold nanoparticles for direct and rapid detection of *Mycobacterium tuberculosis* complex. *Clinical biochemistry*, 46(7-8), pp.633–7.
- Hussain, N., Jaitley, V. & Florence, A.T., 2001. Recent advances in the understanding of uptake of microparticulates across the gastrointestinal lymphatics. *Advanced Drug Delivery Reviews*, 50(1-2), pp.107–142.
- van Ingen, J. et al., 2011. Why Do We Use 600 mg of Rifampicin in Tuberculosis Treatment? *Clinical Infectious Diseases*, 52(9), pp.e194–e199.
- Islam, M.S. et al., 2013. Antimycobacterial efficacy of silver nanoparticles as deposited on porous membrane filters. *Materials Science and Engineering C*, 33, pp.4575–4581.
- Jachak, A. et al., 2012. Transport of metal oxide nanoparticles and single-walled carbon nanotubes in human mucus. *Nanotoxicology*, 6, pp.614–622.
- Jacobsen, N. et al., 2010. Nanomaterial dispersion protocol for toxicological studies in ENPRA. *Natl Res Centre Working Environ 6: Internal ENPRA report*, pp.1–10.
- Jain, S. et al., 2008. Antibiotic Treatment of Tuberculosis: Old Problems, New Solutions. *Microbe*, 3(6), p.285.
- Jiang, H.S. et al., 2012. Physiological analysis of silver nanoparticles and AgNO<sub>3</sub> toxicity to *Spirodela polyrhiza*. *Environmental Toxicology and Chemistry*, 31(8), pp.1880–1886.
- Jiang, W., Mashayekhi, H. & Xing, B., 2009. Bacterial toxicity comparison between nano- and micro-scaled oxide particles. *Environmental pollution*, 157, pp.1619–25.
- Johnston, H. et al., 2012. Investigating the relationship between nanomaterial hazard and physicochemical properties: Informing the exploitation of nanomaterials within therapeutic and diagnostic applications. *Journal of Controlled Release*, 164, pp.307–313.
- Johnston, H. et al., 2015. Mechanism of neutrophil activation and toxicity elicited by engineered nanomaterials. *Toxicology in vitro : an international journal published in association with BIBRA*, 29, pp.1172–84.
- Jokerst, J. V et al., 2011. Nanoparticle PEGylation for imaging and therapy. *Nanomedicine*, 6, pp.715–728.
- De Jong, W.H. & Borm, P.J. a, 2008. Drug delivery and nanoparticles: applications and hazards. *International journal of nanomedicine*, 3(2), pp.133–149.
- Jung, W.K. et al., 2008. Antibacterial activity and mechanism of action of the silver ion in *Staphylococcus aureus* and *Escherichia coli*. *Applied and environmental microbiology*, 74, pp.2171–2178.
- Kalbassi, M.R. et al., 2013. Particle Size and Agglomeration Affect the Toxicity levels of Silver Nanoparticle types in Aquatic Environment. , 1(3), pp.247–264.

- Kalluru, R. et al., 2013. Poly(lactide-co-glycolide)-rifampicin nanoparticles efficiently clear *Mycobacterium bovis* BCG infection in macrophages and remain membrane-bound in phago-lysosomes. *Journal of cell science*, 126(Pt 14), pp.3043–54.
- Kamaly, N. et al., 2012a. Targeted polymeric therapeutic nanoparticles: design, development and clinical translation. *Chemical Society reviews*, 41, pp.2971–3010.
- Kamaly, N. et al., 2012b. Targeted polymeric therapeutic nanoparticles: design, development and clinical translation. *Chemical Society reviews*, 41(7), pp.2971–3010.
- Kaufmann, S.H.E., 2013. Tuberculosis vaccines: Time to think about the next generation. *Seminars in Immunology*, 25, pp.172–181.
- Kermanizadeh, A. et al., 2012. In vitro assessment of engineered nanomaterials using a hepatocyte cell line: cytotoxicity, pro-inflammatory cytokines and functional markers. *Nanotoxicology*, pp.1–13.
- Kermanizadeh, A. et al., 2013. In vitro assessment of engineered nanomaterials using a hepatocyte cell line: cytotoxicity, pro-inflammatory cytokines and functional markers. *Nanotoxicology*, 7(3), pp.301–313.
- Kermanizadeh, A. et al., 2014. Toxicological effect of engineered nanomaterials on the liver. *British journal of pharmacology*, 171(17), pp.3980–7.
- Kim, J. et al., 2011. Effects of copper nanoparticle exposure on host defense in a murine pulmonary infection model. *Particle and Fibre Toxicology*, 8(1), p.29.
- Kim, J.S. et al., 2007. Antimicrobial effects of silver nanoparticles. *Nanomedicine: Nanotechnology, Biology, and Medicine*, 3, pp.95–101.
- Kirkwood, C. et al., 2009. *Mycobacterium avium* subspecies paratuberculosis in children with early-onset Crohn's disease. *Inflammatory bowel diseases*, 15, pp.1643–1655.
- Kleinstreuer, C., Feng, Y. & Childress, E., 2014. Drug-targeting methodologies with applications: A review. *World journal of clinical cases*, 2, pp.742–56.
- Kremer, L. et al., 1995. Green fluorescent protein as a new expression marker in mycobacteria. *Molecular Microbiology*, 17(5), pp.913–922.
- Kuenstner, J. et al., 2015. Resolution of Crohn's disease and complex regional pain syndrome following treatment of paratuberculosis. *World journal of gastroenterology*, 21, pp.4048–4062.
- Kuenstner, J.T., 2006. *Mycobacterium Avium* Subspecies Paratuberculosis: A Human Pathogen Causing Most Cases of Crohn's Disease. *The American Journal of Gastroenterology*, 101, pp.1157–1158.
- Lanoix, J. et al., 2015. Selective inactivity of pyrazinamide against tuberculosis in C3HeB/FeJ mice is best explained by neutral pH of caseum. *Antimicrobial agents and chemotherapy*, 16, pp.735–743.
- Larimer, C. et al., 2014. Mutation of environmental mycobacteria to resist silver nanoparticles also confers resistance to a common antibiotic. *BioMetals*, 27, pp.695–702.
- Laurenson, I. & Smith, M., 2015. *Scottish Mycobacteria Reference Laboratory Annual Report 2015*, Available at: <http://www.documents.hps.scot.nhs.uk/labs/smrl/ar-smrl-2014-2015.pdf>.
- Laurenzo, D. & Mousa, S., 2011. Mechanisms of drug resistance in *Mycobacterium tuberculosis* and current status of rapid molecular diagnostic testing. *Acta tropica*, 119(1),

pp.5–10.

- Lee, M. et al., 2015. Delamanid for Extensively Drug-Resistant Tuberculosis. *New England Journal of Medicine*, 373(3), pp.290–291.
- Lemire, J.A., Harrison, J.J. & Turner, & R.J., 2013. Antimicrobial activity of metals: mechanisms, molecular targets and applications. *Nature Reviews microbiology*, 11, pp.371–84.
- Leo, B., Chen, S. & Kyo, Y., 2013. The stability of silver nanoparticles in a model of pulmonary surfactant. *Science & technology*, 47, pp.11232–11240.
- Li, L. et al., 2005. The complete genome sequence of Mycobacterium avium subspecies paratuberculosis. *Proceedings of the National Academy of Sciences of the United States of America*, 102, pp.12344–9.
- Li, M., Zhu, L. & Lin, D., 2011. Toxicity of ZnO nanoparticles to Escherichia coli: mechanism and the influence of medium components. *Environmental science & technology*, 45(5), pp.1977–83.
- Li, N., Xia, T. & Nel, A.E., 2008. The role of oxidative stress in ambient particulate matter-induced lung diseases and its implications in the toxicity of engineered nanoparticles. *Free Radical Biology and Medicine*, 44(9), pp.1689–1699.
- Li, X. et al., 1997. Deletions of the Aequorea victoria Green Fluorescent Protein Define the Minimal Domain Required for Fluorescence. *Protein Chemistry and structure*, 272, pp.28545–28549.
- Lienhardt, C. et al., 2011. Efficacy and safety of a 4-drug fixed-dose combination regimen compared with separate drugs for treatment of pulmonary tuberculosis: the Study C randomized controlled trial. *The journal of the American Medical Association*, 305, pp.1415–1423.
- Lin, P.L. et al., 2012. Metronidazole prevents reactivation of latent Mycobacterium tuberculosis infection in macaques. *Proceedings of the National Academy of Sciences*, 109(35), pp.14188–14193.
- Liu, B., Li, S. & Hu, J., 2004. Technological advances in high-throughput screening. *American journal of pharmacogenomics: genomics-related research in drug development and clinical practice*, 4, pp.263–276.
- Liu, Y., Miyoshi, H. & Nakamura, M., 2007. Nanomedicine for drug delivery and imaging: a promising avenue for cancer therapy and diagnosis using targeted functional nanoparticles. *International journal of cancer. Journal international du cancer*, 120, pp.2527–2537.
- Löfmark, S., Edlund, C. & Nord, C.E., 2010. Metronidazole is still the drug of choice for treatment of anaerobic infections. *Clinical Infectious Diseases*, 50(Suppl 1), pp.S16–S23.
- Lok, C.-N. et al., 2007. Silver nanoparticles: partial oxidation and antibacterial activities. *Journal of biological inorganic chemistry : JBIC : a publication of the Society of Biological Inorganic Chemistry*, 12(4), pp.527–534.
- Longo, D.L. et al., 2015. Treatment of Tuberculosis. *New England Journal of Medicine*, 373, pp.2149–2160.
- Lu, C., Bentley, W. & Rao, G., 2004. A high-throughput approach to promoter study using green fluorescent protein. *Biotechnology Progress*, 20, pp.1634–1640.
- Lucas, V.S. et al., 2002. Comparison of lysis filtration and an automated blood culture system (BACTEC) for detection, quantification, and identification of odontogenic bacteremia in

- children. *Journal of Clinical Microbiology*, 40(9), pp.3416–3420.
- Maartens, G. & Wilkinson, R., 2007. Tuberculosis. *Lancet*, 370, pp.2030–43.
- Madison, B. et al., 2002. Multicenter evaluation of ethambutol susceptibility testing of mycobacterium tuberculosis by agar proportion and radiometric methods. *Journal Clinical of Microbiology*, 40(11), pp.3976–3979.
- Makhlouf, H.A. et al., 2008. A prospective study of antituberculous drug-induced hepatotoxicity in an area endemic for liver diseases. *Hepatology international*, 2(3), pp.353–60.
- Malik, Z., Denning, G. & Kusner, D., 2000. Inhibition of Ca(2+) signaling by Mycobacterium tuberculosis is associated with reduced phagosome-lysosome fusion and increased survival within human macrophages. *The Journal of experimental medicine*, 191(2), pp.287–302.
- Manivannan, S., Rao, N. V & Ramanathan, V.D., 2012. Role of complement activation and antibody in the interaction between Mycobacterium tuberculosis and human macrophages. *Indian journal of experimental biology*, 50(8), pp.542–50.
- Martin, A. et al., 2003. Resazurin microtiter assay plate testing of Mycobacterium tuberculosis susceptibilities to second-line drugs: rapid, simple, and inexpensive method. *Antimicrobial agents and chemotherapy*, 47(11), pp.3616–9.
- McCarron, P.A. et al., 2008. Antibody targeting of camptothecin-loaded PLGA nanoparticles to tumor cells. *Bioconjugate Chemistry*, 19, pp.1561–1569.
- McDonald, T. et al., 2015. Nanoengineering: Global approaches to health and safety issuesDolez, P. In P. Dolez, ed. Amsterdam: Elsevier, pp. 173–208.
- McDonald, T.O. et al., 2014. Antiretroviral Solid Drug Nanoparticles with Enhanced Oral Bioavailability: Production, Characterization, and In Vitro-In Vivo Correlation. *Advanced Healthcare Materials*, 3, pp.400–411.
- Mcdonald, T.O. et al., 2014. Antiretroviral Solid Drug Nanoparticles with Enhanced Oral Bioavailability: Production, Characterization, and In Vitro-In Vivo Correlation. *Advanced Healthcare Materials*, 3, pp.400–411.
- Medici, S. et al., 2015. Noble metals in medicine: Latest advances. *Coordinaation Chemistry Reviews*, pp.329–350.
- Meerovich, G. et al., 2008. Influence of Liposome Size on Accumulation in Tumor and Therapeutic Efficiency of Liposomal Near-IR Photosensitizer for PDT based on Aluminum hydroxide tetra-3-phenylthiophthalocyanine. *Nsti Nanotech 2008, Vol 2, Technical Proceedings*, 2, pp.41–44.
- Meng, X.-Y. et al., 2011. Molecular docking: a powerful approach for structure-based drug discovery. *Current computer-aided drug design*, 7(2), pp.146–157.
- Merdzan, V. et al., 2014. The effects of different coatings on zinc oxide nanoparticles and their influence on dissolution and bioaccumulation by the green alga, *C. reinhardtii*. *Science of the Total Environment*, 488-489, pp.316–324.
- Minh, N. et al., 2012. Molecular characteristics of rifampin- and isoniazid-resistant mycobacterium tuberculosis strains isolated in Vietnam. *Journal of clinical microbiology*, 50(3), pp.598–601.
- Mizoe, T., Ozeki, T. & Okada, H., 2008. Application of a four-fluid nozzle spray drier to prepare inhalable rifampicin-containing mannitol microparticles. *AAPS PharmSciTech*, 9(3), pp.755–761.

- Mohanty, S. et al., 2013. Cationic Antimicrobial Peptides and Biogenic Silver Nanoparticles Kill Mycobacteria without Eliciting DNA Damage and Cytotoxicity in Mouse Macrophages. *Antimicrobial Agents and Chemotherapy*, 57(8), pp.3688–3698.
- Mokaddas, E. et al., 2015. Discordance between Xpert MTB/RIF and BACTEC MGIT 960 culture system for detection of rifampin-resistant Mycobacterium tuberculosis isolates in a low TB incidence country. *Journal of clinical microbiology*, 53, pp.1–14.
- Montoya, J. et al., 2013. A randomized, controlled dose-finding Phase II study of the M72/AS01 candidate tuberculosis vaccine in healthy PPD-positive adults. *Journal of Clinical Immunology*, 33, pp.1360–1375.
- Morones-Ramirez, J. et al., 2013. Silver Enhances Antibiotic Activity Against Gram-negative Bacteria. *Sci Transl Med*, 5(190).
- Müller, K.H. et al., 2014. The effect of particle agglomeration on the formation of a surface-connected compartment induced by hydroxyapatite nanoparticles in human monocyte-derived macrophages. *Biomaterials*, 35(3), pp.1074–1088.
- Mumper, C. et al., 2013. Influence of ammonia on silver nanoparticle dissolution and toxicity to *Nitrosomonas europaea*. *Chemosphere*, 93(10), pp.2493–2498.
- Naser, S., Schwartz, D. & Safran, I., 2000. Isolation of Mycobacterium avium subsp paratuberculosis from breast milk of Crohn's disease patients. *American Journal of Gastroenterology*, 95, pp.1094–1095.
- Navalakhe, R. & Nandedkar, T., 2007. Application of nanotechnology in biomedicine. *Indian journal of experimental biology*, 45(2), pp.160–5.
- Neyrolles, O., Mintz, E. & Catty, P., 2013. Zinc and copper toxicity in host defense against pathogens: Mycobacterium tuberculosis as a model example of an emerging paradigm. *Frontiers in Cellular and Infection Microbiology*, 3, pp.3–6.
- NHS, 2012. BCG tuberculosis (TB) vaccine. Available at: <http://www.nhs.uk/Conditions/vaccinations/Pages/bcg-tuberculosis-TB-vaccine.aspx> [Accessed December 2, 2013].
- NHS, 2015. NHS News. Available at: <https://www.england.nhs.uk/2015/01/19/tuberculosis/> [Accessed April 13, 2015].
- NHS, 2014. TB Treatment NHS Choices. *NHS Choices*. Available at: <http://www.nhs.uk/Conditions/Tuberculosis/Pages/Treatment.aspx> [Accessed October 25, 2015].
- NHS, 2011. Tuberculosis (TB) - Symptoms. Available at: <http://www.nhs.uk/Conditions/Tuberculosis/Pages/Symptoms.aspx> [Accessed October 10, 2012].
- Niemirowicz, K. et al., 2012. Magnetic nanoparticles as new diagnostic tools in medicine. *Advances in medical sciences*, 57(2), pp.196–207.
- Oberdörster, G., Stone, V. & Donaldson, K., 2007. Toxicology of nanoparticles: A historical perspective. *Nanotoxicology*, 1(1), pp.2–25.
- Odzak, N. et al., 2014. Dissolution of metal and metal oxide nanoparticles in aqueous media. *Environmental Pollution*, 191, pp.132–138.
- Ohara, N., 2012. Current status of tuberculosis and recombinant bacillus Calmette-Guérin vaccines. *Journal of Oral Biosciences*, 54, pp.92–95.

- Ohashi, K. et al., 2009. One-step preparation of rifampicin/poly(lactic-co-glycolic acid) nanoparticle-containing mannitol microspheres using a four-fluid nozzle spray drier for inhalation therapy of tuberculosis. *Journal of Controlled Release*, 135(1), pp.19–24.
- Onoshita, T. et al., 2010. The behavior of PLGA microspheres containing rifampicin in alveolar macrophages. *Colloids and surfaces. B, Biointerfaces*, 76(1), pp.151–7.
- Onoue, S., Yamada, S. & Chan, H.K., 2014. Nanodrugs: Pharmacokinetics and safety. *International Journal of Nanomedicine*, 9(1), pp.1025–1037.
- Owens, B., 2013a. *Nature News: Silver makes antibiotics thousands of times more effective*, Available at: <http://www.nature.com/news/silver-makes-antibiotics-thousands-of-times-more-effective-1.13232>.
- Owens, B., 2013b. *Nature News: Silver makes antibiotics thousands of times more effective*,
- Ozeki, Y. et al., 2015. A New Screen for Tuberculosis Drug Candidates Utilizing a Luciferase-Expressing Recombinant Mycobacterium bovis Bacillus Calmette-Guérin. *Plos One*, 10(11), p.e0141658.
- Padmavathy, N. & Vijayaraghavan, R., 2008. Enhanced bioactivity of ZnO nanoparticles—an antimicrobial study. *Science and Technology of Advanced Materials*, 9(3), p.035004.
- Pal, S., Tak, Y.K. & Song, J.M., 2007. Does the antibacterial activity of silver nanoparticles depend on the shape of the nanoparticle? A study of the Gram-negative bacterium Escherichia coli. *Applied and environmental microbiology*, 73, pp.1712–20.
- Pandey, R. et al., 2003. Nanoparticle encapsulated antitubercular drugs as a potential oral drug delivery system against murine tuberculosis. *Tuberculosis*, 83(6), pp.373–378.
- Pandey, R. & Ahmad, Z., 2011. Nanomedicine and experimental tuberculosis: facts, flaws, and future. *Nanomedicine : nanotechnology, biology, and medicine*, 7(3), pp.259–72.
- Pandey, R. & Khuller, G., 2006. Nanotechnology based drug delivery system(s) for the management of tuberculosis. *Indian journal of experimental biology*, 44(5), pp.357–366.
- Pandey, R. & Khuller, G.K., 2005. Solid lipid particle-based inhalable sustained drug delivery system against experimental tuberculosis. *Tuberculosis*, 85(4), pp.227–234.
- Pandey, U.B. & Nichols, C.D., 2011. Human Disease Models in Drosophila melanogaster and the Role of the Fly in Therapeutic Drug Discovery. *Drug Delivery*, 63(2), pp.411–436.
- Panyam, J. et al., 2002. Rapid endo-lysosomal escape of poly(DL-lactide-co-glycolide) nanoparticles: implications for drug and gene delivery. *The FASEB journal : official publication of the Federation of American Societies for Experimental Biology*, 16(10), pp.1217–1226.
- Park, H. et al., 2009. Silver-ion-mediated reactive oxygen species generation affecting bactericidal activity. *Water research*, 43(4), pp.1027–1032.
- Parker, A.E. & Bermudez, L.E., 1997. Expression of the green fluorescent protein (GFP) in Mycobacterium avium as a tool to study the interaction between Mycobacteria and host cells. *Microb Pathog*, 22, pp.193–198.
- Pasquet, J. et al., 2014. The contribution of zinc ions to the antimicrobial activity of zinc oxide. *Colloids and Surfaces A: Physicochemical and Engineering Aspects*, 457, pp.263–274.
- Patel, B.K., Parikh, R.H. & Aboti, P.S., 2013. Development of oral sustained release rifampicin loaded chitosan nanoparticles by design of experiment. *Journal of drug delivery*, 2013, p.370938.

- Pati, R. et al., 2014. Topical application of zinc oxide nanoparticles reduces bacterial skin infection in mice and exhibits antibacterial activity by inducing oxidative stress response and cell membrane disintegration in macrophages. *Nanomedicine: Nanotechnology, Biology and Medicine*, 10(6), pp.1195–1208.
- Patino, S. et al., 2008. Autofluorescence of Mycobacteria as a Tool for Detection of Mycobacterium tuberculosis. *Journal of Clinical Microbiology*, 46(10), pp.3296–3302.
- Pecora, R., 2000. Dynamic light scattering measurement of nanometer particles in liquids. *Journal of Nanoparticle Research*, 2, pp.123–131.
- Pelgrift, R.Y. & Friedman, A.J., 2013. Nanotechnology as a therapeutic tool to combat microbial resistance. *Advanced drug delivery reviews*, 65, pp.1803–1815.
- Peñuelas-Urquides, K. et al., 2013. Measuring of Mycobacterium tuberculosis growth. A correlation of the optical measurements with colony forming units. *Brazilian journal of microbiology*, 44(1), pp.287–289.
- Pericleous, P. et al., 2012. Quantum dots hold promise for early cancer imaging and detection. *International journal of cancer. Journal international du cancer*, 131(3), pp.519–28.
- Perry, J. et al., 2011. PRINT: a novel platform toward shape and size specific nanoparticle theranostics. *Accounts of Chemical Research*, 10, pp.990–8.
- Pham, D.-D., Fattal, E. & Tsapis, N., 2015. Pulmonary drug delivery systems for tuberculosis treatment. *International Journal of Pharmaceutics*, 478(2), pp.517–529.
- Pieters, J., 2008. Mycobacterium tuberculosis and the macrophage: maintaining a balance. *Cell host & microbe*, 3, pp.399–407.
- Pinto, R.J.B. et al., 2013. Antibacterial activity of nanocomposites of copper and cellulose. *BioMed research international*, 2013, p.280512.
- Plain, K.M. et al., 2011. Indoleamine 2,3-dioxygenase, tryptophan catabolism, and Mycobacterium avium subsp. paratuberculosis: a model for chronic mycobacterial infections. *Infection and immunity*, 79, pp.3821–3832.
- Podinovskaia, M. et al., 2013. Infection of macrophages with Mycobacterium tuberculosis induces global modifications to phagosomal function. *Cellular microbiology*, 15, pp.843–59.
- Prach, M., Stone, V. & Proudfoot, L., 2013. Zinc oxide nanoparticles and monocytes: impact of size, charge and solubility on activation status. *Toxicology and applied pharmacology*, 266(1), pp.19–26.
- Prezzemolo, T. et al., 2014. Functional Signatures of Human CD4 and CD8 T Cell Responses to Mycobacterium tuberculosis. *Frontiers in Immunology Immunology*, 5, p.180.
- Primm, T.P. & Franzblau, S.G., 2007. Recent Advances in Methodologies for the Discovery of Antimycobacterial Drugs. *Current Bioactive Compounds*, 3, pp.201–208.
- Public Health England, 2015. Tuberculosis cases UK: 2000 to 2014. Available at: [https://www.gov.uk/government/uploads/system/uploads/attachment\\_data/file/464361/PH\\_E\\_TB\\_Official\\_Statistics\\_v2.1\\_final.pdf](https://www.gov.uk/government/uploads/system/uploads/attachment_data/file/464361/PH_E_TB_Official_Statistics_v2.1_final.pdf).
- Public Health England, 2014a. *Tuberculosis in the UK 2014 report*, Available at: [https://www.gov.uk/government/uploads/system/uploads/attachment\\_data/file/360335/TB\\_Annual\\_report\\_\\_4\\_0\\_300914.pdf](https://www.gov.uk/government/uploads/system/uploads/attachment_data/file/360335/TB_Annual_report__4_0_300914.pdf) [Accessed August 13, 2015].
- Public Health England, 2014b. Tuberculosis in the UK: 2014 report. *Public Health England*,



- p.97. Available at: <https://www.gov.uk/government/publications/tuberculosis-tb-in-the-uk>.
- Puzyn, T. et al., 2011. Using nano-QSAR to predict the cytotoxicity of metal oxide nanoparticles. *Nature nanotechnology*, 6(3), pp.175–178.
- Rai, M. et al., 2015. Strategic role of selected noble metal nanoparticles in medicine. *Critical Reviews in Microbiology*, 19, pp.1–24.
- Rai, M., Yadav, A. & Gade, A., 2009. Silver nanoparticles as a new generation of antimicrobials. *Biotechnology advances*, 27, pp.76–83.
- Raj, C.A., Kumar, P.S. & Kumar, K.S., 2012. KINETICS AND DRUG RELEASE STUDIES OF ISONIAZID ENCAPSULATED WITH PLA-COPEG/ GOLD NANOPARTICLES. *International Journal of Pharmacy and Pharmaceutical Sciences*, 4(4), pp.1–7.
- Ramani, M. et al., 2013. Morphology-directed synthesis of ZnO nanostructures and their antibacterial activity. *Colloids and surfaces. B, Biointerfaces*, 105, pp.24–30.
- Rampersad, S.N., 2012. Multiple Applications of Alamar Blue as an Indicator of Metabolic Function and Cellular Health in Cell Viability Bioassays. *Sensors*, 12(12), pp.12347–12360.
- Remijnsen, Q. et al., 2011. Dying for a cause: NETosis, mechanisms behind an antimicrobial cell death modality. *Cell death and differentiation*, 18, pp.581–588.
- Ren, G. et al., 2009. Characterisation of copper oxide nanoparticles for antimicrobial applications. *International Journal of Antimicrobial Agents*, 33(6), pp.587–590.
- Repasy, T. et al., 2013. Intracellular Bacillary Burden Reflects a Burst Size for Mycobacterium tuberculosis In Vivo. *PLoS Pathogens*, 9(2).
- Robbe-Austerman, S., Bravo, D.M. & Harris, B., 2013. Comparison of the MGIT 960, BACTEC 460 TB and solid media for isolation of Mycobacterium bovis in United States veterinary specimens. *BMC veterinary research*, 9(1), p.74.
- Rowland, K., 2012. Totally drug-resistant TB emerges in India. Discovery of a deadly form of TB highlights crisis of “mismanagement.” *Nature News*. Available at: <http://www.nature.com/news/totally-drug-resistant-tb-emerges-in-india-1.9797> [Accessed August 11, 2015].
- Ruparelia, J. et al., 2007. Strain specificity in antimicrobial activity of silver and copper nanoparticles. *Acta biomaterialia*, 4(3), pp.707–716.
- Russell, D.G. et al., 2010. Foamy macrophages and the progression of the human TB granuloma. *Nature immunology*, 10, pp.943–948.
- Russell, D.G., 2011. Mycobacterium tuberculosis and the intimate discourse of a chronic infection. *Immunological reviews*, 240, pp.252–68.
- Sandhya, R. et al., 2013. Pulmonary Toxicity of Copper Oxide (CuO) Nanoparticles in Rats. *Journal of Medical Sciences*, 7, pp.571–577.
- Sartor, R.B., 2005. Does Mycobacterium avium subspecies paratuberculosis cause Crohn’s disease? *Gut*, 54(7), pp.896–898.
- Schindelin, J. et al., 2012. Fiji: an open-source platform for biological-image analysis. *Nature methods*, 9, pp.676–682.
- Sechi, L. et al., 2005. Detection and Isolation of Mycobacterium avium subspecies paratuberculosis from intestinal mucosal biopsies of patients with and without Crohn’s disease in Sardinia. *The American Journal of Gastroenterology*, 100, pp.1529–1536.

- Semete, B. et al., 2010. In vivo evaluation of the biodistribution and safety of PLGA nanoparticles as drug delivery systems. *Nanomedicine: Nanotechnology, Biology and Medicine*, 6(5), pp.662–671.
- Seth, D. et al., 2011. Nature-inspired novel drug design paradigm using nanosilver: efficacy on multi-drug-resistant clinical isolates of tuberculosis. *Current Microbiology*, 62(3), pp.715–26.
- Sharma, S. et al., 2014. Simple and Rapid Method To Determine Antimycobacterial Potency of Compounds by Using Autoluminescent Mycobacterium tuberculosis. *Antimicrobial Agents and Chemotherapy*, 58, pp.5801–5808.
- Sharma, V. et al., 2012. Induction of oxidative stress, DNA damage and apoptosis in mouse liver after sub-acute oral exposure to zinc oxide nanoparticles. *Mutation Research/Genetic Toxicology and Environmental Mutagenesis*, 745(1-2), pp.84–91.
- Sharma, V.K., Yngard, R.A. & Lin, Y., 2009. Silver nanoparticles: Green synthesis and their antimicrobial activities. *Advances in Colloid and Interface Science*, 145, pp.83–96.
- Shu, C.C. et al., 2013. Hepatotoxicity due to first-line anti-tuberculosis drugs: A five-year experience in a Taiwan medical centre. *International Journal of Tuberculosis and Lung Disease*, 17, pp.934–939.
- Sigma, 1997. *Rifampicin product sheet*, Available at: [https://www.sigmaaldrich.com/content/dam/sigma-aldrich/docs/Sigma/Product\\_Information\\_Sheet/1/r3501pis.pdf](https://www.sigmaaldrich.com/content/dam/sigma-aldrich/docs/Sigma/Product_Information_Sheet/1/r3501pis.pdf).
- da Silva, P.E.A. & Palomino, J.C., 2011. Molecular basis and mechanisms of drug resistance in Mycobacterium tuberculosis: Classical and new drugs. *Journal of Antimicrobial Chemotherapy*, 66(7), pp.1417–1430.
- Silver, L.L., 2011. Challenges of antibacterial discovery. *Clinical microbiology reviews*, 24(1), pp.71–109.
- Simeone, R. et al., 2015. Cytosolic Access of Mycobacterium tuberculosis: Critical Impact of Phagosomal Acidification Control and Demonstration of Occurrence In Vivo. *PLoS Pathogens*, 11, pp.1–24.
- Smith, I., 2003. Mycobacterium tuberculosis Pathogenesis and Molecular Determinants of Virulence. *Clinical Microbiology Reviews*, 16, pp.463–96.
- Smith, J., 2011. Nanoparticle delivery of anti-tuberculosis chemotherapy as a potential mediator against drug-resistant tuberculosis. *The Yale journal of biology and medicine*, 84(4), pp.361–9.
- Smith, N., 2006. A re-evaluation of M. prototuberculosis. *PLoS Pathogens*, 2, pp.0809–0811.
- Somoskovi, A., Parsons, L.M. & Salfinger, M., 2001. The molecular basis of resistance to isoniazid, rifampin, and pyrazinamide in Mycobacterium tuberculosis. *Respiratory research*, 2, pp.164–8.
- Song, H. et al., 2012. Expression of the ompATb operon accelerates ammonia secretion and adaptation of Mycobacterium tuberculosis to acidic environments. *Molecular Microbiology*, 80, pp.900–918.
- Song, Y., Li, X. & Du, X., 2009. Exposure to nanoparticles is related to pleural effusion, pulmonary fibrosis and granuloma. *European Respiratory Journal*, 34(3), pp.559–567.
- Sosnik, A. et al., 2010. New old challenges in tuberculosis: potentially effective nanotechnologies in drug delivery. *Advanced drug delivery reviews*, 62(4-5), pp.547–59.

- Sreevatsan, S., Stockbauer, K., et al., 1997. Ethambutol resistance in *Mycobacterium tuberculosis*: critical role of embB mutations. *Antimicrobial agents and chemotherapy*, 41, pp.1677–81.
- Sreevatsan, S., Pan, X., et al., 1997. Restricted structural gene polymorphism in the *Mycobacterium tuberculosis* complex indicates evolutionarily recent global dissemination. *Proceedings of the National Academy of Sciences of the United States of America*, 94, pp.9869–9874.
- Srivastava, R. et al., 1998. Green fluorescent protein as a reporter in rapid screening of antituberculosis compounds in vitro and in macrophages. *Biochemical and biophysical research communications*, 253, pp.431–436.
- Steff, A.M. et al., 2001. Detection of a decrease in green fluorescent protein fluorescence for the monitoring of cell death: An assay amenable to high-throughput screening technologies. *Cytometry*, 45(4), pp.237–243.
- Stevenson, K. & Sharp, J., 1997. The Contribution of Molecular Biology to *Mycobacterium avium* Subspecies Paratuberculosis Research. *The Veterinary Journal*, 153, pp.269–286.
- Steyn, D., Plessis, L. & Kotzé, A., 2010. Nasal Delivery of Recombinant Human Growth Hormone : In Vivo Evaluation with Pheroid™ Technology and N-Trimethyl Chitosan Chloride. , 13(2), pp.263–273.
- Suarez, S. et al., 2001. Respirable PLGA microspheres containing rifampicin for the treatment of tuberculosis: screening in an infectious disease model. *Pharm Res*, 18(9), pp.1315–1319.
- Sun, Z., Scorpio, A. & Zhang, Y., 1997. The pncA gene from naturally pyrazinamide-resistant *Mycobacterium avium* encodes pyrazinamidase and confers pyrazinamide susceptibility to resistant *M. tuberculosis* complex organisms. *Microbiology*, 143, pp.3367–3373.
- Swaminathan, S. & Narendran, G., 2008. HIV and tuberculosis in India. *Journal of Biosciences*, 33(4), pp.527–537.
- Szymański, P., Markowicz, M. & Mikiciuk-Olasik, M., 2012. Adaptation of high-throughput screening in drug discovery-toxicological screening tests. *International Journal of Molecular Sciences*, 13(1), pp.427–452.
- Tameris, M.D. et al., 2013. Safety and efficacy of MVA85A, a new tuberculosis vaccine, in infants previously vaccinated with BCG: a randomised, placebo-controlled phase 2b trial. *Lancet*, 381(9871), pp.1021–1028.
- Tan, S. et al., 2013. *Mycobacterium tuberculosis* Responds to Chloride and pH as Synergistic Cues to the Immune Status of its Host Cell W. R. Bishai, ed. *PLoS Pathogens*, 9, p.e1003282.
- The Times of India, 2016. Surge in drug-resistant TB cases across state. Available at: <http://timesofindia.indiatimes.com/city/pune/Surge-in-drug-resistant-TB-cases-across-state/articleshow/50635131.cms> [Accessed January 21, 2016].
- Theophel, K. et al., 2014. The importance of growth kinetic analysis in determining bacterial susceptibility against antibiotics and silver nanoparticles. *Frontiers in microbiology*, 5(10), p.544.
- Thit, A., Selck, H. & Bjerregaard, H.F., 2013. Toxicity of CuO nanoparticles and Cu ions to tight epithelial cells from *xenopus laevis* (A6): Effects on proliferation, cell cycle progression and cell death. *Toxicology in Vitro*, 27, pp.1596–1601.
- Tostmann, A. et al., 2008. Antituberculosis drug-induced hepatotoxicity: Concise up-to-date

- review. *Journal of Gastroenterology and Hepatology*, 23(2), pp.192–202.
- Tran, C. et al., 2000. Inhalation of poorly soluble particles. II. Influence Of particle surface area on inflammation and clearance. *Inhalation Toxicology*, 12, pp.1113–1126.
- Trunz, B.B., Fine, P. & Dye, C., 2006. Effect of BCG vaccination on childhood tuberculous meningitis and miliary tuberculosis worldwide: a meta-analysis and assessment of cost-effectiveness. *Lancet*, 367(9517), pp.1173–11780.
- Vandebriel, R.J. & De Jong, W.H., 2012. A review of mammalian toxicity of ZnO nanoparticles. *Nanotechnology, Science and Applications*, 5(1), pp.61–71.
- Verschoor, J., Baird, M. & Grooten, J., 2012. Towards understanding the functional diversity of cell wall mycolic acids of Mycobacterium tuberculosis. *Progress in lipid research*, 51(4), pp.325–39.
- Völker, C. et al., 2013. Comparative toxicity assessment of nanosilver on three Daphnia species in acute, chronic and multi-generation experiments. *PloS one*, 8(10), p.e75026.
- Warheit, D.B., Reed, K.L. & Sayes, C.M., 2009. A role for surface reactivity in TiO<sub>2</sub> and quartz-related nanoparticle pulmonary toxicity. *Nanotoxicology*, 3(3), pp.181–187.
- Waters, W.R. et al., 2003. Early Induction of Humoral and Cellular Immune Responses during Experimental Mycobacterium avium subsp . paratuberculosis Infection of Calves Early Induction of Humoral and Cellular Immune Responses during Experimental Mycobacterium avium subsp . paratube. *Infection and Immunity*, 71, pp.5130–5138.
- Weissleder, R., Nahrendorf, M. & Pittet, M.J., 2014. Imaging macrophages with nanoparticles. *Nature materials*, 13(2), pp.125–38. Available at: <http://www.ncbi.nlm.nih.gov/pubmed/24452356>.
- WHO, 2014a. Antimicrobial resistance Global Report on Surveillance. Available at: [http://apps.who.int/iris/bitstream/10665/112642/1/9789241564748\\_eng.pdf?ua=1](http://apps.who.int/iris/bitstream/10665/112642/1/9789241564748_eng.pdf?ua=1) [Accessed June 20, 2015].
- WHO, 2015a. Global summary of the HIV/AIDS epidemic 2014. Available at: [http://www.who.int/hiv/data/epi\\_core\\_july2015.png?ua=1](http://www.who.int/hiv/data/epi_core_july2015.png?ua=1) [Accessed October 30, 2015].
- WHO, 2015b. *Global TB Report 2015*, Available at: [http://apps.who.int/iris/bitstream/10665/191102/1/9789241565059\\_eng.pdf?ua=1](http://apps.who.int/iris/bitstream/10665/191102/1/9789241565059_eng.pdf?ua=1).
- WHO, 2011. *Global Tuberculosis Report 2011*, Available at: [http://www.who.int/tb/publications/global\\_report/2011/gtbr11\\_full.pdf](http://www.who.int/tb/publications/global_report/2011/gtbr11_full.pdf).
- WHO, 2012. *Global Tuberculosis Report 2012*, Available at: [http://apps.who.int/iris/bitstream/10665/75938/1/9789241564502\\_eng.pdf](http://apps.who.int/iris/bitstream/10665/75938/1/9789241564502_eng.pdf).
- WHO, 2013. *Global Tuberculosis Report 2013*, Available at: [http://apps.who.int/iris/bitstream/10665/91355/1/9789241564656\\_eng.pdf](http://apps.who.int/iris/bitstream/10665/91355/1/9789241564656_eng.pdf).
- WHO, 2014b. *Global Tuberculosis Report 2014*, Available at: [http://www.who.int/tb/publications/global\\_report/en/](http://www.who.int/tb/publications/global_report/en/).
- WHO Factsheet, 2012. WHO TB DIAGNOSTICS Xpert MTB/RIF Test. Available at: [http://who.int/tb/features\\_archive/factsheet\\_xpert.pdf](http://who.int/tb/features_archive/factsheet_xpert.pdf).
- Williams, S.L., Harris, N.B. & Barletta, R.G., 1999. Development of a firefly luciferase-based assay for determining antimicrobial susceptibility of Mycobacterium avium subsp. paratuberculosis. *Journal of clinical microbiology*, 37, pp.304–309.
- Wirth, T. et al., 2008. Origin, spread and demography of the Mycobacterium tuberculosis

- complex. *PLoS Pathogens*, 4(9), p.e1000160.
- Wong, K.-W. & Jacobs, W.R., 2016. Postprimary Tuberculosis and Macrophage Necrosis: Is There a Big ConNEction? *American Society for Microbiology*, 7, pp.e01589–15.
- Wong, S.W.Y. et al., 2010. Toxicities of nano zinc oxide to five marine organisms: Influences of aggregate size and ion solubility. *Analytical and Bioanalytical Chemistry*, 396(2), pp.609–618.
- Wu, B. et al., 2010. Bacterial responses to Cu-doped TiO<sub>2</sub> nanoparticles. *Science of The Total Environment*, 408(7), pp.1755–1758.
- Yacobi, N.R. et al., 2010. Mechanisms of alveolar epithelial translocation of a defined population of nanoparticles. *American Journal of Respiratory Cell and Molecular Biology*, 42, pp.604–614.
- Yajko, D.M. et al., 1995a. Colorimetric method for determining MICs of antimicrobial agents for *Mycobacterium tuberculosis*. *Journal of clinical microbiology*, 33, pp.2324–7.
- Yajko, D.M. et al., 1995b. Colorimetric method for determining MICs of antimicrobial agents for *Mycobacterium tuberculosis*. *Journal of clinical microbiology*, 33(9), pp.2324–7.  
Available at:  
<http://www.pubmedcentral.nih.gov/articlerender.fcgi?artid=228403&tool=pmcentrez&rendertype=abstract>.
- Yang, H., Kruh-Garcia, N. & Dobos, K., 2012. Purified protein derivatives of tuberculin - past, present, and future. *FEMS immunology and medical microbiology*, 66(3), pp.273–80.
- Yang, H., Zhu, S. & Pan, N., 2004. Studying the mechanisms of titanium dioxide as ultraviolet-blocking additive for films and fabrics by an improved scheme. *Journal of Applied Polymer Science*, 92(5), pp.3201–3210.
- Yasuyuki, M. et al., 2010. Antibacterial properties of nine pure metals: a laboratory study using *Staphylococcus aureus* and *Escherichia coli*. *Biofouling*, 26(7), pp.851–858.
- Yuan, Z. et al., 2012. Interaction of silver nanoparticles with pure nitrifying bacteria. *Chemosphere*, 90(4), pp.1404–1411.
- Zanetti, S. et al., 2006. “In vitro” activities of antimycobacterial agents against *Mycobacterium avium* subsp. paratuberculosis linked to Crohn’s disease and paratuberculosis. *Annals of clinical microbiology and antimicrobials*, 3, pp.4–6.
- Zhang, P. et al., 2015. *Mycobacterium avium* subspecies hominissuis in Crohn’s disease: a case report. *Gastroenterology Report*, pp.1–4.
- Zhang, Y. et al., 2003. Mode of action of pyrazinamide: disruption of *Mycobacterium tuberculosis* membrane transport and energetics by pyrazinoic acid. *The Journal of antimicrobial chemotherapy*, 52, pp.790–795.
- Zhang, Y., 2014. Persisters, persistent infections and the Yin-Yang model. *Emerging microbes & infections*, 3, p.e3.
- Zhang, Y. & Yew, W., 2009. Mechanisms of drug resistance in *Mycobacterium tuberculosis*. *The International Journal of Tuberculosis and Lung Disease*, 13, pp.1320–1330.
- Zhang, Y., Yew, W.W. & Barer, M.R., 2012. Targeting persisters for tuberculosis control. *Antimicrobial Agents and Chemotherapy*, 56(5), pp.2223–2230.
- Zhao, C.-M. & Wang, W.-X., 2012. Importance of surface coatings and soluble silver in silver nanoparticles toxicity to *Daphnia magna*. *Nanotoxicology*, 6(4), pp.361–70.

Zinjarde, S., 2012. Bio-inspired nanomaterials and their applications as antimicrobial agents.  
*Chronicles of Young Scientists*, 3(1), p.74.